REACTIVE TRANSPORT IN BIOFOULED AND BIOMINERALIZED POROUS MEDIA

by

Logan Nicholas Schultz

A thesis submitted in partial fulfillment
of the requirements for the degree

of

Master of Science

in

Chemical Engineering

MONTANA STATE UNIVERSITY
Bozeman, Montana

January, 2010

APPROVAL

of a thesis submitted by

Logan Nicholas Schultz

This thesis has been read by each member of the thesis committee and has been found to be satisfactory regarding content, English usage, format, citation, bibliographic style, and consistency, and is ready for submission to the Division of Graduate Education.

Dr. Robin Gerlach

Approved for the Department Chemical and Biological Engineering

Dr. Ronald Larsen

Approved for the Division of Graduate Education

Dr. Carl A. Fox

STATEMENT OF PERMISSION TO USE

In presenting this thesis in partial fulfillment of the requirements for a master's degree at Montana State University, I agree that the Library shall make it available to borrowers under rules of the Library.

If I have indicated my intention to copyright this thesis by including a copyright notice page, copying is allowable only for scholarly purposes, consistent with "fair use" as prescribed in the U.S. Copyright Law. Requests for permission for extended quotation from or reproduction of this thesis in whole or in parts may be granted only by the copyright holder.

Logan Nicholas Schultz

January, 2010

ACKNOWLEDGEMENTS

This work was supported by the U.S. Department of Energy (DOE) Zero Emissions Research and Technology project, award no. DE-FC26-04NT42262, the DOE Office of Science, Environmental Remediation Science Program (ERSP), contract no. DE-FG02-09ER64758, and the U.S. Department of Energy EPSCoR program under grant number DE-FG02-08ER46527. I acknowledge funding for the Environmental and Biofilm Mass Spectrometry Facility at MSU through the Defense University Research Instrumentation Program, contract number: W911NF0510255. Imaging facilities were provided by the Center for Biofilm Engineering, Bozeman, MT, and the confocal microscope was funded through a grant from the M.J. Murdock Charitable Trust.

In developing this thesis, several individuals deserve credit for shaping my investigations and personal growth. I thank Betsey Pitts for her microscopy expertise. I thank Adie Phillips for her efforts in developing the high pressure systems. I thank Dr. Andrew Mitchell for his expertise in biomineralization and manuscript preparation. I thank Stacy Biebel for her lab companionship. I thank Hans Bernstein, Rob Gardner, Liz Sandvik, Steve Bugni, Elliot Barnhart, Erin Field, Kelly O'Shea, Kristen Brileya, Sabrina Behnke, and Marcus Dieser for their office camaraderie.

I thank my committee members, Dr. Al Cunningham, Dr. Steven Rutherford, and especially my advisor, Dr. Robin Gerlach for the countless opportunities, patience, and respect he has shown me as a student, and the time he has spent helping me grow as a researcher and person over the past four and a half years.

TABLE OF CONTENTS

TABLE OF CONTENTS - CONTINUED

TABLE OF CONTENTS - CONTINUED

TABLE OF CONTENTS - CONTINUED

LIST OF TABLES

LIST OF TABLES – CONTINUED

LIST OF FIGURES

LIST OF FIGURES - CONTINUED

LIST OF FIGURES - CONTINUED

LIST OF FIGURES - CONTINUED

LIST OF FIGURES - CONTINUED

LIST OF FIGURES - CONTINUED

LIST OF FIGURES - CONTINUED

LIST OF FIGURES - CONTINUED

LIST OF FIGURES - CONTINUED

LIST OF FIGURES - CONTINUED

Figure Page

LIST OF FIGURES - CONTINUED

Figure Page

LIST OF FIGURES - CONTINUED

LIST OF FIGURES - CONTINUED

LIST OF FIGURES - CONTINUED

LIST OF FIGURES - CONTINUED

LIST OF FIGURES - CONTINUED

ABSTRACT

The geologic subsurface environment contains regions of high porosity where fluid flows both naturally and during engineered technologies such as carbon sequestration, enhanced oil recovery, and bioremediation of contaminants. In these porous media regions, microbes can have both desirable and undesirable effects on the hydrodynamics and fluid chemistry by inducing the formation of microbial aggregates, which can include extracellular polymeric substance and abiotic particles such as mineral precipitates. While not the focus of this research, these analyses are likewise applicable to biomatter control scenarios in filtration systems and other industrial reactors with a high surface area to volume ratio.

Microbially-induced ureolytic calcium carbonate precipitation has been suggested as a means to mitigate leakage from geologic CO_2 sequestration sites and as a means to immobilize divalent contaminants such as strontium-90 in remediation scenarios. In this process, microbes hydrolyze urea, increasing the solution pH, generating carbonate ions, and ultimately shifting the saturation state of the fluid and leading to solid calcium carbonate ($CaCO_3$) formation in a calcium-rich environment. Experiments were conducted to assess the distribution and effects of biofouling and biomineralization in two-dimensional flat plate reactors with 1mm pore spaces simulating a tortuous porous media environment. In biomineralization experiments, calcium carbonate was formed under flow conditions, and strontium was effectively immobilized within the crystal lattice, suggesting the applicability of subsurface biotechnical applications utilizing this technology.

Image, residence time distribution, and piezometer analyses of biofouling experiments quantified porosity and hydraulic conductivity reductions. Biofilms were grown under constant flow and head conditions and were shown to be more channeled and evenly distributed along the flow path in constant flow conditions. Biofilms were challenged with chlorinated bleach, which temporarily increased the hydraulic conductivity, yet failed to remove significant biofouling unless coupled with significant fluid shear. *In situ* methods utilizing stereo and confocal microscopy were developed to visualize and quantify the distribution of biomatter formation and analyze the biological environment at the surface of bio-induced minerals.

INTRODUCTION

Biofilms and Biofouling in Porous Media

A biofilm can be defined as a community of microbial cells among extracellular polymeric substance (EPS). Once attached to a surface, the development of a biofilm structure will depend on a number of parameters including availability of growth-limiting nutrients, presence of inhibitors, and the prevailing hydrodynamics (Gerlach and Cunningham, 2010). The phenomenon of biofilm accumulation on surfaces is referred to as biofouling, which can be further referred to as bioclogging when associated with porous media. Porous media are highly conducive to biofilm-forming bacteria due to a high surface area to volume ratio. The relationship between biofilm formation and hydrodynamics is mutual; biofilms both influence and rely on the hydrodynamics.

In the traditional perception, the distribution of biomass in porous media was that of a uniformly thick biofilm covering the pore surfaces. Researchers have more recently found that microorganisms often grow in micro-colonies, and that plugs of biomass, rather than a biofilm, can be responsible for changes in small and large scale hydrodynamics. Nambi et al. (2003) looked at location of biomass accumulation within the porous media, differentiating between pore spaces and pore throats. They found that biomass did not grow in pore throats due to unfavorable shear forces. Dupin and McCarty (2000) observed the appearance of a uniform biofilm with a thickness up to 60μm and aggregates of biomass with diameters of up to 200μm in bioclogging experiments in two-dimensional micro-models. Paulsen et al. (1997) found aggregate

size to be greater in high flow zones (i.e., pore throats) where nutrient fluxes were greater. Modeling results suggest that aggregates cause a much greater decrease in the hydraulic conductivity than biofilms or filaments (Dupin et al., 2001). Reductions of hydraulic conductivity by biofilms and/or aggregates can significantly affect industrial and environmental processes in porous media.

The value of porous media hydraulic conductivity can be calculated from measured values of permeability (i.e., Darcy's Law).

$$\frac{Flux}{Unit\ Area} = q = -\frac{k}{\mu}\nabla P \qquad (1.1)$$

Where k is the permeability (m^2), μ is the fluid viscosity (kg/(m*s)), and ∇P (Pa/m) is the pressure gradient along a specified flow path length. The conversion from permeability to hydraulic conductivity, K, is based on the fluid density (ρ [=] kg/m^3), the gravitational influence (g [=] m/s^2) and μ.

$$k = K\frac{\mu}{\rho g} \qquad (1.2)\ \text{(Gerlach and Cunningham, 2010)}$$

Cunningham et al. (2003) found that *Pseudomonas fluorescens* biofilms were capable of reducing the average hydraulic conductivity, K, by 99% in a porous media reactor. In several other bioclogging studies, a 2-3 order of magnitude decrease in the hydraulic conductivity has been found within a time span of a few weeks to four months (Frankenberger et al., 1979; Okubo and Matsumoto, 1983; Taylor and Jaffe, 1990; Vandevivere and Baveye, 1992; Seki et al., 1996, 1998, 2002; Albrechtsen et al., 1998; Holm, 2000; Dupin and McCarty, 2000; Bielefeldt et al., 2002). Seifert and Engesgaard (2007) investigated the temporal evolution of biofouling, and observed a decrease in bulk

hydraulic conductivity by up to three orders of magnitude, and an increase in the bulk dispersivity of up to one order of magnitude.

Disinfectants are often used to control the effects of biofilms in filters and pipes. These effects can result in a loss of pumping or reaction efficiency, as well as contamination. Using hypochlorite as a disinfectant, Seifert and Engesgaard (2007) observed the hydraulic conductivity and dispersion return to near normal values. While the effect of disinfectants on suspended cultures is well-understood, their effect on biofilms is much less understood, particularly when alterations in flow paths and substrate availability must be accounted for.

Developing highly accurate relationships between the reduction in hydraulic conductivity and the reduction in porosity remains an important work in progress. Since a biofilm contains a significant amount of water, an analysis of the pore volume can be divided into a mobile, immobile, and a biomass domain:

$$\theta = \theta_m + \theta_{im} + \theta_{bio} \qquad (1.3)$$

where θ is the total porosity, θ_m is the mobile porosity, θ_{im} is the immobile porosity (e.g., no-flow zones), and θ_{bio} is the biomass porosity (Seifert and Engesgaard, 2007). To predict hydraulic conductivity reduction as a function of porosity reduction, at least three types of models have been proposed, increasing in complexity: 1) homogeneous biofilm models (e.g., Taylor and Jaffe, 1990) 2) parametric models (e.g., Okubo and Matsumoto, 1983) and 3) pore network models (e.g., Thullner et al., 2002). A biofilm model assumes a uniformly thick distribution of biofilm on the surface, which decreases porosity and hydraulic conductivity by reducing the cross-sectional area of the flow channel. The

D'Arcy-Weisbach Equation, which is commonly used to predict head loss in a pipe, can be used for this relationship:

$$\Delta h = \lambda\,(l / D)\,(\rho v^2 / 2g) \qquad (1.4)$$(The Engineering Toolbox, Dec. 8, 2009)

In this equation Δh (m) is the head loss, λ (unitless) is the friction coefficient, l (m) is the length of the flow path, D (m) is the hydraulic diameter, ρ (kg/m^3) is the fluid density, v (m/s) is the average velocity, and g is the gravitational force (9.81 m/s^2).

Parametric models can be written as an expression for reduced hydraulic conductivity as a function of the mobile porosity, θ_m, with a fitting parameter, c.

$$\frac{K(\beta)}{K_{ini}} = \beta^c \quad (1.5) \qquad \text{valid for } \beta > \sqrt[c]{\frac{K_{\min}}{K_{ini}}}$$

In this equation, β is θ_m/θ, and the value of c varies between models. This model allows for a fitting parameter to adapt the model to the degree of non-linearity in the relationship between the reduced values.

The pore network model to obtain K(β), proposed by Thullner et al. (2002), is similarly based solely on changes of the mobile porosity fraction, β, as follows:

$$\frac{K(\beta)}{K_{ini}} = a\left(\frac{(\beta-\beta_{\min})}{(1-\beta_{\min})}\right)^3 - (1-a)\left(\frac{(\beta-\beta_{\min})}{(1-\beta_{\min})}\right)^2 \qquad (1.6) \quad \text{where} \quad \beta_{\min} = \frac{\theta_{\min}}{\theta}$$

In this case, θ_{min} is the minimum mobile porosity, at which point the hydraulic conductivity reaches zero. This model allows for the possibility of giving a large reduction in hydraulic conductivity with small changes in the porosity. For example, Thullner (2004) used glass beads, and yielded the values of a = -1.6 and β_{min} = 0.75; in practical terms, this means that the hydraulic conductivity reaches zero when the pore space is 25% filled with biomass.

While many studies of biofilms in porous media have yielded a significant amount of information for potential technologies, most have been conducted under constant flow rate conditions due to the experimental convenience of pump-generated flow. While there are situations in nature and industry with constant flow conditions, a reality of many subsurface environments is that flow is generated by a gradient in pressure, or a head difference (e.g., aquifers). The nature of constant head affects the physical and chemical environment surrounding biofilms, thus creating complications in the delivery of technologies and the sustainability of the biofilm over time.

Under constant flow conditions a pore space reduction leads to an increase in ΔP, average flow velocity, and shear stress. Under constant head conditions, a permeability reduction is manifested in a lower flux, with ΔP remaining constant (Darcy's Law, Equation 1.1).

Technological Applications of Biofilms

Biofilms are most often associated with detrimental effects (e.g., ship hull drag, corrosion, filter clogging, infection, dental plaque). Biofilm-related investigations can be viewed from this preventative perspective, to assess efforts to control and eliminate biofilms. However, the growth of biofilms in porous media has beneficial applications in the fields of water and wastewater treatment, microbial mining, and *in situ* bioremediation. Research has been conducted regarding the ability of biofilm-producing bacteria to reduce contaminants such as Cr(VI), U(VI), TNT, and TCE, suggesting that biofilms can simultaneously act as means to alter fluid flow and treat contamination (Viamajala et al., 2008) (see Figure 1.1 for application schematic). Cost is a major issue

in these remediation scenarios, and since traditional excavation and pump & treat methods are often costly, *in situ* biofilm applications may be more feasible.

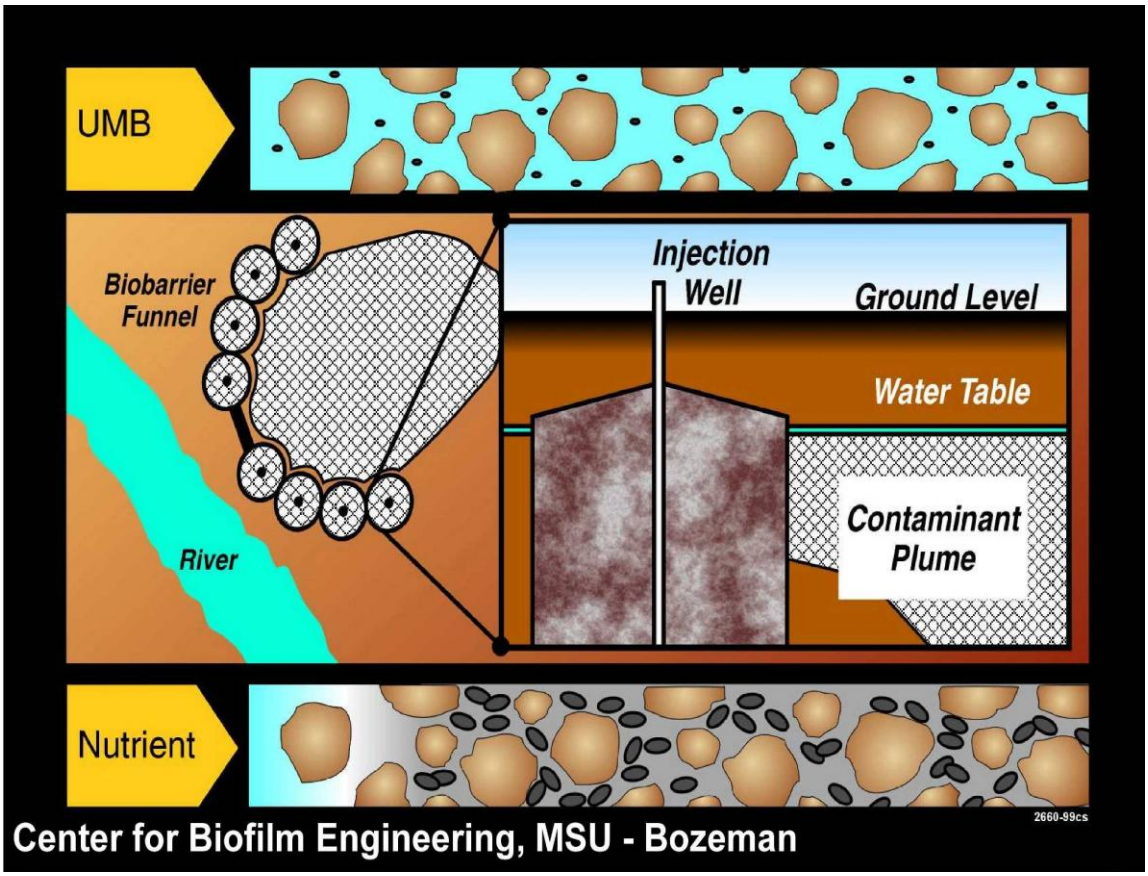

Figure 1.1. Schematic for the application of a subsurface biofilm barrier. The biobarrier in this instance may prevent the migration of the contaminant plume moving toward the river and may simultaneously degrade harmful chemicals. (Image courtesy of the Center for Biofilm Engineering, MSU)

Groundwater contamination by organic solvents and other contaminants is a matter of serious concern in industrialized countries where past activities were conducted without knowledge of potential risks (Nambi et al., 2003). In traditional remediation techniques, an appropriate substrate is mixed with water and injected into groundwater through and around the contaminant source, and desired processes such as reductive

dechlorination occur. Much of the degradation occurs along the plume margins, where contaminants mix with nutrients due to dispersion.

Fluid Mixing in Biofilm-Affected Porous Media

Many strategies for biotechnologies in subsurface porous media involve the injection of one fluid into another, where each fluid contains a necessary substrate for the desired process. For biomass and mineral precipitates to form, reactants must be mixed at the molecular level by diffusion, dispersion and transverse mixing in porous media. While these phenomena have been carefully studied in the absence of microbial growth, they remain to be well-understood in the presence of biofilms and biominerals (Grane et al., 1961, Klenk et al., 2002, Oya et al., 1998, Raje et al., 2000).

Diffusion, described by Fick's Law, is the transport of molecules from regions of higher to lower fluid concentration by means of random molecular motion. Dispersion in porous media is nearly identical to diffusion, but is based on differences in trajectory and rates of fluid transport through networks of pores and channels (i.e., dispersion accounts for porous structure, while diffusion does not). The relationships for diffusive and dispersive flux are given as follows:

$$Flux_{diff} = -D_{diff} \nabla C \quad \text{(Fick's First Law)} \qquad (1.7)$$

$$Flux_{disp} = \theta D_{disp} \nabla C \qquad (1.8)$$

In these relationships, θ is the average media porosity, D (m^2/s) is the diffusion or dispersion coefficient (dependent on pore geometry and fluid), and ∇C is the gradient in molecular concentration. The influences of dispersion and diffusion can be combined to obtain a convective-diffusion equation.

Dispersion is more commonly measured as dispersivity (length units), which is the dispersion coefficient divided by the flow velocity for one-dimensional analysis. In general, dispersivity increases over time in biofilm-affected porous media, but eventually reaches a steady state value, where growth equals death (Gerlach and Cunningham, 2010).

Despite the extensive research on diffusion and dispersion, it is not entirely clear what effect pore geometry will have on a mixing–limited reaction. Acharya et al. (2007) used pore-scale simulation to investigate whether classical transverse dispersion coefficients can be applied to model mixing controlled reactive transport (i.e., comparing D for conservative tracers with D from reactive solutes). They looked at three types of pore trends: random, periodic, and macroscopic. It was concluded that regardless of the geometric properties of the media, product formation can be predicted using transverse dispersion coefficients determined from a conservative tracer, provided that dispersion coefficients are determined beyond some critical distance down gradient where the plume has spread over a sufficiently large transverse distance compared to the mean grain diameter (Acharya et al., 2007).

Willingham et al. (2008) assessed the effects of porous media geometry on a transverse mixing-limited reaction. They varied grain size, grain orientation, and intraparticle porosity, and calculated the extent of a fast bimolecular reaction. They concluded that while grain orientation significantly affects mixing and the extent of reaction, grain size alone is not sufficient to quantify mixing at the pore scale. Overall results indicated that the contact area between reactive plumes was a controlling factor

for mixing and reaction, and that this must be considered when evaluating reactive transport.

In simple laboratory flow systems where reactants and substrates typically enter the reactor in the same inlet stream, it is very difficult to evaluate the effects of mixing along plume margins.

Ureolytic Calcite Precipitation

It has been known for many years that microbes can alter fluid chemistry, affect the saturation state of ionic solutions, and instigate mineral precipitation (Ferris et al., 1996). A classical example is the biologically-induced formation of calcium carbonate ($CaCO_3$), one of the most common and widespread minerals on earth. It is naturally found in sedimentary rock masses, such as limestone, marble, and calcareous sandstones in marine, freshwater, and terrestrial environments (Hammes and Verstraete, 2002; Klein and Hurlbut, 1999). The mineralogy and solution chemistry of $CaCO_3$ as well as the chemistry of the carbonic acid system have been extensively described (Oelkers et al., 2008; Warren et al., 2007, Mitchell and Ferris, 2006). In the classical picture of crystallization, when a favorable saturation state is reached the flat surfaces grow via layer by layer adsorption of solute atoms or molecules onto an existing crystal face (Meldrum and Coelfen, 2008).

The precipitation of calcium carbonate is governed by four parameters: 1) calcium concentration, 2) carbonate concentration, 3) pH of the environment (which affects carbonate speciation and calcium carbonate solubility), and 4) presence of nucleation

sites (Hammes and Verstraete, 2002). $CaCO_3$ can be precipitated by heterotrophic organisms, by the production of carbonate or bicarbonate and modification of the environment to favor precipitation (Castanier et al., 1999). One method to achieve $CaCO_3$ precipitation is bacterially-facilitated urea hydrolysis (ureolysis).

The production of ammonium and dissolved inorganic carbon during decomposition of urea by bacteria at the active site of the urease enzyme tends to increase pH and carbonate concentration, which favor solid calcium carbonate precipitation in a calcium-rich environment, as illustrated in the following equations (Ferris et al., 2003):

$CO(NH_2)_2 + H_2O \rightarrow NH_2COOH + NH_3 \rightarrow 2\ NH_3 + CO_2$ (1.9) (Urea hydrolysis)

$2NH_3 + 2H_2O \leftrightarrow 2NH_4^+ + 2OH^-$ (1.10) (pH increase)

$CO_2 + 2\ OH^- \leftrightarrow CO_3^{2-} + H_2O$ (1.11) (Carbonate formation)

$CO_3^{2-} + Ca^{2+} \leftrightarrow CaCO_{3\ (solid)}$ (1.12) (Precipitation)

Ureolysis is special in that it is one of the few biologically-occurring reactions that can generate carbonate ions without an associated production of protons (Whiffin et al., 2004). While the direct addition of a basic solution could also lead to precipitation, the use of bacteria to raise the pH in the environment may be preferable because the gradual hydrolysis of urea is likely to promote a wider spatial distribution of precipitates, whereas the direct addition of base is likely to cause immediate precipitation at the injection site (Ferris et al., 2003). The ample availability and affordability of urea, the chief nitrogenous waste produced by vertebrates, renders potential technologies highly economical (Mitchell and Ferris, 2005).

Previous researchers have found the soil bacterium *Sporosarcina pasteurii*, formerly known as *Bacillus pasteurii*, to produce urease and efficiently induce ureolysis (Mitchell and Ferris, 2005, 2006; Ferris et al., 2003; Fujita et al., 2008). The effectiveness of *S. pasteurii* can be attributed to its ability to produce high levels of the urease enzyme in the presence of ammonium. Further, *S. pasteurii* is a moderate alkaliphile with a pH optimum for growth of 9.25, which is similar to the half-dissociation constant (pKa) of the NH_3/NH_4^+ equilibrium, making it well-suited for ureolytic biomineralization (Brown et al., 2003). Furthermore, cells have been shown to be great nucleation sites during mineral formation (Ferris et al., 1986; Ferris et al., 1987).

The kinetics of $CaCO_3$ precipitation are of utmost importance in any biotechnological application. The rate at which the process occurs will ultimately dictate the optimization and feasibility of a technology. Further, for the case of strontium co-precipitation strategies, it has been shown that increased precipitation kinetics lead to greater partitioning of strontium in $CaCO_3$ (Mitchell and Ferris, 2006). The overall kinetics of the process can be divided into two interrelated steps: The hydrolysis of urea by bacteria, and the precipitation of $CaCO_3$. The kinetics of urea hydrolysis have been described by means of a modified Michaelis-Menten reaction rate expression, which incorporates pH-dependent kinetics, substrate inhibition, and noncompetitive product inhibition by NH_4^+.

$$\frac{d[urea]}{dt} = \frac{v_{\max}[urea]}{\left[K_m + [urea] \bullet (1 + \frac{[urea]}{K_{urea}})\right]\left[1 + \frac{[NH_4^+]}{K_{NH4}}\right]} \quad (1.13)$$ (Moynihan et al., 1989)

In this equation, v_{max} (concentration/time) is the maximum specific reaction rate, K_M (a function of pH with units of concentration) is the Michaelis-Menten constant, and K_{urea} (concentration) and K_{NH4} (concentration) are the inhibition constants.

The potential for precipitation is dictated by thermodynamic principles and can be expressed in the saturation ratio, S, where a particular reaction is favorable for S > 1 (with the reverse reaction favored for S < 1), according to the following relationship

$$S = \frac{\{Ca^{2+}\}\{CO_3^{2-}\}}{Kso} \qquad (1.14)$$

Where $\{Ca^{2+}\}$ and $\{CO_3^{2-}\}$ represent the activities of dissolved Ca^{2+} and CO_3^{2-} respectively, and Kso (concentration^2) is the solubility constant for calcite at a given temperature (i.e., product of the component activities at equilibrium). Carbonate precipitation may theoretically occur in natural environments by increasing the concentration of calcium and/or carbonate in solution or by decreasing the solubility of calcium and/or carbonate. Precipitation kinetics are generally believed to be related to S, at the simplest level, by commonly accepted steady-state empirical relationships such as:

$$Rate = \frac{d[Ca^{2+}]}{dt} = k_p (S-1)^2 \quad (1.15) \quad \text{(Teng et. al, 2000)}$$

In this equation, k_p (concentration/time) is the rate coefficient of precipitation. While a higher saturation state has been previously correlated with faster precipitation, the process remains to be completely understood.

The supersaturation level of carbonate ions can be influenced by controlling the pH. The proportion of inorganic carbon that exists as CO_3^{2-} in solution at any time is highly dependent on the pH. Below pH 8, the carbonate concentration is very low

(Figure 1.2), which means that if desired, the saturation state can be altered with changes in pH.

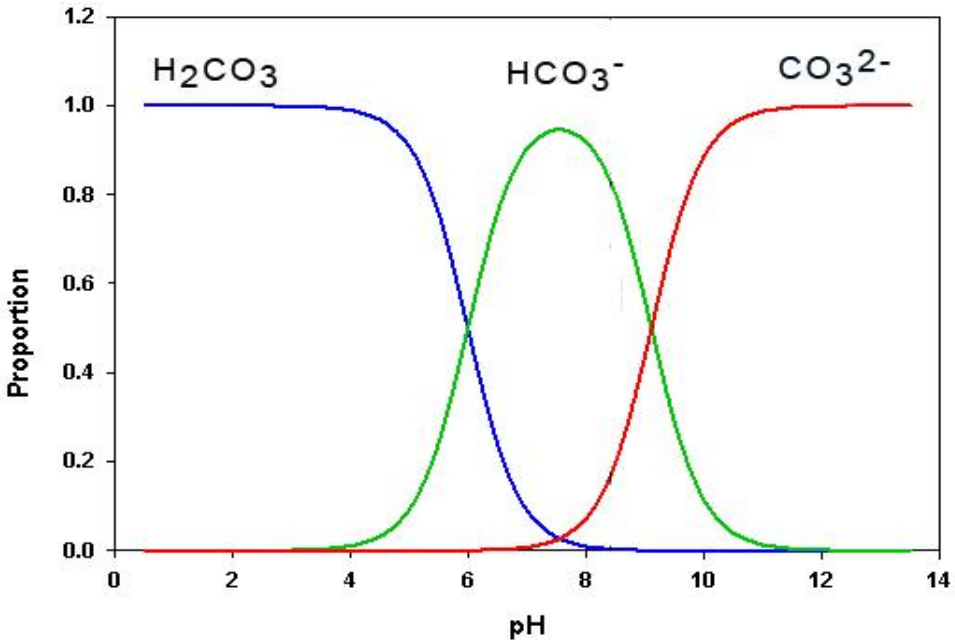

Figure 1.2. Chemical speciation of H_2CO_3 calculated at T = 25 °C, P = 1 atm, and the average salinity of sea water (S=35 g dissolved minerals per kg of seawater). The proportion is the concentration of a particular species divided by the concentration of all three species combined. For these conditions, pK_1 = 5.95 and pK_2 = 9.05 (Jury, 2008).

Biotechnologies Utilizing Ureolytic Biomineralization in Porous Media

Recently, technologies have been proposed to capitalize on this phenomenon for beneficial purposes. Several scenarios, which would occur in the geologic subsurface, may be more financially and environmentally feasible than traditionally applied methods. Some examples are highlighted in the following subsections.

Wastewater Treatment: In wastewater recycling and release systems, removing soluble calcium can effectively prevent pipe clogging (Hammes et al., 2003). Here,

ureolytic $CaCO_3$ precipitation can remove dissolved Ca^{2+} in crystallization reactors prior to distribution in pipes.

Soil Improvement: Whiffin et al. (2007) determined that enhanced soil stability can be attained and permeability maintained when the bacteria and reagents are injected at low velocities. Further, the ureolysis rate can be balanced with the reactant flow rate to achieve soil strengthening in desired locations.

Statue Preservation: Tiano et al. (1999) evaluated biologically-mediated calcite precipitation treatment on limestone samples for the preservation of monumental stones and statues. After wetting limestone samples and brushing them with bacterial suspensions, they assessed the impact on pore volume, shear strength, and color. They recorded an increase in shear strength, but determined that the greatest challenge would be transporting the bacteria beyond the surface region of the samples. Rodriquez-Navarro and Sebastian (1996) used a similar process to strengthen and protect the surface of monumental stones from air pollution and weathering agents.

Co-precipitation of Strontium and other Divalent Ions: The US Department of Energy is responsible for several sites in the Western US where previous operations have left groundwater and soils contaminated with divalent metal ions (e.g., Pb, Zn, Cd), and radionuclides (^{90}Sr, UO_2^{2+}, and ^{60}Co) (Riley and Zachara, 1992). The large volume of contaminated material in the subsurface calls for a cost-effective, *in situ* method for containment and stabilization of potential threats to groundwater sources (Fujita et al., 2000, 2004; Mitchell and Ferris, 2005). Ureolytic carbonate precipitation has been

investigated for the solid-phase capture of the divalent radionuclide, strontium-90, which is a byproduct of uranium fission, and has been identified in the Snake River and Columbia Basin aquifers. The co-precipitation of $SrCO_3$ is proposed to prevent the spread of radionuclide contamination in the subsurface with the moving groundwater (Fujita et al., 2000; Warren et al., 2001). This is a possible means to remediate and immobilize these contaminants. The process is illustrated in Figure 1.3.

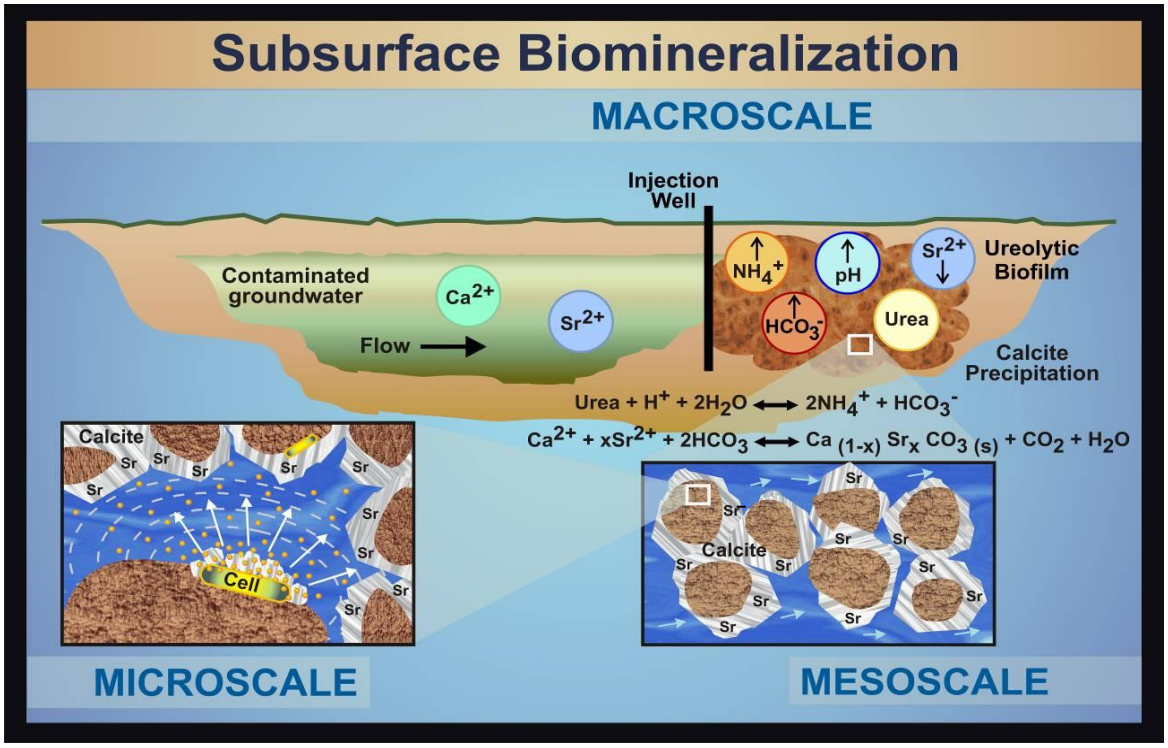

Figure 1.3. Diagram portraying the application of ureolysis-induced coprecipitation of ^{90}Sr in calcite in a contaminated aquifer. (Image courtesy of the Center for Biofilm Engineering)

Previous studies have elucidated the effective immobilization of strontium within the lattice of calcite during ureolysis (Mitchell and Ferris, 2006; Warren et al., 2001), in which case the rate of incorporation is a function of precipitation kinetics and the adsorption interactions between the calcite surface and the strontium ions (Ferris et al.,

2003). Mitchell and Ferris (2006) found that the presence of Sr inhibited calcite growth in a batch system. This finding exposes a potential challenge with ^{90}Sr co-precipitation applications.

In a field investigation conducted in the Eastern Snake River Plain Aquifer, Fujita et al. (2008) demonstrated that injecting molasses prior to urea effectively increased total cell numbers and increased ureolysis rates from <0.1 to >25 nmol L^{-1} hr^{-1} using native bacteria. These data suggest that introducing engineered bacteria may not be necessary, and that controlled stimulation of the native microbial community may provide a means of controlling the rate of precipitation and enhancing overall ^{90}Sr sequestration. However, they encountered high rates of ureolysis and precipitation near the injection site, leading to a restricted transport of nutrients. This exposes the need to understand and ultimately control precipitate distribution along a flow path. Ultimately, the effectiveness of a field scale delivery will be dictated by phenomena that occur at the micron scale, and will be influenced by controllable variables (e.g., concentrations, flow rates, and injection strategies).

Geologic Carbon Sequestration: The process of carbon capture and storage (CCS) has the potential to reduce future world emissions from energy by 20% (International Energy Agency, 2008). CO_2 capture methods proposed include pre-combustion processes (e.g., coal gasification), post-combustion (e.g., amine scrubbing), and atmospheric collection (Rochelle, 2009). Proposed storage locations include deep saline aquifers, oil reservoirs, and highly porous rock. Although no fully functioning CCS

power plant has been constructed, more than 20 experiments and pilot plants are currently operating (Scottish Center for Carbon Storage, 2009).

In geologic carbon sequestration, captured CO_2 may be compressed into a dense, low-viscosity supercritical phase ($scCO_2$) and injected into subsurface formations where it will be retained. Large volumes of pore space that might be used to contain CO_2 exist in sedimentary rocks distributed widely around the world. Estimated storage capacity ranges from 1,700 to 11,000 gigatons of CO_2 (Intergovernmental Panel on Climate Change, 2005).

A concern remains that the CO_2 will migrate back to the earth's surface, and bacteriogenic mineral plugging is a strategy that is being considered to help prevent this. It remains to be fully understood how the bacterial activity and reaction products will be affected by the exposure to $scCO_2$ and the deep subsurface environment.

Enhanced Oil Recovery: Fifty percent or more of the original oil-in-plane is left in a typical oil reservoir by traditional (primary and secondary) recovery (Sahimi, 1993). This unrecovered oil is a large target for enhanced or tertiary oil recovery methods now being developed. Biomineralization has been suggested as a way to selectively plug high permeability areas and enhance water-flooding technologies (Ferris et al., 1996). This application may be used collaboratively with CO_2 sequestration to reduce drilling and injection costs. At the same time, liquid or supercritical CO_2 reduces the viscosity of oil as it pushes the oil toward production bore holes, often allowing enhanced secondary recovery. This process is illustrated in Figure 1.4:

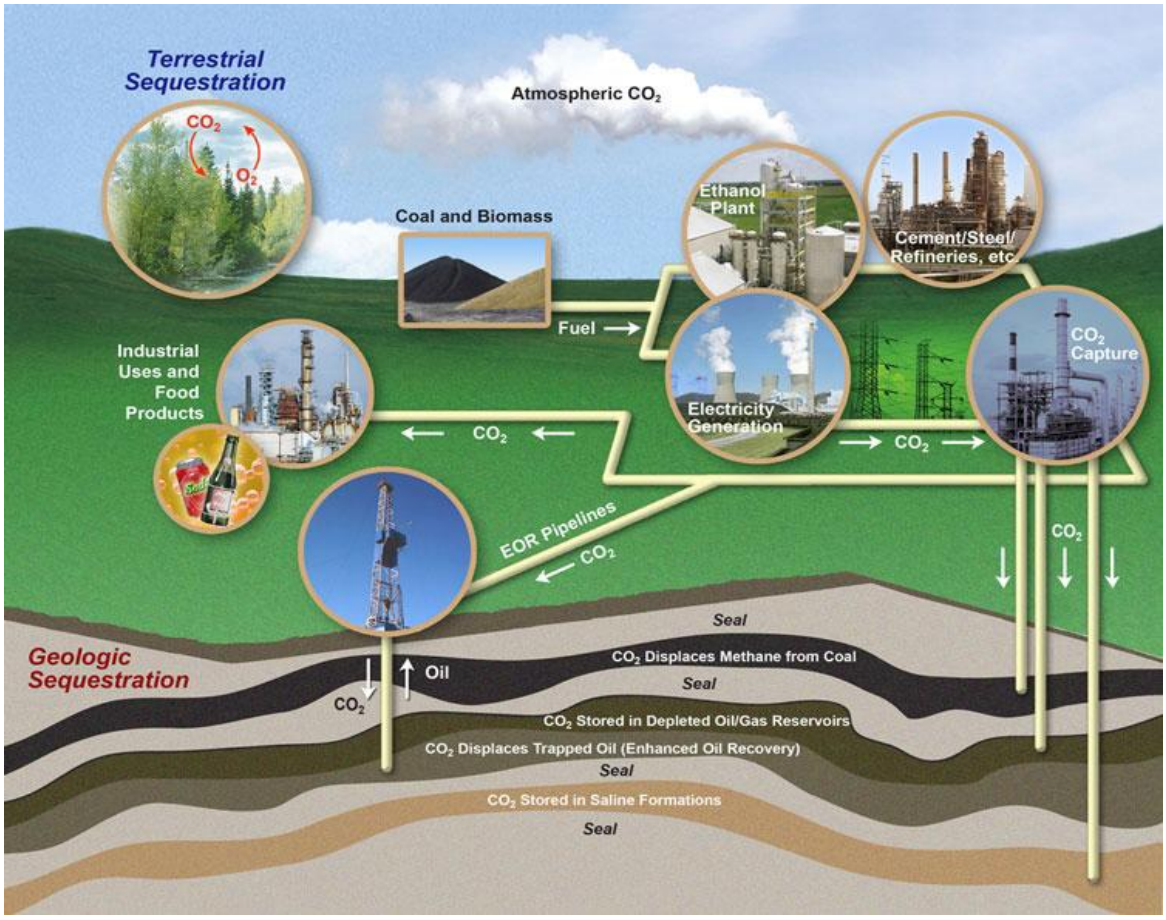

Figure 1.4. Schematic showing a potential process of carbon dioxide injection at various subsurface formations for storage and enhanced hydrocarbon extraction. Diagram from DOE (http://www.fossil.energy.gov/images).

In situ Imaging of Biological Reactors

Photography- and microscopy-based methods provide invaluable tools to understand reactive transport in porous media and ultimately aid in the development of biotechnologies. Sharp et al. (1999) used image analysis and dye tracer methods to characterize channels and dispersion in biofilm-affected porous media. In microscopically analyzing ureolysis-induced carbonate precipitates, Mitchell and Ferris (2006) used an image-based crystal count technique to measure size and density of

precipitates as they accumulated on the surface of glass bottles. From this, they estimated the solubility of each individual precipitate from the molar surface area, based on the equation by Stumm and Morgan (1996):

$$\ln\left(KsO_{(A)}\right) = \ln\left(KsO_{(A=0)}\right) + \frac{3\gamma A}{3RT} \qquad (1.16)$$

In this equation, $\ln Ks0_{(A=0)}$ is the published solubility constant at equilibrium (for an infinite molar surface area, A = 0 m^2/mol), γ is the solid-liquid interfacial free energy for calcite (0.094 J/m^2)(Stumm and Morgan, 1996), R is the gas constant (J/mol K) and T is the temperature (K).

Pitts and Stewart (2008) developed a method to grow biofilms in 1mm x 1mm glass capillary tubes with walls that were the thickness of a microscopy cover slip (0.17mm). This allowed them to non-invasively image biofilm development under a confocal laser scanning microscope (CLSM) with a water immersion lens (2mm working distance). This is a very attractive method that provides high-resolution images of a fully-hydrated environment.

With recent improvements in resolution and differentiation, magnetic resonance microscopy (MRM) has become an increasingly useful method in analyzing biologically-affected reactors. This method allows for the differentiation of porous media, biofilm, and minerals within the reactor while overcoming the optical limitations that face other microscopy techniques (see Seymour et al. 2009 manuscript included in Appendix D).

Research Objectives and Approaches

This research was conducted as part of three Department of Energy (DOE) sponsored projects: 1) Zero Emissions Research and Technologies (ZERT), 2) Experimental Program to Stimulate Competitive Research (EPSCoR), 3) Environmental Remediation Sciences Program (ERSP). The interest of the funding agency is to perform reactor studies to assess the fundamentals of biofouling and biomineralization processes, which have application in a broad range of potential technologies, including bioremediation and carbon sequestration. The objectives and general approaches of this thesis can be summarized by the following:

I. *Assess ureolytic $CaCO_3$ precipitation and co-precipitation of strontium in a flow system*. Calcium carbonate precipitation was viewed microscopically, and the chemistry of the reactor effluent and precipitates was analyzed. Reactors with and without dissolved strontium were compared to assess potential inhibitory effects of strontium on the precipitation of $CaCO_3$.

II. *Evaluate the effects of biofouling in a porous media reactor to provide data for modeling.* Microscopy, photography, and residence time distribution analyses were utilized to assess porosity and permeability alterations over time in biofilm-affected reactors. Biofilms grown under constant head and constant flow conditions were compared, and the accumulation of biofilm was modeled using the Biofilm Accumulation Model.

III. *Develop imaging methods to understand and quantify biomineralization and biofouling in flow systems*. Stereo microscopy was utilized to view and quantify

macroscopic precipitate and biofilm deposition in reactors, and confocal microscopy was used to analyze the bacteria-mineral interactions in capillary flow cells under biomineralization conditions. To expand our image analysis capabilities, work was performed collaboratively with the magnetic resonance microscopy (MRM) lab group in the Montana State University Department of Chemical and Biological Engineering.

BACTERIALLY-INDUCED CALCITE PRECIPITATION AND STRONTIUM CO-PRECIPITATION UNDER FLOW CONDITIONS IN POROUS MEDIA SYSTEMS

Manuscript Preface

In addressing calcite precipitation in flow systems, an experiment was conducted in two-dimensional porous media reactors. This investigation was formulated into a manuscript titled 'Bacterially-Induced Calcite Precipitation and Strontium Co-Precipitation under Flow Conditions in a Porous Medium'. This manuscript, which will be submitted to Environmental Science and Technology, seeks primarily to address the ability of *Sporosarcina pasteurii* to induce ureolytic carbonate precipitation and co-precipitation of strontium in two-dimensional flat plate reactors. These processes have broad implications in environmental bioremediation and carbon management technologies. The primary inspirations for the experiment leading to this manuscript were papers published by Fujita et al. (2008) and Mitchell and Ferris (2006). Fujita et al. conducted a field experiment and found prolific precipitation near the injection region that limited transport objectives, and Mitchell and Ferris observed an inhibitory effect of strontium on calcite mineralization in batch systems. This research sought to better understand the mineral deposition along the flow path encountered by Fujita et al. (2008), and to compare the precipitation of calcite with and without the presence of strontium in a flow system to test the potential inhibition of strontium on $CaCO_3$ precipitation. This manuscript has been included in this chapter.

In the process of developing the information for this manuscript, significant amounts of data were collected. Due to the emphasis on concision by the journal, much

information was not included. Hence, details pertinent to the manuscript and to the goals of this chapter are included in the appendices.

It shall be noted that all of the experiments contained in this chapter were conducted under atmospheric pressure and room temperature. Many proposed biotechnologies related to carbon sequestration occur in the deep subsurface, where the environmental conditions are at higher temperatures and pressures. To analyze ureolytic calcite formation at pressures and temperatures that are more representative of the conditions that would be found in these scenarios, experiments were conducted at high pressure and temperature. A reactor experiment in which biomineralization was assessed under pulse flow conditions at pressures greater than 1200 psi is contained in Appendix A. High pressure and temperature batch experiments were also conducted using a high pressure vessel. Details of the vessel and the related experiments are outlined in Appendices B.1-B.4. Further, in the case of geologic carbon sequestration these processes must additionally be viable under the exposure of $scCO_2$, which is a solvent and sterilizing agent (CO_2 phase information in Appendix C).

A supplementary study using MRM was conducted in collaboration with Fridjonsson and Seymour at Montana State University. In this experiment, ureolytic biomineralization was engineered in a packed bed column. A manuscript, titled 'NMR Measurement of Hydrodynamic Dispersion in Porous Media Subject to Biomediated Reactive Precipitation Flow', was generated from this experiment. The submitted manuscript is included in Appendix D.

This manuscript, titled BACTERIALLY-INDUCED CALCITE PRECIPITATIONAND STRONTIUM CO-PRECIPITATION UNDER FLOW CONDITIONS IN POROUS MEDIA SYSTEMS will be submitted to Environmental Science and Technology

Authors

Logan Schultz, Andrew C. Mitchell, Robin Gerlach*, Alfred B. Cunningham
Center for Biofilm Engineering, Montana State University, Bozeman, MT
**robin_g@biofilm.montana.edu*

Abstract

Ureolytic calcite precipitation and co-precipitation of strontium by *Sporosarcina pasteurii* was examined in two-dimensional flat plate porous media reactors with an initial average flow velocity of 0.58 cm/min and an average hydraulic residence time of 18.38 minutes. Complete reactor plugging due to biofilm formation and calcium carbonate precipitation was achieved in the Sr-free system after 14 hours and in the Sr-inclusive system after 15 hours. Comparison of the reactor influent and effluent after 11 hours indicated that Ca^{2+} concentration in the Sr-free reactor effluent was reduced to approximately 0.48% of the influent concentration while the Ca^{2+} and Sr^{2+} concentrations of the Sr-inclusive effluent were reduced to 0.64% and 2.34% of the influent concentration, indicating a slight inhibitory effect of strontium on calcium carbonate precipitation. Despite this slight inhibition, more than 98% of the calcium entering each reactor was precipitated. Calcite was identified as the main mineral formed and a larger mean crystal size and density were observed near the reactor influent. Homogeneous

partition coefficients calculated from extracted precipitates suggest higher Sr^{2+} partitioning near the inlet region, where higher precipitation rates were observed. Results confirmed the possibility of effective calcite-based co-precipitation of Sr^{2+} under flow conditions and will contribute towards the development of field-scale calcium carbonate mineral-based immobilization strategies.

Introduction

The process of *in situ* carbonate mineral formation has implications in many environmental applications, including, but not limited to aquifer decontamination, enhancement of soil stability, and carbon capture and storage (CCS). The high stability of carbonates and the potential for co-precipitation of contaminants within carbonates are attractive attributes for several potential engineering applications.

The US Department of Energy (DOE) is responsible for remediating numerous sites where large volumes of subsurface media are contaminated with radionuclides, heavy metals, and organic compounds. A noteworthy case is strontium-90, a uranium fission byproduct that is present at several DOE sites in the Western US. The mobility and known carcinogenic effects of ^{90}Sr pose a risk to groundwater usability (Fujita et al., 2008). As a potential long-term sequestration mechanism, *in situ* co-precipitation of ^{90}Sr with calcium carbonate has been suggested as a control strategy (Mitchell and Ferris, 2006, Ferris et al., 2003, Fujita et al., 2008).

One method to achieve calcium carbonate precipitation uses stimulated native ureolytic bacteria to facilitate urea hydrolysis (ureolysis). The production of ammonium

and dissolved inorganic carbon during ureolysis (Equation 2.1) by bacteria tends to increase pH and dissolved inorganic carbon concentrations, which favors the precipitation of calcium carbonate in the presence of dissolved calcium (Equation 2.2) (Ferris et al., 2003).

$$NH_2CONH_2 + H^+ + 2H_2O \leftrightarrow 2NH_4^+ + HCO_3^- \qquad (2.1)$$

$$Ca^{2+} + 2HCO_3^- \leftrightarrow CaCO_3(s) + CO_2 + H_2O \qquad (2.2)$$

Previous research has demonstrated that the soil bacterium *Sporosarcina pasteurii*, formerly *Bacillus pasteurii*, can efficiently induce ureolysis (Mitchell and Ferris, 2005, 2006, Ferris et al., 2003, Fujita et al., 2008). Further, *S. pasteurii* is a moderate alkaliphile with a pH optimum for growth of 9.25, which is similar to the half-dissociation constant (pKa) of the NH_3/NH_4^+ equilibrium, making it well suited for ureolytic biomineralization (Brown et al., 2003).

The precipitation of $CaCO_3$ is governed by four parameters: Ca^{2+} concentration, CO_3^{2-} concentration, pH, and presence of nucleation sites. Nucleation is a complex phenomenon which is not yet well understood outside of pure species systems, but bacterial cells have been shown to function as nucleation sites and studies have confirmed the precipitation of calcite on bacterial cell surfaces (Ferris et al., 1987, Fujita et al., 2000).

Even though the presence of Sr can slightly inhibit calcite crystal growth (Mitchell and Ferris 2006), previous studies have demonstrated the effective immobilization of strontium within the lattice of calcite during ureolysis (Mitchell and Ferris, 2006, Warren et al., 2001). In a field investigation conducted in the Eastern Snake

River Plain Aquifer, Fujita et al. demonstrated that injecting molasses prior to urea effectively increased total cell numbers and increased ureolysis rates from <0.1 to >25 nmol L^{-1} hr^{-1} (Fujita et al., 2008). An increase in Sr incorporation in the crystal lattice with increasing precipitation rates has been demonstrated (Mitchell and Ferris 2005, 2006). This data suggests that controlled stimulation of the native microbial community may provide a means to control the rate of urea hydrolysis and $CaCO_3$ precipitation, ultimately enhancing overall ^{90}Sr sequestration. However, Fujita et al. (2008) also encountered high rates of ureolysis and calcite (a polymorph of calcium carbonate) precipitation near the injection site, leading to a restricted transport of nutrients. These observations indicate the need to understand and ultimately control precipitate distribution along a flow path. Ultimately, the effectiveness of a field scale delivery will be dictated by phenomena that occur at the micron scale, and will be influenced by parameters that might be controllable at the field scale, such as concentrations, flow rates, abundance and activity of microorganisms as well as amendment injection strategies.

It has been suggested that attached microbial communities (e.g., biofilms) are more influential than planktonic cultures in affecting aquifer chemistry (Alfreider et al., 1997, Hazen et al., 1991, Lehman et al., 2001, Lehman and O'Connell, 2002, Thomas et al., 1987). In the work presented here, we examine, spatially and temporally, the process of ureolysis induced $CaCO_3$ precipitation by *S. pasteurii* under flow conditions, where the ureolytic bacteria predominantly exist in biofilms. The primary objectives are to: 1) understand biofilm formation and distribution of mineral precipitates along the flow path to provide insight into transport optimization and 2) assess the potential inhibitory effects

of Sr on mineral precipitation and therefore Sr removal in a flow system. The experimental systems employed allowed for visual evaluation of the plugging phenomena observed by Fujita et al. (2008) and will, combined with the aqueous chemistry and mineral phase analysis, contribute towards improved field scale immobilization strategies.

Experimental Methods

Reactor Systems

Continuous flow systems were constructed with 8.5cm x 3.8cm flat plate polycarbonate reactors (Figure 2.1). The flow path was etched with 1mm x 1mm diagonal channels, creating a tortuous flow path approximating a homogeneous porous medium. Silicon dioxide tubing (Masterflex size 16) connected the media source to the reactors via a peristaltic pump (Masterflex model 7521-50). The systems were tuned to a flow rate of 0.15 ml/min, resulting in an average reactor residence time of approximately 18.38 minutes in the porous media region, assuming a tortuous flow path.

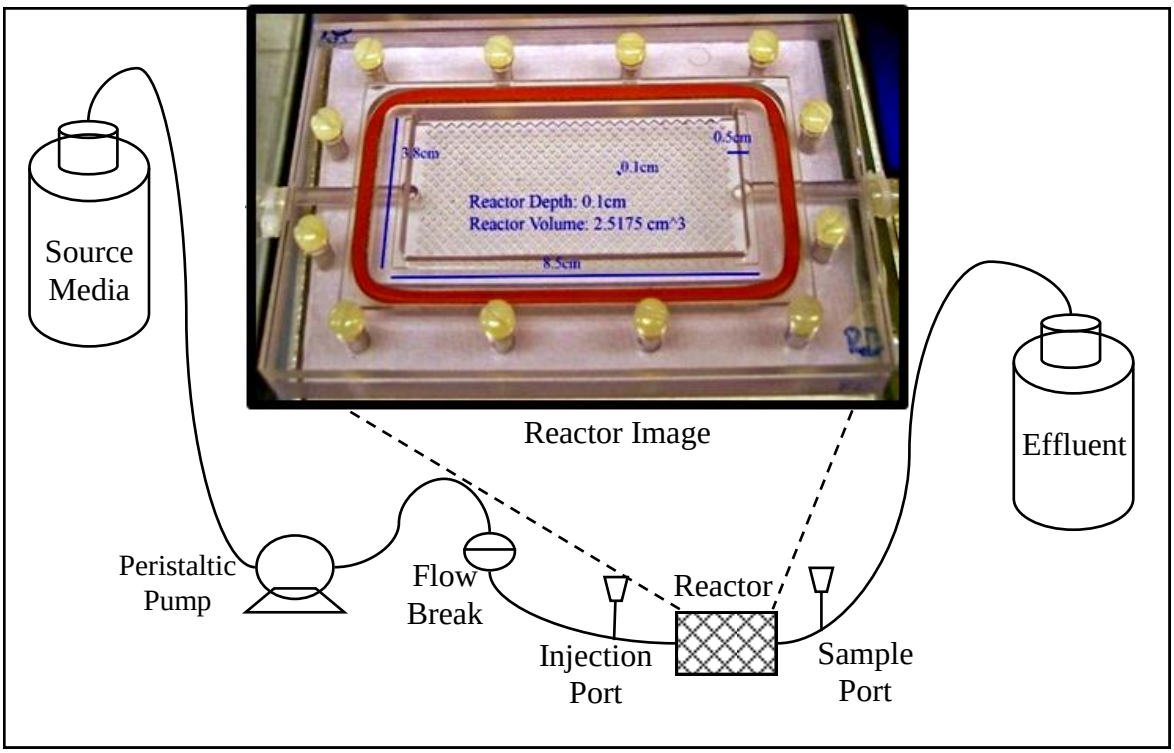

Figure 2.1. Reactor system schematic with flow proceeding left to right. The reactors (inset) have 1mm x 1mm etched pore spaces that are covered by a 1mm thick glass cover slip. They include a mixing zone at the inlet and outlet to minimize entrance effects. Immediately preceding the reactor are injection ports and flow breaks to reduce upstream contamination. At the outlets are sample ports to allow effluent sample extraction.

Fluid Flow Medium

The medium, previously used by Ferris and Stehmeier (1996), used for the experiments contained nutrient broth (Becton, Dickinson and Company, 3 g/L), urea (Fisher Scientific, 20 g/L), ammonium chloride (Fisher Scientific, 10 g/L), sodium bicarbonate (Fisher Scientific, 2.1 g/L), calcium chloride dihydrate (Acros, 3.7 g/L).

The medium was prepared by first autoclaving the Nutrient Broth in deionized water. Urea, NH_4Cl, and $NaHCO_3$ were added, the solution pH was adjusted to 6.0 with concentrated HCl before $CaCl_2 \cdot 2H_2O$ was added, and the entire solution was filter-

sterilized. For the Sr-inclusive medium, 63.9 mg/L of $SrCl_2 \cdot 6H_2O$ were added before filtration to yield a final concentration of 21 mg/L of Sr.

Culturing and Inoculation

A frozen stock culture of *S. pasteurii* was grown in brain heart infusion (Oxoid Ltd., Cambridge, UK) amended with urea (20 g/L) on a 30°C shaker at 150 rpm for 24 hours. The culture was transferred into fresh medium and grown for another 18 hours. The culture was centrifuged at 4°C and 4,455 g for 30 minutes (Sorvall Instruments, RC5C). The supernatant was decanted, and the cells were re-suspended in the previously defined flow medium devoid of Ca. The process was repeated once more before 4 mL, or approximately two reactor pore volumes, of the culture were injected into the flow system and the bacteria were allowed to attach for 1.5 hours before medium flow was started.

Analytical Methods

The Sr-free reactor was monitored continuously using a stereo microscope (Nikon SMZ1500) focused near the inlet region with variable magnification (7.5x-40x). Effluent samples from each system were collected at 0, 1, 6, and 11 hours after flow was started and analyzed for the following parameters:

Ammonium Production: Ammonium, a direct product of ureolysis (Equation 2.1), was determined by a modified Nessler method. Effluent samples were diluted appropriately in deionized water and ammonium concentrations were determined by comparison to standards made from $(NH_4)_2SO_4$. Each sample and standard (250 µL) was

added in triplicate to a 96-well microplate. Three (3) µl of mineral stabilizer, 3µl of polyvinyl alcohol, and 10µl of Nessler reagent (potassium tetraiodomercurate(II)) were added. Ammonium was quantified in the resulting solution after 10 minutes via spectrophotometry at 425nm (BioTek, Synergy HT). For the full assay protocol, see Appendix E.

pH: The pH of effluent samples was assessed with a Fisher Scientific pH meter (model 50) equipped with a Corning glass electrode, which was calibrated daily.

Calcium and Strontium Concentration: Concentrations of dissolved (i.e., filtered), and total (i.e., dissolved and particulate) Ca and Sr were measured on an Agilent 7500 ICP-MS after a 1:100 dilution in 5% nitric acid and by comparison with certified standards (Agilent Technologies, Environmental Calibration Standard 5183-4688). Samples for dissolved metal analysis were previously filtered through a 0.2µm syringe filter (Corning Incorporated, New York).

Colony Forming Units: CFUs were measured to estimate the concentration of active bacteria in the reactor effluent. Effluent samples were diluted in phosphate-buffered saline solution and drop-plated on agar plates with brain heart infusion and urea (20 g/L)(Herigstad 2001).

Protein Concentration: Protein was measured using a Pierce Coomassie Protein Assay. 200µl of each sample were mixed with 200µl of 1 N NaOH and digested in a water bath at 90°C for 10 minutes. Samples were cooled, mixed with 70µl of HCl, and

stored at -5°C until the protein assay was conducted. The samples were thawed and 50µl of each sample and appropriate standardized solution of bovine serum albumin were added to 50µl of Pierce Coomassie reagent in a 96 well micro-plate. After 15 minutes, the extent of this reaction was quantified by spectrophotometry at 595 nm. For full assay protocol, see Appendix F.

Size, Distribution, and Solubility of Precipitates: Stereo microscope crystal images were analyzed with ImageJ analysis software (National Institute of Health: Version 1.41o). At locations along the length of the reactors, the stereo microscope was focused on the glass surface at the top of the pore space and on the etched polycarbonate surface at the bottom of the pore space and images were acquired using Metamorph software. With ImageJ, at each location crystal size and density (precipitates/mm^2) were measured at each focal plane. To determine the average crystal size, 20 crystals in each image were randomly selected and measured. To quantify density, isolated precipitates in the image were counted and divided by the area of reactor surface imaged. To determine an average size and density at each reactor location, the values from each focal plane were weighted accordingly to account for 75% polycarbonate and 25% glass surface within the pore space. The solubility constant of each measured crystal was estimated for the given molar surface area ($K_s0_{(A)}$) (Stumm and Morgan, 1996, Schindler, 1967), according to:

$$lnKs0_{(A)} = lnKs0_{(A=0)} + \frac{3\gamma A}{3RT} \qquad (2.3)$$

where $\ln Ks0_{(A=0)}$ is the published solubility constant at equilibrium (for an infinite molar surface area, A=0 m^2/mol), γ is the solid-liquid interfacial free energy for calcite (0.094 J/m^2)(Stumm and Morgan, 1996), R is the gas constant and T is the temperature (K). Accordingly, small crystals tend to have a larger free surface energy than larger crystals, which makes them thermodynamically less stable and more soluble (Stumm and Morgan, 1996, Schindler, 1967, Morse and Mackenzie, 1990).

Spatial Distribution of Precipitated Calcium and Strontium: The distribution of immobilized Ca and Sr was assessed by disassembling the reactors and sampling after complete plugging. Swabs of crystal precipitates were taken at several locations in each reactor and dissolved in 10% HNO_3 to provide a relative concentration of Sr and Ca at several locations in the reactor. Additionally, crystals were taken from various locations of the reactor, dried, and weighed. Samples were dissolved, and Ca and Sr concentrations were measured by ICP-MS analysis to provide a weight % of Ca and Sr in the precipitates.

Homogeneous Partition Coefficient: Based on Equation 2.4, a homogeneous partition coefficient was calculated from the extracted precipitates to quantify the extent of incorporation of Sr into the calcium carbonate lattice.

$$D_{Sr} = \frac{X_{Sr}}{X_{Ca}} * \frac{[Ca]}{[Sr]} \qquad (2.4)$$ (Curti et al., 1997)

In this equation, x_{Sr} indicates the concentration of Sr in the solid phase at a specific reactor location, and [Sr] indicates the fluid concentration of Sr^{2+} at a specific reactor location. Since only the inlet and outlet fluid concentrations were measured, two

different concentration profiles were assumed to exist in the reactor: a) linearly decreasing gradient and b) exponentially decreasing concentration profile.

Results and Discussion

Effluent Solution Chemistry

Sr-Inclusive Reactor Substrate Conversion: At the final sample time (11 hours), ICP-MS analysis indicated that the effluent contained 0.64% of the source calcium concentration and 2.34% of the source strontium concentration. A mass balance over the experimental duration concluded that 98.61% of available calcium (82.4mg) and 95.76% of available strontium (2.3mg) was precipitated. The data for this calculation is in Appendix G.

Sr-Free Reactor Substrate Conversion: At the final sample time (11 hours), ICP-MS analysis indicated that the effluent contained only 0.48% of the source calcium. A mass balance indicated an overall experimental $Ca^{2+} \rightarrow CaCO_3$ conversion of 98.88%. The data for this calculation is in Appendix G.

General Observations: Changes in the effluent chemistry of both systems indicated that ureolysis had occurred (Figure 2.2). Increases in ammonium concentration and pH occurred (Figure 2.2 a,b), protein was measured, and CFU counts on agar with urea confirmed the existence of an active culture (Figure 2.2 c,d). Only very small differences between total and dissolved concentrations of Ca and Sr were detected (Figure 2.2 e,f), indicating that particulate Ca or Sr was not transported out of the reactor.

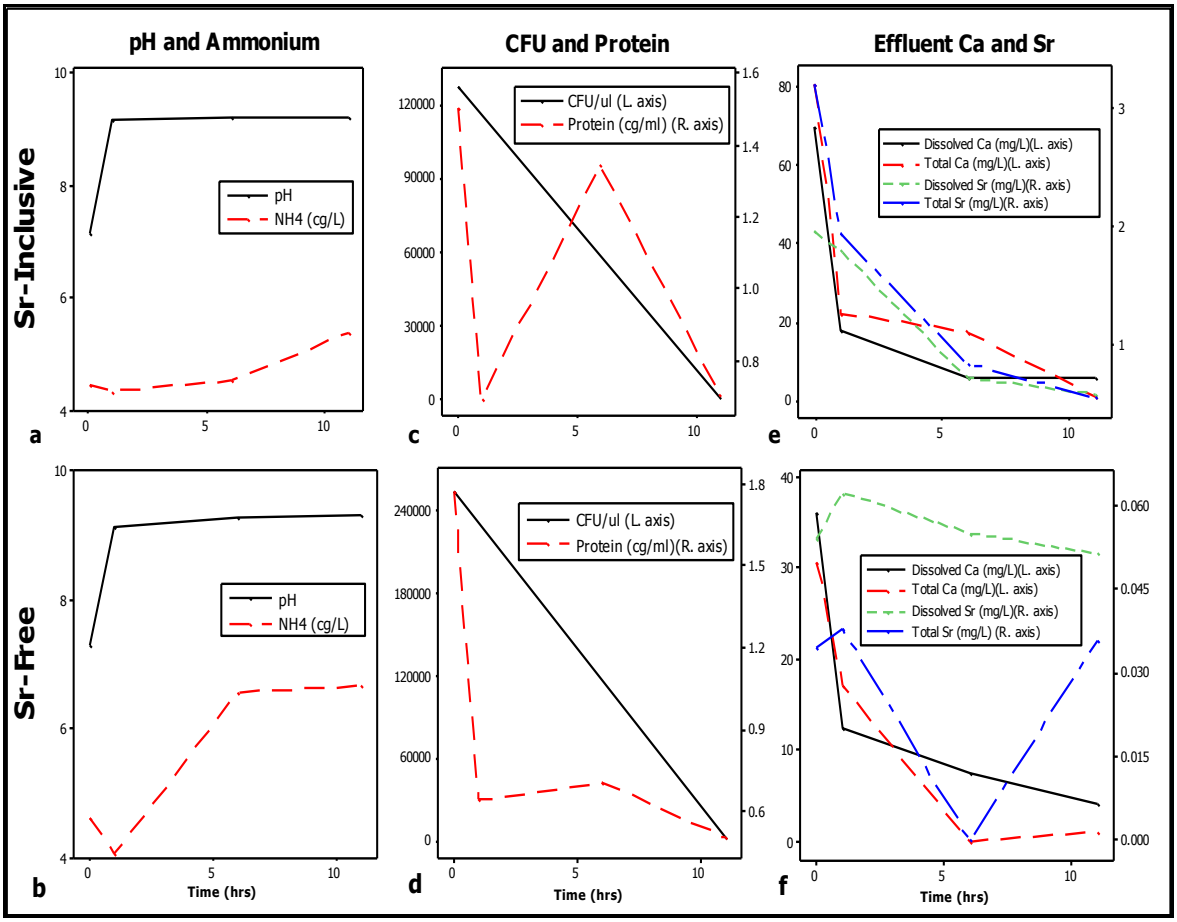

Figure 2.2. Graphs on the top show the effluent samples of the Sr-inclusive reactor, and graphs on the bottom show the Sr-free reactor. Both reactors show an increase in pH and ammonium (1cg/L = 10^{-2} g/L) (a,b), suggesting that ureolysis occurred (left graphs). Measurable quantities of CFUs and protein (1cg/mL = 10^{-2} g/mL) indicated the presence of an active culture (c,d). Effluent concentrations of calcium and strontium decreased over time, and were at all times much less than the influent concentrations (844 mg/L for Ca, and 21 mg/L for Sr) (e,f)

The total and dissolved effluent Ca concentrations were higher in the Sr-inclusive system throughout the experiment, indicating a minor inhibitory effect of strontium on $CaCO_3$ precipitation. This supports the conclusions by Mitchell and Ferris (2006), who demonstrated that a higher saturation state must be reached before calcite can nucleate in the presence of Sr, which may reflect the ability of Sr to potentially block heterogeneous nucleation sites. Despite this slight decrease in Ca precipitation rates, high overall

precipitation efficiency was achieved, suggesting that the presence of Sr will not severely affect $CaCO_3$ precipitation strategies on large scales (e.g., field-scale).

Precipitation of Calcium Carbonate:

Precipitation was visible and led to complete reactor plugging in the Sr-free system after 14 hours and the Sr-inclusive system after 15 hours. A replicate study found complete reactor plugging at a similar time. XRD analysis of the solid phase showed a signal for calcite with possible additional patterns for halite and ammonium chloride. The XRD data is included in Appendix H.

As observed by stereoscope analysis, a gradient in crystal size was evident (Figure 2.3). Quantitative assessment of crystal size and density confirmed that the average size decreased but the density remained fairly constant (Figure 2.4), while the calculated solubility increased (Figure 2.5). Calculations were performed - based on the averaged size and density of the crystals. However, there was a difference between the glass surface and the etched polycarbonate surface. The data for this observation, showing the precipitate size and density on the glass and polycarbonate surfaces, are included in Appendix I. Precipitate diameters, which ranged from approximately 0.02mm to 0.06mm, were significantly larger than the batch precipitates measured by Mitchell and Ferris (2006), which grew over four days to approximately 1000nm (0.001mm). This reflects the continuous influx of Ca^{2+} in the flow system environment compared to the closed-system experiments performed by Mitchell and Ferris, where only 1.75 mM of Ca was available to precipitate.

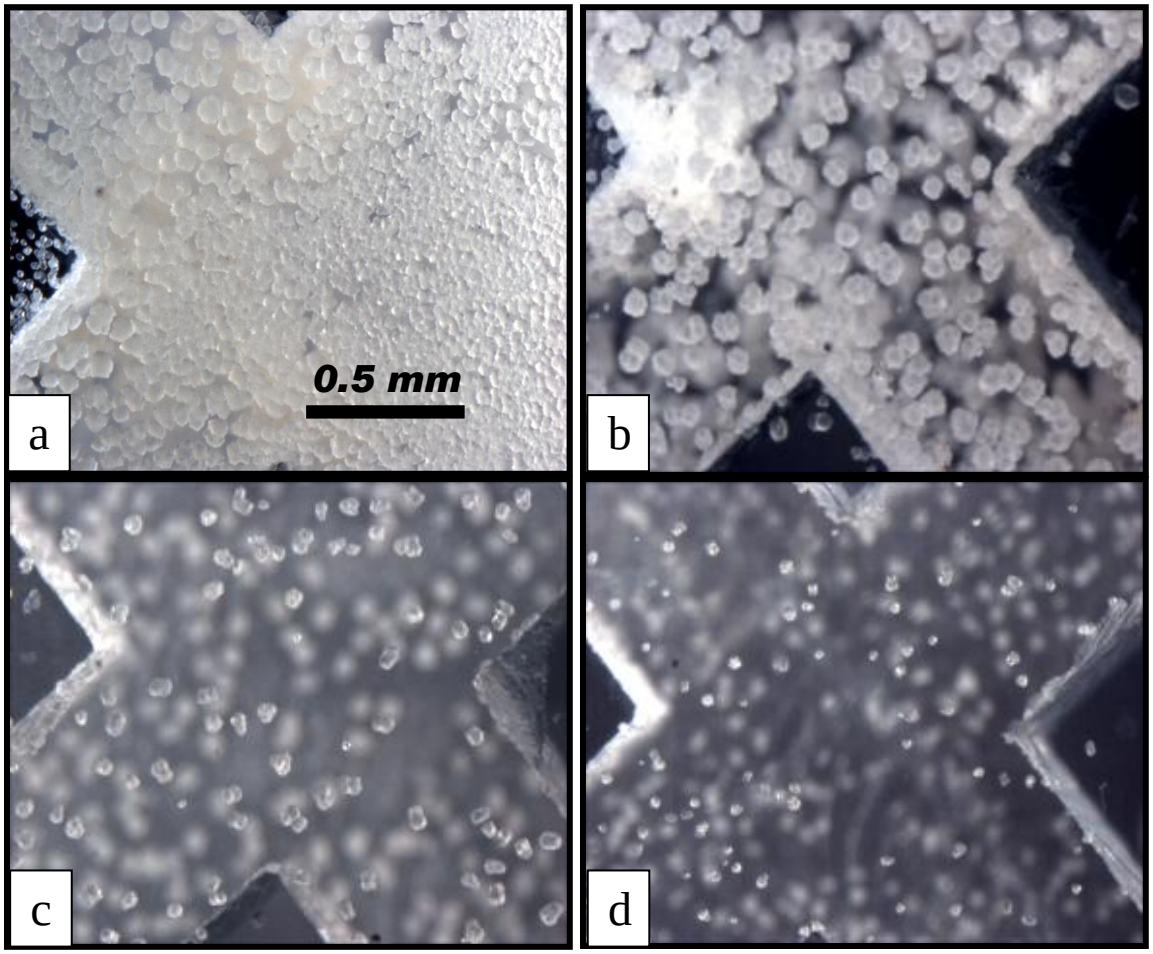

Figure 2.3. Selected stereomicroscopy images taken from above a reactor (Sr-inclusive) and focused on mineral formation on the interior surface of the glass cover slip. (a) inlet region, (b) 2cm from inlet, (c) 5cm, and (d) outlet region. Note the size gradient from inlet to outlet. Images such as these provided the data for size, density, and solubility calculations.

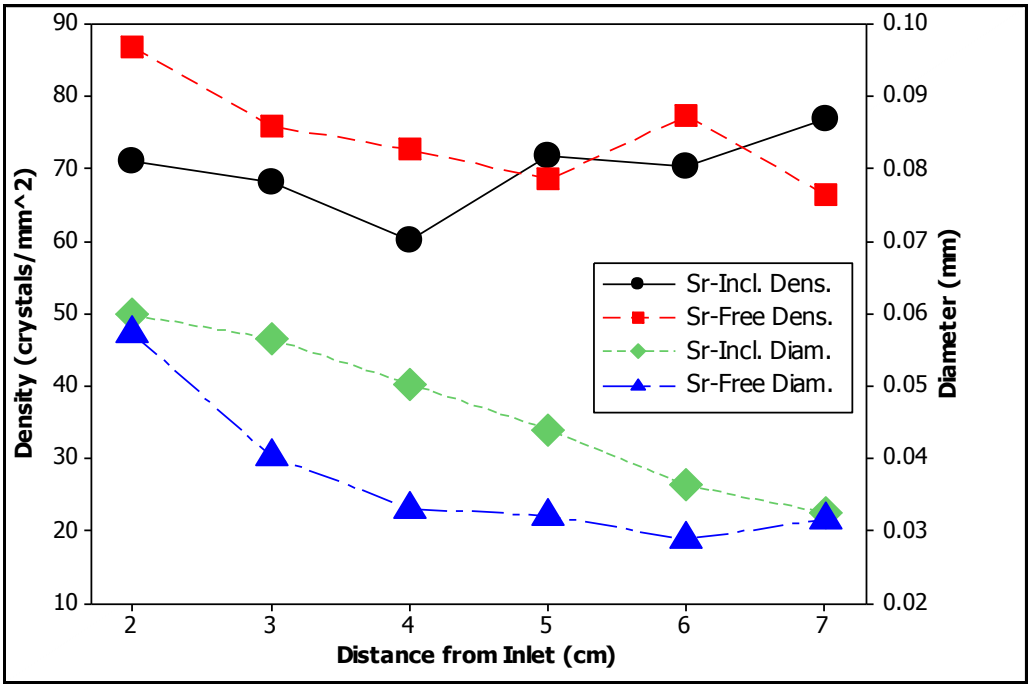

Figure 2.4. Mean density (crystals/mm^2) and crystal diameter (mm) at each reactor location (cm from inlet), as measured by ImageJ analysis. At reactor position 1, the data is omitted because the extent of precipitation was too high to reliably differentiate and measure separate precipitates (see Figure 2.3a).

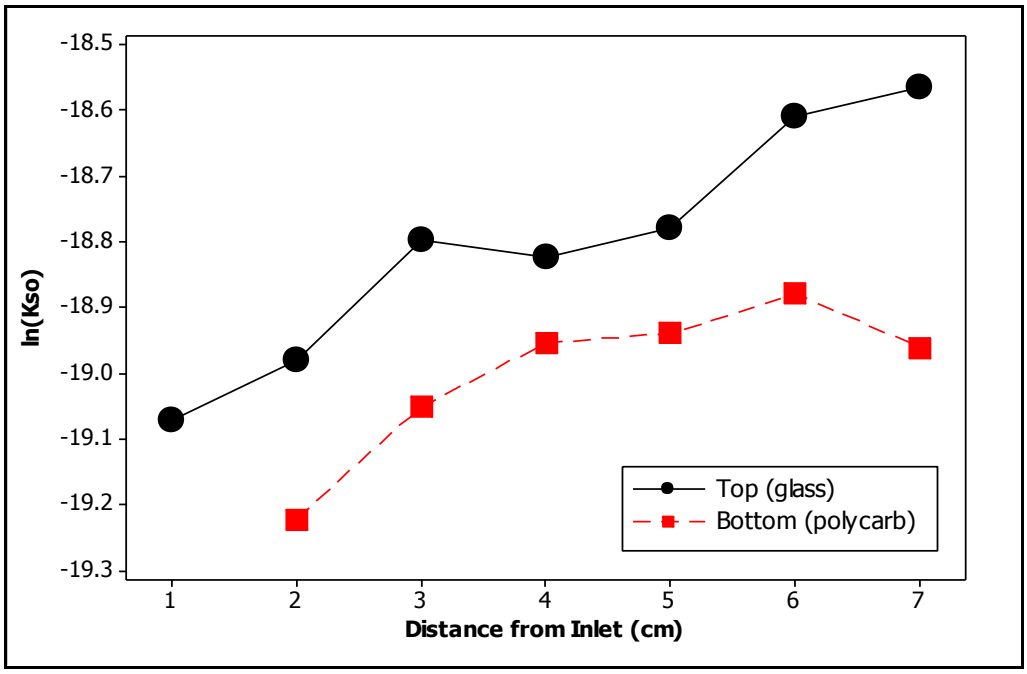

Figure 2.5. Crystal solubility estimates based on precipitate size. The smaller crystals in the effluent region are assumed to be more soluble due to a larger surface energy, as outlined in Equation 2.3.

Based on the image data describing crystal density and size, a mass balance on calcite was performed. The images and data for size and density of precipitates are included in Appendix J. Assuming the crystals to be uniformly distributed along the reactor width and spherical in shape, an average calcium density (g Ca/mm^2 surface area) was calculated for each reactor and multiplied by the reactor surface area (9194 mm^2). These calculations, contained in Appendix K, assume the precipitates to be pure calcite with a density of 2.71 g/cm^3 and 40 wt% calcium (Mindat.org).

Table 2.1. Comparison of the extent of calcium immobilization within the reactors as estimated by image-based analysis with effluent-based analysis. This data estimates the percent immobilized based on image analysis to be much lower. This discrepancy may be due to the inability to measure the most densely precipitated inlet region, the assumption of spherical precipitates, and the possible presence of crystals smaller than the detection limit of the stereoscope analysis.

	Image-Based Mass Balance		*Effluent-Based Mass Balance*	
	Sr-Free	Sr-Inclusive	Sr-Free	Sr-Inclusive
Calcium Precipitated	30.84 mg	49.13 mg	83 mg	82 mg
Percent Immobilized	36.91 %	58.79 %	98.8 %	98.6 %

Compared to the effluent mass balance, a lower extent of precipitation was calculated for each reactor (Table 2.1). This could be due to the fact that the dense region near the inlet (Figure 2.3a) and the tubing immediately upstream of the reactor were not accounted for in the image analysis and the possibility of the existence of precipitates too small to be detected using the stereo microscope (precipitates smaller than approximately 0.02mm) were not accounted for, and if numerous, would provide a significant addition to the image-based mass balance. An additional difference was that a higher conversion

was calculated for the Sr-inclusive system by image analysis, in contrast to the effluent analysis and order of plugging which supported a higher conversion in the Sr-free system.

Co-precipitation and Potential Inhibitory Effects of Strontium

Swab and dried-crystal samples were collected post-plugging from several reactor locations were dissolved in dilute nitric acid and analyzed by ICP-MS. This data, shown in Appendix L, confirmed the presence of Sr in the crystals from the Sr-inclusive system. The measured ionic concentrations were much greater in the swabbed samples than the dried-crystal samples. The low concentrations detected in the dried and acid digested crystal samples were close to the detection limit of the ICP-MS instrument and thus potentially associated with higher uncertainty. Therefore, the swab data were used to provide a ratio of immobilized Sr to Ca at various locations. Based on the assumptions of a linear and exponential reactor gradient in fluid concentrations, homogeneous partition coefficients were calculated. A linear fluid concentration assumption assumes that the reaction rate was zero order along the flow path, while an exponential fluid concentration gradient assumes that the reaction rate is dependent on substrate concentrations (i.e., greater than zero order). The data are included in Appendix M. The results shown in Figure 2.6 indicated that there was greater partitioning of Sr^{2+} near the inlet region.

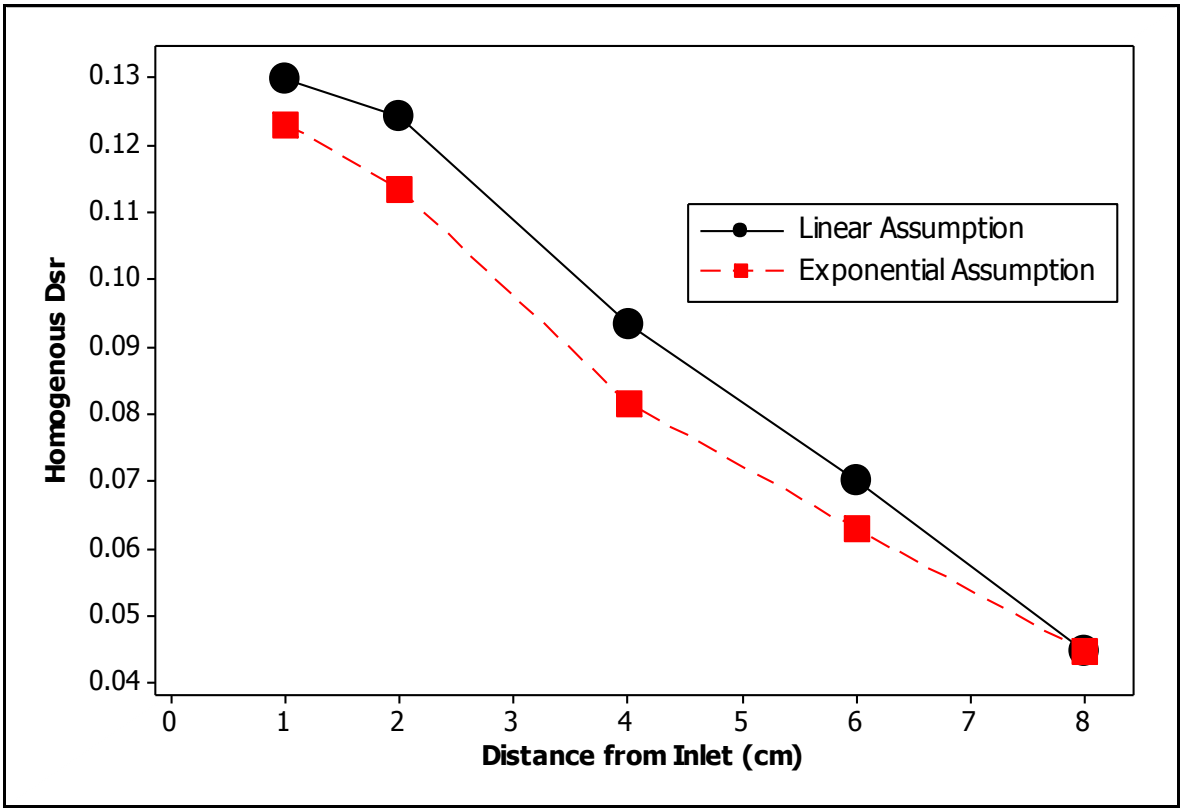

Figure 2.6. Homogeneous partition coefficient as a function of reactor position (cm from inlet). Values were calculated using Equation 2.4, with the fluid ionic concentrations based on linear and exponential decrease from inlet to outlet measured concentrations. Both assumptions show a similar trend in a decreasing Sr homogeneous partition coefficient from inlet to outlet.

Greater partitioning of Sr and other contaminants has previously been correlated with higher calcite precipitation rates (Mitchell and Ferris, 2006). Since the inlet region of the flow reactors displayed more extensive precipitation (Figure 2.3), indicative of higher calcite precipitation rates, this data further suggests that there is a correlation with greater Sr^{2+} partitioning. This means that it may be beneficial for co-precipitation strategies to maximize precipitation rates, while at the same time avoiding extensive plugging that would limit transport objectives.

Environmental Significance

Principal findings from this study supported the applicability of divalent contaminant sequestration in groundwater by confirming the ability of *S. pasteurii* to rapidly induce calcite precipitation in the presence of Sr^{2+} while simultaneously immobilizing Sr within the crystal lattice under flow conditions. A higher than 95% conversion of dissolved ions to precipitate was achieved for each divalent species (Ca and Sr). The potential for inhibition of calcite formation by Sr was shown to be minimal from a practical standpoint. Future studies should seek to maximize transport objectives and kinetics, particularly since this study indicated increased partitioning of Sr in regions of higher kinetic activity. This may potentially involve stimulation of the microbial community, similar to the use of molasses by Fujita et al. (2008).

Several studies have demonstrated that the success of *in situ* remediation relies on the transverse mixing of substrates along the plume margins. For two-dimensional reactors, Acharya et al. (2007) suggested that product formation can be predicted using transverse dispersion coefficients obtained from a tracer, regardless of pore geometry and size. Tartakovsky et al. (2008) demonstrated that calcium carbonate precipitation can further induce effects on dispersive mixing and flow dynamics. These types of analyses of the effect of fluid substrate mixing on ureolytic calcite precipitation must be considered in future reactor studies since mixing limitations may be present. The ample availability (e.g., feedlots and other sources of animal waste) and affordability of urea render potential technologies highly feasible, but a detailed economic analysis will be necessary prior to field-scale application.

IMAGING BIOLOGICALLY-INDUCED MINERALIZATION AND BIOFILM FORMATION IN A FULLY-HYDRATED FLOW SYSTEM

Manuscript Preface

To gain a more complete understanding of the phenomena observed in the flat plate reactors, studies were conducted in capillary flow cells to allow a better microscopic analysis of biomineralization. These investigations have been included in the format of a manuscript that was submitted to Microscopy Today. The experiments sought to replicate the flow environment of the previously-mentioned flow experiments in the 1mm x 1mm capillary reactors previously used by Pitts and Stewart (2008), so that the minerals and bacteria could be viewed *in situ* using high resolution microscopy techniques.

The flat plate experiments, conducted in a network of 1mm x 1mm pores elucidated macroscopic trends in crystallization patterning. However, due to the thickness of the cover slip (1mm), an *in situ* assessment of the micron-scale environment that was ultimately responsible for the macroscopic trends was not possible. To address this, glass capillary flow cells (Friedrich & Dimmock Inc., Millville, NJ), which have the outside wall thickness of a standard microscopy cover slip (0.17mm), were utilized (Figure 3.1). They were incorporated into a constant flow system (Figure 3.2):

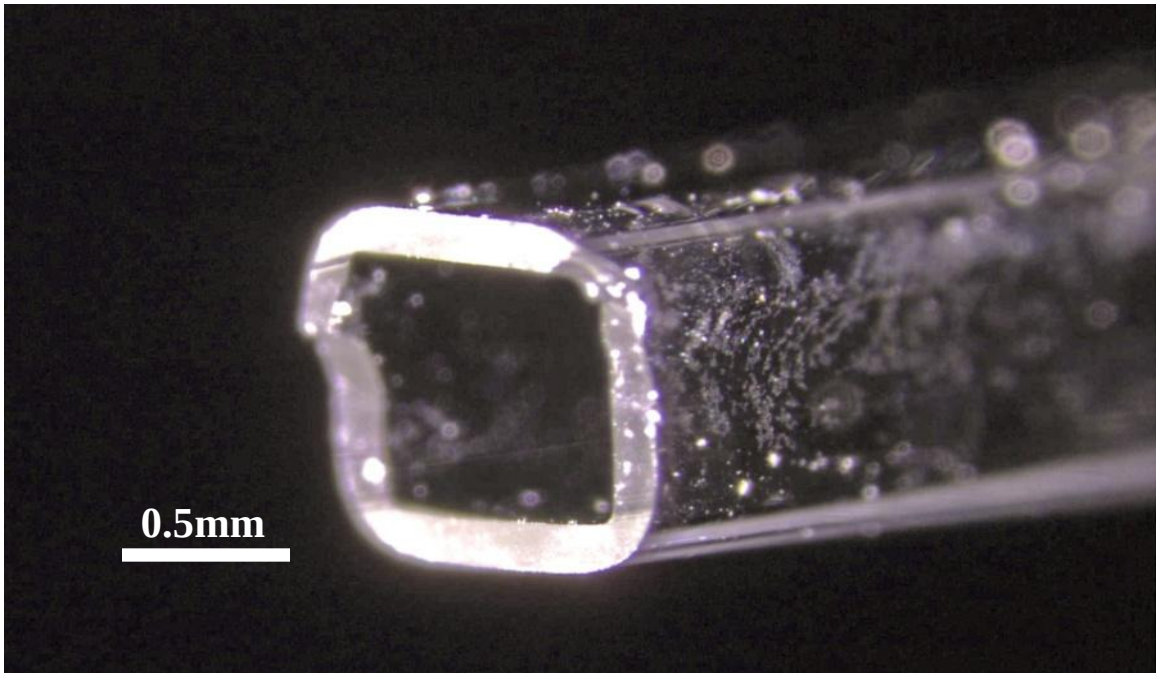

Figure 3.1. Image of the end of a glass capillary flow cell custom made by Friedrich and Dimmock (Millville, NJ). The interior flow channel is 0.9mm by 0.9mm wide, and the wall thickness is 0.17mm.

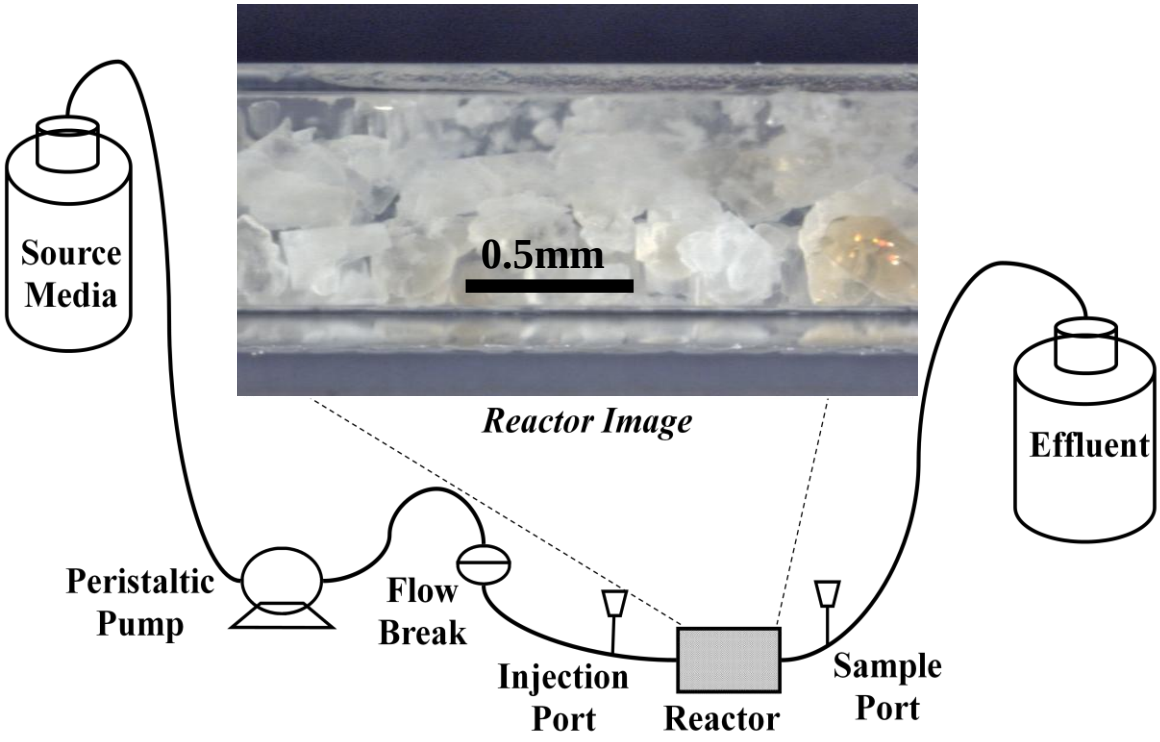

Figure 3.2. Schematic of capillary flow system. In this diagram, flow proceeds from left to right. The inset image shows a capillary reactor with visible $CaCO_3$ precipitates.

The experimental conditions were designed to simulate the media, inoculum, and pore size of the previous experiment (see Chapter 2). The flow rate used was 0.02 ml/min, which translates to an average pore velocity of approximately 2.5 cm/min.

This study focused solely on imaging, and did not account for effluent chemistry, substrate balances, or co-precipitation. The general results showed the formation of $CaCO_3$ and biofilm (Figures 3.3 – 3.5).

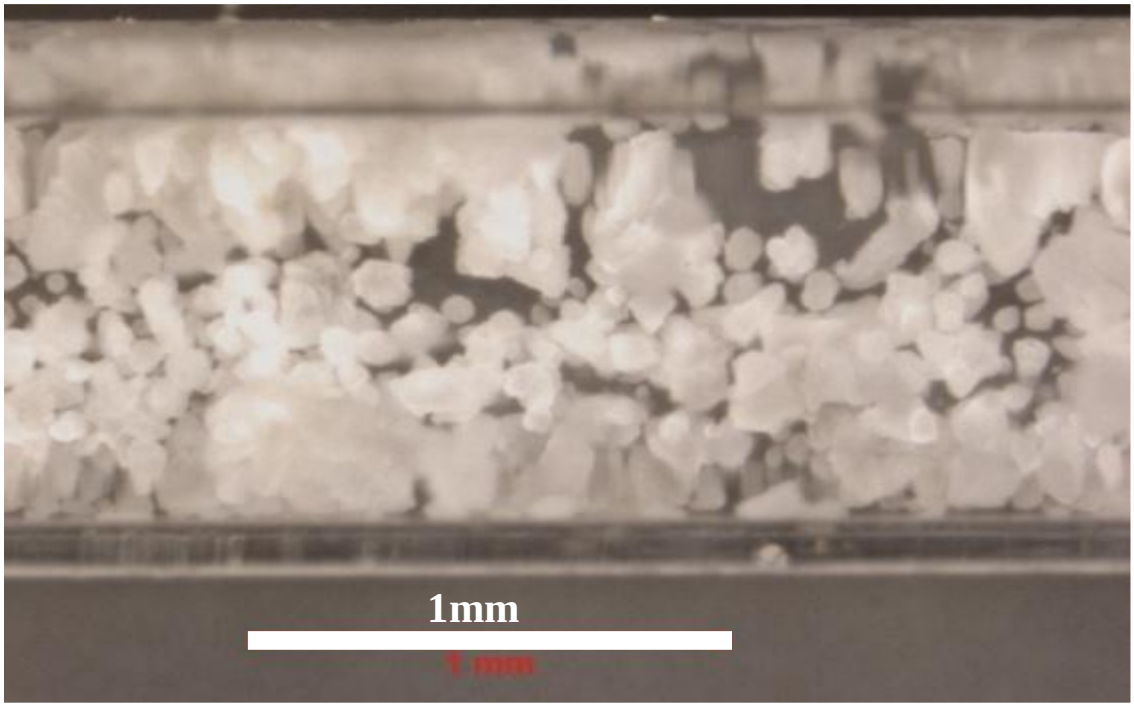

Figure 3.3. Stereo microscope image of ureolytic $CaCO_3$ precipitation in a flow cell.

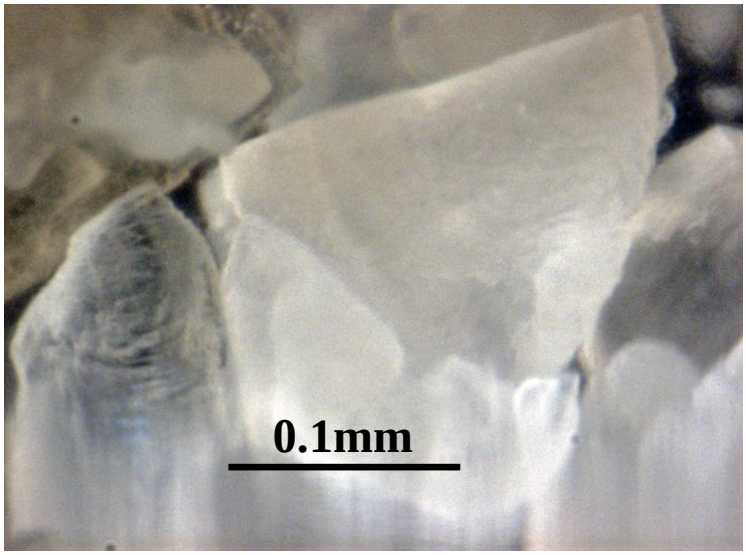

Figure 3.4. Stereo microscope image of precipitates

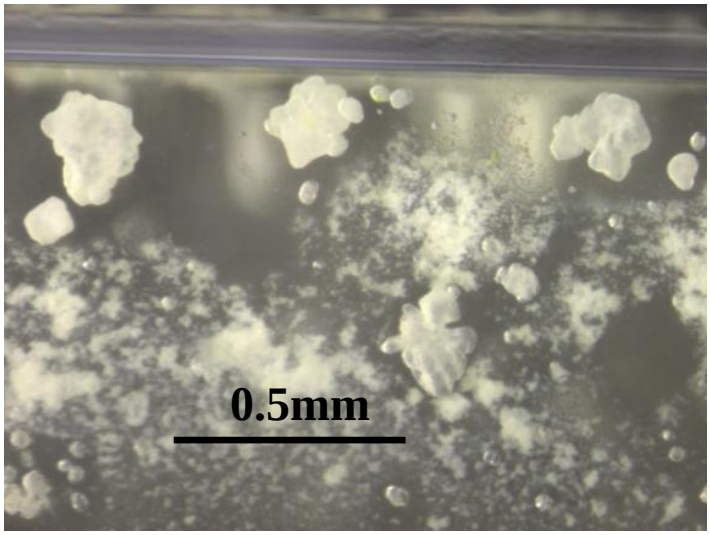

Figure 3.5. Stereo microscope image of biofilm and calcite precipitates attached to the surface of the glass capillary

Much of this research was presented at the 2009 Microscopy and Microanalysis Conference in Richmond, VA on July 26, 2009. The abstract for this presentation is included in Appendix N. The following pages include the manuscript that was submitted to Microscopy Today.

This manuscript, titled IMAGING BIOMINERALIZATION PROCESSES IN FULLY-HYDRATED FLOW SYSTEMS, was submitted to Microscopy Today on October 14, 2009.

Authors

Logan Schultz, Betsey Pitts, Andrew C. Mitchell, Alfred B. Cunningham, Robin Gerlach*
Center for Biofilm Engineering, Montana State University, Bozeman, MT 59717
**robin_g@biofilm.montana.edu*

Introduction

A number of proposed technologies involve the controlled implementation of biologically-induced carbonate mineral precipitation in the geologic subsurface. Examples include the enhancement of soil stability (Whiffin et al., 2007), immobilization of groundwater contaminants such as strontium and uranium (Mitchell and Ferris, 2006), the enhancement of oil recovery (Ferris et al., 1996), and geologic carbon sequestration via controlled permeability reduction. The most significant challenge in these technologies remains to identify and better understand an industrially, environmentally, and economically viable carbonate precipitation route. One of the most promising routes is ureolytic biomineralization, due to the ample availability of urea and controllable reaction rate. In this process, ureolytic bacteria hydrolyze urea, leading to an increase in pH. In the presence of calcium, this process favors the formation of solid calcium carbonate, as illustrated in the following equations:

$CO(NH_2)_2 + H_2O \rightarrow NH_2COOH + NH_3 \rightarrow 2\ NH_3 + CO_2$ (3.1) (Urea hydrolysis)

$2NH_3 + 2H_2O \leftrightarrow 2NH_4^+ + 2OH^-$ (3.2) (pH increase)

$CO_2 + 2\ OH^- \leftrightarrow CO_3^{2-} + H_2O$ (3.3) (Carbonate formation)

$CO_3^{2-} + Ca^{2+} \leftrightarrow CaCO_3\ _{(solid)}$ (3.4) (Precipitation)

This process relies on molecular level chemical and biological processes that must be better understood for large scale implementation. Researchers at the Center for Biofilm Engineering at Montana State University have conducted several biomineralization experiments in simulated porous media reactors. Microscopy has proven to be one of the most useful analytical tools in these studies, providing the ability to non-invasively visualize, differentiate, and quantify the various components, including the cells, cell matrix, and mineral precipitates. Due to the possibility of real-time observation and lack of dehydration artifacts, this imaging situation has been tremendously useful for elucidating temporal and spatial relationships of these components. A stereo microscope was used to provide a macroscopic view, and to quantify the orientation and volume occupation of precipitates within the pore networks. Confocal laser scanning microscopy (CLSM) was used to evaluate the micro-scale interaction between the crystalline surfaces and the biofilm. This article discusses some techniques and examples of imaging biomineralization in flow reactors with these tools.

Bacterium/Flow Medium

The soil bacterium *Sporosarcina pasteurii* was used to induce ureolysis. For each study, the flow reactor was inoculated with a culture of *S. pasteurii*, and the cells were

allowed to attach for 1.5 hours before flow was started. The flow medium, consisting of nutrient broth, urea, and dissolved calcium, was pH-adjusted to 6.0 to avoid immediate mineral precipitation.

Stereo Microscopy

To characterize the spatial and temporal development of precipitates in a network of pores, a Nikon SMZ 1500 stereo microscope was placed over the following reactor system (Figure 3.6):

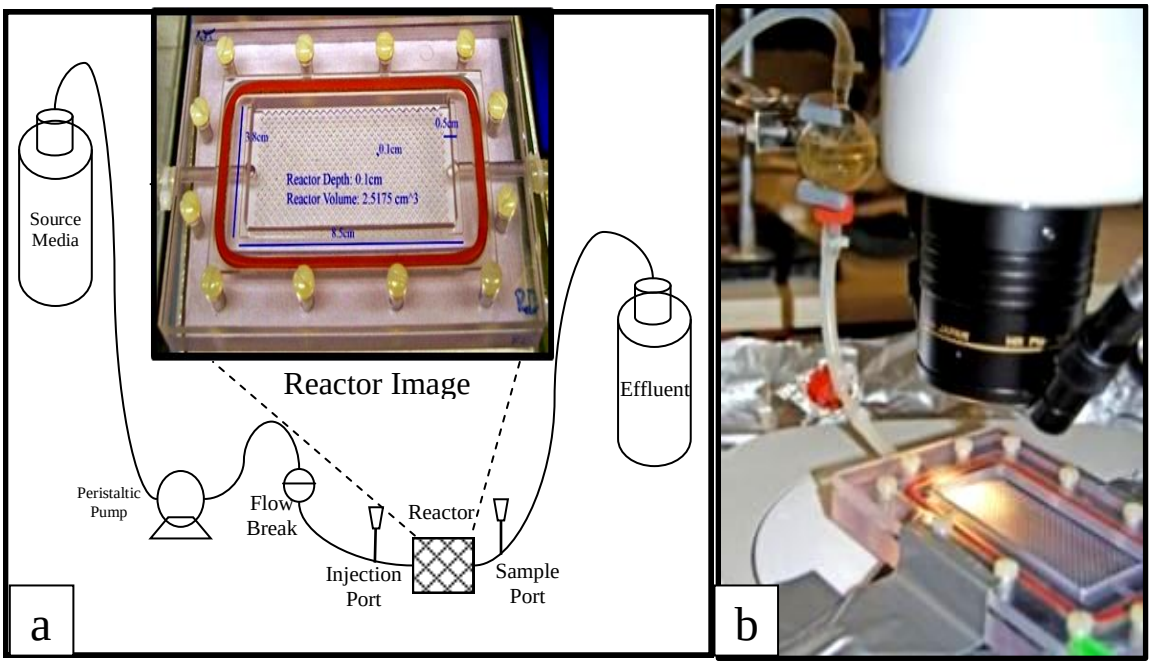

Figure 3.6: (a) Schematic of 2-dimensional reactor with a network of 1mm pores. (b) Photograph of reactor being imaged by Nikon SMZ 1500 stereo microscope during biomineralization experiment.

Throughout the 15 hour experimental duration, images of one region near the inlet were taken at regular time intervals, allowing for a time-lapse video of the mineral growth to be constructed. This video provided insight into nucleation and precipitation

kinetics. Images from this video are included in Appendix O. At the end of the experiment, when the reactor had been terminally plugged, images were taken along the length of the reactor to assess spatial distribution. These images, displayed in Figure 3.7 below, highlight a gradient in mineral size, from inlet to outlet.

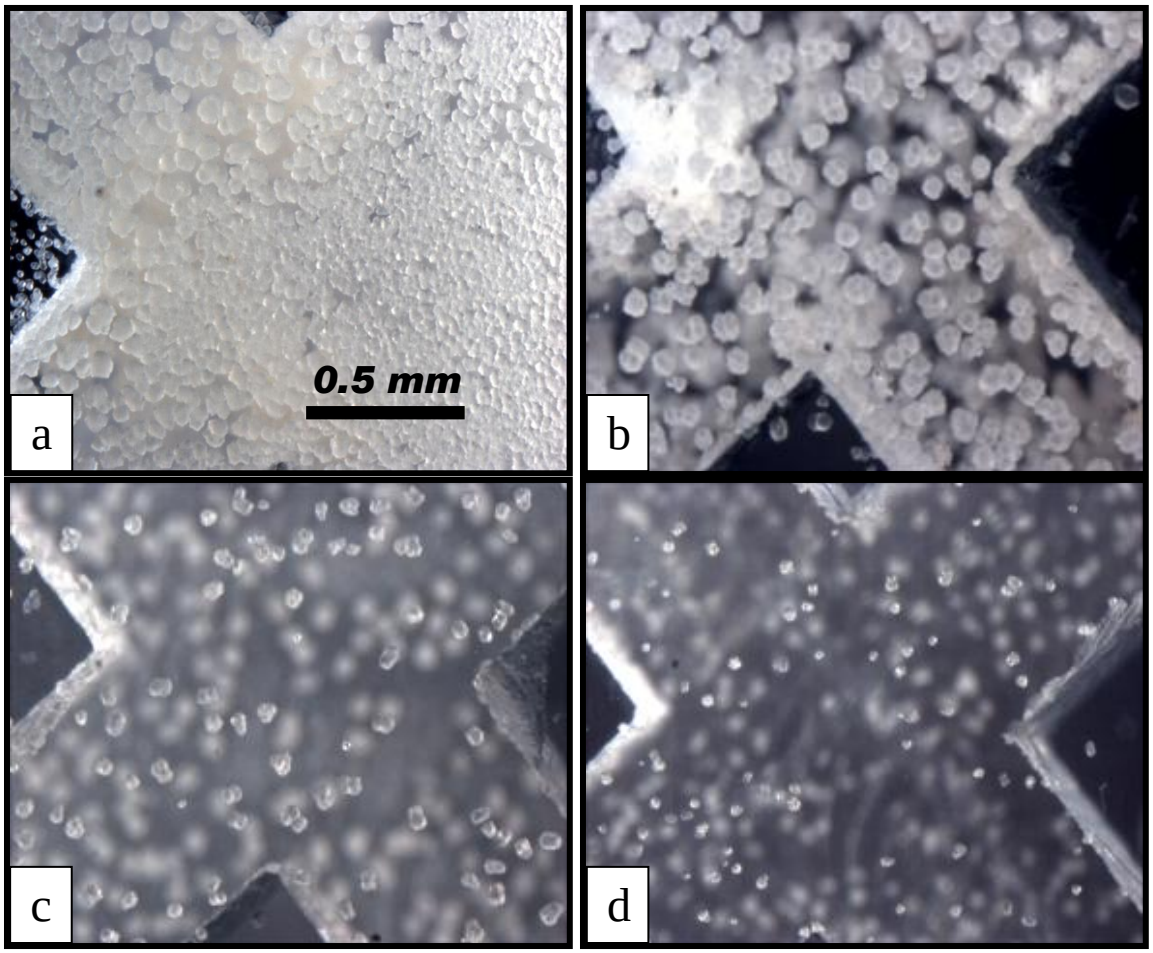

Figure 3.7(a-d). Selected stereomicroscopy images taken from above the reactor and focused on mineral formation on the interior surface of the glass cover slip. (a) Inlet region, (b) 2cm into the reactor (c) 5cm into the reactor, and (d) Outlet region (approx. 8 cm into the reactor). Note the size gradient from inlet to outlet. Images such as these provided the data for size, density, and solubility calculations as a function of reactor location and retention time.

From images such as those in Figure 3.7, a significant amount of quantitative data can be obtained. Using ImageJ software (Rasband, 1997-2009), the precipitates in each

field of view were counted and measured. The images used for these analyses are included in Appendix J. A later analysis of extracted precipitates with X-ray diffraction (Appendix H) showed that calcite was the predominant mineral. Assuming the precipitates to have the density of calcite, 2.71 g/cm^2 (Mindat.org), the total amount of calcium immobilized within the reactor was calculated (Appendix K). Knowing the chemical composition of the inlet, outlet, and the flow rate of the fluid, the overall experimental conversion of dissolved calcium to solid calcite was calculated (Appendix G). The conversion rates based on the effluent-chemistry and based on image analysis were found to be similar, suggesting that this imaging situation can effectively assess mineral precipitation reaction phenomena. A solubility constant of each measured crystal was estimated for the given molar surface area, and the crystal solubility was calculated for each region of the reactor, based on the solubility equation developed by Stumm and Morgan (1996). The results suggested that the crystal solubility increased with distance into the porous media reactor due to a larger free surface energy of the smaller crystals.

Confocal Laser Scanning Microscopy

The large-scale processes observed by stereo microscopy and chemical analysis were ultimately dictated by processes that occurred on a much smaller scale, thus demanding the ability to visualize microbe-mineral interactions on a smaller scale. High resolution differentiation of the components involved in the biologically-induced mineralization processes will aid in our ability to understand and ultimately control the overall process. Glass capillary flow systems previously used in our laboratories were

used for this purpose (Figure 3.8) (Pitts and Stewart, 2008). The 0.17mm thick glass walls allowed for non-invasive high resolution CLSM. A Leica TCS-SP2 AOBS confocal microscope and Leica 63x water immersion lens (2mm working distance) were used. Imaris image analysis software (Bitplane Scientific Software, St. Paul, MN) was used to compile the z-stacks into 3-dimensional images.

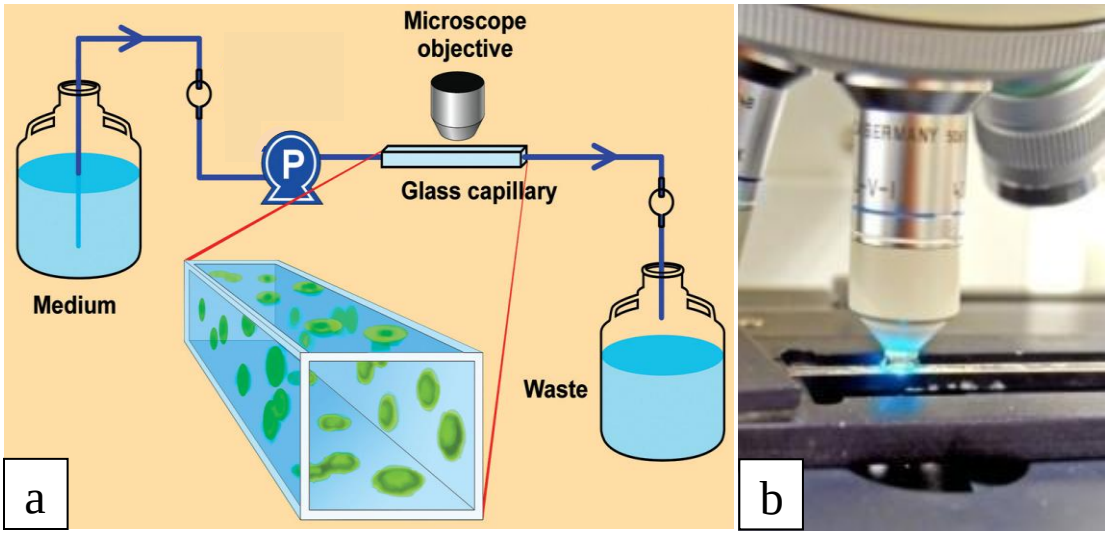

Figure 3.8. (a) Illustration of a 1mm square glass capillary flow cell. Minerals and bacteria are imaged through the glass ceiling of the capillary. Drawing by J.Meyer, MSU-CBE (Pitts and Stewart, 2008). (b) Photograph of reactor being imaged.

After the system was run for 2 days and visible minerals had formed, fluorescent stains were applied to the reactors to differentiate the various components. In the first study, SYTO-11 and C_2-dichlorotriazine (C_2d) (Invitrogen, Carlsbad, CA) were used. C_2d (red) is expected to bind to alcohols and polysaccharides and thus most likely compounds associated with the extracellular matrix; SYTO-11 (green) is a nucleic acid stain that is expected to penetrate cell walls and bind to the DNA in bacteria.

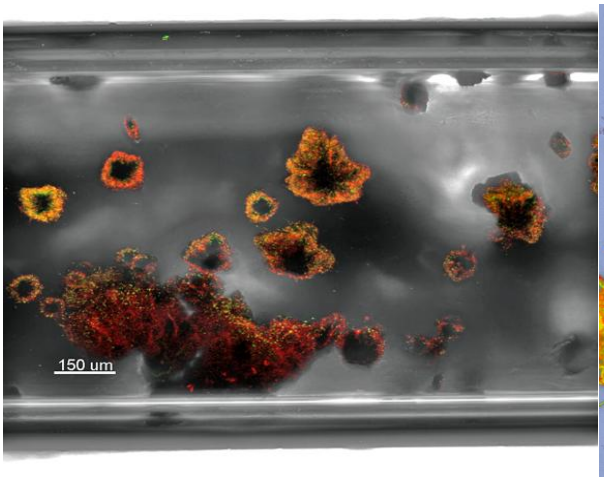

Figure 3.9. CLSM image of capillary stained with SYTO-11 (green) and C2-d (red) highlighting the intimate relationship between cell attachment and $CaCO_3$ surface.

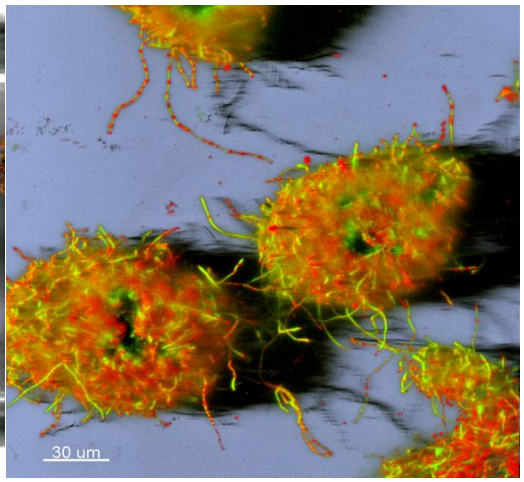

Figure 3.10. Reconstructed CLSM image from the perspective of the inside of the capillary showing cells and cell matrix surrounding $CaCO_3$ crystals.

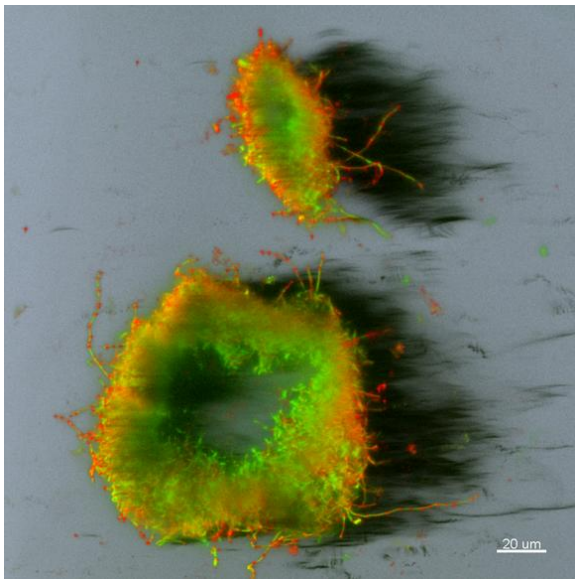

Figure 3.11. Reconstructed CLSM image of cells and cell matrix from the perspective of outside the capillary. The apparent void space at the cluster centers is believed to be occupied by $CaCO_3$

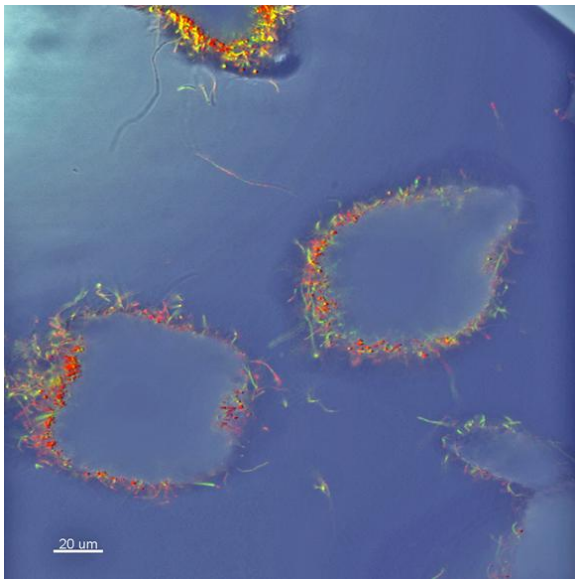

Figure 3.12: 2-D CLSM image slice highlighting a cross section at the interior of precipitates.

Figures 3.9 - 3.12 show cell attachment that is surrounding what appear to be mineral precipitates. The cells seem to be attached preferentially to the $CaCO_3$ surface

compared to the glass surface. This close relationship may further promote formation of $CaCO_3$ via the attached microbes altering the chemical environment at the calcite surface.

In the previous CLSM images, there was an apparent void space where the precipitates were located (Figures 3.11 and 3.12). A second study was conducted with the goal of overlaying a reflection stack to visualize surface topography of the $CaCO_3$ attached to the glass. In this experiment, the fluorescent stains used were SYTO-9 (green) and propidium iodide (red) (i.e., Invitrogen LIVE/DEAD® stain).

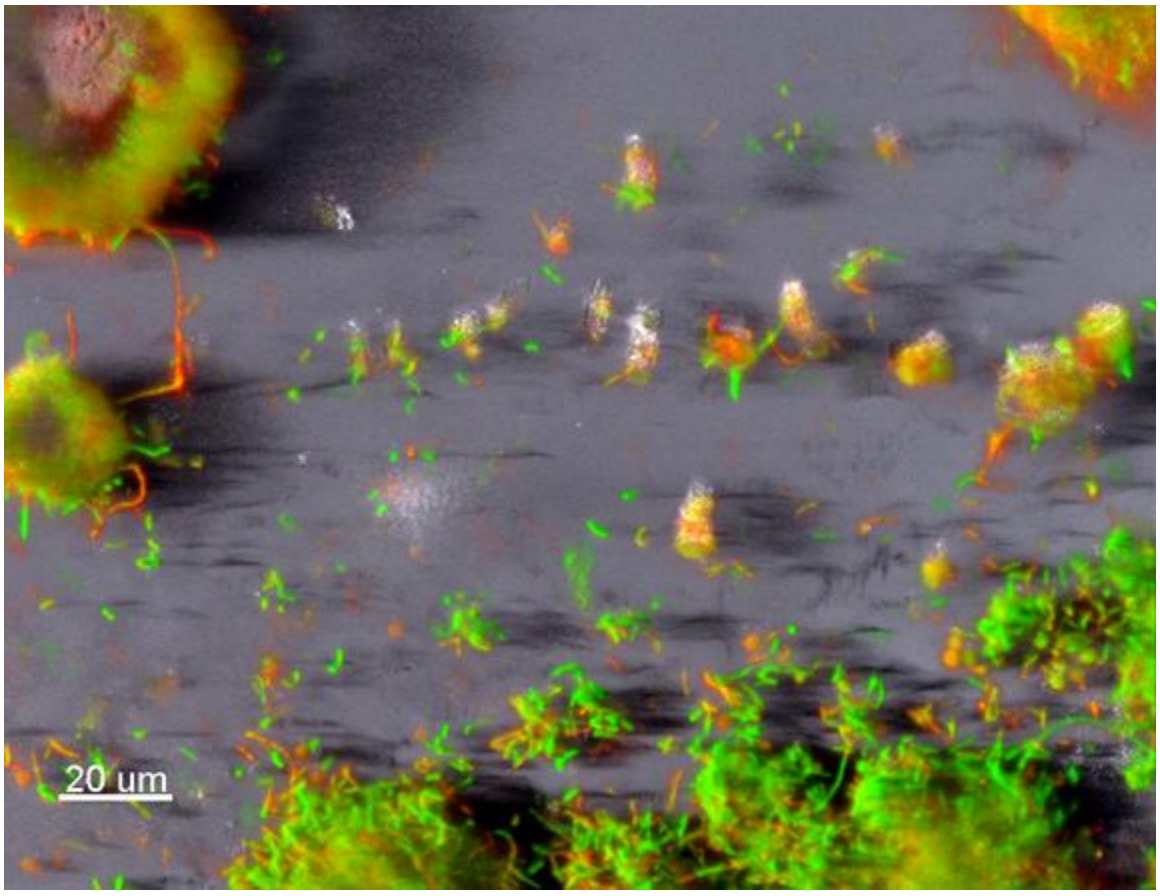

Figure 3.13. CLSM image of a capillary stained with SYTO-9 (green) and propidium iodide (red). A reflection stack is overlaid, showing small precipitates in close proximity to cells.

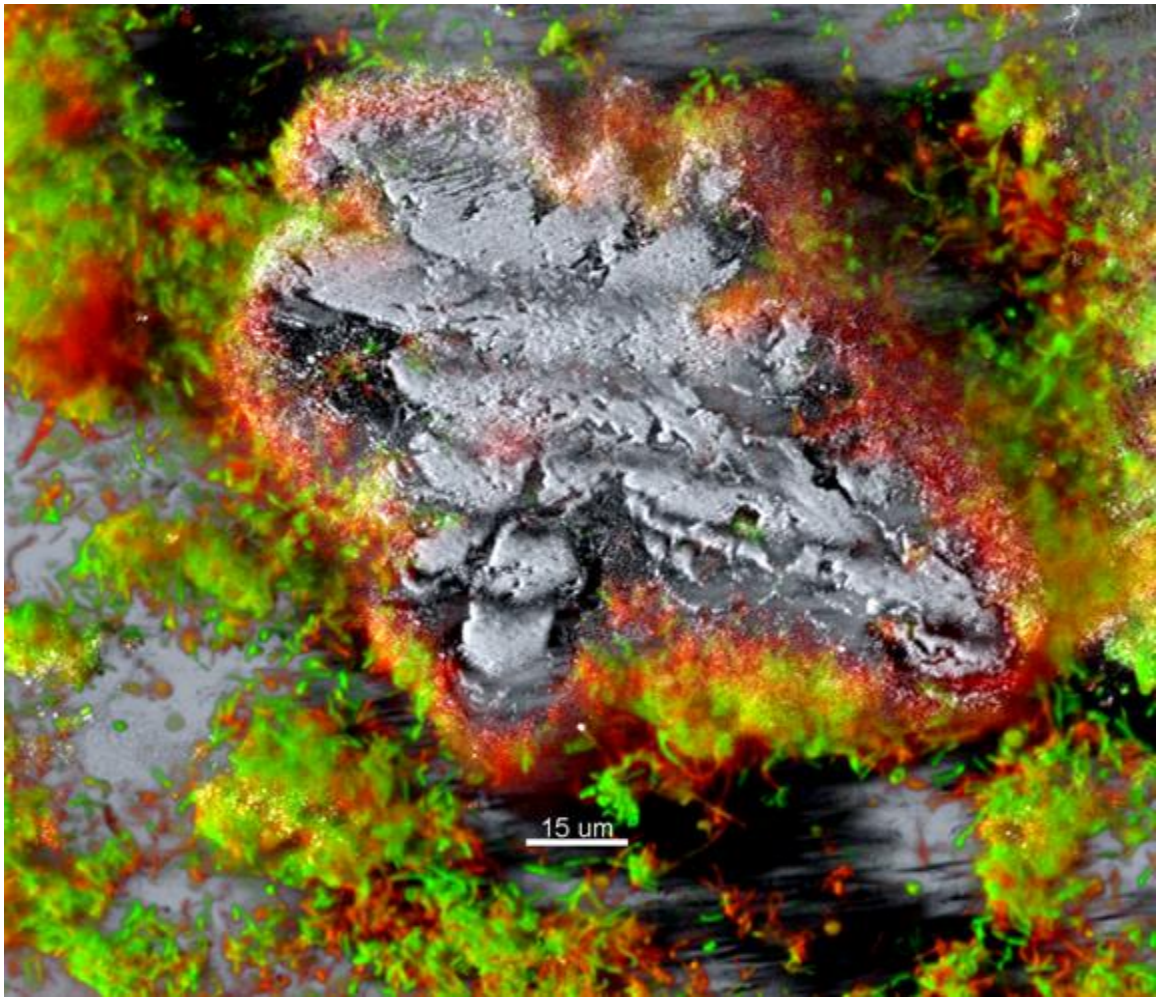

Figure 3.14. CLSM image from the perspective of outside the capillary. The reflection overlay indicates the surface topography of a large precipitate attached to the glass, and the fluorescent stains show the attached cells and cell-matrix surrounding the precipitates.

These images demonstrate the surface topography of the precipitates and the co-location of crystals and attached microbial cells. Very few cells were visible between the mineral and the glass surface (Figure 3.14), suggesting that the environment between the mineral and glass is not highly conducive to bacterial accumulation. There appears to be a higher proportion of red stain (propidium iodide) associated with the large calcite mineral in Figure 3.14, as compared to the glass, possibly indicating a larger number of

cells with compromised cell membranes (‘dead cells’). Additional confocal images can be found in Appendix P.

Conclusions

These studies have highlighted the usefulness of microscopic techniques at a variety of scales to better understand the process of biomineralization quantitatively and qualitatively. The ability to use stereo microscopy non-invasively to quantify precipitate size, density, and solubility as a function of time and location is greatly beneficial in engineering analysis and design. Furthermore, these processes, which are controlled by the local biological environment, are better understood with the use of CLSM to understand the location and physiological state of the bacteria surrounding the precipitates.

Ongoing investigations will seek to gain a better understanding of the association of bacteria throughout the process of precipitate formation. For instance, it is unclear at this point whether cells attach prior to mineral nucleation or calcium carbonate precipitates form first and bacteria attach subsequently. Additional experimental work will also focus on better understanding the distribution of cells in the interior of the mineral precipitates. Understanding the micro-scale interactions and associations of microbes and minerals is essential for the successful design of engineered biomineralization strategies. Microscopy-based methods will provide invaluable tools for the development of strategies to manipulate porous media permeability and reactive

transport on large scales and ultimately aid in the development of technologies such as contaminant co-precipitation, geologic carbon sequestration, and soil stabilization.

REACTIVE TRANSPORT IN BIOFOULED POROUS MEDIA

Introduction and Goals

A greater understanding of biofilm formation in porous media will ultimately enhance biofilm technologies and biofilm control scenarios. Contaminant remediation, microbially-enhanced oil recovery (MEOR), and carbon sequestration are just a few examples of these technologies. Filtration system biofouling, contamination, material degradation/corrosion, and lost pumping efficiency are issues linked to controlling biofilms in porous media, which can also benefit from a greater understanding. The contents of this chapter will focus on the design and implementation of flow systems to assess four main areas:

- The relationship between porosity and hydraulic conductivity in biofilm-affected reactors
- The difference between biofilms formed under constant flow rate and constant head conditions
- Channel formation and changes in effective dispersivity
- The resistivity of biofilms to biocide exposure

In biofilm-affected reactors, three types of porosity can generally be considered: 1) overall porosity of the porous media (i.e., void space), 2) effective porosity (i.e., void space in which fluid flows), and 3) internal porosity of the biofilm itself (Gerlach and Cunningham, 2010). This multi-scale perspective of porosity can also be applied to fractured rock formations, where one must consider the influence of fractures as well as

of the pores within the rock. The location of biofilm-induced porosity reduction is greatly important, since severe plugging of only one small region can often lead to high decreases in hydraulic conductivity; this phenomenon is difficult for models to incorporate.

The conditions of constant flow (pump generated) and constant head (pressure gradient generated) provide unique environments for biofilm development. This comparison is important, particularly since the vast majority of previous research in this area has considered only constant flow conditions. Biofouling under constant flow conditions leads to an increase in pore velocity and shear stress, while biofouling under constant head leads to a decrease in flow rate, as explained by Darcy's Law (Eqn. 1.1). Since biofilms both alter and rely upon flow conditions and substrate availability, this is an important area of research.

Unwanted biofouling is often addressed with biocide exposure, and it is important to understand how the biofilm responds to various types of exposure (e.g., stagnant exposure to decrease cost and increase exposure time, or flowing exposure to utilize more biocide and introduce shear stress).

A critical area of biofilm research involves the development and testing of models, and the most accurate and complete models possible are necessary for the optimization and affordability of biofilm technologies and control scenarios. This chapter will generate data that can be used for modeling purposes, and will assess the capability of the Biofilm Accumulation Model to assimilate previously-obtained

temporal/spatial biofouling data and predict perturbations to adjustable system conditions.

Materials and Methods

Experimental Flow System Designs

Much time was spent designing and evolving systems to achieve desired observational capabilities. One of the most significant challenges of characterizing biofouling and biomineralization in porous media is the inability to visualize the interior of the porous medium due to the opaque nature of most porous media. To address this, systems were designed using 3.5cm wide by 8.5cm long polycarbonate flat plate reactors that simulate two-dimensional porous media and can be visualized through a glass cover. The flow path was etched with 1mm by 1mm diagonal channels creating a tortuous flow path approximating a homogeneous porous medium. Assuming a 'zig-zag' flow path, the tortuosity (τ) of the porous media region, which is, by definition, the length of the flow path divided by the reactor length, is $\sqrt{2}$. The first system was developed on a lab bench to include two identical constant flow reactor systems (Figures 4.1 and 4.2).

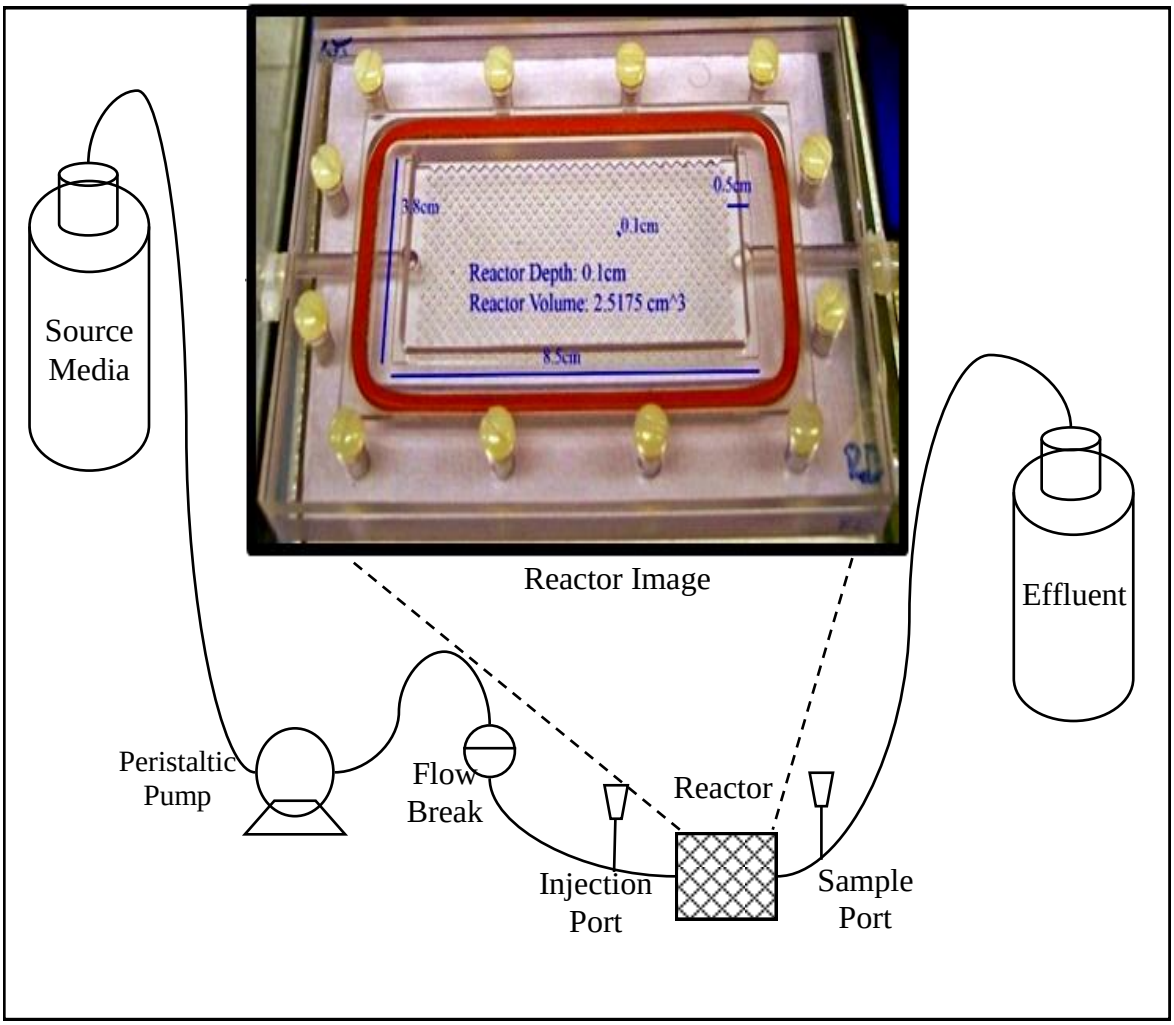

Figure 4.1. Reactor system schematic with flow proceeding from left to right. The reactors (inset) have 1mm x 1mm etched pore spaces that are covered by a 1mm thick glass cover slip. They include a mixing zone at the inlet and outlet to minimize entrance effects. Immediately preceding the reactor is an injection port and flow break to reduce upstream contamination. At the outlet is a sample port to allow effluent sample extraction.

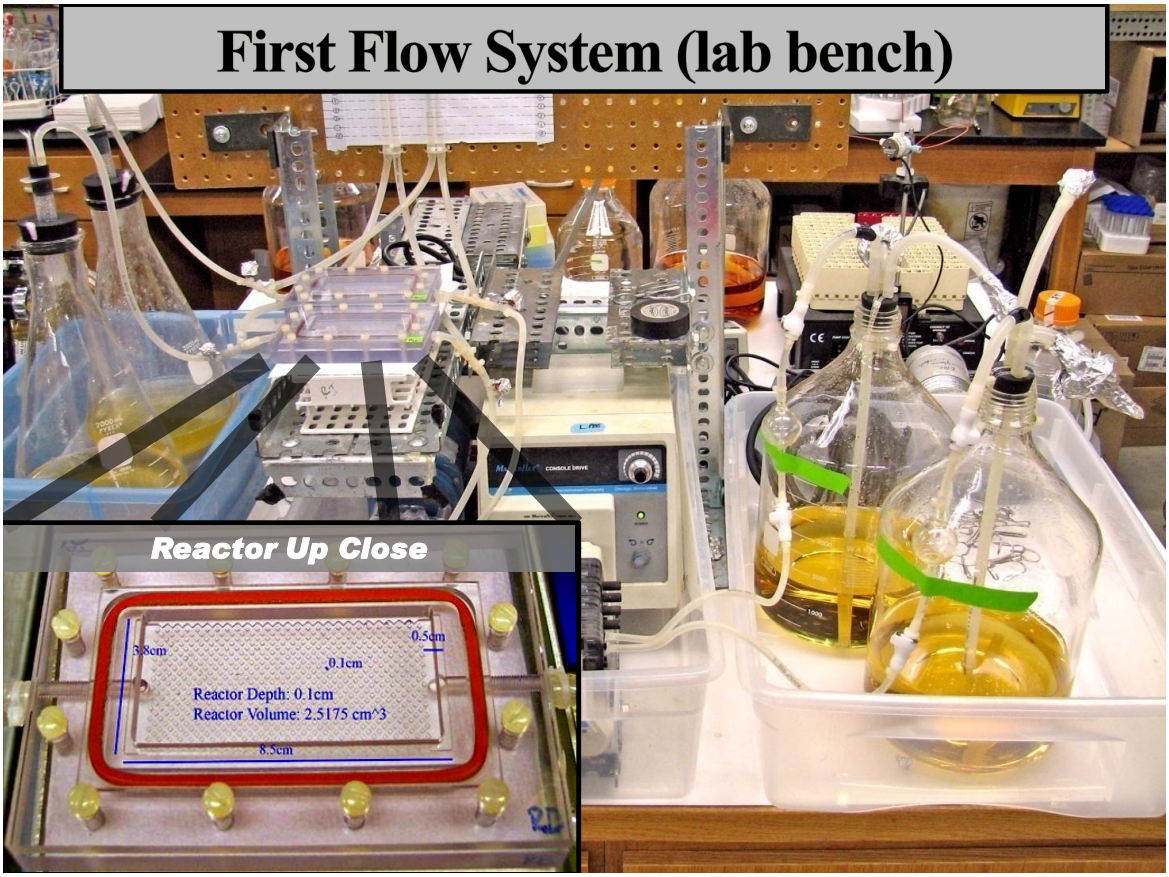

Figure 4.2. Image of dual constant flow systems constructed on a lab bench.

Silicon dioxide tubing (Masterflex, size 16) connected the media source to the reactors via a peristaltic pump (Masterflex, model 7521-50). Piezometers were installed at the inlet and outlet of each reactor to measure the pressure gradient.

A second system was designed using the same components, although spatially-altered in order to fit on a 3’ by 2’ laboratory cart (Figure 4.3). This allowed for transport of the system to a separate image analysis facility during the experiment.

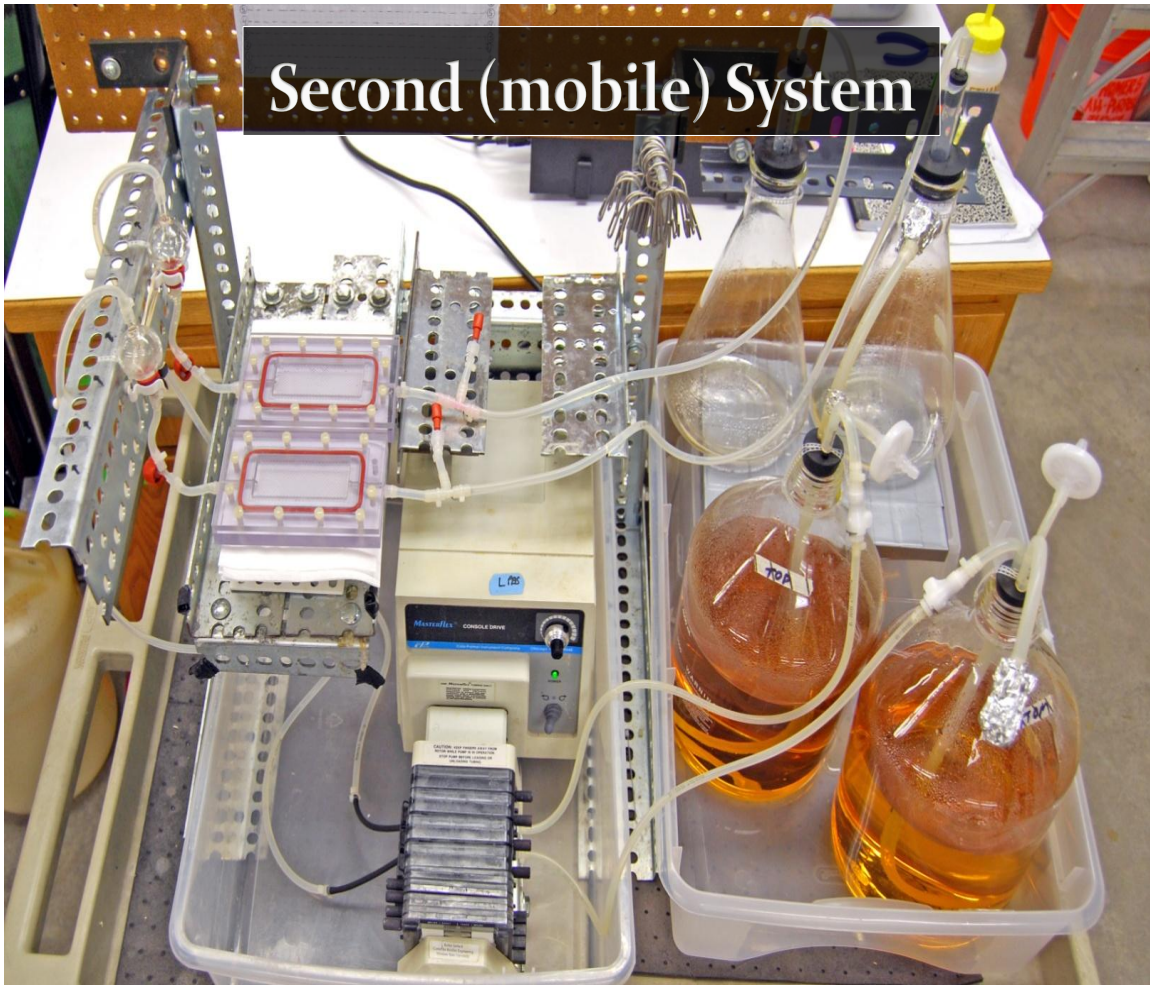

Figure 4.3. Image of system design on a mobile cart. Piezometers had been removed for this particular experiment.

The third system replaced one of the constant flow systems with an adjustable constant head system (Figures 4.5 and 4.6). The main alteration of the constant head system was the addition of a constant head reservoir (Figure 4.4) that was placed on an adjustable platform. This reservoir contained an inlet and two outlets.

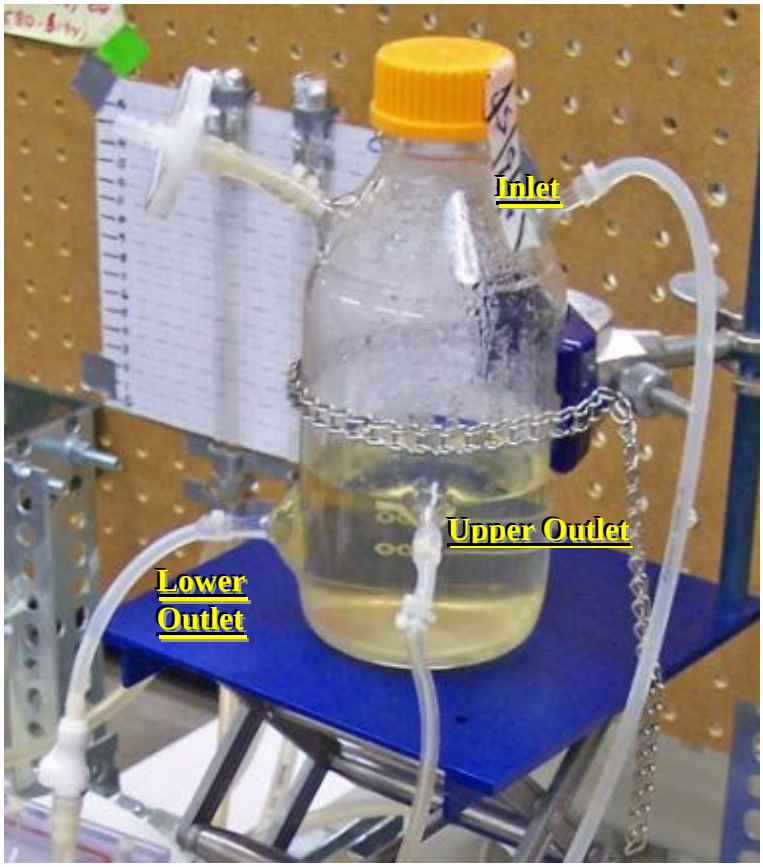

Figure 4.4 Constant Head Reservoir

The inlet supplied pump-generated flow at a rate that exceeded the reactor system flow rate. The upper outlet drained the excess flow back into the media source from a constant level, and the lower outlet was connected to the porous media reactor. The system effluent was positioned at a constant level. The section of tubing between the lower outlet and the reactor was designed to be replaceable with quick disconnects and sterile tubing in lieu of a flow break. This section was replaced with a new, sterile section approximately every two days in order to prevent bacteria in the reactor from migrating upstream and contaminating the source media.

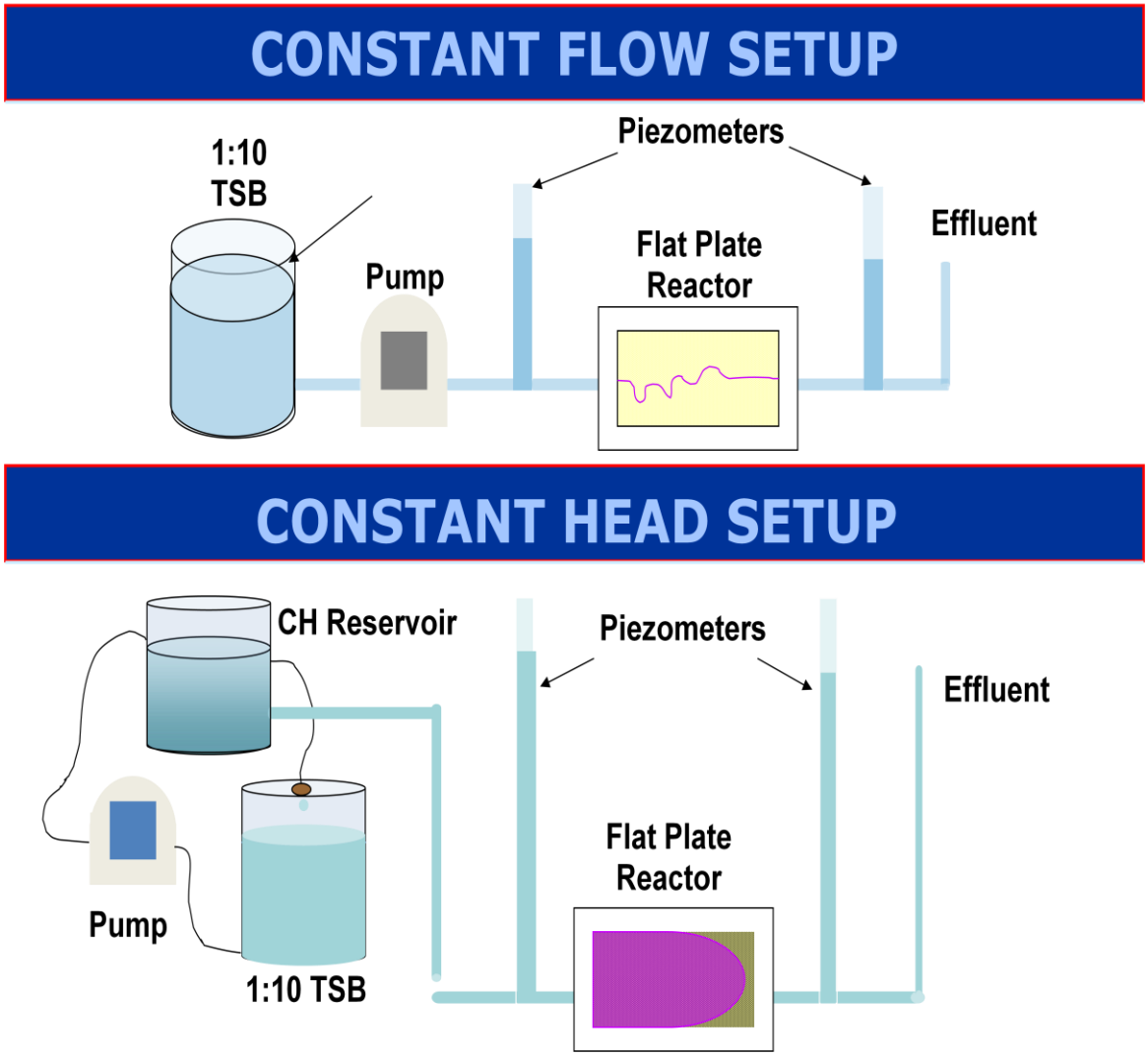

Figure 4.5. Schematic of constant flow (top) and constant head (bottom) experimental systems. Flow in each system progresses from left to right. In the constant head system, the pump continuously recirculates flow into the CH reservoir; excess flow drains back into the 1:10 TSB supply so that the same water level is maintained regardless of the flow rate through system.

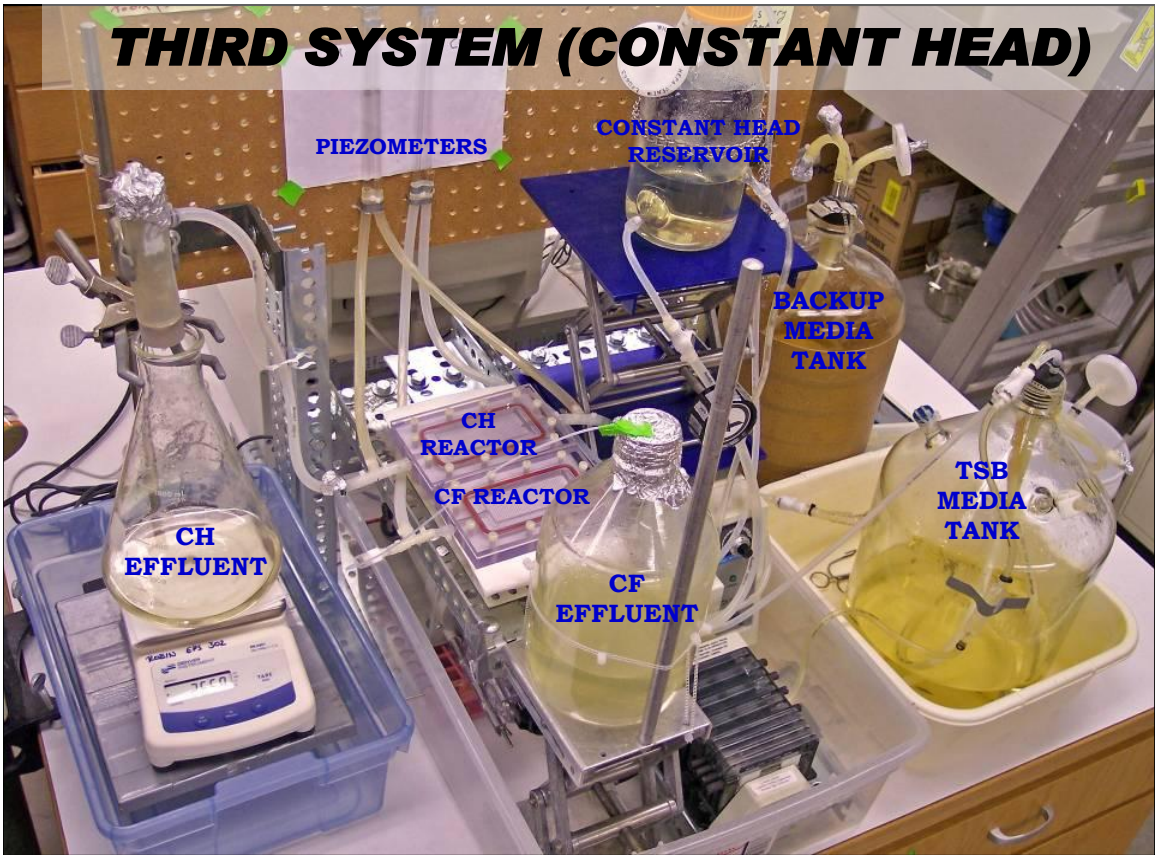

Figure 4.6. Image of a system that places two reactors side by side and compares a constant head environment with a constant flow environment. The constant head effluent flow rate was continually monitored using a balance. The blue platform on which the constant head reservoir rests allowed for an adjustable influent head level, while the effluent was maintained at the same level. The piezometers measured the head difference across each system.

Prior to the establishment of the previously described flat plate reactor systems, a preliminary study was conducted using packed bed column reactors with variable-sized beads. An explanation, data, and images of this study are contained in Appendix Q.

Bacterial Growth Media and Inoculum

A 1:10 dilution of tryptic soy broth (TSB) (Becton, Dickenson and Company) was used as the flow medium. The media dilution was chosen due to the high substrate availability provided by the flow environment and to reduce cost. The fermentative,

chemoorganotrophic, Gram-positive soil bacterium *Cellulomonas* sp. ES6, was used as the inoculum due to its proven ability to produce biofilm (Borch et al., 2005, Viamajala et al., 2008). One half milliliter (0.5ml) of a frozen cryostock of the culture was mixed with 50ml TSB and placed on a shaker (150rpm) at 30□ C. One half ml of the culture was transferred into 50ml of fresh TSB at 24 hours. Eighteen hours after the transfer, the flow systems were inoculated with 4ml of the culture. Flow was started in each system 12 hours after inoculation.

Chlorinated Bleach Exposure

To assess the effects of chlorinated bleach exposure on biofilms formed under constant flow and constant head conditions, a 1:10 dilution of chlorinated bleach (sodium hypochlorite) (Chlorox) was used. This solution was applied in two different manners to both the constant head and constant flow systems. It was first applied under no-flow conditions, in which 5ml of a 1:10 bleach solution were injected into stagnant systems and allowed to interact with the biofilm for 1 hour prior to restarting media flow. This allowed for a more even distribution of bleach exposure throughout the reactor, as opposed to preferential exposure in the flow channels. Secondly, bleach was applied with flow, in which case the media was swapped with the bleach solution for 24 hours before being switched back to the previous growth media. This allowed exposure coupled with fluid shear stress, and increased the total amount of bleach entering the reactor. A real world application of this study is highly tangible; for example, when clearing a clogged filter, differences could be expected depending on whether the pump is

stopped during exposure, which would have financial and environmental benefits due to less bleach used.

Residence Time Distribution Analysis

A residence time distribution (RTD, also referred to as tracer curve analysis) can be used to compare the flow behavior of a plug flow reactor (PFR) or laminar flow reactor (LFR). An RTD contains three principle assumptions: the fluid is incompressible, the reactor is at steady state, and transport at the inlet and outlet are due only to advection. In an ideal PFR with a pulse dye input, there is no spatial variance and all of the tracer dye would exit the reactor at the same time. A non-zero variance indicates dispersion along the flow path, which may be attributed to turbulence, a non-uniform velocity profile, or diffusion. Since these systems and experiments were not designed to extensively analyze dispersion or diffusion, the analysis was strictly qualitative. In all systems, RTD tests consisted of the following method:

1. Pump was stopped and system was clamped upstream of injection port
2. 0.1 ml of filter-sterilized, 1:10 dilution red food dye (McCormick) was injected very slowly (i.e., > 5 seconds) so that the biofilm was not significantly disrupted
3. Clamp was removed and pump was re-started
4. Effluent samples were collected from the extraction port at regular time intervals and placed in a 96-well microplate
5. After nearly all dye had passed through the reactor and all samples had been collected, 200µl of each sample was mixed with 100µl of deionized water in a fresh 96-well plate

6. The absorbance of each sample was measured at 450nm with an EL808 Ultra Microplate Reader (BioTek Instruments, Winooski, VT)
7. The absorbance, which is relative to the dye concentration, was graphed on the y-axis, and the volume of fluid (i.e., flow rate x time) was graphed on the x-axis.

A sample RTD is shown in Figure 4.7:

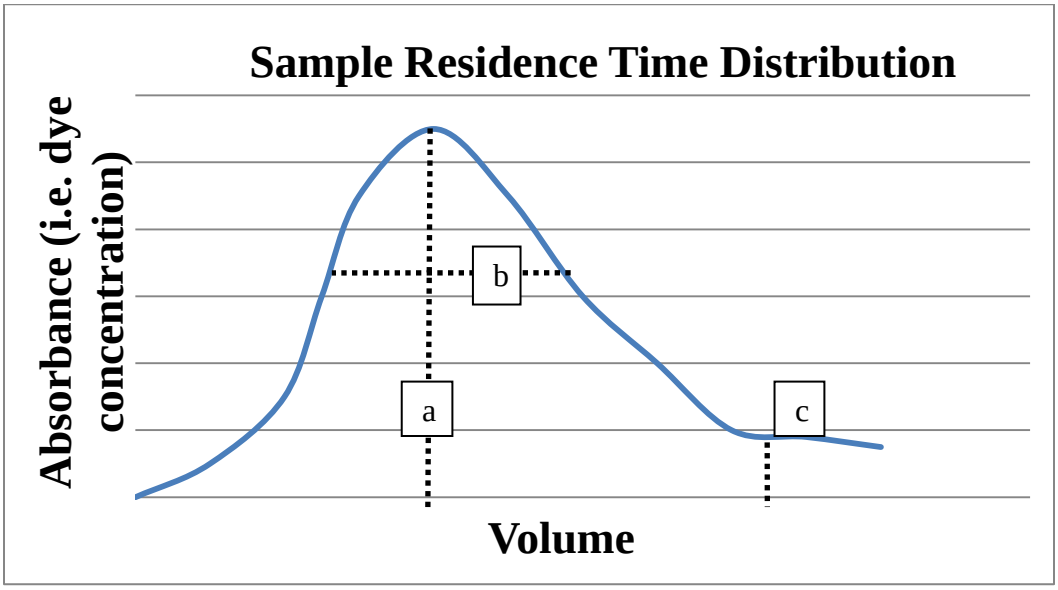

Figure 4.7. Sample residence time distribution, showing the dye concentration in the effluent over time. The volume at which point line 'a' falls relates the effective pore volume, the width of line 'b' relates to the dispersivity of the reactor, and the height of line 'c' relates to the dye retention in dead zones or biofilm.

RTD curves can be utilized to assess hydraulic characteristics of a system.

- The peak of the curve (max absorbance) is related to the mobile pore space from the point of injection to the point of extraction (volume at line 'a')
- The width of the curve (line 'b') is related to the dispersivity of the system as the residence times of the individual dye molecules deviate from the flow time of the average flow path

- The height of the tracer curve tail (line ‘c’), represents dye that has been retained within dead zones or biofilms and slowly diffuses out

An RTD image series of a clean (i.e., not biofilm-affected) reactor is shown in Figure 4.8.

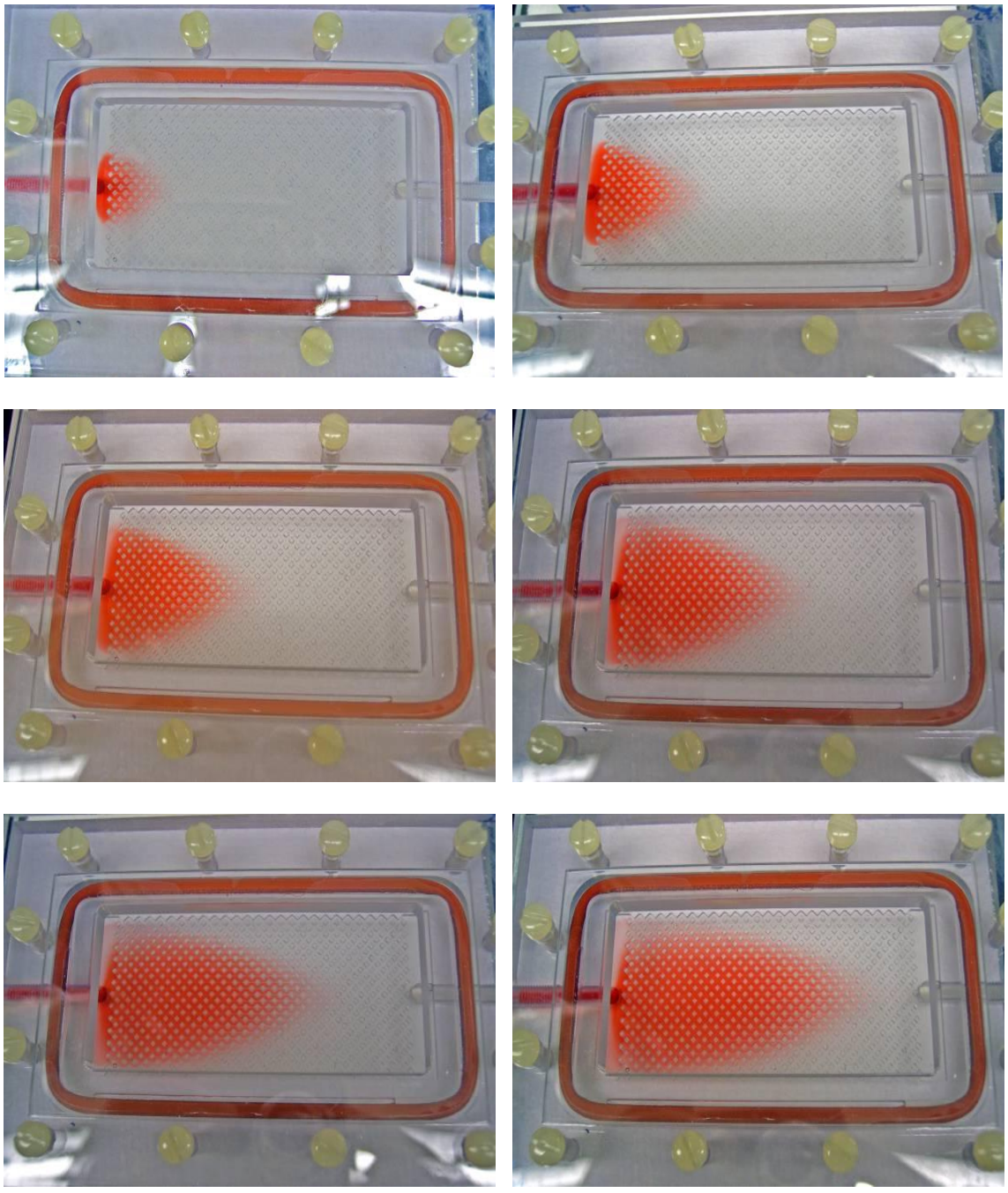

Figure 4.8. Images showing dye flowing from left to right through the reactor. Flow path appears to be laminar (i.e., two-dimensional) in nature.

As biofouling occurs in the reactors, pore reduction and channeling become evident as exemplified in Figure 4.9 and through residence time distribution analysis.

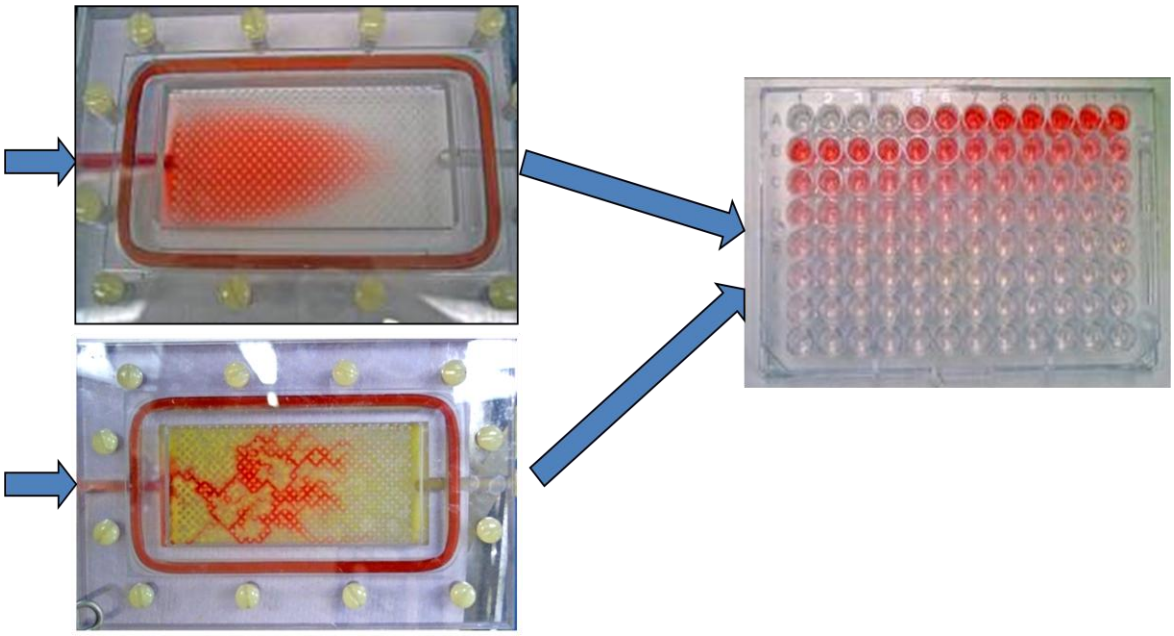

Figure 4.9. (Top left) Image of dye flowing left to right across a clean reactor. (Lower left) Dye flowing left to right across a biofouled reactor showing channel formation and porosity reduction. (Right) 96-well microplate with effluent samples collected over time, from left to right and top to bottom. The lines in the figure represent the path of the dye throughout the RTD analysis.

Imaging Biofouling

The opaqueness of most porous media renders imaging processes in porous media very difficult. However, there is no substitute for the spatial, temporal, and reactive analysis that can be accomplished with non-destructive, *in situ* imaging techniques. Imaging allows for quantification of pore space reduction and insight into favorable conditions. The ability to visualize the location of biofilm accumulation provides a glimpse of biofilms formed under variable substrate concentrations and fluid flow environments. High resolution electron microscopy, X-ray tomography, ultrasound, and

other destructive techniques can be very beneficial, but have clear limitations that hinder real-time understanding (Gerlach and Cunningham, 2010).

The flat plate reactors previously-described are highly conducive to long working distance (i.e., > 1mm) imaging techniques. The ability to visualize the channel development and porosity reduction can be complementary to RTD analysis. For example, porosity calculated from RTD analysis could be compared to porosity calculated from images; in this method, porosity could simply be calculated by flowing dye through the reactor and counting the amount of red and non-red 1mm x 1mm pore spaces available for flow. This analysis was not done in this work.

In this study, a Nikon SMZ 1500 stereo microscope was used to image the pore space on a millimeter scale, and a Nikon D40x digital camera with an 18-55mm Nikkor Lens was used to image the millimeter-scale channel distribution and qualitative dye dispersion.

Results and Discussion

Biofilm Accumulation and Residence Time Distributions

Visual and RTD analyses showed significant biofouling in the pore space, which altered the fluid flow across the reactors. The following series of images (Figure 4.10) highlights the development of a biofilm in the reactors at various stages. It was apparent from images such as these that biofilm accumulation occurred more on the leeward (i.e., downstream) side of the porous media elements. This supports the findings of Nambi et al. (2003), who found that biofilm accumulation favored regions of low shear stress.

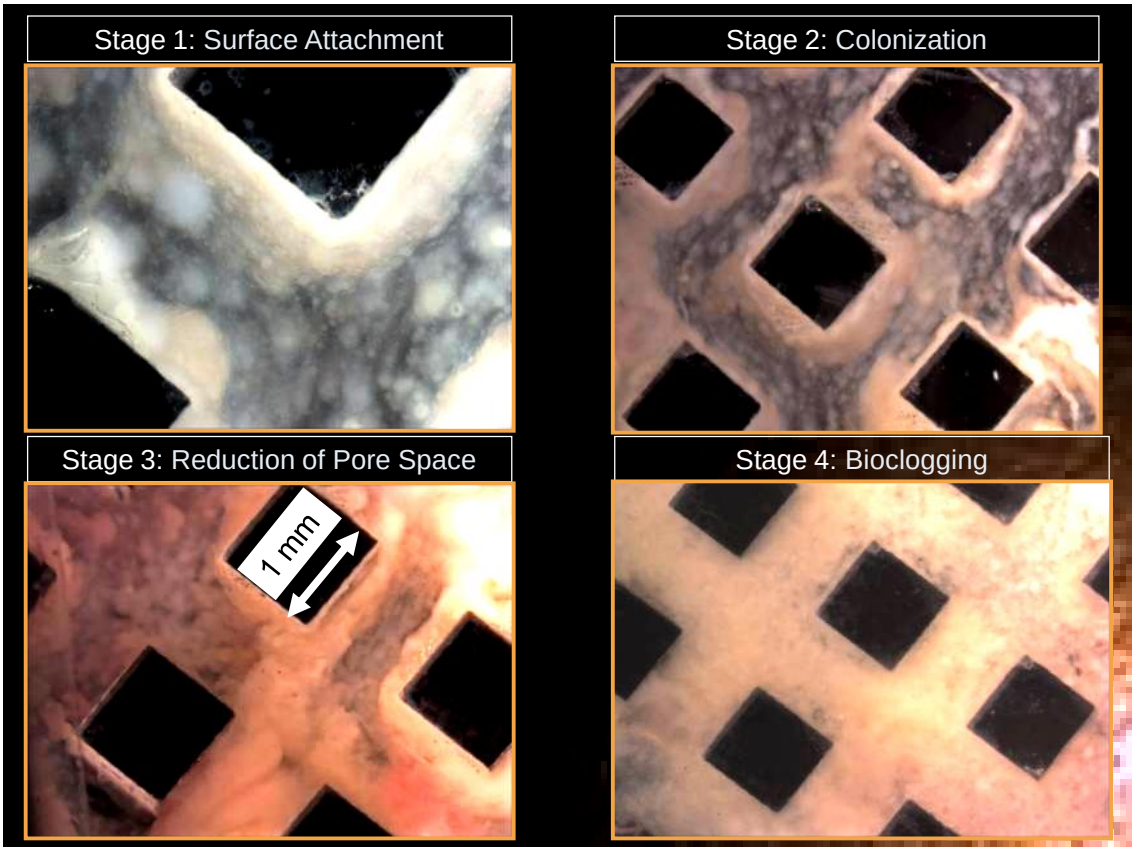

Figure 4.10. Stereo microscope images showing the progression of biofilm development within the reactor pore space.

RTD analysis showed clear changes in the reactor hydrodynamics as biofilm developed. A dye tracer broke through rapidly before releasing slowly, showing the apparent effects of fluid transport from channels to and from the biofilm. As illustrated in the Figures 4.11 and 4.12, the pore volume decreased over time, particularly in the CF reactor.

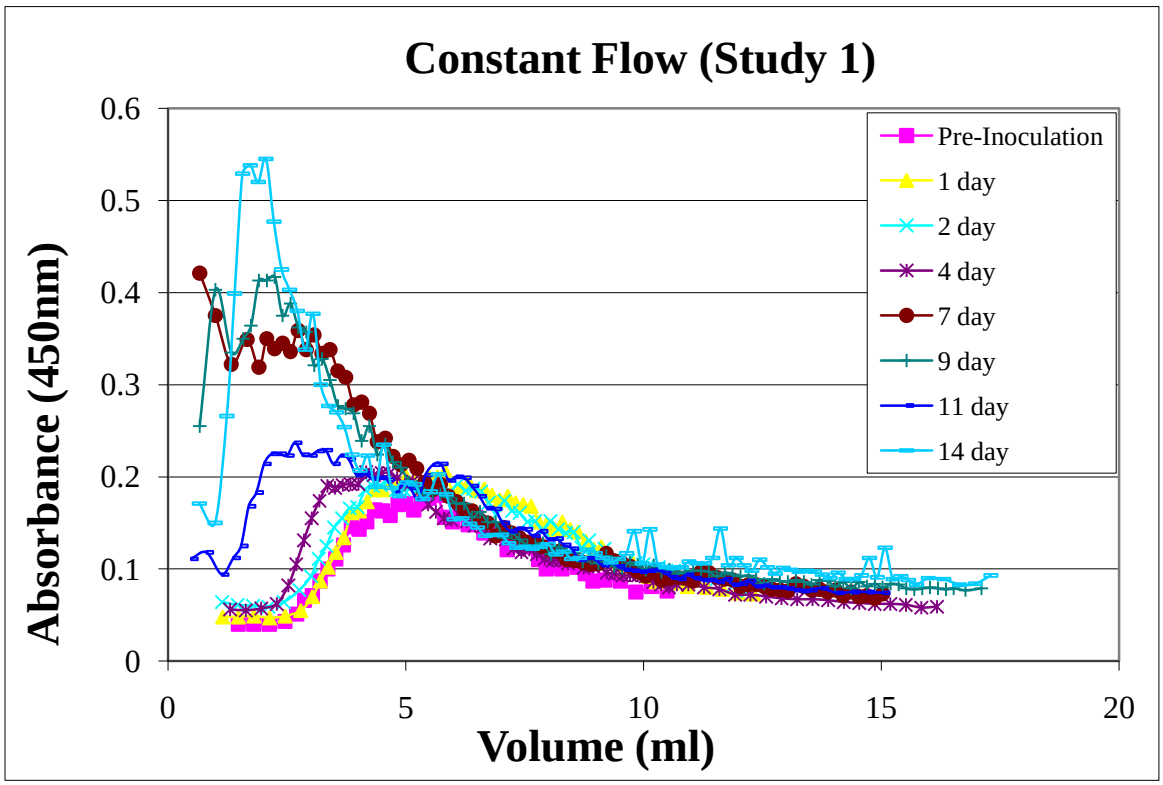

Figure 4.11. Residence time distribution for constant flow biofilm accumulation

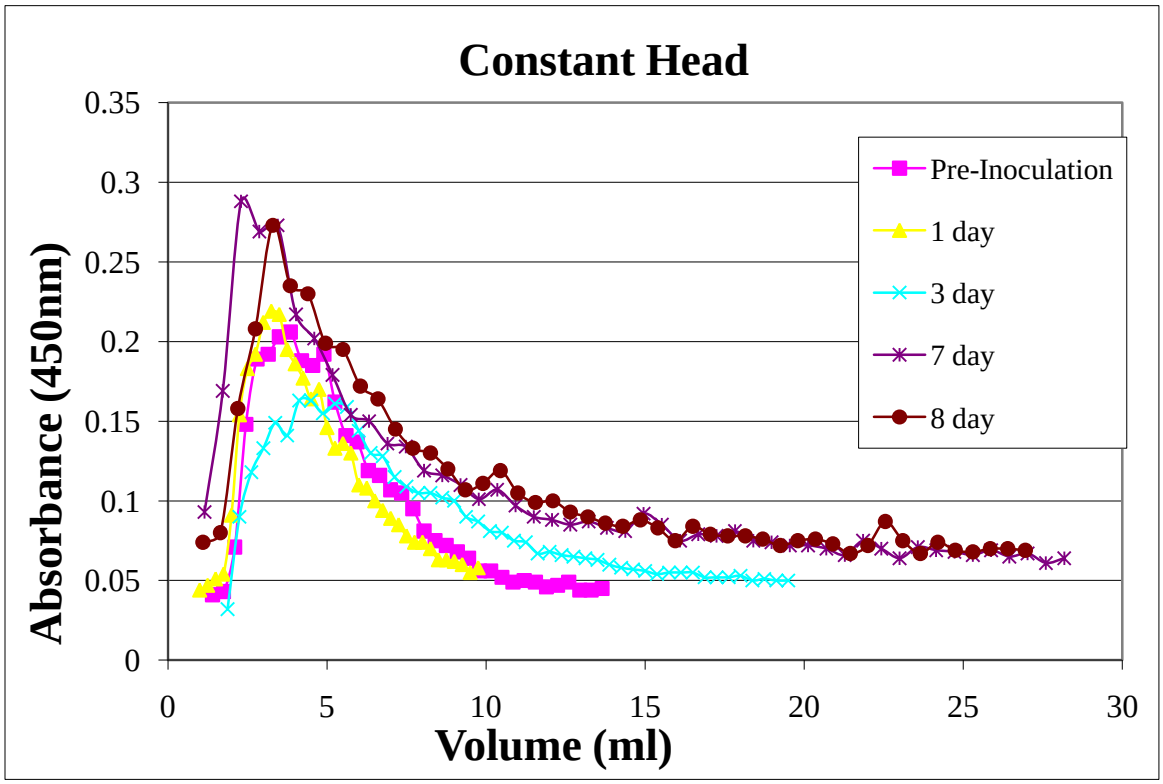

Figure 4.12. Residence time distribution for constant head biofilm accumulation

In Figure 4.11, the noise that appears early in the dye breakthrough (e.g., days 7 and 9) is believed to be due to the distinct channel formation that occurred in the constant flow reactor. This could be compared to a bypass route through the reactor, in which some of the dye passes very rapidly. Images illustrating dynamic channel formation over time are shown in Figure 4.13:

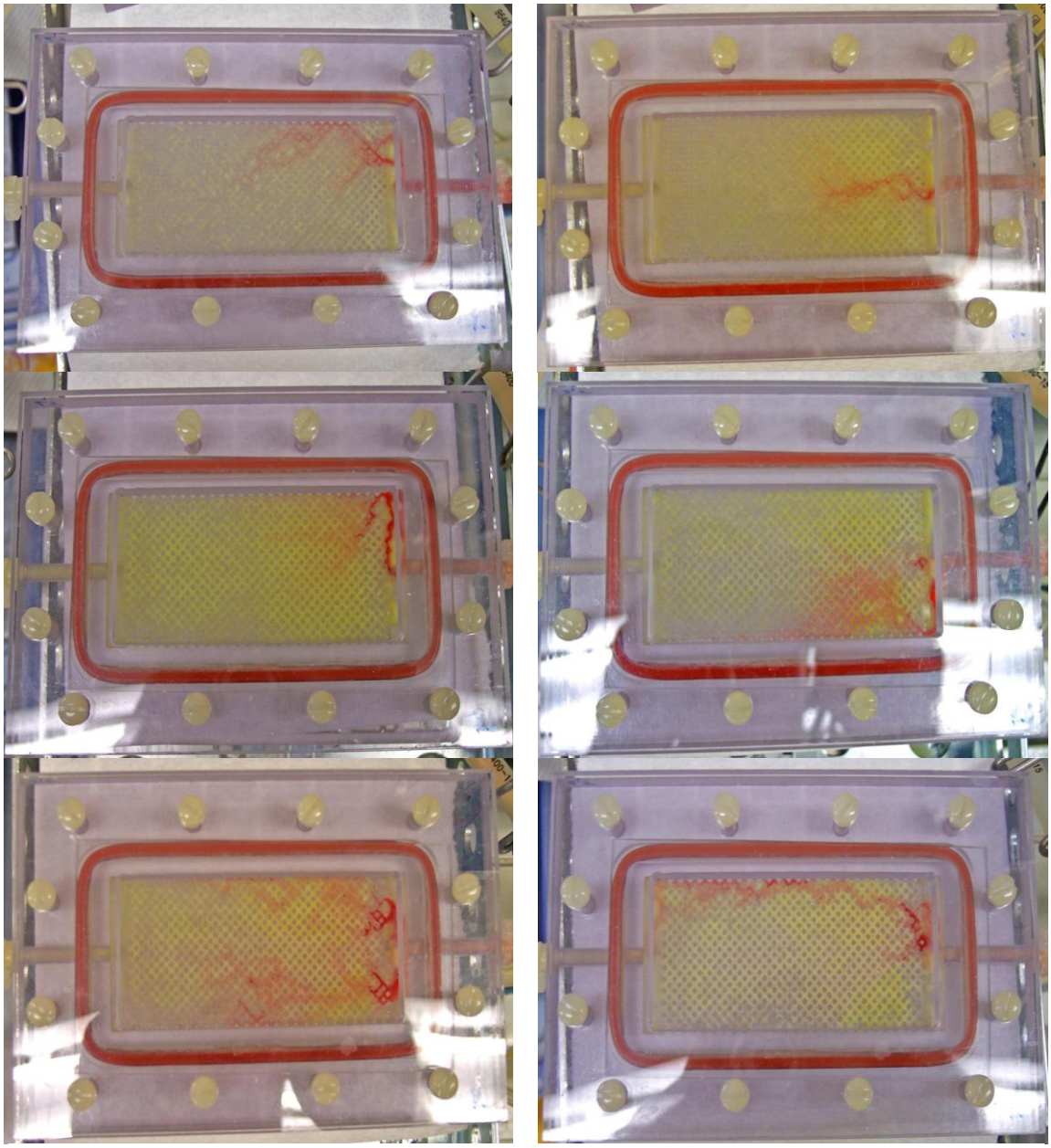

Figure 4.13. Image series showing the dynamic formation of channels in a constant flow reactor at 4 (top left), 7 (top right), 9 (middle left), 11 (middle right), 14 (lower left), and 16 (lower right) days after inoculation

As these channels dynamically opened and closed, there were fluctuations evident in the form of spikes of hydraulic head across the reactor (Figure 4.14).

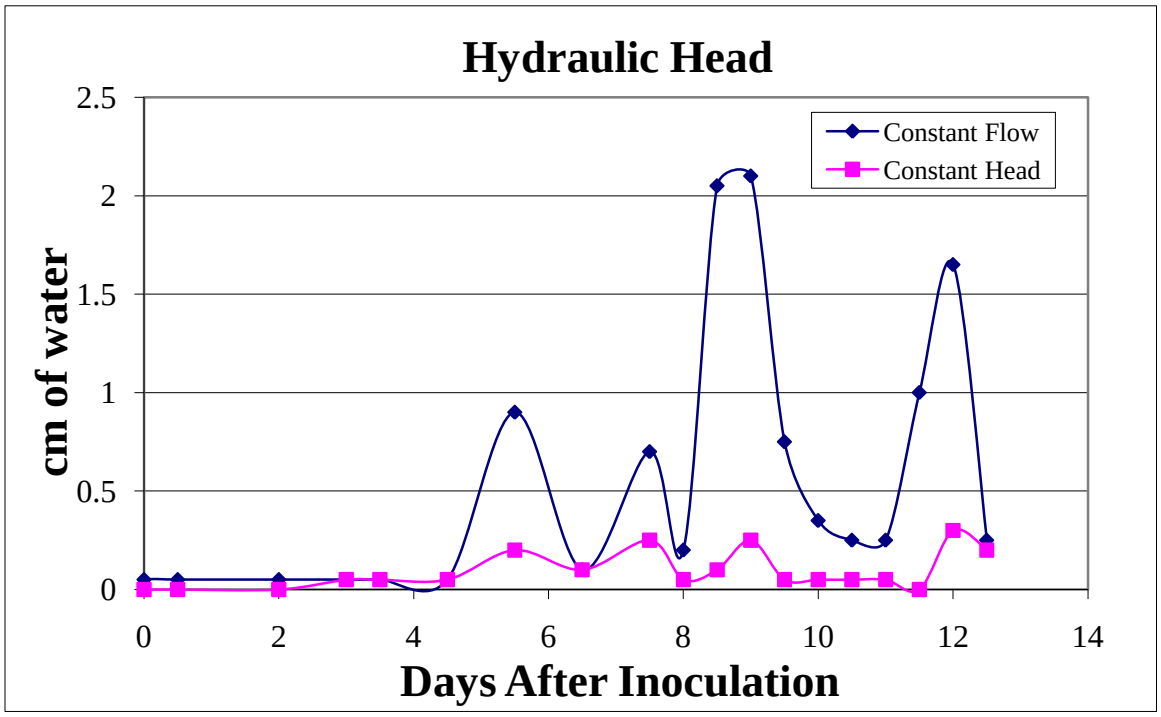

Figure 4.14. Hydraulic head data showing sinusoidal spikes in the constant flow reactor that are believed to be a result of dynamic channel formation and reformation.

Porosity and Hydraulic Conductivity

Constant head data were not used to extensively analyze porosity and permeability, since tracers became very difficult with low and sporadic flow rates resulting from fluctuations in hydraulic conductivity. Further, the reactor dispersion coefficient is affected by velocity, and RTDs become less comparable with velocity fluctuations. A second constant flow experiment (Study 2) was conducted over a longer time period in order to assess porosity and hydraulic head. The RTD from this study is shown in Figure 4.15.

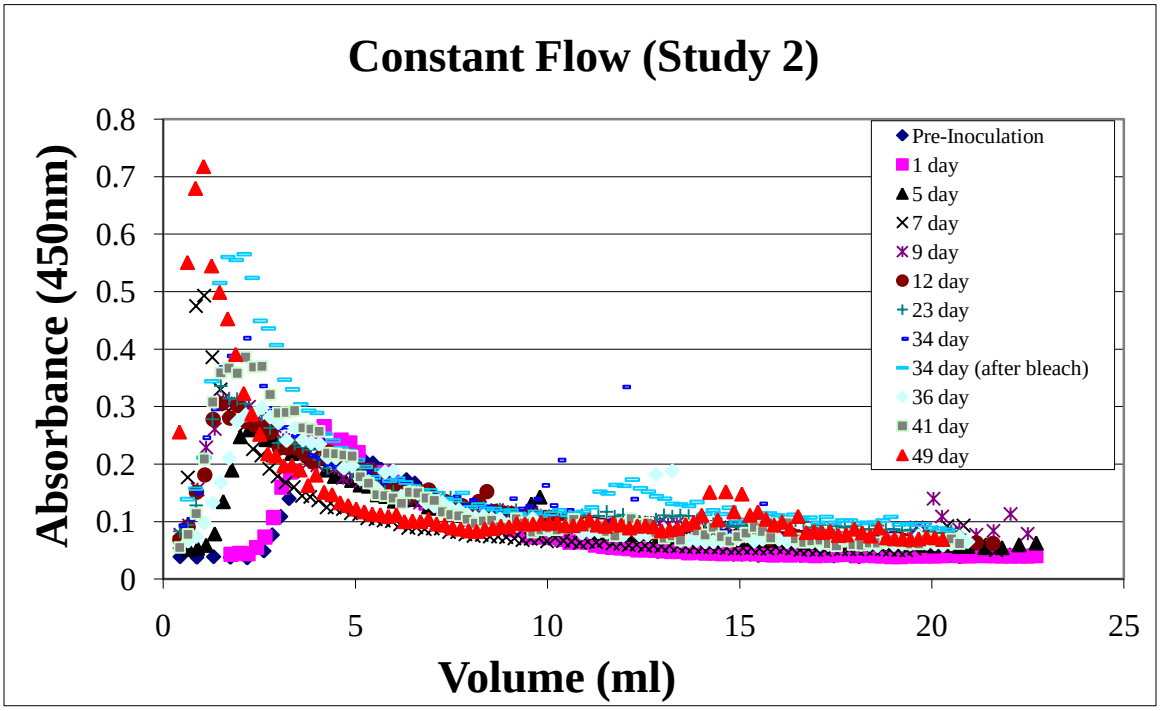

Figure 4.15. Residence time distribution from constant flow study, showing data that were used to evaluate porosity reduction over time.

The volume at which the RTD peak occurred was assumed to be the effective (i.e., mobile) porosity, Θ_m. This was determined, and a reduced porosity ($\frac{effective\ pore\ space}{pore\ space\ of\ reactor\ before\ inoculation}$) was calculated. The pore space of the clean reactor was determined to be 3.98ml, based on the RTD peaks of the clean reactor. The data (Table 4.1) and graph (Figure 4.16) are shown below.

Table 4.1. Pore volume and biofilm thickness data

Day	0	1	5	7	9	12	23	34	34.	36	41	49
Pore Vol. (ml)	3.98	3.97	2.45	1.30	1.60	1.51	1.50	1.90	2.10	2.50	2.10	1.20
Porosity Ratio (V/Vo)	1	0.99	0.62	0.33	0.40	0.38	0.38	0.48	0.53	0.63	0.53	0.30
Reduced Pore Vol (ml). (Vo-V)	0	0.01	1.53	2.68	2.38	2.47	2.48	2.08	1.88	1.48	1.88	2.78
Average Biofilm Thickness (mm) ((Vo-V)/SA)	0	0.00	0.17	0.29	0.26	0.27	0.27	0.23	0.20	0.16	0.20	0.30

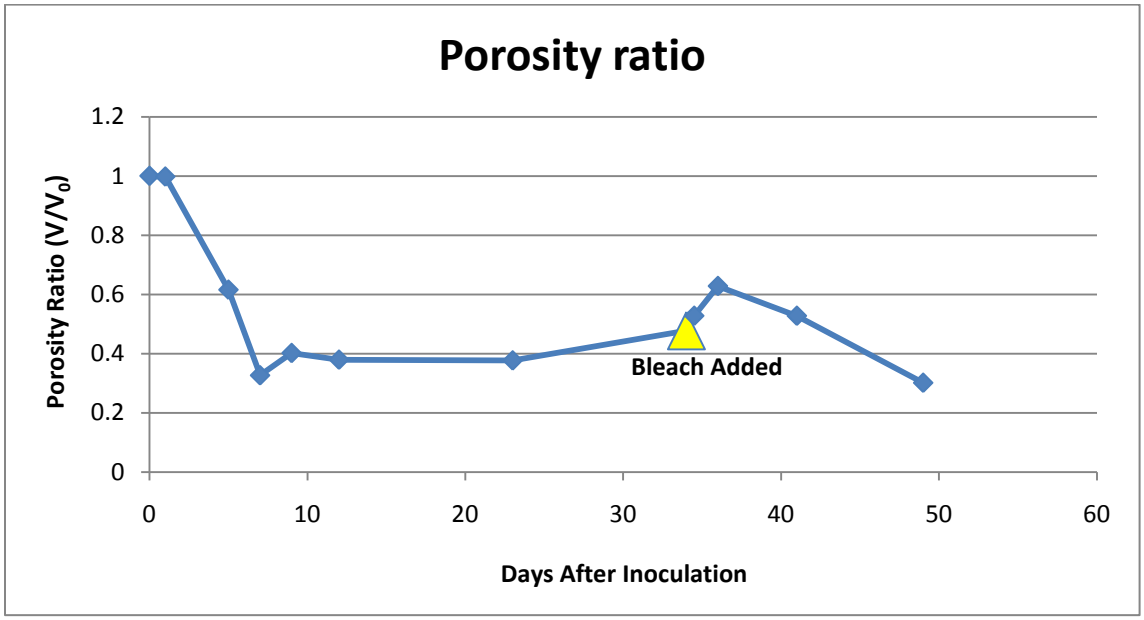

Figure 4.16. Porosity ratio over time in the biofouled reactor

From this porosity reduction, a biofilm thickness was calculated, assuming that the porosity reduction resulting from the development of a uniformly thick biofilm throughout the reactor. In this method, the mobile pore volume reduction can be converted to a thickness by dividing by the reactor surface area, which was found to be 91.95cm^2, based on the estimations and calculations in Table 4.2:

Table 4.2. Reactor surface area estimation

Surface area estimation:					**Units in mm^2**
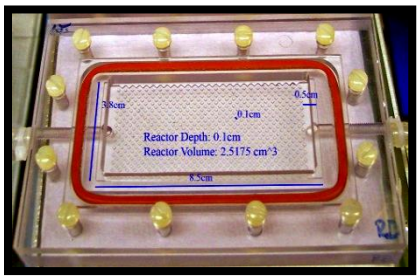	**Sides of interior squares:**				
	663	squares	4 mm^2/square	=	2652
	Top and Bottom above square matrix:				
	75mm*38mm*0.75(Fraction of surface)*2surfaces			=	4275
	Mixing Zones:				
	5mm*38mm*4surfaces			=	760
	Entry/Exit piping:				
	(3mm*2π)*80mm			=	1508
	Estimated Total Surface Area (mm^2):			=	9194
	Estimated Total Surface Area (cm^2):			=	91.95cm^2

With the porosity reduction and the surface area estimation, the biofilm thickness over time could then be graphed (Figure 4.17).

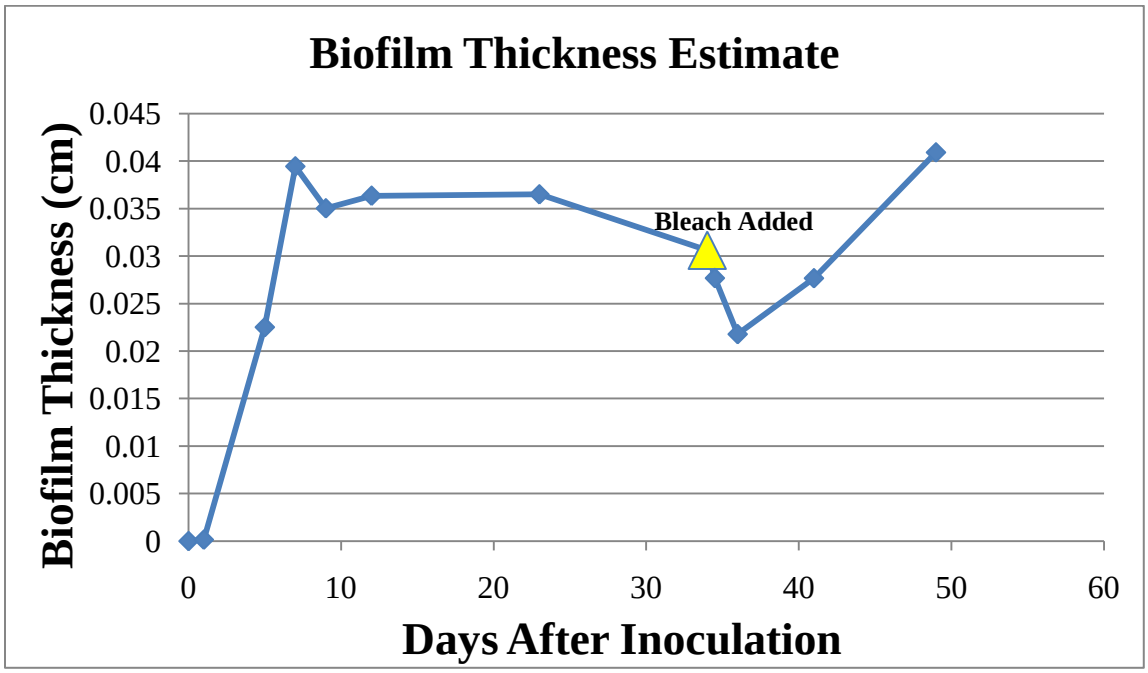

Figure 4.17. Biofilm thickness over time. Notice that there appears to be a small spike in the thickness prior to the establishment of a pseudo steady state thickness. It is possible that this is due to a period in which the biofilm thickness exceeds the critical thickness, at which point sloughing and death outcompete growth.

Piezometer data were also collected in this study in order to assess changes in the hydraulic conductivity. The numerical data are shown in Table 4.3, and the graphical display is in Figure 4.18.

Table 4.3. Piezometer data over time in a constant flow reactor

Days after Inoculation	**0**	**0.5**	**1**	**1.5**	**2**	**3**	**4.5**	**5**	**5.5**	**6**	**6.5**
cm of H_2O	0.01	0.01	0.01	0.01	0.01	0.01	0.3	1.5	4	6.55	2.1
Days after Inoculation	**7**	**8**	**9**	**10**	**11**	**11.5**	**12**	**13**	**13.5**	**14**	**14.5**
cm of H_2O	5.5	1	3.5	3	3.1	2.5	1.95	1	1.7	1.5	1.5
Days after Inoculation	**15**	**15.5**	**16**	**16.5**	**17**	**18**	**18.5**	**19.5**	**20**	**22**	**23.5**
cm of H_2O	2.6	1.5	1.2	1	1.85	2.95	1.7	3	3.5	2.6	1.7
Days after Inoculation	**25.5**	**26.5**	**27**	**28.5**	**30.5**	**32**	**34**	**35**	**37**	**40**	**41.5**
cm of H_2O	1.3	1.35	1.3	1.3	2.2	1.75	1.9	1.5	1	0.55	0.25
Days after Inoculation	**42**	**43**	**43.5**	**44.5**	**47**	**47.5**	**48**	**49**	**49.5**	**50**	
cm of H_2O	0.2	1	2.9	2	0.8	1.85	1.4	2.85	1	1.25	

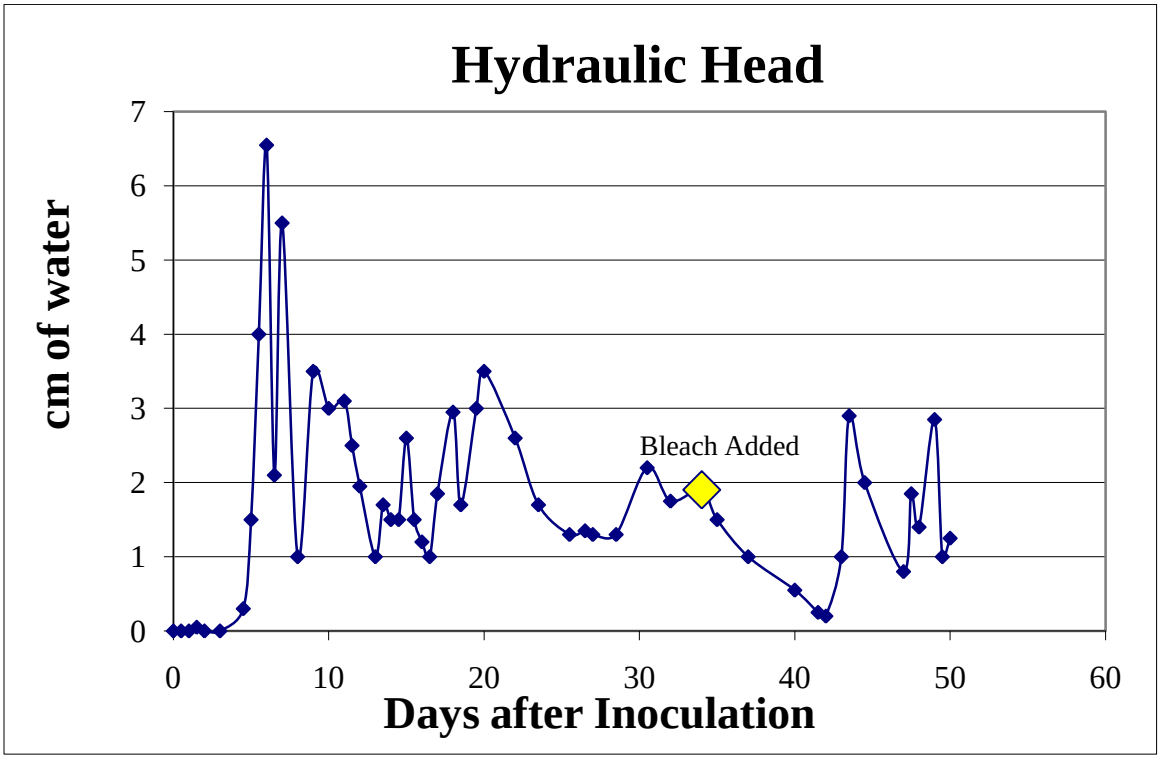

Figure 4.18. Graph of Piezometer data for a constant flow reactor. Similar to the porosity data, there appears to be a point at approximately 7 days when a maximum influence of biofilm occurs prior to the establishment of a pseudo steady state head difference of approximately 2cm of water.

According to Darcy's Law, a reduction in pressure drop is inversely related to a reduction in hydraulic conductivity. Values of reduced hydraulic conductivity were determined from this the inverse pressure drop ratio (Figure 4.19). Since there was no

measurable pressure drop in the reactor during the first few days of sampling (i.e., initial K was theoretically infinite), an arbitrary pressure drop of 0.01cm water was introduced for mathematical purposes.

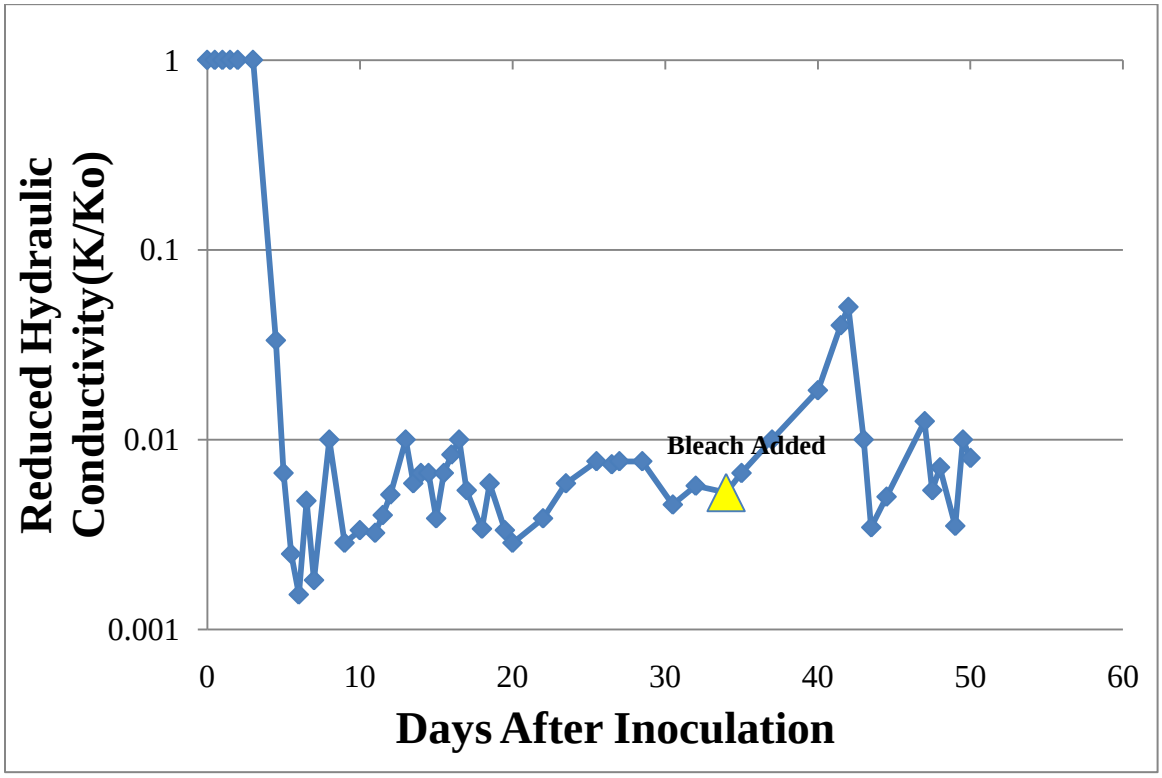

Figure 4.19. Reduced hydraulic conductivity as a function of time after inoculation

The pressure drop data generated was compared to predictions of the biofilm assumption, a parametric model, and a pore network model (see Equations 1.4-1.6 in the introduction for details). Several assumptions were made for the D'Arcy-Weisbach Equation, which predicts head loss (m) in a flow channel (i.e., biofilm model). Recall the D'Arcy-Weisbach Equation:

$$\Delta h = \lambda \, (l / D) \, (\rho v^2 / 2g) \qquad (4.1)$$ (*engineeringtoolbox.com*, December, 2009)

In this equation Δh is head drop (m), λ is the friction coefficient, l is the length of the flow path (m), D is hydraulic diameter (m), ρ is the fluid density (kg/m^3), v is the velocity (m/s), and g is the gravitational force (9.81 m/s^2). The flow velocity in these studies, 3.46 cm/min in a clean reactor, yields a Reynolds number of 5.77 (assuming the kinematic viscosity of water at 20°C, 1*10^{-6} m^2/s). This Reynolds number is well inside the laminar flow regime, so regardless of the roughness factor, the Moody diagram will yield a friction coefficient that is near 0.1 (Figure 4.20).

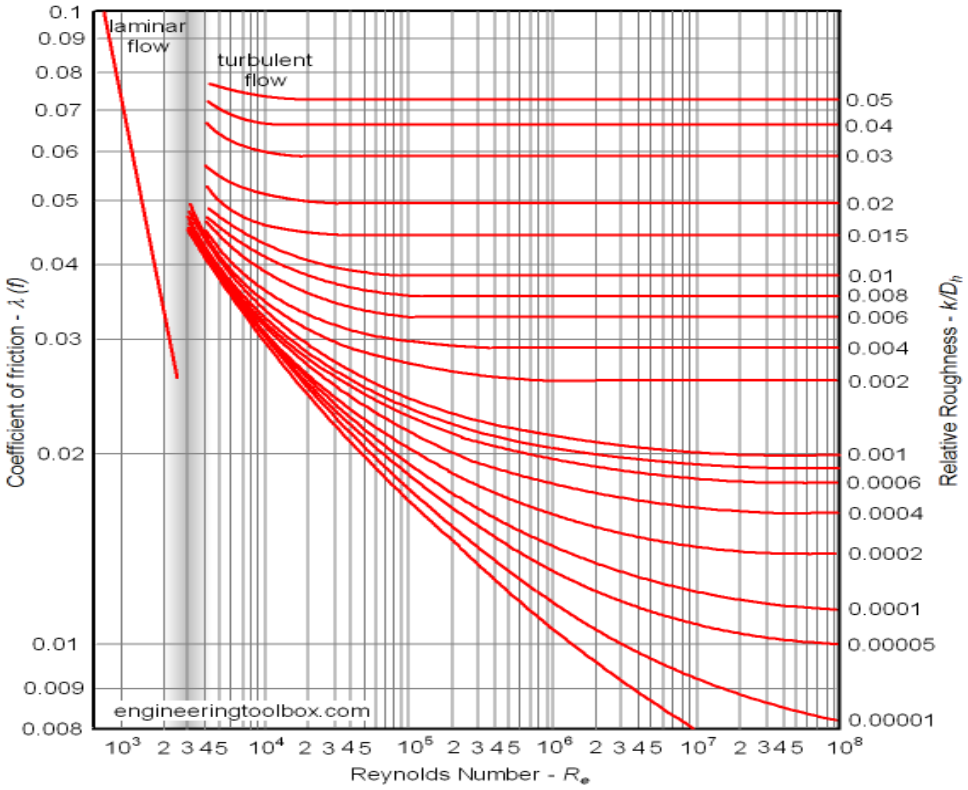

Figure 4.20. Moody Diagram to estimate fri*ction coefficient*. (engineeringtoolbox.com, December, 2009)

This value for the friction coefficient was assumed for all calculations. The change in head loss resulting from biofilm was therefore manifested in the change of the hydraulic diameter, which was assumed to be D_{clean} = 1mm, minus twice the biofilm

thickness (Figure 4.17), as well as the change in velocity, assumed to be v_{clean} (3.46 cm/min) divided by the porosity ratio (Figure 4.16). The fitting parameters for the parametric and pore network models were adjusted on a spreadsheet to provide the closest fit (least-square method) while staying in the ranges suggested in the literature. These suggested ranges were ($2 < c < 19/6$) for the parametric model and ($-2 < a < -0.5$) for the pore network model (Seifert and Engesgaard, 2007). Since the lowest reduced porosity recorded was approximately 0.3, a value of $\beta_{min} = 0.2$ was used for the pore network model. Figure 4.21 shows the various models:

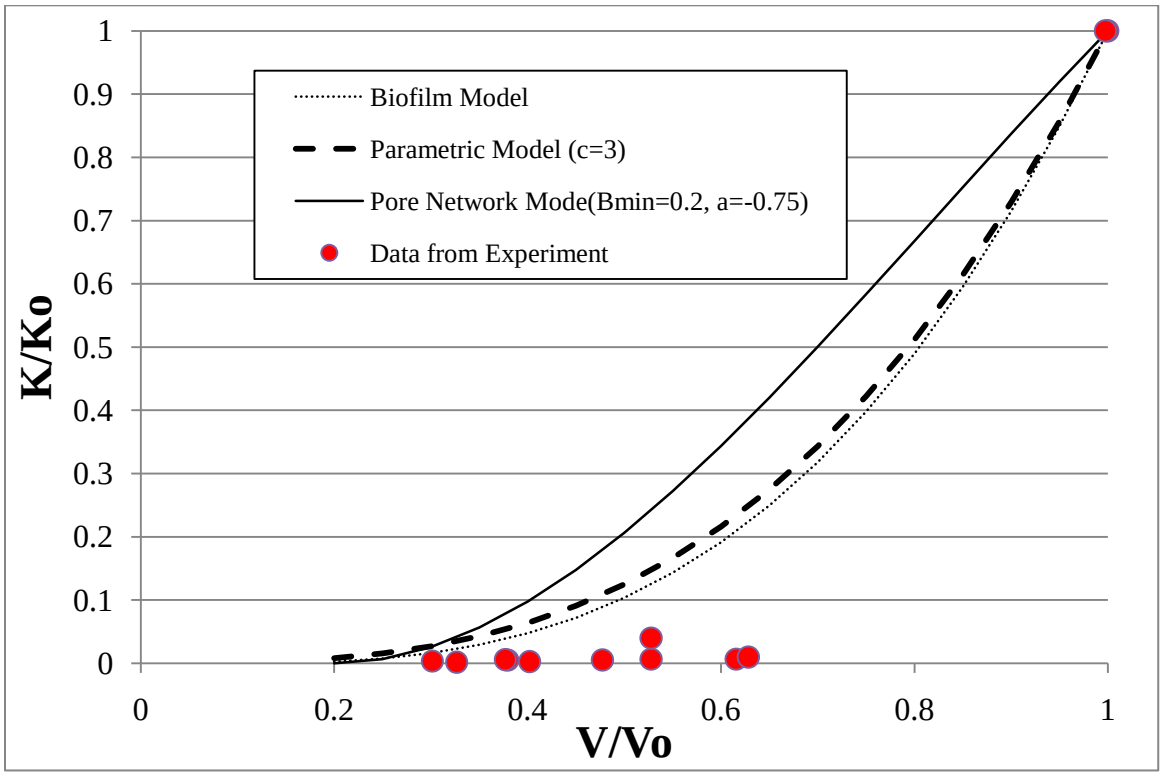

Figure 4.21. Graph showing reduced hydraulic conductivity data and values predicted by models.

The spreadsheet for these calculations is included in Appendix R. It is apparent that none of the models fit the data very closely. It is believed that this is the case mainly

because these reactors are not designed to accurately assess reductions in hydraulic conductivity. Since the pores are relatively large (i.e., 1mm), a clean reactor does not register a measureable pressure drop (i.e., hydraulic conductivity). For this reason, an initial head difference (or hydraulic conductivity) must be arbitrarily chosen. In this study, an arbitrary head difference of 0.01cm of water was chosen for mathematical purposes. With this assumption, all models were found to over predict K/K_0. Furthermore, there were no measured porosity reductions in the range of 65% to 95%. As shown in Figure 4.21, the models show that values in that range have a strong influence on the slope of the relationship, and thus the fitting parameters 'c' and 'a'.

Constant Head vs. Constant Flow

In studies using the third system design (i.e., constant head vs. constant flow system, Figure 4.6), biofilms formed under constant flow conditions were more prolific in occupying space and forming distinct channels than biofilms formed under constant head conditions. This is likely due to the increased amount of substrate available in the constant flow reactors (i.e., higher flux into reactor). The biofilm distribution along the reactor flow path appeared more homogeneous in the constant flow reactor, while it appeared to be more congregated near the inlet region in the constant head reactor (Figure 4.22).

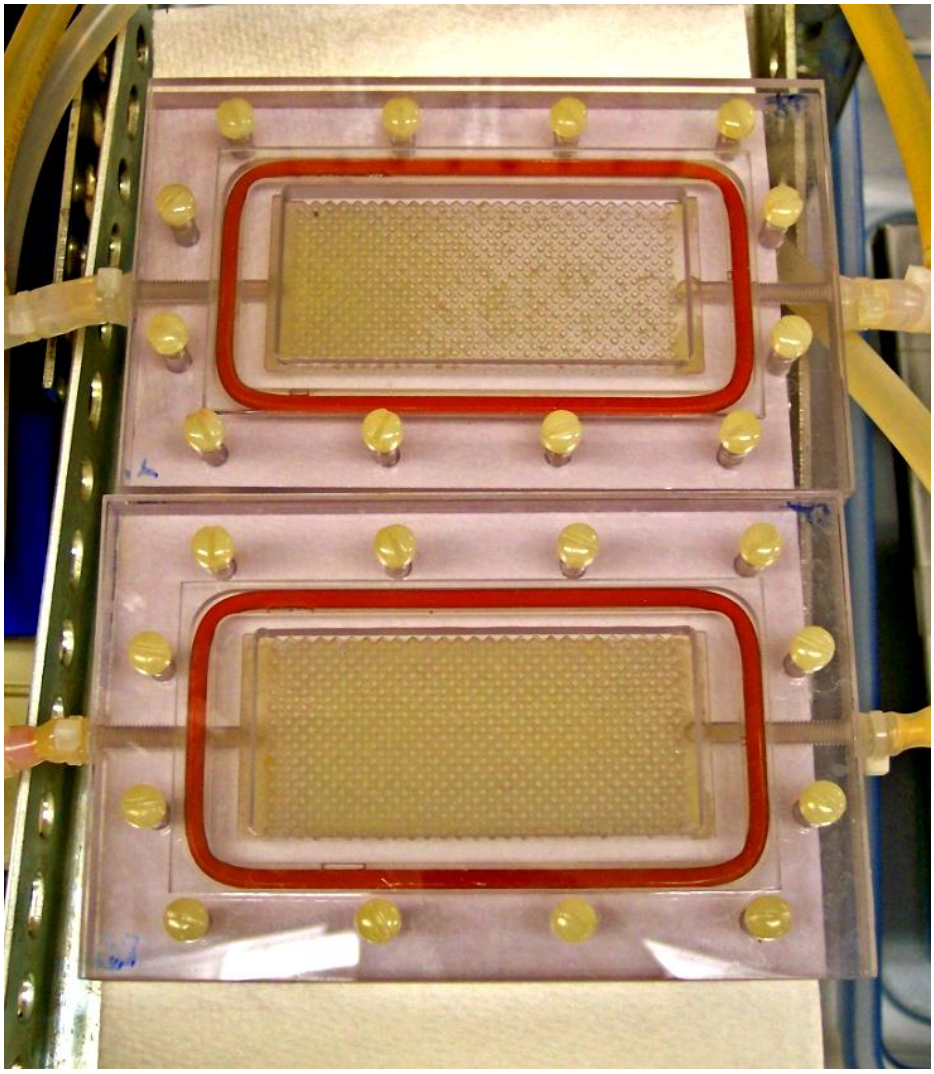

Figure 4.22. Image of biofilms formed under constant head (top) and constant flow (bottom). Flow proceeds from left to right through these reactors. While the biofilm in the constant flow reactor appears uniformly distributed, the biofilm in the constant head reactor appears to have a higher density near the inlet region.

The image-based observation that there was more biofilm in the constant flow reactor (Figure 4.22) was supported by RTD analysis (Figures 4.11 and 4.12), which show a greater reduction in effective porosity in the constant head reactor. The RTDs appear to be similar in clean reactors, but differences become obvious during the later stages of biofilm development.

Another RTD observation suggests that there is more dye retention in the constant head reactor (i.e., higher concentration of dye at extended times beyond the main breakthrough in the RTD). This may have been a result of several phenomena: 1) the lower flow rates (i.e., increased residence time) in the constant head reactor provided more time for the dye to diffuse into the biofilm, 2) less-channeled flow characteristics observed in the constant head reactor increased the amount of biofilm that was exposed to dye, and 3) the biofilm formed under constant head conditions may have been less dense due to lower nutrient availability and lower shear stress, thus giving it a higher diffusion coefficient (see Fick's First Law, Equation 1.7) compared to the biofilm formed under constant flow.

Chlorinated Bleach Exposure

Stagnant Exposure: The following images show tracer dye flowing from left to right through the constant flow reactor immediately preceding (top) and after (bottom) stagnant bleach exposure. It is apparent from the images (Figures 4.23 and 4.24) that the channel in the inlet region was replaced by a more direct path.

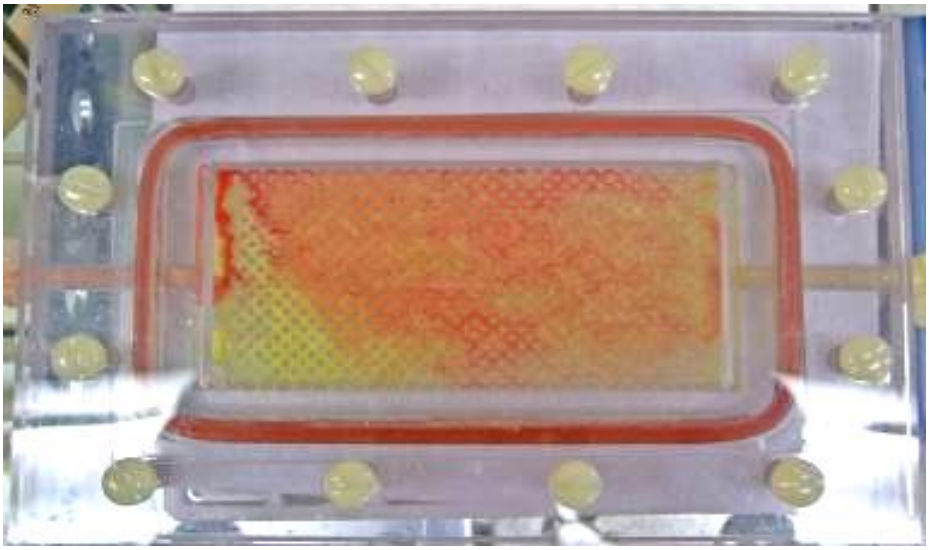

Figure 4.23. Constant flow reactor immediately prior to stagnant bleach exposure

Figure 4.24. Constant flow reactor immediately following stagnant bleach exposure

Figures 25 and 26 show the three days prior to the stagnant exposure in each system, as well as several days after exposure.

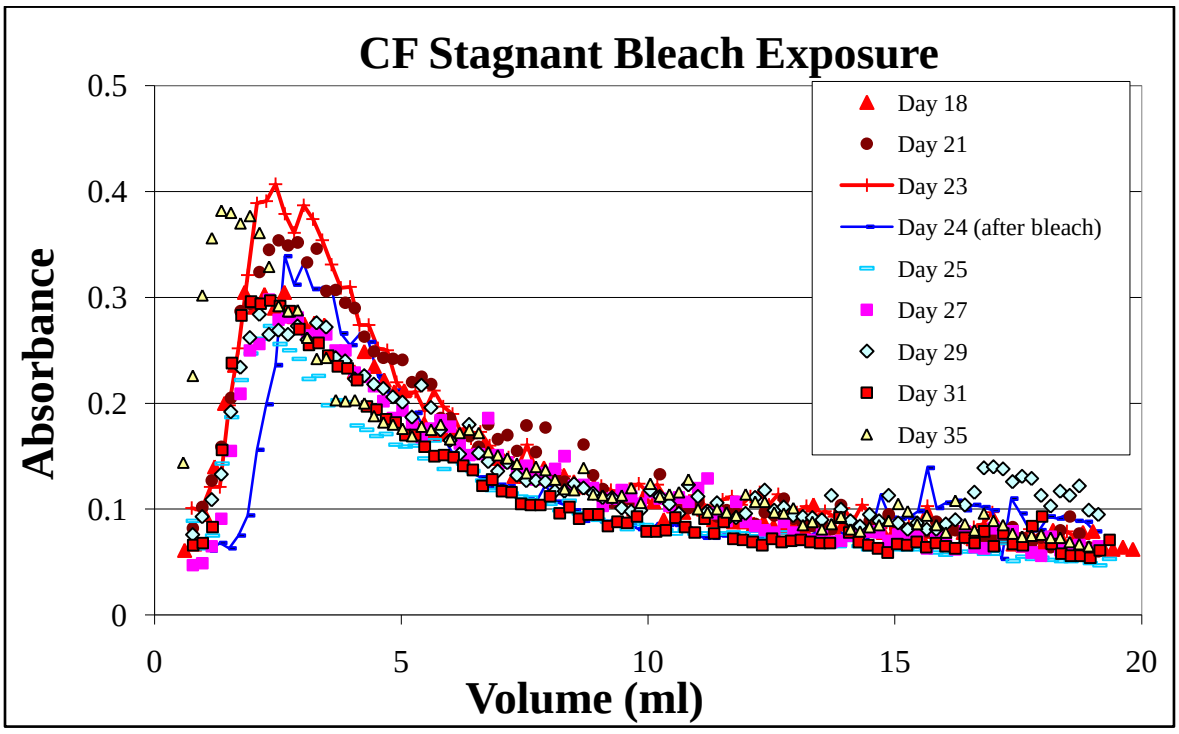

Figure 4.25. RTD for constant flow reactor before and after stagnant bleach exposure

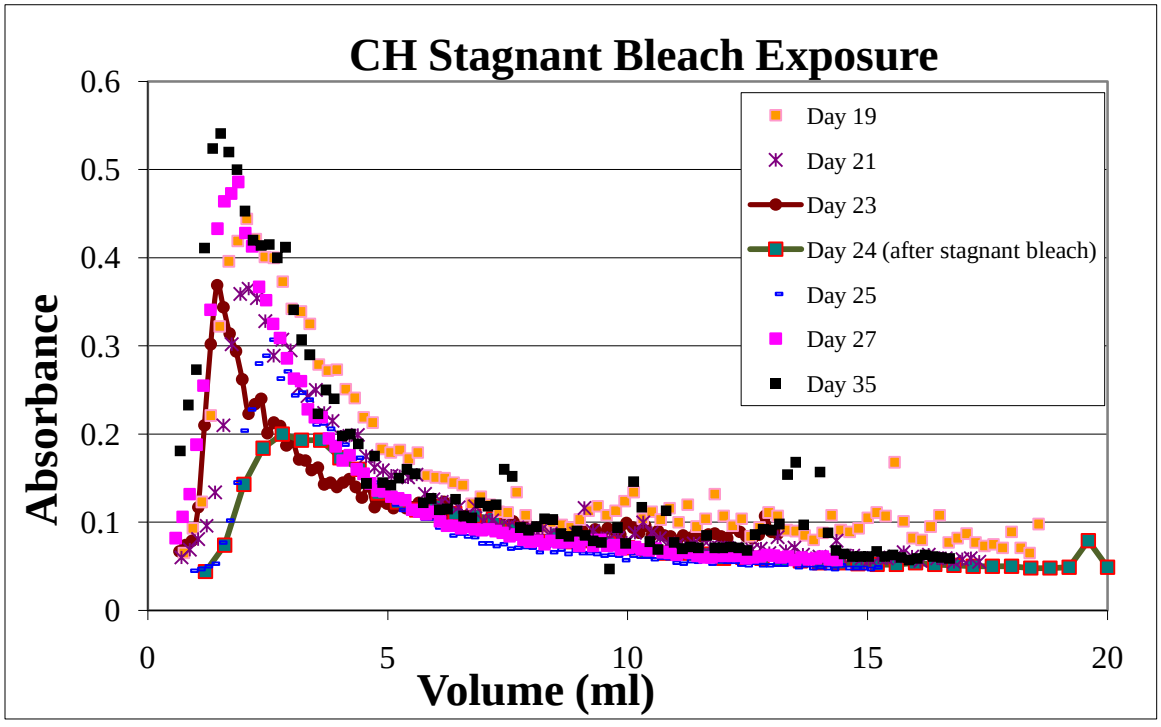

Figure 4.26. RTD for constant head reactor before and after stagnant bleach exposure

From these RTDs, it is apparent that the pore space appeared to increase only slightly in the constant flow system. This is evident in the change in the peaks between day 23 and day 24 in Figure 4.25, which are highlighted with lines. The increase appeared more significant in the constant head system, as shown in the difference between day 23 and day 24 in Figure 4.26. The estimated porosity reduction becomes clearer in Figure 4.27, which was derived from RTD peaks:

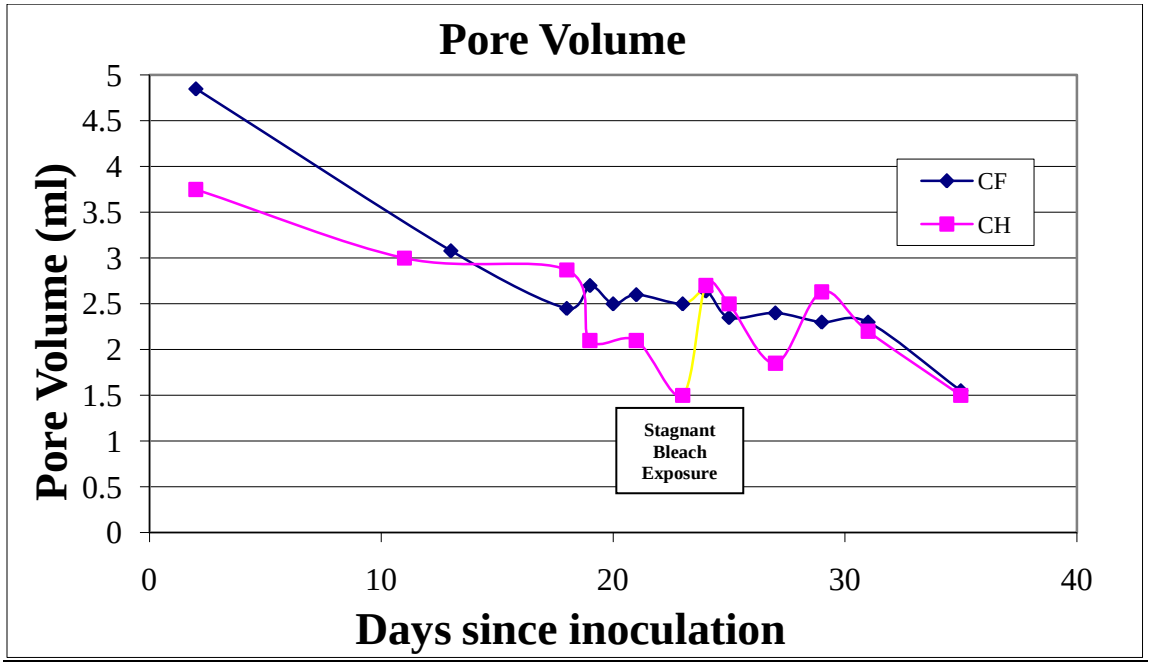

Figure 4.27. Change in pore volume in response to stagnant bleach exposure.

The increased effect in the CH reactor may have been a result of the less-dense biofilm formed under CH conditions or a change in pore velocity. With a comparable, stagnant exposure, it is hypothesized that this may have resulted in more susceptibility to the biocide, for the same reason that there appeared to be more dye retention in the CH reactor (i.e., higher diffusion coefficient for a less-dense biofilm).

While the pore volume increased only slightly in the constant flow reactor (Figure 4.24), the measured hydraulic head decreased to nearly zero immediately following the exposure (Figure 4.28). This may be due to the fact that hydraulic head is ultimately dictated by the singular path of least resistance in media with large pore spaces, and that the bleach exposure may have affected a particular region of minimum resistance. However, a measurable resistance returned in the day following exposure, suggesting that some bacteria, as well as the biofilm matrix survived the exposure.

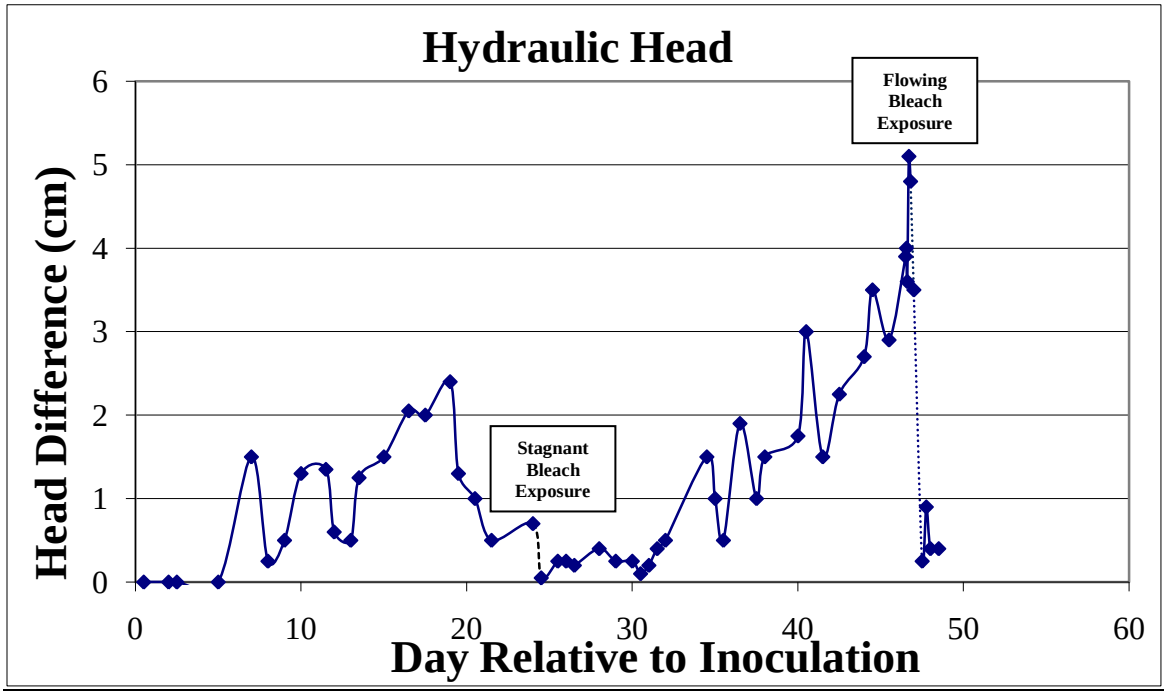

Figure 4.28. Piezometer data for constant flow system. The stagnant bleach exposure occurred at day 24 and virtually eliminated any head difference effects of the biofilm. The flowing bleach exposure began at day 47 and was likewise associated with a rapid decrease in pressure drop.

Flowing Exposure: After the media source was switched to the 1:10 bleach solution for the flowing exposure after day 46, the constant flow reactor showed the primary flow channel increasing in size. The following series of images documents the reactors throughout the first five hours of exposure (Figure 4.29):

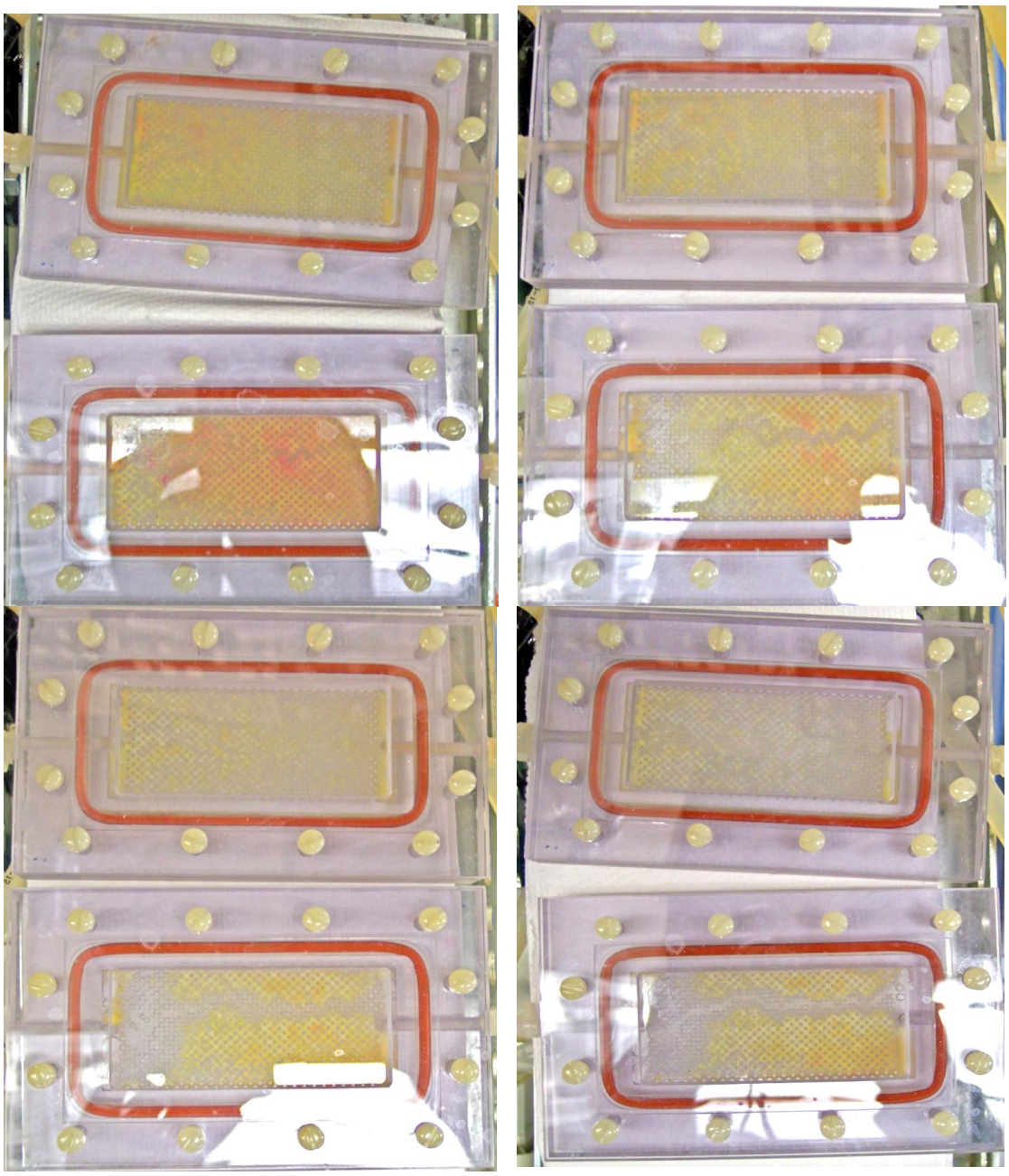

Figure 4.29. Images of the reactors throughout the first five hours of flowing bleach exposure. Flow proceeds from left to right. In each image, the constant head reactor is on top and the constant flow reactor is on bottom. The times are pre-bleach (top left), 1 hour after (top right), 3 hours after (bottom left), and 5 hours after (bottom right). It is evident from these images that biofilm was progressively removed from the constant flow reactor, particularly in the inlet region.

This effect was not apparent in the constant head reactor. The RTD data also showed an increase in pore volume in the constant flow reactor during exposure (notice

the difference in the peak volume between volume of the peak on day 31 and the peak on day 34 in Figure 4.30).

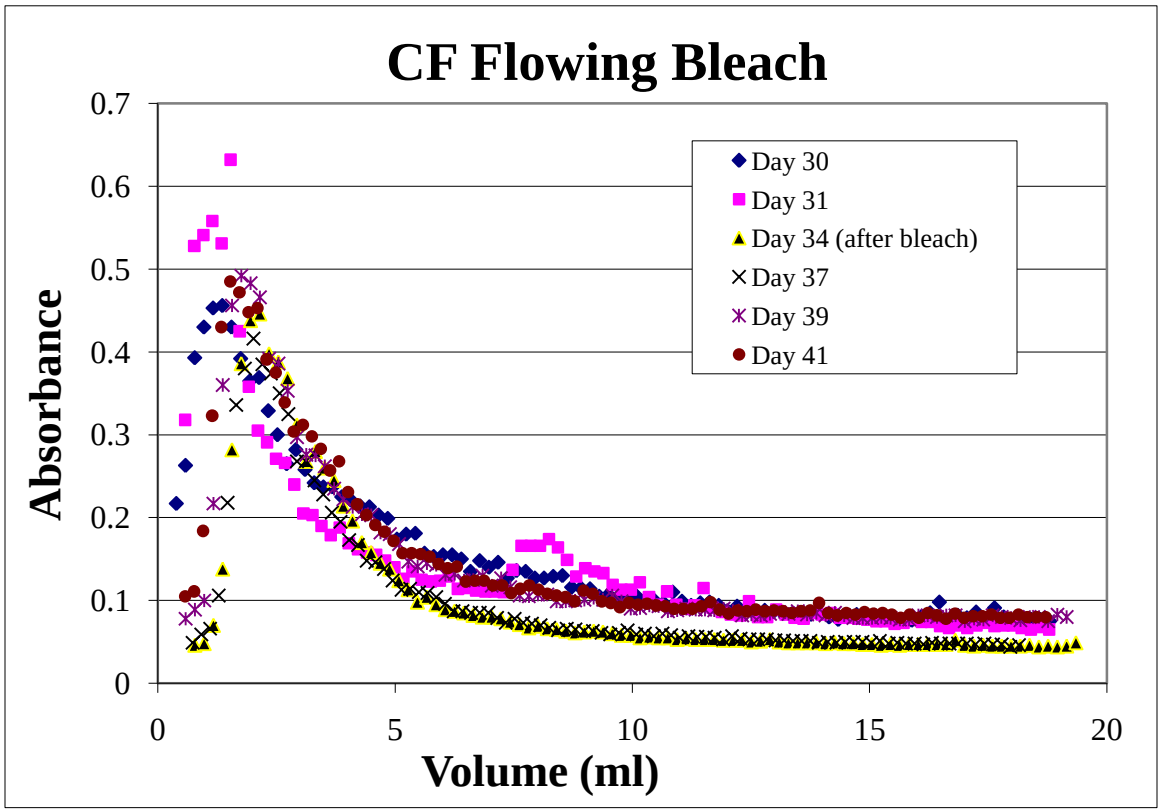

Figure 4.30. Residence time distribution of constant flow exposure to flowing bleach.

The constant head reactor did not experience the same effect. Since the flow rate was so low at this point in the development of the biofilm, it is likely that the flux of bleach into the system was very small in the constant head system. In this case, the presence of the biofilm restricted exposure. The RTD shows a nearly identical, yet slightly smaller, pore volume following the exposure to bleach (Figure 4.31). The noise in the 'Day 31' series is believed to be due to the existence of sloughed cells in the effluent increasing the sample absorbance.

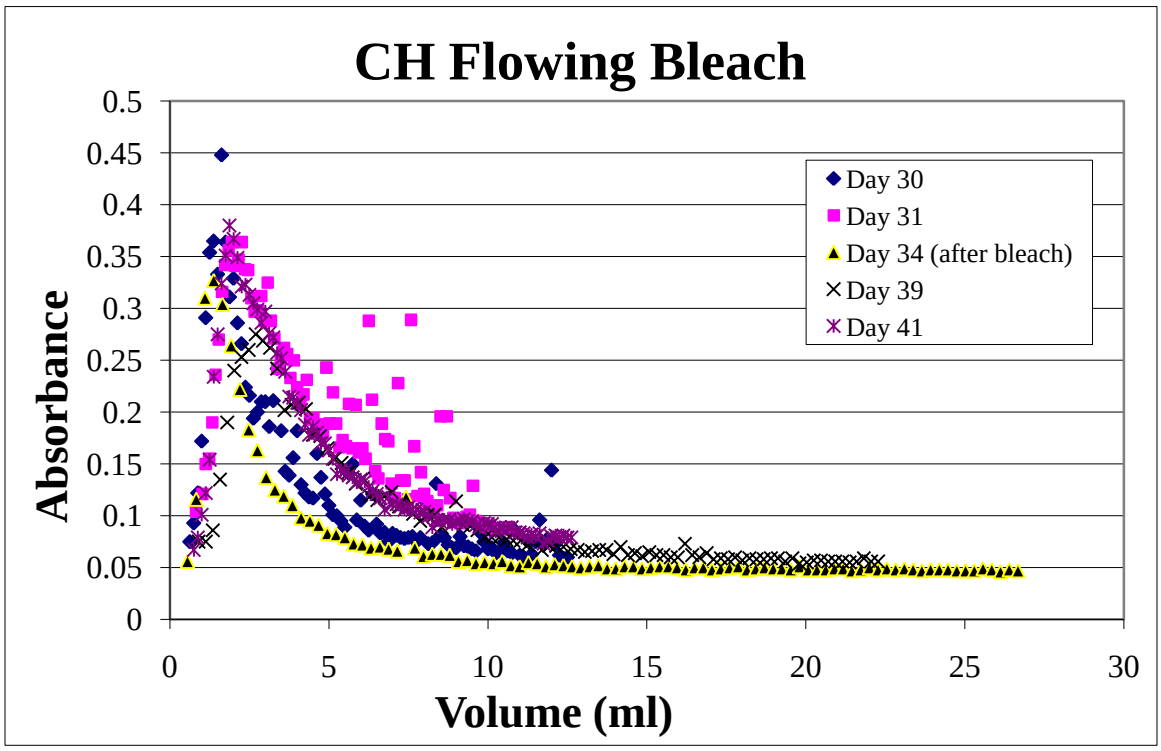

Figure 4.31. Constant head exposure to flowing bleach

General Conclusions from Bleach Studies: In all cases, the exposure to bleach led to a significant increase in hydraulic conductivity (i.e., pressure drop). In no case was the reactor entirely sterilized to a point that re-establishment of biofilm did not occur rather rapidly. This suggests that the biofilm protected much of the bacteria residing in the reactor. For an equal exposure (i.e., stagnant injection), the biofilm formed under constant head conditions appeared to be more susceptible. When bleach was replaced as the flow medium, the constant head conditions restricted the exposure of the biofilm, while the constant flow conditions effectively removed biofilm (see Figure 4.29). This suggests that in order to effectively remove biofouling from a porous media with bleach solution, it should be coupled with forced flow and shear stress.

USING THE BIOFILM ACCUMULATION MODEL TO ASSIMILATE EXPERIMENTAL DATA IN A PLUG FLOW REACTOR

Abstract

Numerical modeling software, such as the Biofilm Accumulation Model (BAM) can be tremendously complementary to laboratory studies. From an *a priori* perspective, numerical modeling can predict experimental results and parameter optimization, and save experimental time, money, and effort while providing theoretical insight. From an *a posteriori* perspective, the phenomena that led to the experimental data can be understood more completely by attempting to replicate the data and assessing perturbation factors. In this study, a *Cellulomonas* (strain ES6) biofilm was grown in an 8.5cm x 3.8cm flat plate simulated porous media reactor (Figures 5.2 and 5.3) with diagonally-etched 1mm pore spaces under constant flow conditions. Over a period of more than thirty days, the pore space reduction and the spatial distribution of biofilm were observed. Utilizing BAM, a numerical model was generated that represents a similar time-scale of biofilm development and describes the dynamics and spatial distribution of the reactor. The plug flow characteristics of the reactor were simulated in BAM with a series of ten perfectly-mixed CSTR reactors.

By altering the input parameters, a base case model was generated that closely resembles the temporal and spatial evolution of biofilm in the reactor. During the process of developing the model, much was learned about the effect of the input parameters. It was found that in developing the desired spatial distribution, the most useful parameters were growth rate, detachment coefficient, and Monod half-saturation constant. In

developing the desired average steady state thickness, the inlet conditions (e.g., flow rate and glucose concentration) were most influential.

While developing this model, several numerical issues were encountered in BAM, highlighting the difficulty of using BAM to simulate a highly specified reactor system. Until some of these model issues are worked out, it is concluded that BAM is more useful for developing a theoretical understanding of biofilm formation and parameter manipulation than it is for precise modeling purposes.

Introduction

Based in principle on a paper by Wanner and Gujer (1986), the Biofilm Accumulation Model (BAM) is a numerical model that uses a continuum approach to predict changes in biofilm thickness and describe the dynamics and spatial distribution of microbial species and substrates in the film. It allows for biomass detachment due to shear stress and sloughing, external mass transfer limitations, as well as variations in bulk liquid concentrations and flow properties (Wanner and Gujer, 1986). The reactive/diffusive transport model is based on a mass balance that incorporates Fick's Law of Diffusion and a reaction term:

$$\frac{dC}{dt} = -D_e \frac{d^2C}{dz^2} + reaction\ rate \qquad (5.1)$$

Integrated within the reaction term, BAM can include many phenomena such as shear stress, sloughing, growth, death, and biocide effects. BAM is programmed to simulate a perfectly mixed CSTR reactor with biofilm growing on the reactor surface. The reactor volume, surface area, and flow rate are input parameters in the model that can

be adjusted accordingly. Furthermore, BAM allows up to ten total reactors to be included sequentially.

The ability of BAM to model ten sequential reactors was utilized to attempt to reproduce laboratory data for the accumulation of a biofilm in a plug flow reactor. The data of interest involved a *Cellulomonas* sp. ES6 biofilm grown under constant flow conditions with a nutrient source of tryptic soy broth (4 g/L).

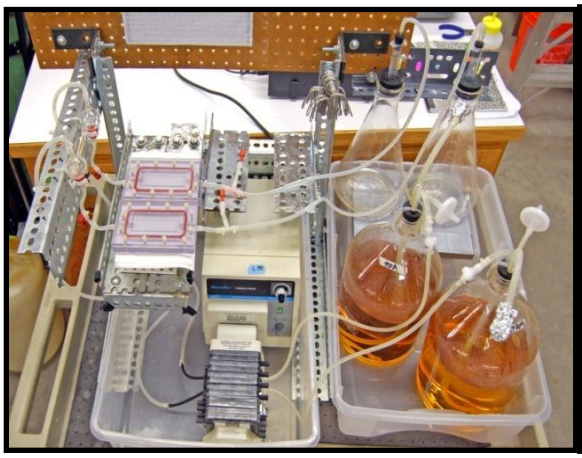

Figure 5.1. Experimental Flow System

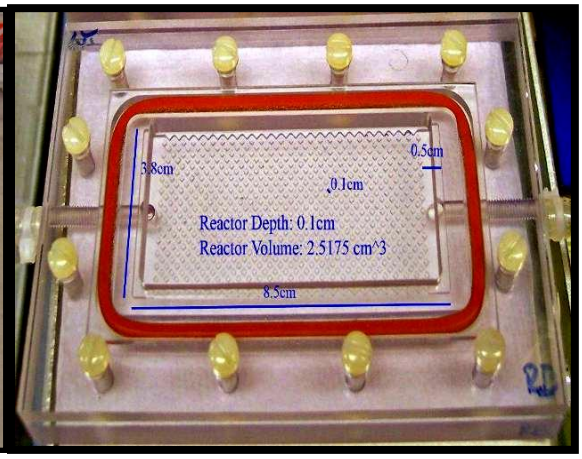

Figure 5.2. Experimental Reactor

Over the course of forty days, the biofilm was observed in the reactor, and the reduction in pore space was measured by residence time distributions and photographs. The pore space reduction over the course of the experiment reached a steady state level at approximately ten days (Figure 5.3). The average thickness of the biofilm was determined by assuming uniform distribution and dividing the biofilm-occupied pore volume by the surface area. However, the spatial distribution of biofilm showed a much thicker biofilm near the influent of the reactor (see Figure 5.4).

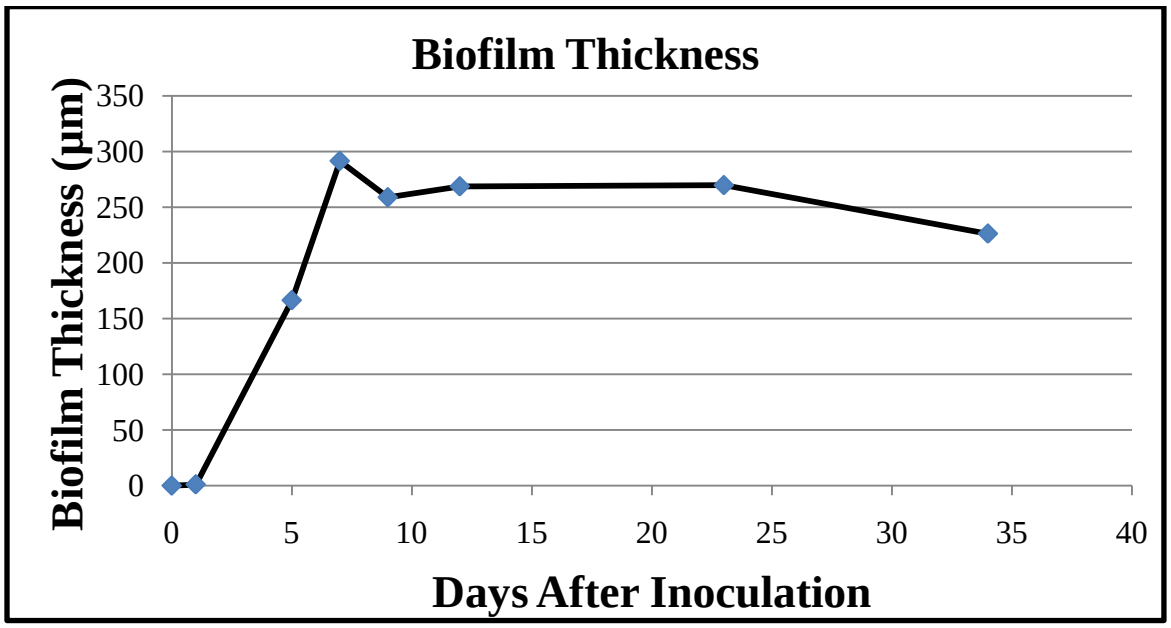

Figure 5.3. Experimental Average Thickness

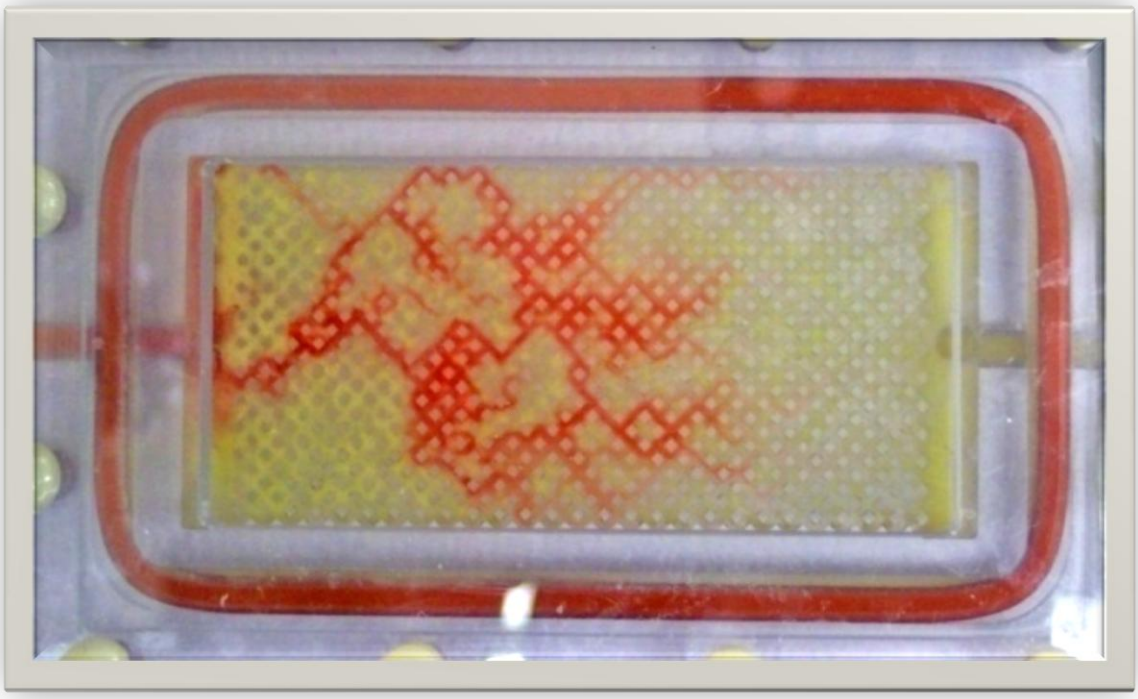

Figure 5.4. Pseudo steady state biofilm showing decreasing biofilm thickness along flow path

In utilizing BAM for the purposes of this research, the objective was to assimilate these observed spatial and temporal phenomena, and furthermore, understand how the various model parameters play a role in these phenomena.

Materials and Methods

To simulate the laminar flow nature of the experimental reactor, the simulation modeled a series of ten sequential CSTR reactors comprising the length of the reactor. Figure 5.5 shows this representation.

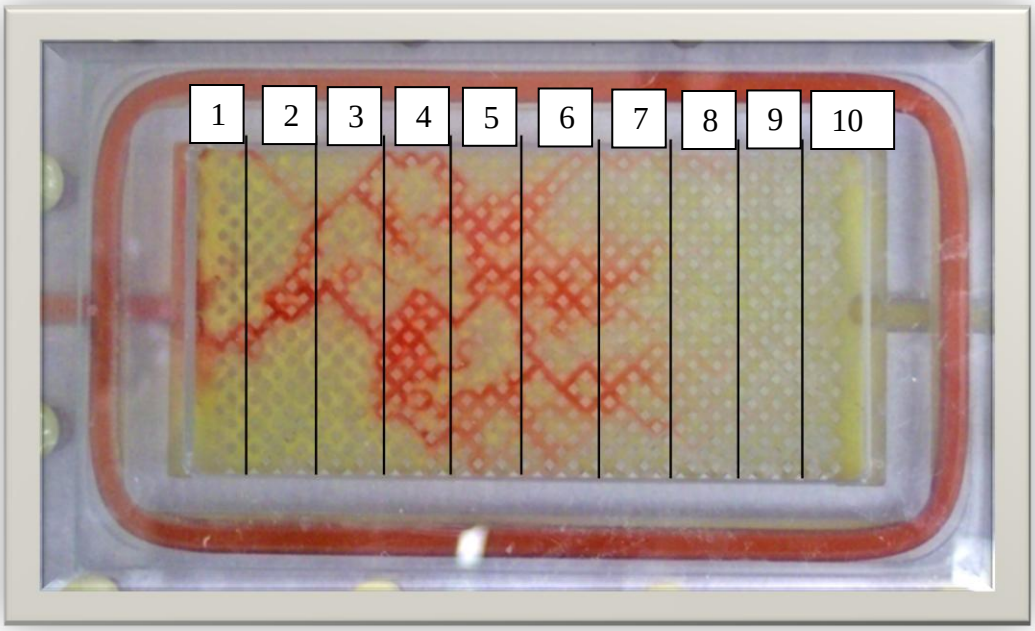

Figure 5.5. PFR divided into ten hypothesized CSTR regions

In attempting to model the system with BAM, several model parameters were assumed to be constant. The assumed constant parameter values were:

- First order growth rate with respect to cells:

$$\frac{dX}{dt} = \mu \qquad (5.2)$$

- Monod order growth rate with respect to substrate (glucose):

$$\frac{dS}{dt} = -\mu \frac{X}{Y_{xs}} \qquad (5.3)$$

- No death in reactor system
- No Boundary Layer
- Void Fraction of water in biofilm: 0.885
- Diffusivity Ratio (film/bulk): 0.8
- Biofilm Phase Density: 3e+04 (g/m^3)
- Yield on Glucose: 0.45
- Initial Biofilm Thickness: 100 µm

The numerical values of the experimental reactor geometry and the inlet flow conditions were used as the initial input parameters for the model. These values are summarized in Table 5.1:

Table 5.1. Table of realistic experimental values input into BAM

BAM Variable	Experimental Value
Surface Area (m^2)	9.2E-05
Volume (m^3)	4.0E-07
SA/Vol. Ratio	2.3E+02
Flow Rate (m^3/day)	1.3E-03
Inlet Glucose Conc. (g/m^3)	1000

Unfortunately, the numerical limitations of BAM would not allow the magnitude of some of these values. Specifically, BAM does not run if the reactor volume is less

than 4e-05 m^3. To accommodate this, the simulated surface area and reactor volume were increased by two orders of magnitude in order to maintain the same surface area to volume ratio; this allowed for volumetric reductions and biofilm thickness to be relatively correlated. The flow rate was scaled up to maintain the same experimental residence time, but another BAM numerical limitation restricted this to be two orders of magnitude higher than desired. To balance the higher flow rate, the inlet glucose concentration was decreased by two orders of magnitude to a final value of 10 g/m^3, so that the total supplied substrate to the reactors would be initially similar.

From this point, trial and error methods were utilized to achieve the experimental steady state average thickness, which was determined from Figure 5.3 to be approximately 250μm, on a similar time-scale and spatial distribution. In particular, the variables that were manipulated in this process were the following:

- Growth rate of the bacteria
- Influent glucose concentration
- Flow rate
- Monod half-saturation constant (K_S)
- Detachment factor

As mentioned and discussed above, these issues were addressed in order to approach a fit with the data. Variables (e.g., glucose concentration) were changed from the original estimates, and the results of these alterations are discussed in the next section.

Results and Discussion

Base Case

A base case model was developed through trial and error manipulation of the previously stated variables. The final model achieved a similar steady state average

thickness (~250μm), and arrived at this steady state at approximately ten days. The input parameters for this model are shown in Table 5.2

Table 5.2. Base Case Values

	BASE CASE
Reactor Units	10
Biofilm Area (m^2)	9.20E-03
Boundary Thickness (m)	0
Unit Vol (m^3)	4.00E-05
Void frac in H_2O	0.885
Diff. ratio (film/bulk)	8.00E-01
SA/Volume Ratio (1/m)	2.30E+02
SUBSTRATE DEF.	
Glucose	
Diffusivity (m^2/day)	5.7E-04
PARTICULATE DEF.	
Cellulomonas (ES6)	
BF phase density (g/m^3)	3.00E+04
REACTION DEF.	
ES6	
Stoich (1 for Cells)	1
Rate Law	First Order
Rate Coeff. (μmax)	7.00E-01
Glucose	
Stoich (-1/Yxs for substrate)	-2.22
Rate Law	Monod
Rate Coeff. (Ks)	10
BOUNDARY CONDITIONS	
Detachment Formula	
Lf^2	1.18E+03
Inlet Flow Table	
Flow Rate (m^3/day)	1.30E-03
Residence time (day)	3.08E-02
INLET CONDITIONS	
Initial Lf (m)	0.0001
Substrate Conditions	
Glucose Inlet Conc. (g/m^3)	50
Particulate Conditions	
ES6 Inlet and Bulk Conc	0
ES6 Film void fraction	0.115

Figure 5.6 shows the similar temporal evolution and steady state between the experiment and the model.

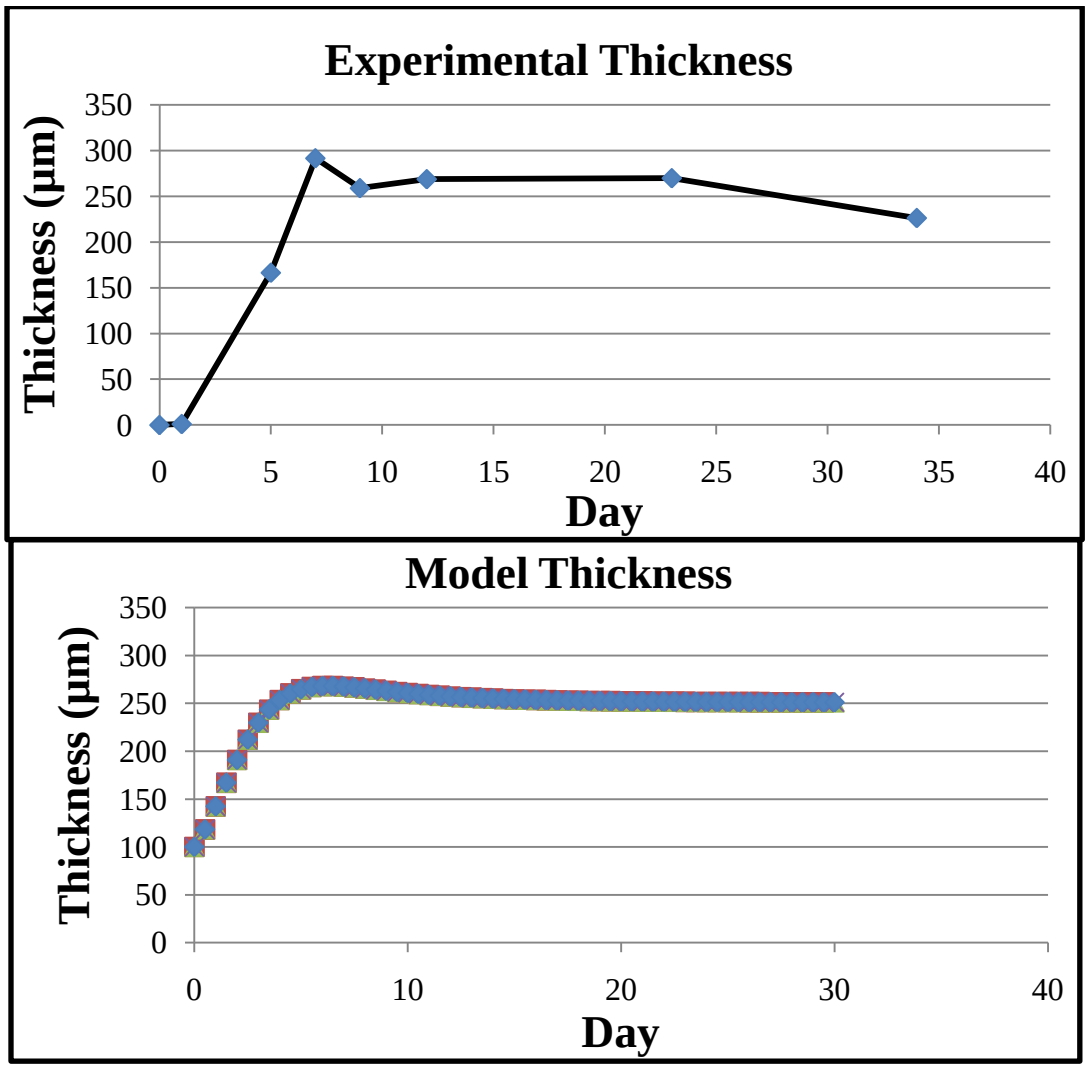

Figure 5.6. Experimental (top) and base case model (bottom) average biofilm thickness over time

The steady state spatial distribution of biofilm predicted by the model was similar to the experimental reactor. From the experiment, the only available spatial data was imaging, so relative comparison is qualitative. However, as seen in Figure 5.7, there is near-complete plugging near the influent of the reactor. Complete plugging would equate to a biofilm thickness of 500µm, completely spanning the pore space. The model's prediction for the influent region is approximately 470µm. From this region of near-

plugging, the thickness decreases significantly, while the total average thickness remains agreeable to the experiment (~250μm). Figures 5.7 and 5.8 illustrate the spatial distribution of the reactor and the model:

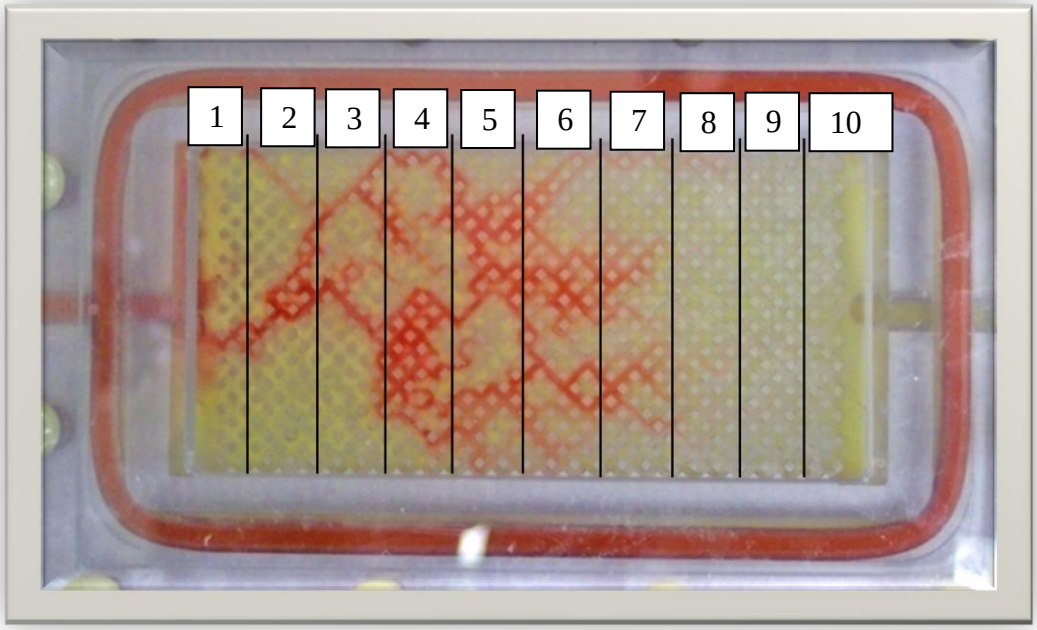

Figure 5.7. Spatial distribution of biofilm in reactor

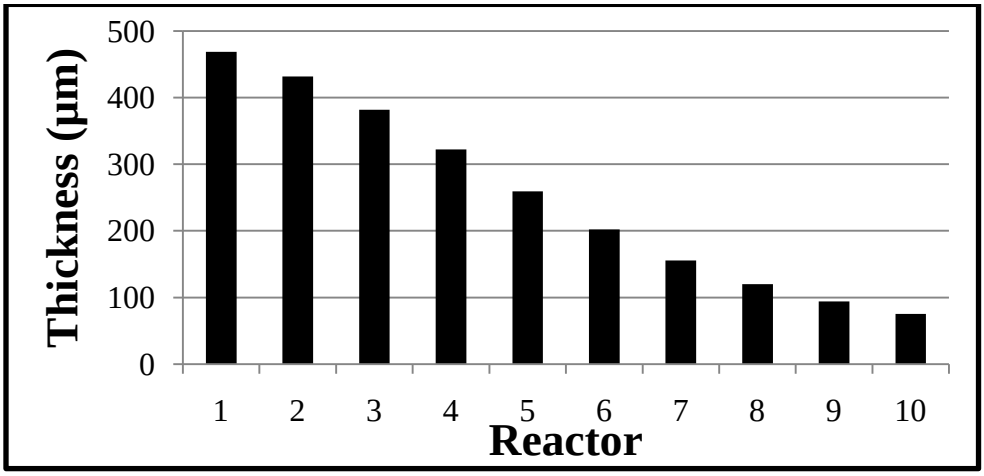

Figure 5.8. Steady state spatial distribution predicted by model. The average thickness throughout the reactor is approximately 250μm.

Manipulation of Spatial Distribution

In order to achieve the spatial variance that was observed in the experiment, several factors were adjusted in the process of creating a similar profile. A summary of those factors and their effect on steady state spatial variance are as follows:

Growth Rate:

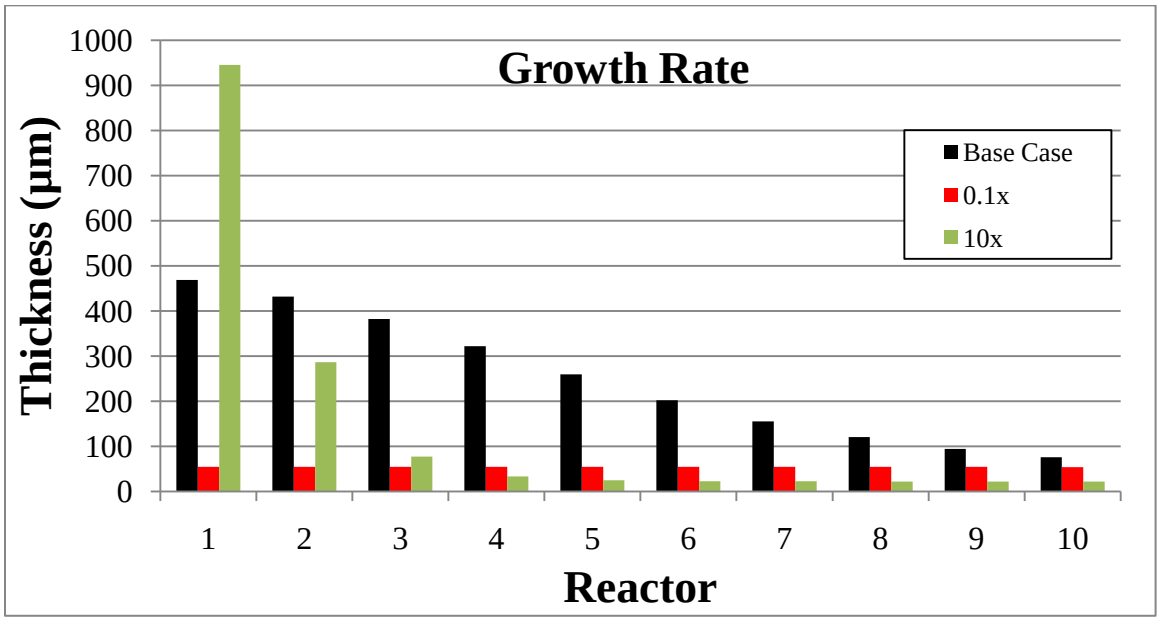

Figure 5.9. Effect of growth rate on steady state spatial distribution. The steady state average biofilm thickness is 250µm for the Base Case, 50µm for 0.1x, and 150µm for 10x.

An increase in growth rate results in more cell growth and glucose conversion in the first reactor. This leads to a thicker biofilm and less available glucose for downstream reactors, resulting in a steeper gradient in biofilm thickness. As can be deduced from Figure 5.9, the overall average biofilm thickness is actually lower when the growth rate is increased by an order of magnitude, which suggests an optimal growth rate for maximum thickness. A higher growth rate leads to a lower average thickness as a

result of an increased detachment effect in the early reactors, and a glucose limitation in downstream reactors. Ultimately, growth rate was manipulated in this experiment to most-accurately simulate the experimental spatial distribution.

Glucose Concentration: By increasing the glucose concentration, a flatter spatial profile and thicker average biofilm was observed (Figure 5.10). More glucose clearly equated to more biofilm, for this reason, glucose concentration was manipulated to affect the SS average biofilm thickness. It was determined that the value of 50 g/m^3 provided for the desired value (250µm).

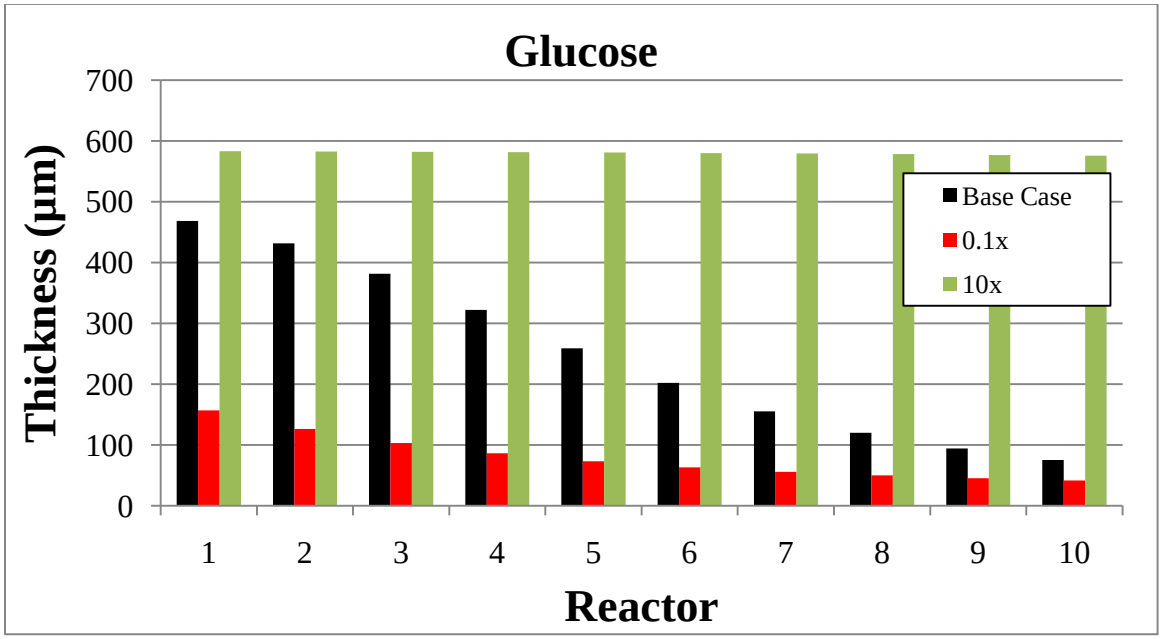

Figure 5.10. Effect of glucose on steady state spatial distribution. The steady state average biofilm thickness is 250µm for the Base Case, 90µm for 0.1x, and 580µm for 10x.

Flow Rate: As seen in Figure 5.11, an order of magnitude increase in flow rate had a similar effect as a similar increase in glucose concentration (i.e., flatter, higher profile). However, a decrease in flow rate had a significantly different effect. A decrease in flow resulted in a steeper profile, and an apparent glucose limitation in downstream reactors. The reason for the observed difference is that a decrease in flow rate does not decrease the growth rate in the first reactor like a decrease in glucose does (see Equation 5.3 for Monod kinetics). However, it decreases the growth rate very significantly in downstream reactors, since the concentration is much lower as a result of the increased residence time. In other words, while the total amount of glucose entering the reactor would be similar for 50% of the base case the concentration or flow rate, the concentration gradient from reactor one to ten (i.e., growth rate gradient) is much greater if the flow rate is decreased. Ultimately, flow rate was used to manipulate the average steady state thickness without significantly altering the spatial variance.

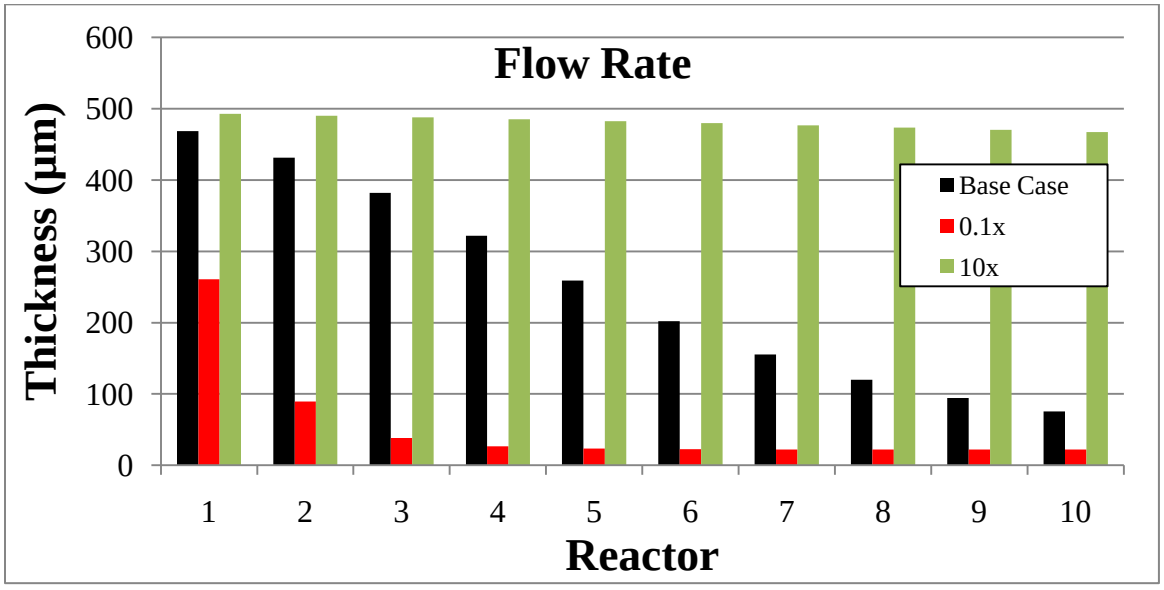

Figure 5.11. Effect of flow rate on steady state spatial distribution. The steady state average biofilm thickness is 250µm for the Base Case, 50µm for 0.1x, and 490µm for 10x.

Detachment Coefficient: The detachment effect in this model was based on dependence of the squared biofilm thickness (L_f^2). This allowed for manipulation of the spatial gradient, and the observed period of biofilm thickness that exceeded the steady state (see Figure 5.6 and the discussion in Chapter 4 concerning the porosity and hydraulic conductivity results). In altering this coefficient, the spatial gradient in biofilm thickness could be manipulated without changing the average thickness significantly (Figure 5.12). The reason for this is that an increased coefficient had a more detrimental effect on the thicker biofilms, leading to a flatter profile. This was a valuable tool in achieving the desired profile once the desired steady state thickness was achieved.

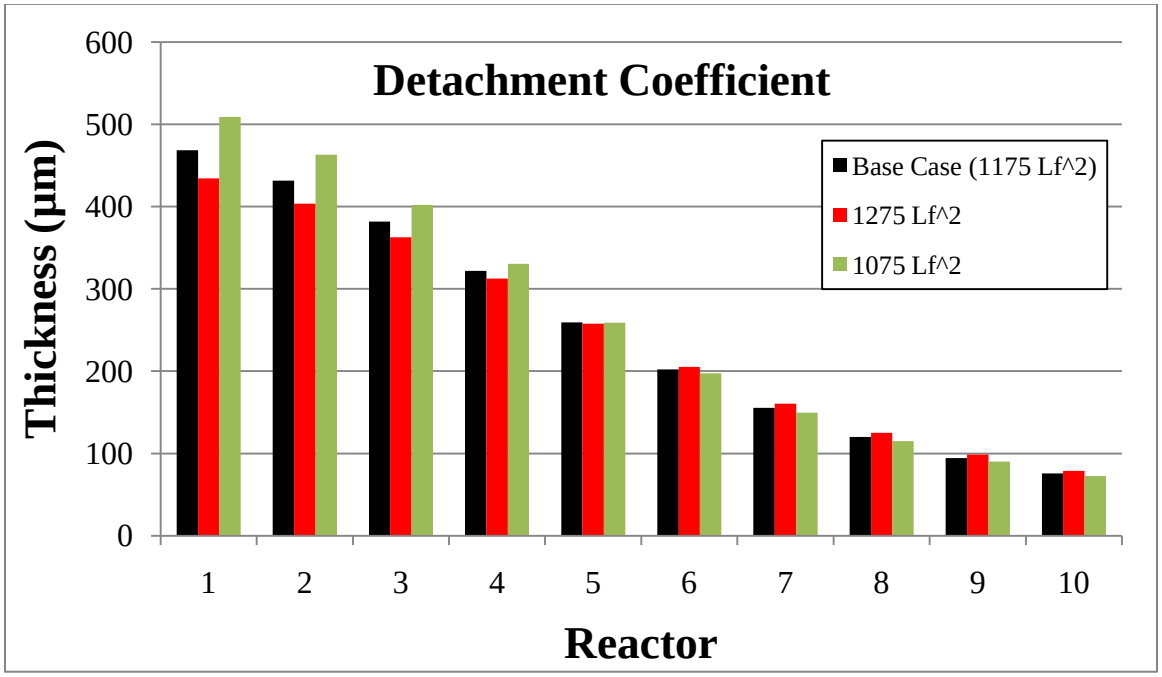

Figure 5.12. Effect of detachment coefficient on steady state spatial distribution. The steady state average biofilm thickness is 250µm for the Base Case, 240µm for 1275 L_f^2, and 260µm for 1075 L_f^2.

Monod Half Saturation Constant (K_s): The effect of an increase in K_s was similar to an increase in the detachment coefficient, as it essentially flattened the profile. The reason for this is that an increase in K_s lowered the effect of the substrate concentration on the growth rate (see Equation 5.3 for Monod kinetics), hence creating a more uniform growth rate. Manipulation of K_s was used in a similar manner as the detachment coefficient, to alter the spatial profile without altering average thickness.

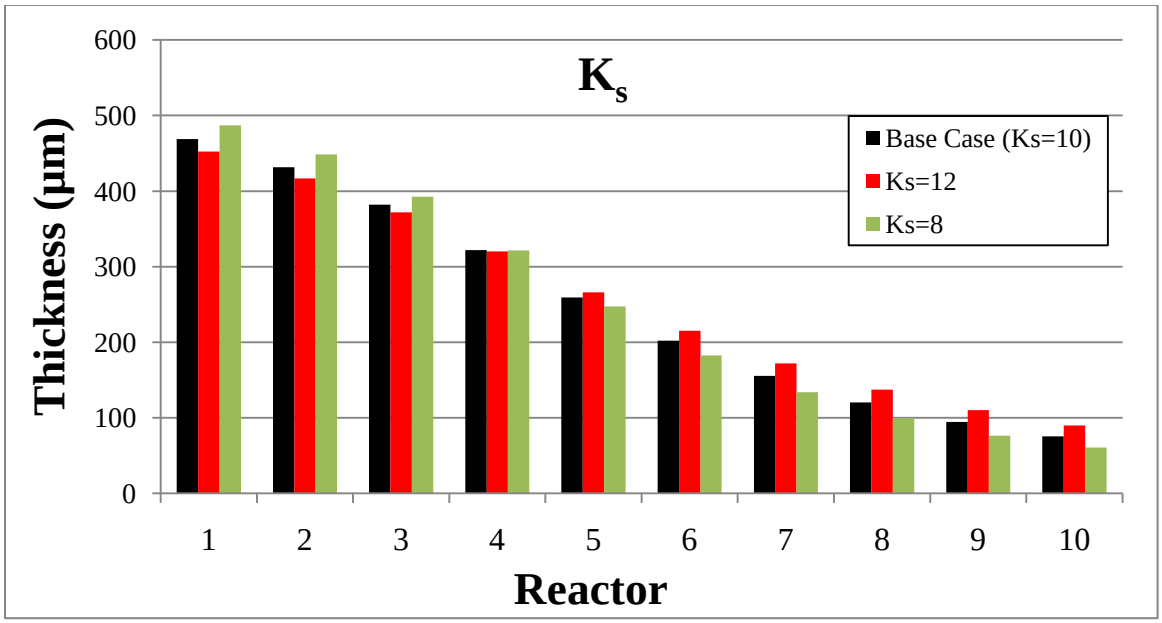

Figure 5.13. Effect of K_s on steady state spatial distribution. The steady state average biofilm thickness is approximately 250µm for all cases in this graph.

Manipulation of Temporal Thickness

In order to achieve the time scale of biofilm accumulation and a similar steady-state thickness to the experimental data, several factors were adjusted. A summary of those factors and their effect of temporal thickness are presented in Figures 5.14-5.18, and their accompanying discussions.

Growth Rate: As growth rate was increased, the most significant effect was the initial rate of biofilm accumulation. However, with regards to the steady state biofilm thickness, there is an apparent optimum that balances substrate availability with the rate of accumulation. An order of magnitude increase in growth rate actually led to a thinner steady state biofilm (Figure 5.14). This is a result of a very fast rate of nutrient consumption, and thus growth in the inlet region, which limits the growth of biofilm in further down the flow path. Ultimately, the growth rate can be altered to affect the initial accumulation rate and the final steady state thickness.

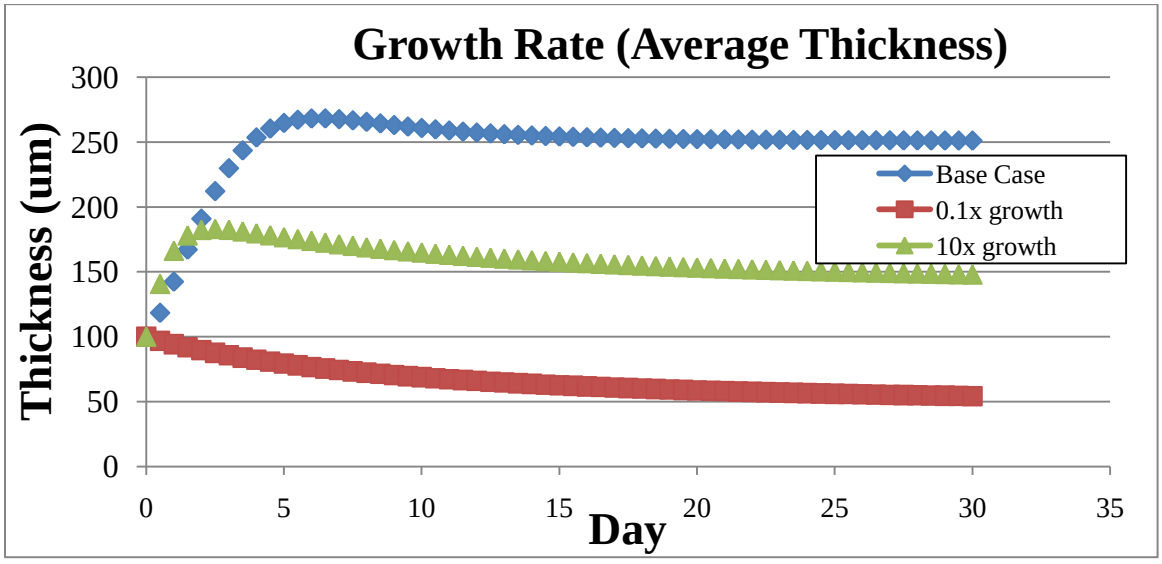

Figure 5.14. Effect of growth rate on temporal average thickness.

Flow Rate: With regards to the final steady state thickness as a function of flow rate, there seems to be a direct relationship without an optimum. A higher flow rate provides more substrate for the reactor as a whole (Figure 5.15). This was used to affect the final steady state thickness.

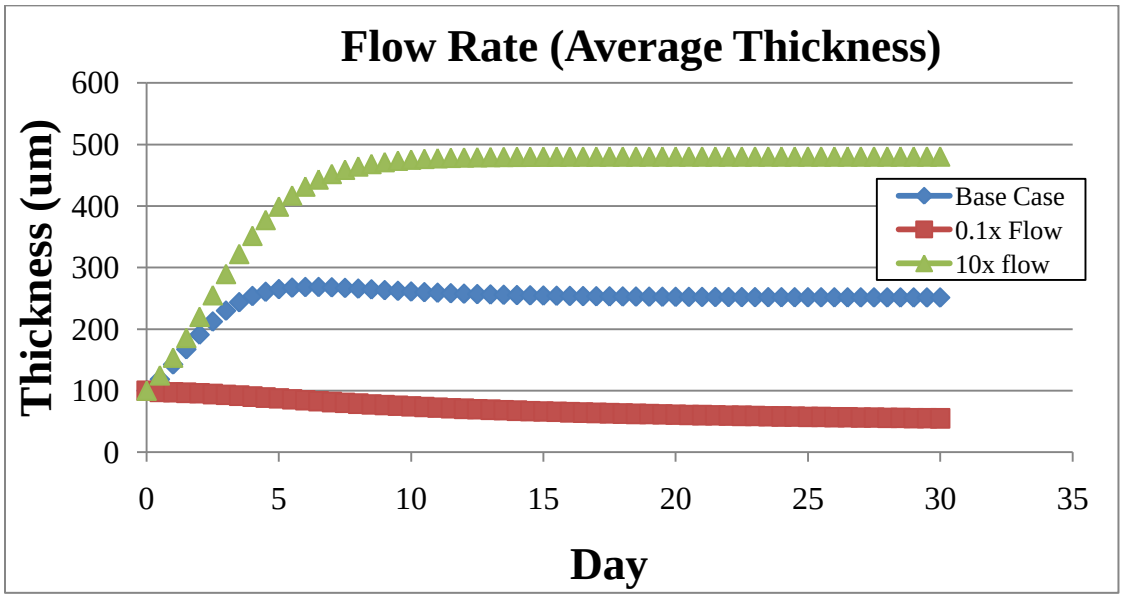

Figure 5.15. Effect of flow rate on temporal average thickness

Glucose Concentration: The effect of glucose increase on the steady state thickness appears very similar to the effect of flow rate increase; there is a direct relationship between overall substrate availability and steady state thickness (Figure 5.16).

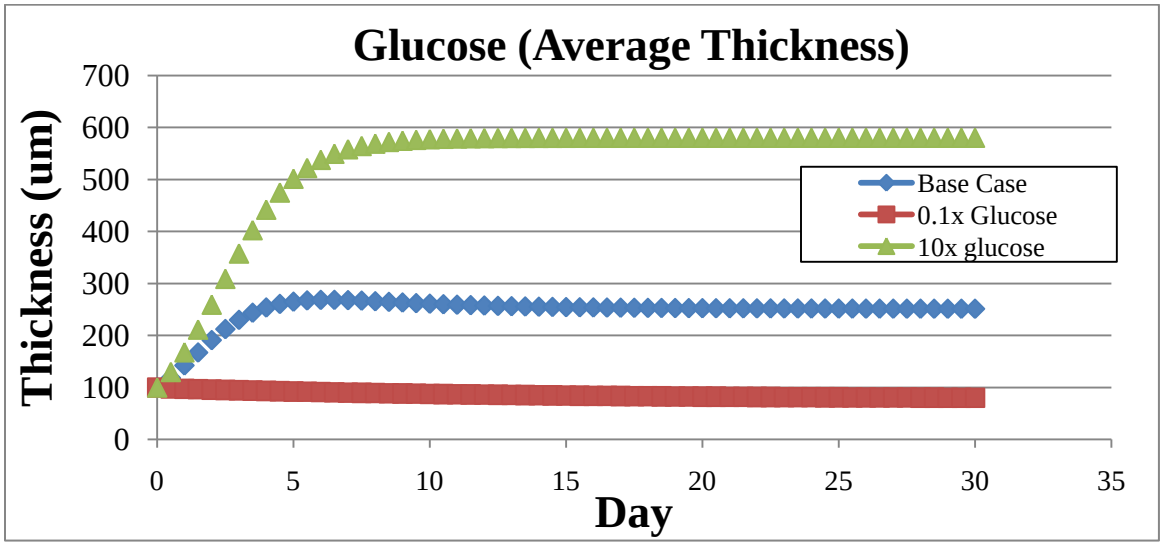

Figure 5.16. Effect of glucose on temporal average thickness

Monod Half Saturation Constant (K_s): In Figure 5.17, it is apparent that an increase in K_s has relatively little effect on the temporal average thickness. This implies that in the base case, K_s = 10 is already high enough with respect to the substrate concentration in most reactors, and a further increase has little effect on the growth rates. However, when K_s is decreased, there is an apparent increase in average thickness as a result of an increase in the growth rates, which approach zero order kinetics at low K_s values.

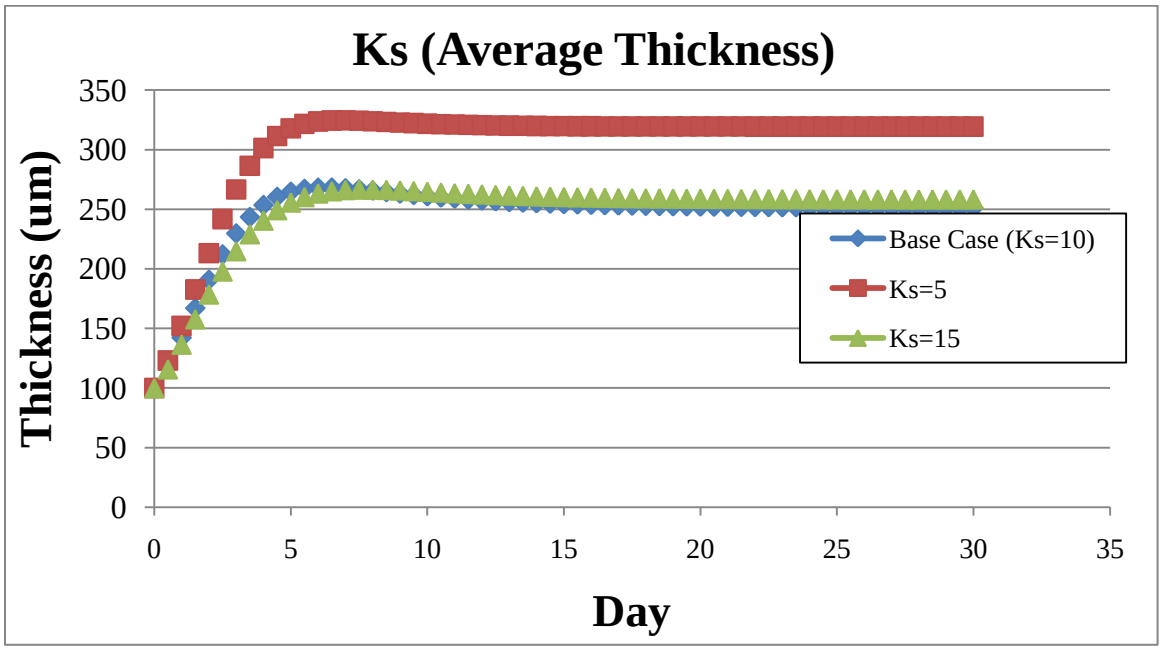

Figure 5.17. Effect of K_s on temporal average thickness

Detachment Coefficient: While manipulating the detachment coefficient has a significant effect on the spatial distribution of biofilm, it must be altered very significantly to have a serious effect on the average thickness. For the sake of this model, manipulating the detachment coefficient was most useful in achieving the observed

period of thickness that exceeded the steady state. It was not used to significantly alter the steady state thickness.

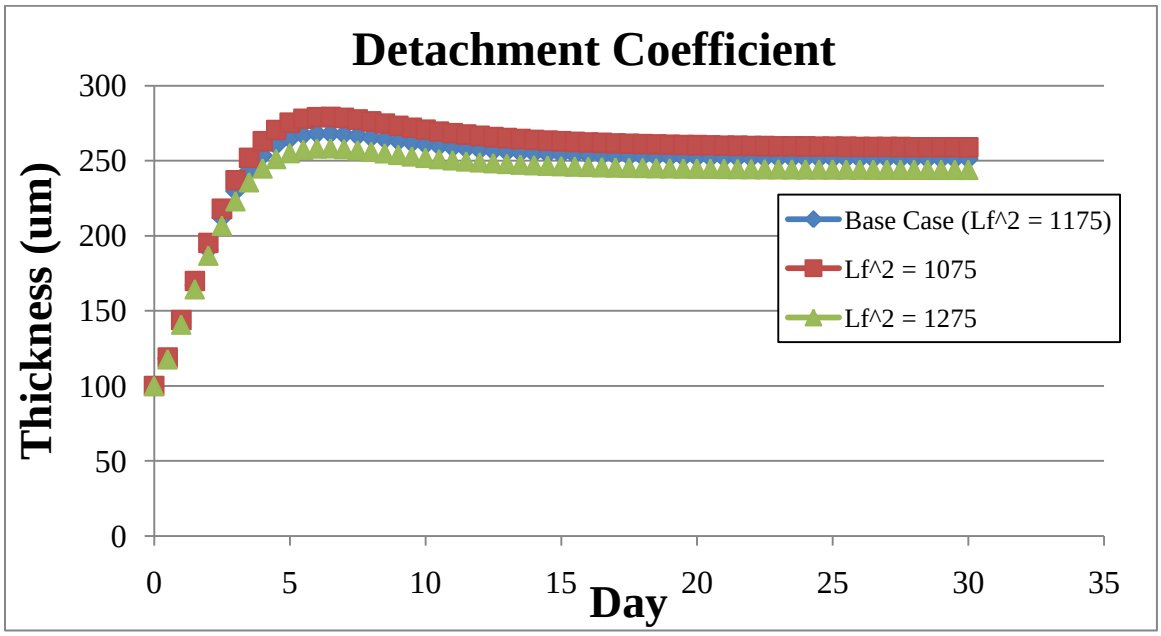

Figure 5.18. Effect of detachment coefficient on temporal average thickness

Summary and Conclusions

In this modeling experiment, BAM was utilized to assimilate experimental data collected from a biofilm-occupied porous media flow reactor. Simulated by a series of ten CSTRs, the model closely replicated the temporal and spatial evolution of biofilm. In the process of arriving at the base case assimilation, several model input parameters were manipulated to eliminate perturbations. These included growth rate, flow rate, glucose concentration, half-saturation constant, and detachment coefficient.

In affecting the spatial variance of the biofilm, the most useful parameters were growth rate, detachment coefficient, and half-saturation constant. These parameters were

useful due to their ability to change the gradient of biofilm thickness without vast changes in total thickness.

In achieving the desired temporal evolution and final steady state thickness, the most influential parameters were found to be the inlet conditions. These parameters, including glucose concentration and flow rate, significantly affected the average thickness in the reactor.

In order to handle the numerical limitations of BAM, some geometric adaptations were necessary to accommodate the numerical solver capabilities. This proved to be very difficult for a small reactor simulation, and forced several alterations. For a reactor system such as the one used in this project, where the pore volume of each reactor is approximately 4 cubic centimeters, the parameters entered into BAM become extremely small, and the numerical solver appears to encounter problems arriving at a solution. A flow rate of higher than the order of 10^{-3} cubic meters per day was not allowed by the model for reasons that are not completely understood. If numerical values are too high or too low for the model's capabilities, there is no notification as to these limitations. For this reason, problems that were encountered in this project were only able to be solved with lengthy trial and error methods. BAM could be much more user-friendly and understandable if notifications were incorporated into the program that would alert the user if they were using values that were too high or low. A user manual that explained the limitations of BAM would also assist in increasing the user-friendliness of the program.

Some of the nonrealistic model inputs required in this section were a result of a fundamental difference between the model and the data. The model applies a continuum approach, while the dynamic channel formation and the percolation-type behavior in the laboratory reactors was statistical in nature.

In conclusion, BAM has the potential to be an effective tool for the modeling of biofilm evolution. For the purpose of gaining an understanding of where and how biofilms form, and understanding the effect of controllable variables, it remains very useful. However, for modeling a precisely-defined system, the numerical limitations and lack of explanations in the program provide many challenges for the user.

CONCLUSIONS

Conclusions from Bacterially-Induced Calcite Precipitation Investigations

Based on the results of investigations contained in Chapters 2 and 3, it became clear that the bacterium *S. pasteurii* can efficiently induce ureolytically-driven calcium carbonated mineralization in laboratory flow systems. This was evident through increases in effluent ammonium concentration and pH, and a more than 95% decrease in dissolved and total calcium concentration in the effluent. The presence of colony forming units and protein in the effluent of the reactors confirmed the presence of an active ureolytic culture, and x-ray diffraction analysis suggested that the visible precipitates contained diffraction patterns consistent with calcite, the rhombohedral polymorph of calcium carbonate.

When dissolved Sr^{2+} was present in the fluid, it was shown to become incorporated within the solid calcium carbonate lattice and have a very minor inhibitory effect on overall precipitation. A higher partitioning of Sr^{2+} was observed near the influent region, suggesting that the degree at which Sr^{2+} is co-precipitated within the lattice of calcite depends on the saturation conditions and/or kinetics of precipitation. These results indicate the potential use of this method for divalent contaminant remediation in the subsurface.

Novel methods to image ureolytic calcite precipitation were developed. Quantification of precipitate distribution and substrate conversion were achieved with a stereo microscope, and it was determined that the precipitate size and density decreased

along the flow path. The conversion of dissolved Ca^{2+} to calcite was estimated based on quantitative image analysis and determined to be slightly lower than the conversion estimated from effluent samples.

Bacteria-mineral interactions were studied using a confocal laser scanning microscope with fluorescent dye stains, and the close spatial relationship between the surface of calcite and bacterial attachment was elucidated. It was apparent that bacterial attachment was much more prolific on the surface of precipitates as compared to the surface of the glass reactors. This suggests that there is a mutualistic relationship between ureolytic bacterial attachment and calcite mineral formation.

Suggestions for Further Studies

In order to progress towards an implementable understanding of biomineralization under flow conditions in subsurface porous media, more research must be done. My suggestions for studies to build on those presented in this thesis are as follows:

I. *A more detailed analysis of precipitation kinetics as a function of substrate conditions and microbial diversity.* This will be important to optimize distribution, and to assess the ability of native microbial cultures to induce ureolysis at rates that are practical for subsurface biotechnical applications. For environmental, legal, and practical reasons, highly ureolytic species such as *S. pasteurii* may not be able to be introduced, and it may be necessary to cultivate exclusively native ureolytic microbes. In a similar context, the further development and improvement of predictive kinetic models appears necessary. Microbiologists understand microbial growth kinetics well, and

geologists understand mineral saturation/precipitation kinetics well, but there seems to be very little connection in the currently available models between these fundamental and interrelated areas of understanding.

II. *A detailed assessment of fluid mixing limitations that may accompany the injection of one fluid into another.* This may be achieved by using reactors that introduce the substrates and reactants from separate streams, and allow them to mix transversely within the porous media. It remains unclear how biomineral and biofilm formation will ultimately affect transport across plume margins in cases where mixing is essential for objectives to be met. A reactor example proposed by Dr. Robin Gerlach is shown below (Figure 6.1).

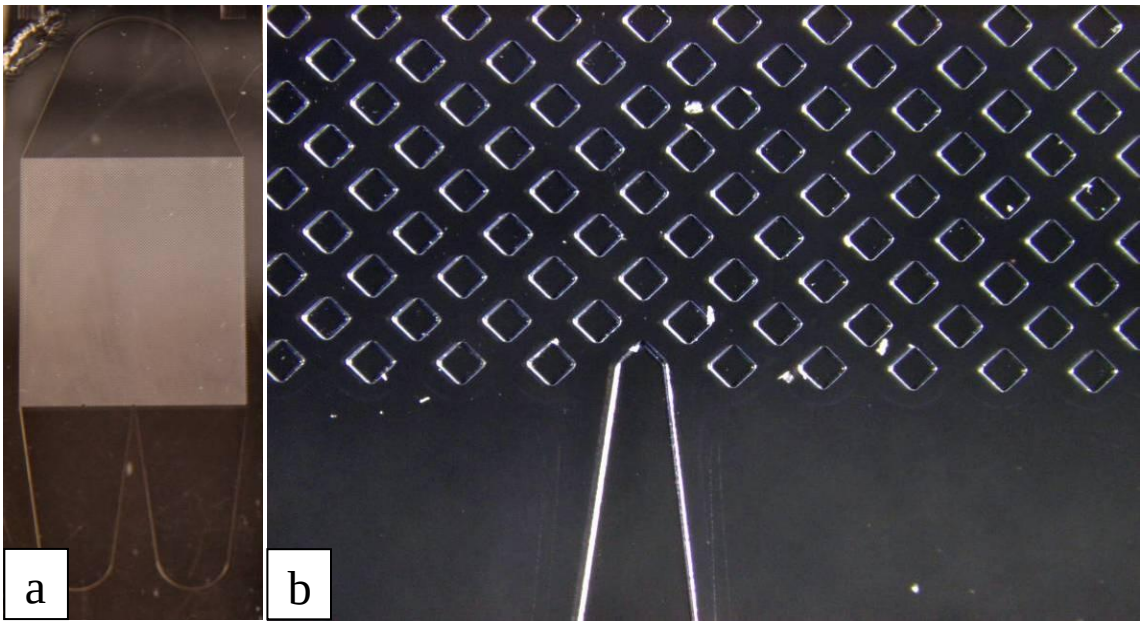

Figure 6.1. This is a reactor prototype, designed by Dr. Robin Gerlach, to allow the assessment of mixing limitations in the presence of biominerals and biofilms. Flow will progress upward in these images. One substrate-containing media can flow through the left inlet while another can flow through the right inlet, and mixing will occur at the start of the porous media elements. (a) Entire reactor (b) Porous elements at the point where the fluids will mix. In these reactors, the porous media elements (i.e., squares) have 100μm sides.

III. *Additional confocal imaging to expand on the data collected in this study*. It would be beneficial to better understand the process of nucleation. This experiment may involve viewing a section of the capillary surface under the confocal or light microscope in real time from the point of inoculation. If a green fluorescent protein could be acquired for an ureolytic organism, then the entire process of nucleation and growth during bacterial attachment/growth may be viewed throughout the experiment without the harmful effects of the stains used in the experiments contained in this thesis. This may provide insight into the question of which precedes the other - bacterial attachment or mineral precipitation.

IV. *A better understanding of the biological environment at the interior of the precipitates*. Fluorescent staining and CLSM imaging during these studies did not reveal the environment at the interior of the precipitates due to stain penetration and/or optical limitations associated with calcite. It may be possible to embed the capillary flow cells with epoxy resin, such as LR White (London Resin Company, London, U.K.), remove the glass walls, slice the cross sections, and conduct TEM tomography analysis to reconstruct a three-dimensional image that incorporates the cells at the precipitate interior. A suggested protocol for this process has been written and included in Appendix S.

V. *Additional studies of more environmentally realistic porous media systems.* This will be necessary to predict reactive transport and attachment

phenomena. This may be achieved by performing studies with subsurface core samples or soil columns.

VI. *A more complete understanding of the effect of $scCO_2$ exposure on biominerals, particularly in the presence of saline solution***.** This will be necessary to assess the process under the conditions of geologic carbon sequestration. A proposed experimental procedure for this is included in Appendix B.3.

Conclusions from Biofouling Investigations

In these investigations, several studies showed the development of a *Cellulomonas* sp. ES6 biofilm in two-dimensional porous media reactors. Residence time distributions were taken over the course of biofilm development; reductions in effective porosity, decreases in reactor dispersivity, and an increase in sustained dye retention were observed. These phenomena appeared to reach a pseudo-steady state after a period of growth. Prior to the establishment of the steady state thickness, there was a brief period in which the biofilm thickness exceeded the steady state value. This phenomenon was observed as a peak in porosity reduction as well as a peak in pressure drop across the reactor.

Piezometer data showed increases in pressure drop (i.e., decreases in hydraulic conductivity) as a result of biofilm formation. This effect was shown to fluctuate as a result of biofilm channel formation, and appeared to reach a dynamic pseudo-steady state that correlated in time with the pseudo-steady state porosity reduction.

Biofilms were formed under constant flow rate and constant head conditions. The biofilms formed under constant flow conditions appeared to be more evenly distributed along the flow path but also formed more distinct channels. The biofilm formed under constant head conditions appeared to be localized more near the inlet, and the visualization of tracer dye showed a more laterally homogeneous flow path. These observational differences are believed to be a result of the difference in substrate availability and shear stress.

Biofilms were exposed to chlorinated bleach (i.e., sodium hypochlorite), a biocide, in both stagnant and flowing methods. In all conditions, a decrease in hydraulic conductivity was immediately observed. A significant increase in porosity resulting from the visible removal of biofilm was observed in a constant flow reactor that was exposed to bleach at a constant flow rate. This suggests that the removal of biofilm by bleach is greatly assisted by an environment with shear stress. For all bleach studies, microbes survived within the reactor and re-established their effects on permeability and porosity in a brief time. While chlorinated bleach has long been used as an effective means to kill suspended bacteria, it does not appear to be highly effective in completely removing biofouling.

The continuum approach of the Biofilm Accumulation Model (BAM) was used to model previously obtained spatial and temporal biofouling data in a porous media reactor. Variables were adjusted in the model to predict perturbations, and it was determined that the temporal evolution of the biofilm was most affected by the detachment factor and kinetic parameters incorporated, while the steady state spatial

distribution was most affected by the inlet conditions (e.g., flow rate, substrate concentration). BAM provided much insight into understanding the development of biofilm in a porous media reactor, but the numerical limitations and lack of a user-friendly interface limited the ability of BAM to efficiently and precisely model reactors as small as those used in this experiment. Furthermore, the channeling dynamics exhibited in the reactors exhibited a statistical nature which cannot be efficiently modeled with a continuum model such as BAM.

Suggestions for Further Studies

Much work remains before a complete understanding is available of the effects that biofouling can have on hydraulic flow through porous media. After conducting the investigations contained in this thesis, my suggestions for further studies are as follows:

I. *A more detailed assessment of the effect of biofouling on fluid mixing limitations that may accompany the injection of one fluid into another.* Similarly to the development of biomineral formation along plume margins, it appears necessary to better understand how biofilms may affect fluid-fluid mixing in these areas. See Figure 6.1 for a proposed reactor design that will allow for this assessment.

II. *A comparison of the RTD method used in this research to obtain porosity data with a porosity estimate obtained from image analysis.* As described in Chapter 4, a porosity estimate could be made by counting the biofilm-occupied pore spaces in images taken during RTD analysis. This would be a tedious exercise, but would be of interest if this methodology is used to

quantify porosity in the future. Furthermore, the scale of imaging in the reactors used in this study could be reduced so that biofilm thickness could be measured more precisely at various locations, in a manner similar to the way precipitate sizes were measured in Chapter 2.

III. *Conduct similar investigations with smaller and more environmentally-realistic porous media reactors.* Most environmental biotechnologies and control scenario environments contain much smaller pore spaces and a greater surface area to volume ratio. Micro-reactors (e.g., Figure 6.1) can assess these phenomena in smaller pores, but ultimately, similar studies in geologic media (e.g., sandstone) will be highly complementary to these investigations. Reactors with smaller pore spaces may also allow for the determination of a clean reactor hydraulic conductivity, which will be more suitable for modeling the relationship between porosity and hydraulic conductivity.

IV. *Conduct similar investigations under radial flow conditions*. For many subsurface flows where a point of origin exists (e.g., injection well or contaminant plume source), there is a radial velocity gradient as flow flows outward. This is difficult to simulate in a lab setting, but reactor designs do exist. An example is included in Appendix T.

REFERENCES CITED

1. Acharya, R., Valocchi, A., Werth, C., and Willingham, T. 2007. Pore-scale simulation of dispersion and reaction along a transverse mixing zone in two-dimensional porous media. *Water Resour. Res*, 47: W10435.

2. Albrechtsen, H.J., Boe-Hansen, R., Henze, M., Mikkelsen, P.S. 1998. Microbial growth and clogging in sand column experiments simulating artificial recharge of groundwater. Proceedings of the Third International Symposium on Artificial Recharge of Groundwater, Amsterdam, Netherlands, 21-25 September.

3. Alfreider, A.; Krossbacher, M.; Psenner, R. 2007. Groundwater samples do not reflect bacterial densities and activity in subsurface systems. *Water Res.* 31 (4): 832-840.

4. Atkins, P and de Paula, J. 2002. Atkins' Physical Chemistry. 7th edn. Oxford University Press. Oxford.

5. Bielefeldt, A., McEachern, C., Illangasekare, T. 2002. Hydrodynamic changes in sand due to biogrowth on naphthalene and decane. *J. Environ. Eng*. January. 51-59.

6. Borch, T., Inskeep, W., Harwood, J., Gerlach, R. 2005. Impact of ferrihydrite and anthraquinone-2,6-disulfonate on the reductive transformation of 2,4,6-trinitrotoluene by a gram-positive fermenting bacterium. *Environ. Sci. Technol.* 39(18): 7126-7133.

7. Brown, T., Lemay, H., Bursten, B. 2003. Chemistry: The Central Science. 9th Edition. Pearson Education. 639.

8. Castanier, S., Le Metayer-Levrel, G., and Perthuisot, J.P. 1999. Ca-carbonates precipitation and limestone genesis – the microbiolgeologist point of view. *Sedimentary Geology*. 126: 9-23.

9. Cunningham, A.B., Characklis, W.G., Abedeen, F., and Crawford, D. 1991. Influence of Biofilm Accumulation on Porous Media Hydrodynamics. *Environ. Sci. Technol*. 25: 1305-1311.

10. Cunningham, A.B., Sharp, R.R., Heibert, R., and James, G. 2003. Subsurface Biofilm Barriers for the Containment and Remediation of Contaminated Groundwater. *Bioremed. Jour*. 7.

11. Cunningham, A.B., Warwood, B., Sturman, P., Horrigan, K., James, G., Costerton, J.W., and Hiebert, R. 1997. Biofilm processes in porous media – practical applications. p 325-344. *In* P.S. Amy and D.L. Haldeman (ed.), The Microbiology of the Terrestrial Deep Subsurface. CRC Press, Boca Raton, FL.

12. Curti, E. 1997-2000. Coprecipitation of Radionuclides: Basic Concepts, Literature Review and First Applications. PSI-Report 97-10. Paul Sherrer Institut.

13. Dupin, H.J., McCarty, P.L. 2000. Impact of colony morphologies and disinfection on biological clogging in porous media. *Environ. Sci. Technol.*. 34(8): 1513-1520.

14. Dupin, H.J.; Kitanidis, P.K.; McCarty, P.L. 2001. *Water Resour. Res.* 37(12): 2981-2994.

15. Ferris, F.G., Phoenix V., Fujita Y., Smith R.W. 2003. Kinetics of calcite precipitation induced by ureolytic bacteria at 10 to 20°C in artificial groundwater. *Geochimica et Cosmochimica Acta*. 67(8): 1701-1722.

16. Ferris, F.G., T.J. Beveridge, and W.S. Fyfe. 1986. Iron-silica crystallite nucleation by bacteria in a geothermal sediment. *Nature*. 320: 609-611.

17. Ferris, F.G., Fyfe W.S., and Beveridge, T.G. 1987. Bacteria as nucleation sites for authigenic minerals in metal-contaminated lake sediment. *Chemical Geology*. 63. 225-232.

18. Ferris, F.G., Stehmeir L.G., Kantzas A., Mourits F. M.1996. Bacteriogenic mineral plugging. *Journal of Canadian Petroleum Technology*. 13: 57-67.

19. Frankenberger, W.T., Troeh, F.R., Dumenil, L.C. 1979. Bacterial effects on hydraulic conductivity of soils. *Soil Sci. Soc. Am. J.* 43: 333-338.

20. Fujita, Y., Ferris, F.G., Lawson, R.D., Colwell, F.S., and Smith, R.W. 2000. Calcium carbonate precipitation by ureolytic subsurface bacteria. *Geomicrobiology Journal* 17: 305-318.

21. Fujita, Y., Redden G.D., Ingram J.C., Cortez M.M., Ferris F.G., Smith R.W. 2004. Strontium incorporation into calcite generated by bacterial ureolysis. *Geochimica et Cosmochimica Acta,* 68(15), 3261-3270.

22. Fujita, Y, Taylor, J., Gresham, T., Delwiche, M., Colwell, F., Mcling, T., Petzke, L, Smith, R. 2008. Stimulation of Microbial Urea Hydrolysis in Groundwater to Enhance Calcite Precipitation. *Environ. Sci Technol.* 42: 3025-3032.

23. Gerlach, R., Cunningham, A.B. Influence of Biofilms on Porous Media Hydrodynamics. To appear in 2010. Vafai, K. (ed.), Porous Media: Applications in Biological Systems and Biotechnology. Taylor Francis.

24. Hammes F., Seka A., de Knijf S., Verstraete W. 2003. A novel approach to calcium removal from calcium-rich industrial wastewater, *Water Research*. 37: 699-704.

25. Hammes, F., and Verstraete, W. 2002. Key roles of pH and calcium metabolism in microbial carbonate precipitation. *Reviews in Environmental Science & Biotechnology* 1:3-7.

26. Hazen, T. C.; Jimenez, L.; Devictoria, G.L.; Fliermans, C. B. 1991. Comparison of bacteria from deep subsurface sediment and adjacent groundwater. *Microb. Ecol.* 22 (3): 293-304.

27. Herigstad, B; Hamilton, M; Heersink, J. 2001. How to optimize the drop plate method for enumerating bacteria. *J. Microbiol. Methods*. 44: 121-129.

28. Holm, J. 2000. Effects of biomass growth on the hydrodynamic properties of groundwater aquifers, Ph.D. thesis, Series Papers 72, Department of Hydrodynamics and Water Resources, Technical University of Denmark.

29. Intergovernmental Panel on Climate Change. 2005. Special Report on Carbon Capture and Storage. Cambridge University Press, New York.

30. International Energy Agency. 2008. Paris, France. Energy Technology Perspectives. www.iea.org. Accessed November, 2009.

31. Jury, C. 2008. Aquarium Chemistry: The Carbonate System in the Aquarium, and the Ocean, Part I: The Components of the Carbonate System. Advanced Aquarist's Online Magazine. 12. http://www.advancedaquarist.com/2008/12/chemistry. Accessed September, 2009.

32. Klein, C., and C.S.J. Hurlbut. 1999. Manual of Minerology. 21st edn. John Wiley & Sons, Inc., New York.

33. Lehman, R. M., Roberto, F. F., Early, D., Bruhn, D. F., Brink, S. E., O'Connel, S. P., Delwiche, M. E., Colwell, F. S. 2001. Attached and unattached bacterial communities in a 120-meter corehole in an acidic, crystalline rock aquifer. *Appl. Environ. Microbiol.* 67 (5): 2095-2106

34. Lehman, R. M., O'Connell, S.P. 2002. Comparison of extracellular enzyme activities and community composition of attached and free-living bacteria in porous media columns. *Appl. Environ. Microbiol.* 68 (4): 1569-1575.

35. Meldrum, F., Coelfen, H. 2008. Controlling Mineral Morphologies and Structures in Biological and Synthetic Systems. Chemical Reviews, 108(11): 4332-4432.

36. Mindat. Org. The mineral and locality database. http://www.mindat.org/min-859.html. Accessed March 23, 2009.

37. Mitchell, A.C. and Ferris, F.G. 2005. The coprecipitation of Sr into calcite precipitates induced by bacterial ureolysis in artificial groundwater: Temperature and kinetic dependence. *Geochimica et Cosmochimica Acta,* 69(17): 4199-4210.

38. Mitchell, A.C., and Ferris, F.G. 2006. Effect of Strontium Contaminants upon the Size and Solubility of Calcite Crystals Precipitated by the Bacterial Hydrolysis of Urea. *Environ. Sci. Technol.* 40: 1008-1014.

39. Morse, J. W.; Mackenzie, F.T. 1990. Geochemistry of Sedimentary Carbonates; Developments in Sedimentology. *Elsevier*: 48: 707.

40. Moynihan, H., Lee, C., Clark, W., Wang, N. 1989. Urea hydrolysis by immobilized urease in a fixed-bed reactor: analysis and kinetic parameter estimation. *Biotechnol. Bioeng.* 34: 951-963.

41. Nambi, I., Werth, C., Sanford, R., and Valocchi, A. 2003. Pore-Scale Analysis of Anaerobic Halorespiring Bacterial Growth along the Transverse Mixing Zone of an Etched Silicon Pore Network. *Environ. Sci. Technol.*. 37: 5617-5624.

42. Oelkers, E., Gislason, S., Matter, J. 2008. Mineral Carbonation of CO_2. *Elements*. October: 333-337.

43. Okubo, T., Matsumoto, J. 1983. Biological clogging of sand and changes of organic constituents during artificial recharge. *Water Resour. Res*. 17: 813-821.

44. Oya, S., Vallochi, A. J. 1998. *Water Resour. Res.* 34(12): 3323-3334.

45. Paulsen, J.E., Oppen, E., Bakke, R. *Water Sci. Technol.* 1997. 36 (1): 1-9.

46. Pitts, B.; Stewart, P. 2008. Confocal Laser Microscopy on Biofilms: Successes and Limitations. *Microscopy Today*. July 2008: 18-22.

47. Rasband, W. Image J, U.S. National Institutes of Health, Bethesda, Maryland, USA. http://rsb.info.nih.gov/ij/. 1997-2009.

48. Raje, D.; Kapoor, V. 2000. *Environ. Sci. Technol.* 34: 1234-1239.

49. Riley, R.G. and Zachara J.M. 1992. Chemical contaminants on DOE lands and selection of contaminant mixtures for subsurface science research, DOE/ER-0547T, U.S. Department of Energy, Office of Energy Research, Washington, D.C.

50. Rittman, B. 1993. The significance of biofilm in porous media. *Water Resources Research*. 29(7): 2195-2202.

51. Rochelle, G. 2009. Amine Scrubbing for CO_2 Capture. *Science*. 325: 1652-1654.

52. Rodriguez-Navarro, C. and Sebastian, E. 1996. Role of particulate matter from vehicle exhaust on porous building stones (limestone) sulfation *Science of the Total Environment.* 187: 79-91.

53. Sahimi, M. 1993. Flow phenomena in rocks: from continuum models to fractals, percolation, cellular automata, and simulated annealing. *Reviews of Modern Physics*, 65 (4).

54. Sawada, K. 1998. Mechanisms of crystal growth of ionic crystals in solution. Formation, transformation, and growth inhibition of calcium carbonates. Crystallization Processes. Vol. 3: 39-68. John Wiley & Sons.

55. Schindler, P.W. 1967. In *Equilibrium Concepts in Natural Water Systems, Adv. Chem. Ser., No. 67;* American Chemical Society: Washington, DC, p 196.

56. Scottish Center for Carbon Storage. 2009. CCS World Map. Edinburgh. www.futuregenalliance.org. Accessed November, 2009.

57. Seifert, D. and Engesgaard, P. 2007. Use of tracer tests to investigate changes in flow and transport properties due to bioclogging of porous media. *Journal of Contaminant Hydrology*. 93: 58-71.

58. Seki, K., Miyazaki, T., Nakano, M. 1996. Reduction of hydraulic conductivity due to microbial effects. *Trans. JSIDRA*. 181: 137-144.

59. Seki, K., Miyazaki, T., Nakano, M. 1998. Effects of microorganisms on hydraulic conductivity decrease in infiltration. *Eur. J. Soil Sci.* 49: 231-236.

60. Seki, K., Suko, T., Miyazaki, T., 2002. Bioclogging of glass beads by bacteria and fungi. 17th WCSS, 14-21 August 2002. Thailand. Symposium No. 51, Paper 1244.

61. Sharp, R.R., Cunningham, A.B., Komlos, J., and Billmayer, J. 1999. Observation of thick biofilm accumulation and structure in porous media and corresponding hydrodynamic and mass transfer effects. *Water Science and Technology.* 39: 195-201.

62. Sommerdijk, Nico A. J. M., de With, G. 2008. Biomimetic $CaCO_3$ Mineralization using Designer Molecules and Interfaces. *Chemical Reviews*. 108(11): 4499-4550.

63. Stumm, W. and Morgan, J.J. 1996. Aquatic Chemistry, John Wiley & Sons: New York. 1022.

64. Tartakovsky, A., Redden, G., Lichtner, P.C., Scheibe, T.D., Meakin, P. 2008. Mixing-induced precipitation: Experimental study and multiscale numerical analysis. *Water Resources Research*. Vol 44: W06S04.

65. Taylor, S.W. and Jaffe, P.R. 1990. Biofilm growth and the related changes in the physical properties of a porous medium. *Water Resour. Res*. 26: 2153-2159.

66. Teng, H., Dove, P., De Yoreo, J. 2000. Kinetics of calcite growth: surface processes and relationships to macroscopic rate laws. *Geochimica et Cosmochima Acta*. 64(13): 2255-2266.

67. The Engineering Toolbox. http://www.engineeringtoolbox.com/darcy-weisbach-equation-d_646.html. Accessed December, 2009.

68. Thomas, J.M., Lee, M. D., Ward, C.H. 1987. Use of groundwater in assessment of biodegradation potential in the subsurface. *Environ. Toxicol. Chem.* 6 (8): 607-614.

69. Thullner, M., Zeyer, J., Kinzelbach, W. 2002. Influence of microbial growth on hydraulic properties of pore networks. *Transp. Porous Media*. 49: 99-122.

70. Thullner, M., Scroth, M.H., Zeyer, J., and Kinzelhach, W. 2004. Modeling of a microbial growth experiment with bioclogging in a two-dimensional saturated porous media flow field. *J. Contam. Hydrol.* 70(1-2): 37-62.

71. Tiano. P., Biagiotti, L., and Mastromei, G. 1999. Bacterial bio-mediated calcite precipitation for monumental stones conservation: methods of evaluation. *Journal of Microbiological Methods.* 36:139-145.

72. U.S. Environmental Protection Agency. 2002. *EPA Facts about Strontium-90*. U.S. EPA. Washington, DC.

73. Vandevivere, P., Bavaye, P. 1992. Effect of bacterial extracellular polymers on the saturated hydraulic conductivity of sand columns. *Appl. Environ. Microbiol*. 58: 1690-1698.

74. Viamajala, S., Peyton, B., Gerlach, R.,Vaideeswaran, S., Apel, W., Petersen, J. 2008. Permeable Reactive Biobarriers for In Situ Cr(VI) Reduction: Bench Scale Tests Using *Cellulomonas* sp. Strain ES6. *Biotechnology and Bioengineering*. Vol. 101(6): 1150-1162.

75. Wanner, A. and Gujer, W. 1986. A Multispecies Biofilm Model. *Biotechnology and Bioengineering.* Vol. 27: 314-328.

76. Warren, L.A., Maurice, P.A., Parmar, N., and Ferris, F.G. 2001. Microbially mediated calcium carbonate precipitation: Implications for interpreting calcite precipitation and for solid-phase capture of inorganic contaminants. *Geomicrobiology Journal*. 18: 93-115.

77. Whiffin, V.A., van Paassen, L. A., and Harkes M. P. 2007. Microbial carbonate precipitation as a soil improvement technique. *Geomicrobiology Journal*. 24(5): 417-423.

78. Whiffin, V. 2004. Microbial $CaCO_3$ Precipitation for the production of Biocement, Ph.D. thesis, School of Biological Sciences & Biotechnologies, Murdoch University, Australia.

79. Willingham, T., Werth, C., and Valocchi, A. 2008. Evaluation of the Effects of Porous Media Structure on Mixing-Controlled Reactions Using Pore-Scale Modeling and Micromodel Experiments. *Environ. Sci. Technol.* 42: 3185-3193.

APPENDICES

APPENDIX A

HIGH PRESSURE FLOW PRECIPITATION

To assess precipitation at high temperature and pressure levels which may exist in subsurface atmospheres where proposed technologies are directed, a high pressure flow system was utilized. The system, which was designed primarily by Adie Phillips, Randy Hiebert, Robin Gerlach, and Al Cunningham, is outlined in Figure A.1 below:

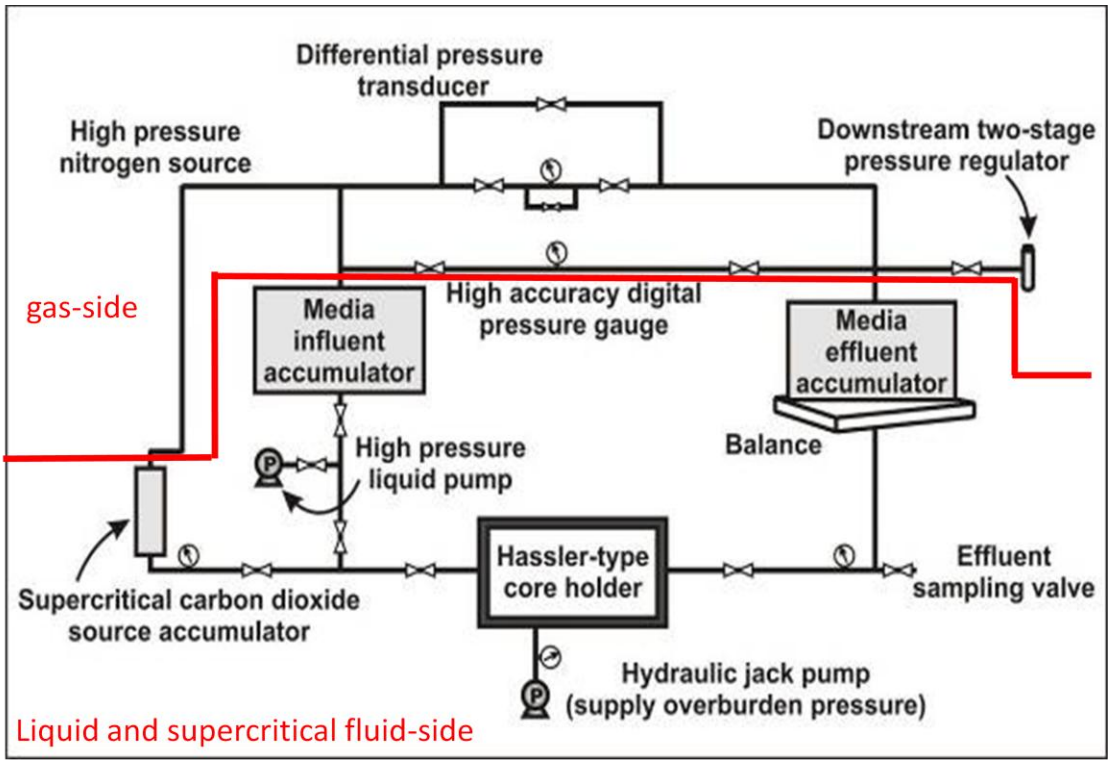

Figure A.1. Schematic of high pressure core system. Flow proceeds from left to right and is powered by a pressure differential that is generated from overburden high pressure nitrogen gas.

A biomineralization experiment in this system was primarily conducted by Andy Mitchell. In this experiment, media was pulsed through a core, which included six 1mm diameter glass tubes simulating pores (see Figure A.2)

Figure A.2. Image of Hassler-type core holder. The black sleeve, which contains the white core inside, has an overburden pressure of mineral oil that was compressed with a hydraulic jack pump. The white core contains six glass tubes (1mm i.d.) simulating pores.

General findings were that ureolytic calcite precipitation occurred at 35□ C and pressures above the supercritical pressure of CO_2. Effluent samples indicated that ureolysis occurred (pH and ammonium increase, calcium decrease). My responsibilities in this study included effluent sampling near the end of the experiment and imaging of the capillaries. The images, which show precipitation in the pore space, are included in Figure A.3.

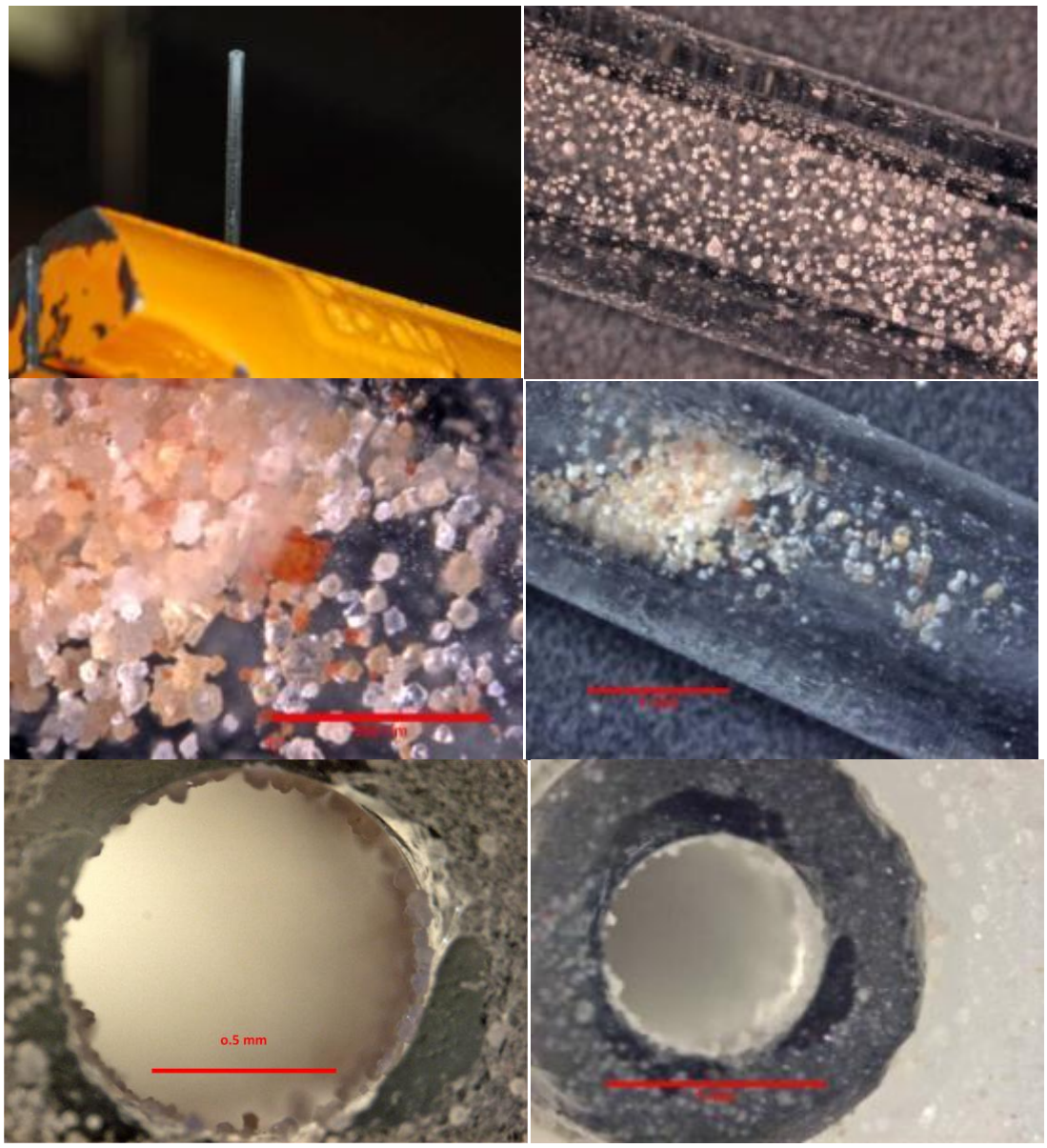

Figure A.3. Selected images of capillaries that were removed from the high pressure test core. High pressure precipitation occurred, which is clearly evident on the inside walls of the capillaries

APPENDIX B.1

HIGH PRESSURE VESSEL

Due to the experimental difficulties associated with running high pressure experiments under flow conditions, but the necessity to address these processes at high temperature, pressure, and exposure to super critical CO_2, a high pressure vessel was used for several experiments. This vessel was designed by Montana State University students Aaron Rhodes, Loren Kairis, and Jordan Ornquist. An image of the system, contained in an incubator, is shown in Figure B.1.1, and a schematic is shown in Figure B.1.2.

Figure B.1.1. Image of high pressure vessel system contained in an incubator. A piston accumulator is behind the right door.

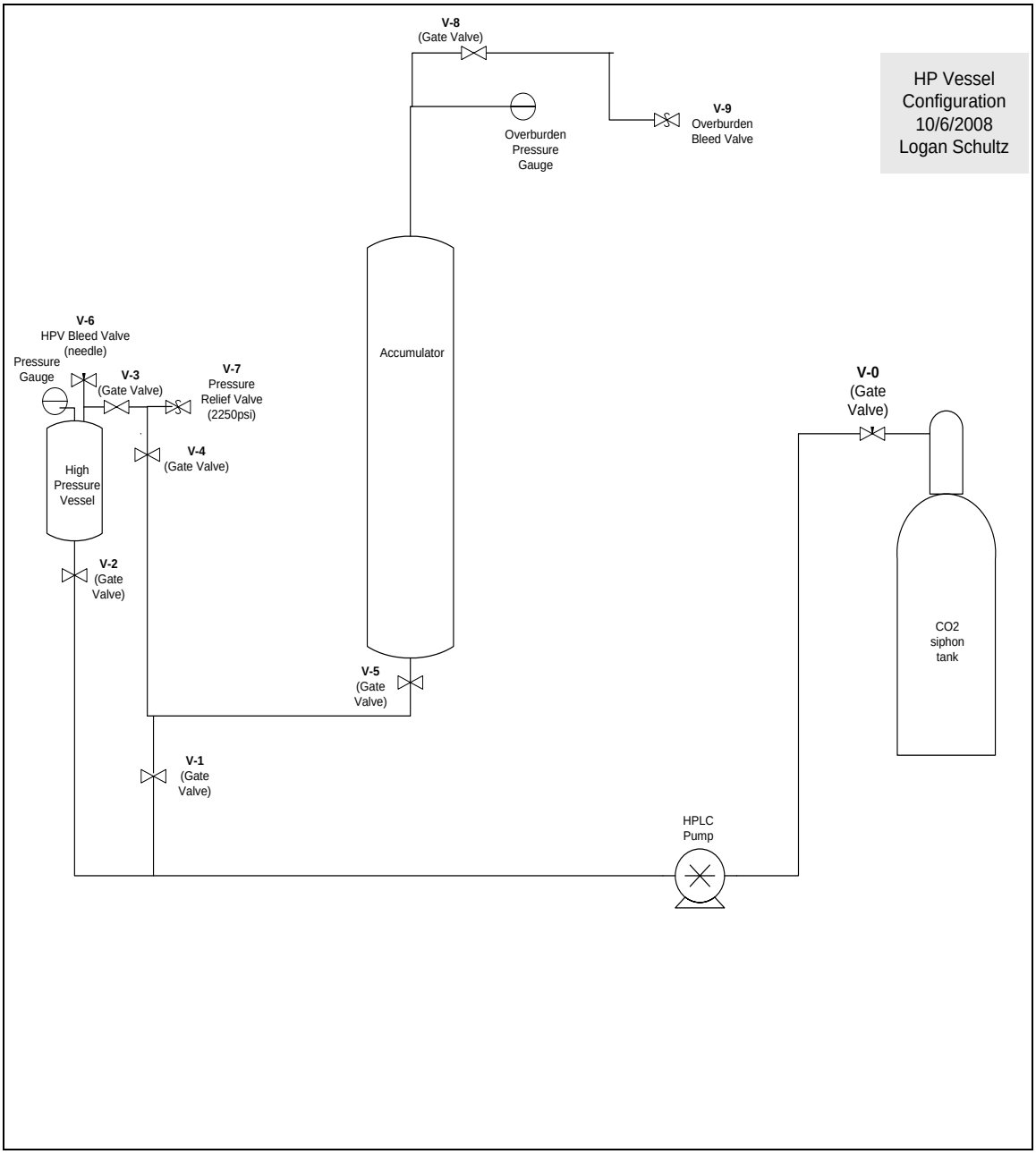

Figure B.1.2. Schematic of high pressure vessel system used to expose various components to high temperature, pressure, and $scCO_2$. A key aspect of this system is the ability to prevent phase transitions in the vessel when assessing the exposure to $scCO_2$. To do this, a regulated overburden nitrogen pressure is set beyond the critical pressure (72.9 bar). With valves V-1, V-4, and V-5 open, liquid CO_2 is pumped from the siphon tank into the 1L piston accumulator contained in an incubator. V-1 is then closed and sufficient time must be allowed to increase the CO_2 temperature beyond the critical point (32.7 C). Finally, valve V-2 is opened, and the $scCO_2$ is instantly delivered into the high pressure vessel where the contents may be exposed.

APPENDIX B.2

ABIOTIC EFFECTS OF PRESSURE ON MEDIA CHEMISTRY

A test was conducted to assess abiotic effects of high pressure on media chemistry. The media previously used by Ferris and Stehmeier (1996) was assessed. The goal was to determine whether any processes would occur as a result of exposure to high pressure that would affect the concentration of calcium or ammonium in the solution. The experimental protocol for the test that was conducted is as follows:

1. Prepare 1L each of filter-sterilized CMM+ and CMM- media
2. Pipette 5ml of each media into 2 vials, labeled as follows:
    a. Ca- (CMM- media, never to be pressurized)
    b. Ca+ (CMM+ media, never to be pressurized)
    c. Ca-P (CMM- media, to be pressurized)
    d. Ca+P (CMM+ media, to be pressurized)
3. For Ca-P and Ca+P vials, carry out the following pressurization method:
    a. Insert vials into HP vessel
    b. Seal vessel and connect to high pressure nitrogen gas source
    c. Pressurize to a final pressure of 1300 psi
    d. Allow vessel to remain pressurized for Overnight
    e. Depressurize
    f. Remove vials from HP vessel
4. For all 4 vials, carry out the following sampling procedure:
    a. If any crystallization or other effects are evident, photograph and document in writing
    b. Pipette 1ml of sample into a microcentrifuge tube for Ph test
    c. Filter sterilize sample into disposable centrifuge tube
        i. Prepare standard dilutions for Nessler Assay (NH4+), according to the protocol described in Appendix E.
            1. Pipette 100ul into 900ul (1:10 dilution)
            2. Continue dilution until 1:1000
            3. Read at 450nm on microplate reader
        ii. Pipette 100ul of filtered solution into 9900ul of 5% HNO3 for ICP-MS analysis of Ca concentration

Results of this study indicated that ammonium, calcium and Ph in the media were not significantly affected by exposure to a pressure of 1300 psi (See Table B.2.1).

Table B.2.1. Data from assessment of abiotic effects on the chemistry of the media previously used by Ferris and Stehmeier (1996).

Quantification limit			0.5	0.005	0.05	**0.05**	0.001
Sample:	Ph	NH4 (mg/L)	Sodium mg/L	Magnesium mg/L	Potassium mg/L	**Calcium mg/L**	Barium mg/L
Ca-P	7.37	3.22	6.76	0.025	1.15	**0.200**	0.001
Ca-	7.15	3.45	6.60	0.025	1.12	**0.18**	0.001
Ca+P	7.31	2.95	6.48	0.025	1.11	**9.71**	0.001
Ca+	7.25	2.35	6.49	0.025	1.06	**9.20**	0.001

APPENDIX B.3

ASSESSMENT OF BRINE, PH, AND $scCO_2$ EXPOSURE ON CALCITE

For All Studies:

- Start with sterile CDC reactor flowing CMM- media at approximately 1 ml/min (~1.5 L/day)
- Inoculate with culture of *S. pasteurii*
- 24 hours later, change media to CMM+
- 2 days later, stop flow and remove biomineralized coupons for tests

TEST 1: Effects of Brine solution and Acidic pH on attached precipitates

Weight Assessment

- Label 9 coupons (three rods)
- Place all 9 coupons in 65 °C incubator for 3 hours to dry
- Cool coupons to room temp., and weigh
    - Place 3 coupons in 100ml of appropriate NaCl solution (Brine) (30 minutes)
    - Place 3 coupons in 100ml of DI water, pH-adjusted to 4.0 with HCl (30 minutes)
    - Place 3 coupons in 100ml of DI water (30 minutes)
- Place all 9 coupons in 65 °C incubator for 3 hours to dry
- Cool coupons to room temp., and weigh, comparing to pre-exposure weight

Calcium Assessment

- Label 9 coupons (three rods)
    - Place 3 coupons in 100ml of appropriate NaCl solution (Brine)(30 minutes)
    - Place 3 coupons in 100ml of DI water, pH adjusted to 4.0 with HCl (30 minutes)
    - Place 3 coupons in 100ml of DI water (30 minutes)
- Wash all coupons in DI water
- Place each individual coupon in a 50ml of 5% HNO_3
    - Vortex to dissolve all deposits and mix well
- Measure Calcium concentration with ICP-MS

Stereoscope Assessment

- Label 6 coupons (two rods)
    - Place 2 coupons in 100ml of appropriate NaCl solution (Brine)(30 minutes)
    - Place 2 coupons in 100ml of DI water, pH adjusted to 4.0 with HCl (30 minutes)
    - Place 2 coupons in 100ml of DI water (30 minutes)

- Wash all coupons in DI water
- View under stereoscope to analyze deposits and estimate thickness

TEST 2: Effects of $scCO_2$ exposure (submerged in brine and exposed)

- Label 20 coupons
- Place 4 coupons (labeled with asterisks to denote "wt. coupons") in 65°C incubator for 3 hours
    - Cool and weigh
    - Place 2 in top tray and 2 in bottom tray (see schematic below)
- Place 4 coupons in brine at room T/P and leave 4 coupons exposed to air at room T/P (controls)
- Place 4 coupons on top rack, and 4 coupons on bottom rack
- Submerge the rack into the HPV
- Seal HPV with pipe sealant and silicone
- Expose to $scCO_2$ for 5 minutes
- De-pressurize, remove cap
- Take the 2 "wt. coupons" out of each rack and place into incubator at 65 °C for 3 hrs.
- Take 3 coupons from each rack and control and place in 50ml of 5% HNO_3
    - Vortex and measure Ca conc. by ICP-MS
- Take 1 coupon from each rack and control and analyze under stereoscope

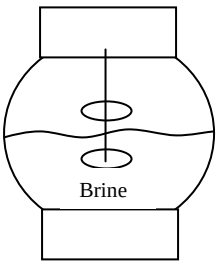

Figure B.3.1. Schematic of submerged trays in the high pressure vessel. One resides above the brine, exposed directly to $scCO_2$, and one resides in the brine.

APPENDIX B.4

RESISTIVITY OF BIOFILM TO $scCO_2$

This test was conducted to assess the resistivity of biofilm to $scCO_2$ exposure. It was planned that by cryosectioning biofilm samples with and without exposure to $scCO_2$, any decrease in thickness due to exposure could be quantified. The experimental protocol is as follows:

1. Grow biofilm with *B. Mojavensus* in a CDC reactor w/ BHI + salt media, including at least 8 coupons

   Brain Heart Infusion (BHI) + Salt medium
   [18 g L-1 BHI (Oxoid, Lenexa, KS)
   0.75 g L-l NH_4Cl
   40 g L-1 NaCl
   3 g L-1 $NaNO_3$ (Fisher, Pittsburgh, PA).
   NOTE: Grow culture until a significant biofilm has been established. The time of growth, the details of the media, reactor rpm, complete sterility, residence time, etc. are not extremely important, as long as the process yields 8 coupons with similar biofilm.

2. Cryosection 1 coupon to determine thickness of biofilm
3. Use Live/Dead (Invitrogen ®) fluorescent stains to stain 3 coupons
   a. View under the confocal microscope and take spatial series in order to provide a thickness and topography assessment
4. Place all 7 remaining coupons in a small plastic petri dish. Cover petri dish with aluminum foil to prevent direct impact of CO_2 injection.
5. Place petri dish in HPV with the pressure gauge removed from the top (HPV will be in incubator at 33□ C to confirm the temperature exceeds the critical temp. of 31.5 °C).
6. Using High pressure pump, charge accumulator with CO_2 and pressurize to 2000 psi (sufficiently higher than targeted vessel pressure, to accommodate a volume expansion)
7. Release some CO_2 from the accumulator in order to flush out the air from the HPV
8. Replace the pressure gauge on top of the HPV
9. Pressurize HPV to a pressure of 1200 psi
10. Allow vessel to remain pressurized for two hours
11. Depressurize vessel and remove coupons
12. Cryosection 1 coupon to determine thickness of biofilm (post exposure)
13. Use Live/Dead (Invitrogen®) fluorescent stains to stain the unstained 3 coupons

a. View all 6 stained coupons under the confocal microscope and take a spatial series

Data analysis

- Utilizing Imaris and Metamorph software, construct a three dimensional representation of each biofilm
- Document topographical and hydration differences between the pressurized and non-pressurized coupons, and conduct quantitative analysis to determine the thickness of the biofilms

While conducting this experiment, the first discovery was that the polycarbononate petri dish used to hold the suspended coupons was permanently deformed due to the solvent capabilities of $scCO_2$ (see Figures B.4.1 and B.4.2 below)

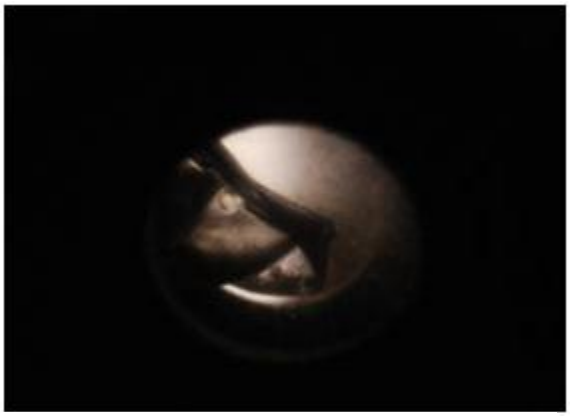

Figure B.4.1. Image taken through the sight glass of the HPV, showing the deformed petri dish.

Figure B.4.2. Image of removed petri dishes that have been deformed by exposure to $scCO_2$

The system was redesigned to incorporate aluminum trays. These trays can be viewed through the sight glass of the system in Figure B.4.3 below:

Figure B.4.3. Image of high pressure vessel, showing suspended aluminum trays inside.

Results of this showed that biofilm was significantly dried by exposure. Cryosectioning and confocal microscopy were not conducted due the extent of detriment and dehydration to the biofilm. This may or may not be the case if this experiment was conducted with the coupons submerged in brine simulating a deep subsurface aquifer.

APPENDIX C

CO_2 PHASE AND DENSITY DIAGRAM

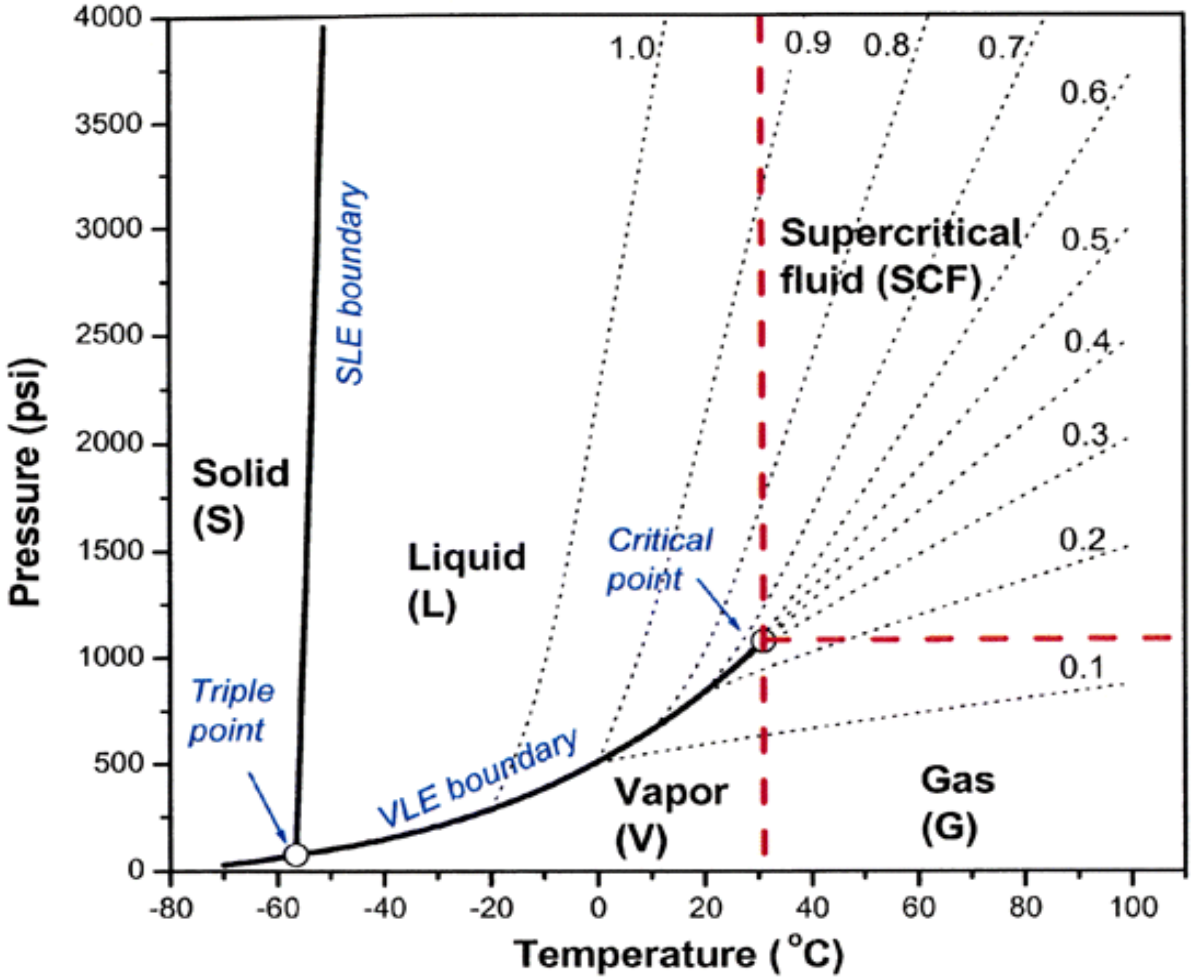

Figure C.1. Pressure and temperature phase diagram for carbon dioxide (http://www.eco2technologies.com.au/). The critical point is at 31 °C and 1070 psi. The dotted lines represent constant density lines (g/cm^3).

APPENDIX D

ANALYSIS OF BIOMINERALIZATION WITH MRM

To analyze biomineralization with magnetic resonance microscopy (MRM), an experiment was conducted by Einar Fridjonsson. The media described by Ferris and Stehmeier (1996) was used, and the reactor was a glass column with a 1cm diameter that was filled with 242µm (diameter) beads. The reactor was placed inside the MRM magnet during the experiment. Overall results showed calcite mineralization and the ability of MRM to successfully distinguish calcite at the interior of the reactor, where optical limitations prevent other means of imaging.

My responsibilities included experimental design, preparation of the flow media, culturing of the bacteria, and imaging of the reactor after being removed from the MRM. A few selected images of the beads, showing precipitation, are as follows:

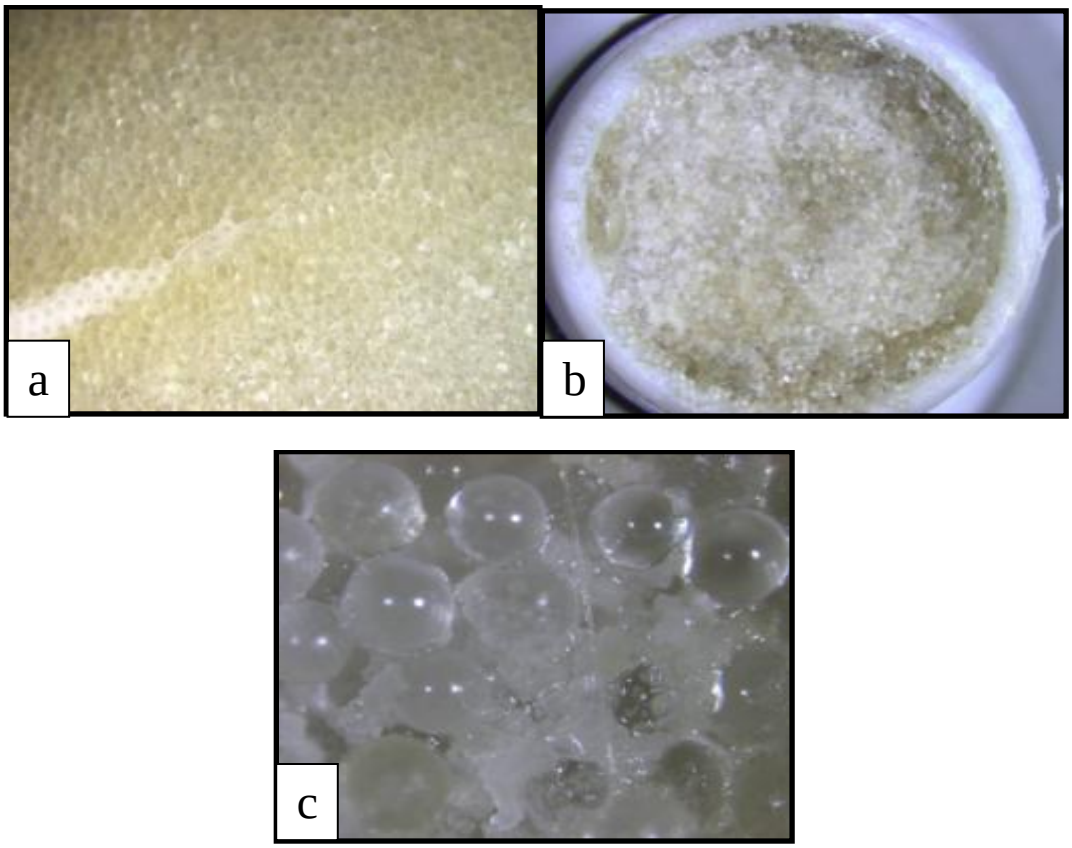

Figure D.1. Selected stereoscope images of biomineralization on beads after the experiment.

To look at bacteria attached to the surface of the beads, some beads were stained with propidum iodide and SYTO 9 (Invitrogen Live/Dead ®) and viewed under a Nikon Eclipse E800 microscope. Two of those images are shown in Figure D.2:

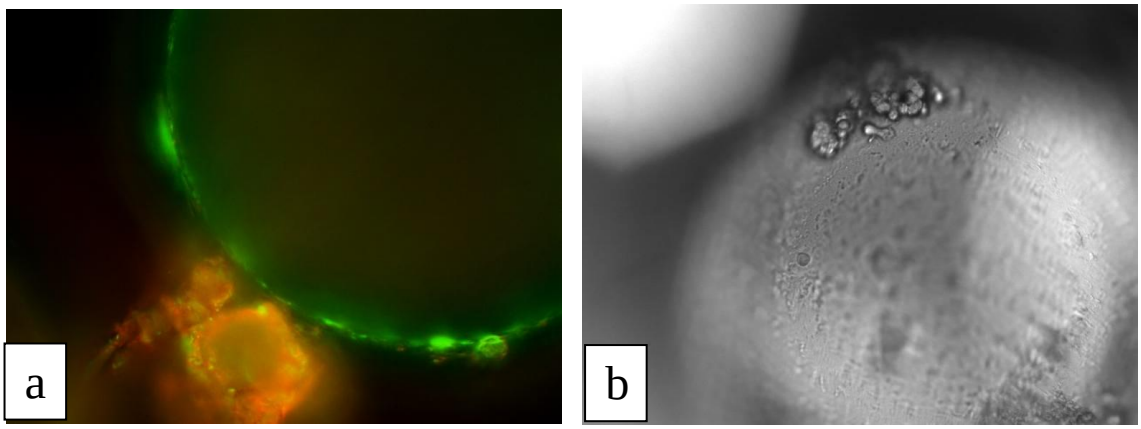

Figure D.2. Selected images of calcite and bacteria attached to the surface of the beads.

This study was summarized in a manuscript that was submitted to the Journal of Contaminant Hydrology. This manuscript is included in the following pages:

This manuscript titled 'NMR Measurement of Hydrodynamic Dispersion in Porous Media Subject to Biomediated Reactive Precipitation Flow', was submitted to the Journal of Contaminant Hydrology on December 8, 2009

Authors

Joseph D. Seymour*[a,b], Einar O. Fridjonsson[a], Logan N. Schultz[a,b], Robin Gerlach[a,b], Al B. Cunningham[b] and Sarah L. Codd[b,c]

[a] *Department of Chemical and Biological Engineering*

[b] *Center for Biofilm Engineering*

[c] *Department of Mechanical and Industrial Engineering*

Montana State University

Bozeman MT 59717-3920

*Corresponding author jseymour@coe.montana.edu

Abstract

Noninvasive measurements of hydrodynamic dispersion by nuclear magnetic resonance (NMR) are made in a model porous system before and after a biologically mediated precipitation reaction. The impact of the precipitation reaction on the pore scale dynamics over a range of displacement length and time scales is determined. The dynamics indicate an increased pore scale mixing which alters the preasymptotic approach to asymptotic Gaussian dynamics governed by a normal advection diffusion equation.

Introduction

Reactive transport in porous media is an important problem in understanding the spread of contaminants in the Earth's subsurface. Precipitation reaction phenomena are important in transport processes of transuranic environmental contaminant species (Kersting et al., 1999; Nagy et al., 1991), while dissolution reactions may play a significant role in supercritical fluid transport for carbon sequestration (Kaszuba et al., 2005). Precipitation and dissolution reactions during flow of fluids in porous media represent a particular level of complexity for transport modeling, due to the evolution of the pore structure due to reaction, altering flow dynamics (Emmanuel and Berkowitz, 2005; Emmanuel and Berkowitz, 2007; Sahimi et al., 1990; Tartakovsky et al., 2007). Models for these types of systems are often categorized as either continuum or statistical and a broad range of approaches exist (Sahimi et al., 1990). While many methods to model these reactive transport processes in porous media have been developed, data on the alteration of pore scale dynamics due to pore structure altering reactions are limited.

Nuclear magnetic resonance (NMR) methods have proven to provide unique data on displacement length and timescale dynamics of hydrodynamic dispersion for flow in three dimensional (3D) porous media (Brosten et al., 2009; Lebon et al., 1996; Manz et al., 1999; Scheven et al., 2007; Seymour and Callaghan, 1997). Another class of pore structure evolving reactions in porous media (Clement et al., 1996; Thullner and Baveye, 2008) to which NMR has been applied is biofouling, *i.e*. biomass generating reactive flows. NMR data have characterized the interaction between pore structure evolution due to biomass growth and the pore dynamics of hydrodynamic dispersion (Graf von der Schulenberg et al., 2008; Seymour et al., 2004; Seymour et al., 2007). In particular NMR has provided data indicating the transition from normal diffusive transport to anomalous diffusive transport due to the alteration of the pore structure by biomass growth from homogeneous to heterogeneous (Seymour et al., 2004; Seymour et al., 2007). In this paper NMR measurements of the hydrodynamic dispersion in a model porous structure before and after a biofilm mediated precipitation reaction are presented.

Theory

Hydrodynamic Dispersion

Due to the extensive nature of the literature on reactive transport and hydrodynamic dispersion models for porous media, a limited discussion of the applicable theory is provided only to lend context to the discussion of the NMR data. Models are often delineated into categories as statistical or continuum based (Sahimi et al., 1990). This demarcation is somewhat artificial due to the fact that the advection diffusion equation (ADE) can be derived from concepts of statistical mechanics (Mazo, 1967) and continuum mechanics (Bird et al., 1960). The ADE

$$\frac{\partial P(Z,t)}{\partial t} = \left[-\langle v_z \rangle \frac{\partial}{\partial Z} + D^* \frac{\partial^2}{\partial Z^2} \right] P(Z,t) + R \qquad \text{(D.1)}$$

gives the time rate of change of probability $P(Z,t)$, or normalized concentration, due to advection by a mean flow $\langle v_z \rangle$ and diffusion due to hydrodynamic dispersion D^*. The appropriate form of the reactive source/sink term R in Eqn. (D.1) for reactive flows is an area of intense research interest (Emmanuel and Berkowitz, 2005; Emmanuel and Berkowitz, 2007; Tartakovsky et al., 2007). However, as discussed below, the NMR data we acquire compares the hydrodynamic dispersion dynamics before and after a pore structure altering reaction event, so our primary interest is in the dynamics not the reaction rate behavior of R.

The ADE generates a normal diffusion process in which the dynamics are Gaussian in the long time limit relative to mixing over many pore lengths. The preasymptotic dynamics reflect the process of the decay of correlation of dynamics due to fluctuations in velocity by mechanical streamline mixing, diffusion across streamlines and hold up in dead end pores (Salles et al., 1993). The pore structure of the porous

media determines the impact of the different dispersion mechanisms and controls the approach of the dynamics to the asymptotic Gaussian behavior. Nonequilibrium statistical mechanics models based on memory function equations (Boon and Yip, 1991) for the time and length scale dependence of preasymptotic dynamics have been developed (Cushman et al., 1994). In heterogeneous pore structure media, where non Gaussian anomalous diffusion scale dependent transport is present for asymptotic times, continuous time random walk (CTRW) models (Berkowitz et al., 2006) and non-local continuum approaches (Koch and Brady, 1988) result in fractional advection diffusion equations (FADE) (Cushman and Ginn, 2000). The applicability of such models to reactive systems with pore evolution and to model preasymptotic dynamics variations during reaction is an open question.

NMR measurement of dispersion

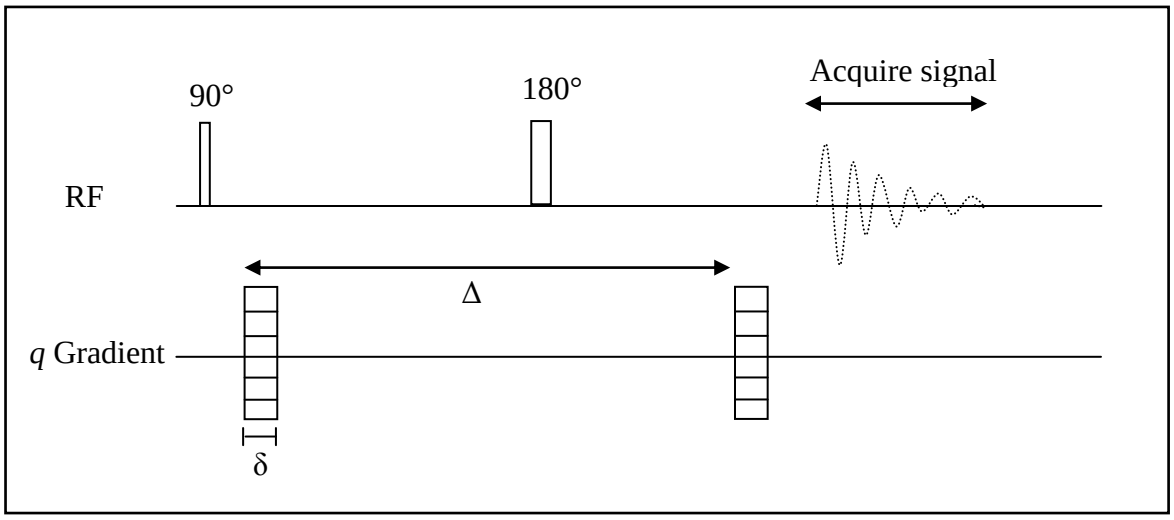

Figure D.3. Pulsed gradient spin echo (PGSE) NMR pulse sequence used to generate propagators of motion over a range of displacement lengths reciprocal to the experimentally incremented wave vector $q = (2\pi)^{-1}\ \gamma g \delta$ and displacement observation time Δ.

NMR provides unique data on transport in porous media due to the ability to noninvasively resolve dynamics within the pore structure. The measurement of dynamics as a function of varying displacement length and time generates data on a hierarchy of displacement scales. The acquired NMR signal using a standard pulsed gradient spin echo (PGSE) method shown in Figure D.3 is encoded in the experimental Fourier domain reciprocal to displacement in terms of the wave vector $q = (2\pi)^{-1}\ \gamma g \delta$ and the displacement observation time Δ (Blümich, 2000; Callaghan, 1991). The voltage signal is given by

$$E(q,\Delta) = S(q,\Delta)/S(q=0,\Delta) = \int P(Z,\Delta)\exp[i2\pi qZ]\mathrm{d}Z\,. \qquad \text{(D.2)}$$

where $Z = z'(\Delta)-z(0)$ is the displacement the NMR active nuclei, or spins, and $P(Z,\Delta)=\int \rho(x,y,z)P_s(z,0|z',\Delta)dxdydz$ is the averaged propagator. There is a Fourier transform relationship between the echo signal $E(q,\Delta)$ acquired by incrementing the gradient amplitude g applied for time δ and the average propagator. The averaged propagator, or van Hove self-correlation function (Boon and Yip, 1991), is the conditional probability $P_S(z,0|z',\Delta)$ that a spin residing at z at time 0 moves to z' at time Δ averaged over the initial spin distribution $\rho(x,y,z)$ (Callaghan, 1991). Complete details of the dynamics are contained within the propagator for all displacement scales sampled by q.

The ability to spatially resolve systems using NMR imaging (MRI) techniques provides the means to vary spatial averaging scales. MRI has limited spatial resolution since NMR is an inherently low signal to noise technique based on the small differences in energy state populations of the spins. The strength of the method is the ability to probe the impact of coarse graining space on measured translational and rotational molecular dynamics. The important point is that as stated above, the pore scale dynamics induced by the structure of the porous media is contained within the scale dependent dynamics measured by the propagator without the use of imaging methods (Callaghan, 1991; Callaghan et al., 1991; Seymour and Callaghan, 1997). The characterization of the pore scale dynamics without imaging is important due to the limited spatial resolution of MRI to about $(20\ \mu m)^3$ under ideal conditions in a porous column of size of the order of 10 mm. Typical spatial resolutions are of the order of $(40\ \mu m)^2$ over a slice thickness of order 100 μm which generates averaging of dynamics over scales that can obscure pore scale information. Rapid MRI velocity methods capable of acquiring spatial distributions of velocity on times of the order of 50 ms have potential to provide data on variations in flow as reaction are occurring (Kose, 1994; Sederman et al., 2004). These methods are limited to spatial resolutions greater than $(100\ \mu m)^3$ due to signal to noise considerations, rendering them ineffective at measuring pore scale dynamics.

Experimental Details

Model Bead Pack and Microbiology

A 10 mm I.D. and 30 mm length liquid chromatography column (Omnifit) with a frit at the entrance and 220 μm mesh at the exit was packed with $d_p = 241$ μm diameter monodisperse polystyrene beads (Duke Scientific 4324A). After assembly the porosity was measured to be $\phi = 0.41$ by analyzing NMR images of the bead pack and confirmed by the measurements of the mean velocity inside the bead pack and total volumetric flow rate through the bead pack. Experiments utilized a dual syringe HPLC pump (Pharmacia P-500) which allows controlled volumetric flow rates. DI water, media without and with calcium was flowed through the bead pack against gravity to a reservoir above the sample height. The DI water was doped with Magnevist to allow for a shortened NMR

experimental repetition time T_R this was unnecessary for the medium with and without calcium as the salts and sugars reduce the spin-lattice T_1 magnetic relaxation time. NMR measurements were conducted for the flow of these three fluids through the clean bead pack (CBP) to acquire baseline results for later comparison with the inoculated and precipitated bead pack (IBP).

For the bacterial experiments, the column was inoculated with an ureolytic culture of *Sporosarcina pasteurii* (formerly classified as *Bacillus pasteurii*) in a growth medium (Ferris and Stehmeier, 1996). The medium includes 3 g/L nutrient broth (Becton, Dickinson and Company), 20 g/L urea (Fisher Scientific), 10 g/L ammonium chloride (Fisher Scientific), and 2.1 g/L sodium bicarbonate (Fisher Scientific). Calcium chloride dehydrate (Acros Organics) is added to the medium at a concentration of 3.7 g/L in order to generate media with sufficiently high calcium concentration for precipitation to occur. In the process of bacterially facilitated urea hydrolysis (ureolysis), the production of ammonium and dissolved inorganic carbon during decomposition of urea by the bacteria increases the solution Ph and carbonate concentration, which increases the saturation state and favors calcium carbonate precipitation in a calcium-rich environment. The reaction mechanism is illustrated in the following equations (Ferris et al., 2003):

$CO(NH_2)_2 + H_2O \rightarrow NH_2COOH + NH_3 \rightarrow 2\ NH_3 + CO_2$ (D.3) (Urea hydrolysis)

$2NH_3 + 2H_2O \leftrightarrow 2NH_4^+ + 2OH^-$ (D.4) (Ph increase)

$CO_2 + 2\ OH^- \leftrightarrow CO_3^{2-} + H_2O$ (D.5) (Carbonate formation)

$CO_3^{2-} + Ca^{2+} \leftrightarrow CaCO_{3\ (solid)}$ (D.6) (Precipitation)

While the hydrodynamic alterations resulting from calcium carbonate precipitation in the porous media were of primary interest in this experiment work is ongoing to further correlate the reaction kinetics to the changes in hydrodynamics.

MR Experiments

The bead pack was secured in a 20mm ID radio frequency (rf) coil and placed inside a 300 MHz vertical standard bore superconducting magnet. A Bruker Avance III spectrometer was networked to the superconducting magnet. A Bruker Micro2.5 microimaging probe and gradient amplifiers were used which allowed imaging using gradients up to 1.48 T/m in all three directions. PGSE experiments were conducted to acquire propagator data on the probability of spin displacement and q-space data to measure any diffraction effects. Additionally, standard imaging sequences were used to acquire images through the whole bead pack and T_2 maps of slices through the bead pack. The experimental parameters for these different experiments are listed below:
PGSE experiments: acq-pts = 512, q-pts = 130, slice thickness: 1mm, T_R = 2sec, δ = 2 ms, Δ = [25, 50, …, 600]ms, g_{max} = 0.19-1.04 T/m, SW = 50kHz, N_A = 8. Experimental time = 35min.

T_2 imaging experiments: pixels = 256x256, FOV = 11x11mm^2, Voxel resolution: 43x43x2000 μm^3, T_E = [10, 20, …160]ms, T_R = 1sec, SW = 50kHz, N_A = 8, Experimental time = 34min.
NMR imaging experiments (5 slices): pixels = 256x256, FOV = 30x11mm^2, voxel resolution: 117x43x2000 μm^3, T_E = 14ms, T_R = 1sec, SW = 50kHz, N_A = 1, Experimental time = 4min.

After NMR experiments had been conducted on the clean bead pack (CBP), the column was inoculated with 6.5 Ml of medium with *Sporosarcina pasteurii* by adding it at the top of the column and reversing flow through the column at 10Ml/hr. The 159noculums was allowed to sit for 60 minutes to allow for bacterial attachment, before a flow of 400Ml/hr of media without calcium was run for 60 minutes and then intermittently stopped and flowed for next 2 hours while MRI data were taken. Approximately 4 hours after inoculation of the bead pack, media with calcium was pumped through the bead pack at 400Ml/hr for 10minutes. PGSE NMR and MRI experiments were conducted. Additional injection of media with calcium was done after about 5 hours of NMR experiments. Between NMR experiments a flow calcium free media at 10Ml/hr was used to maintain nutrient supply for bacterial growth. All PGSE NMR experiments were conducted at a flow rate of 400 Ml/hr. The ureolytic activity of the bacteria was assessed by acquiring fluid samples at the exit of the magnet and measuring the Ph value as a function of flow rate.

Results

Optical Images and MRI

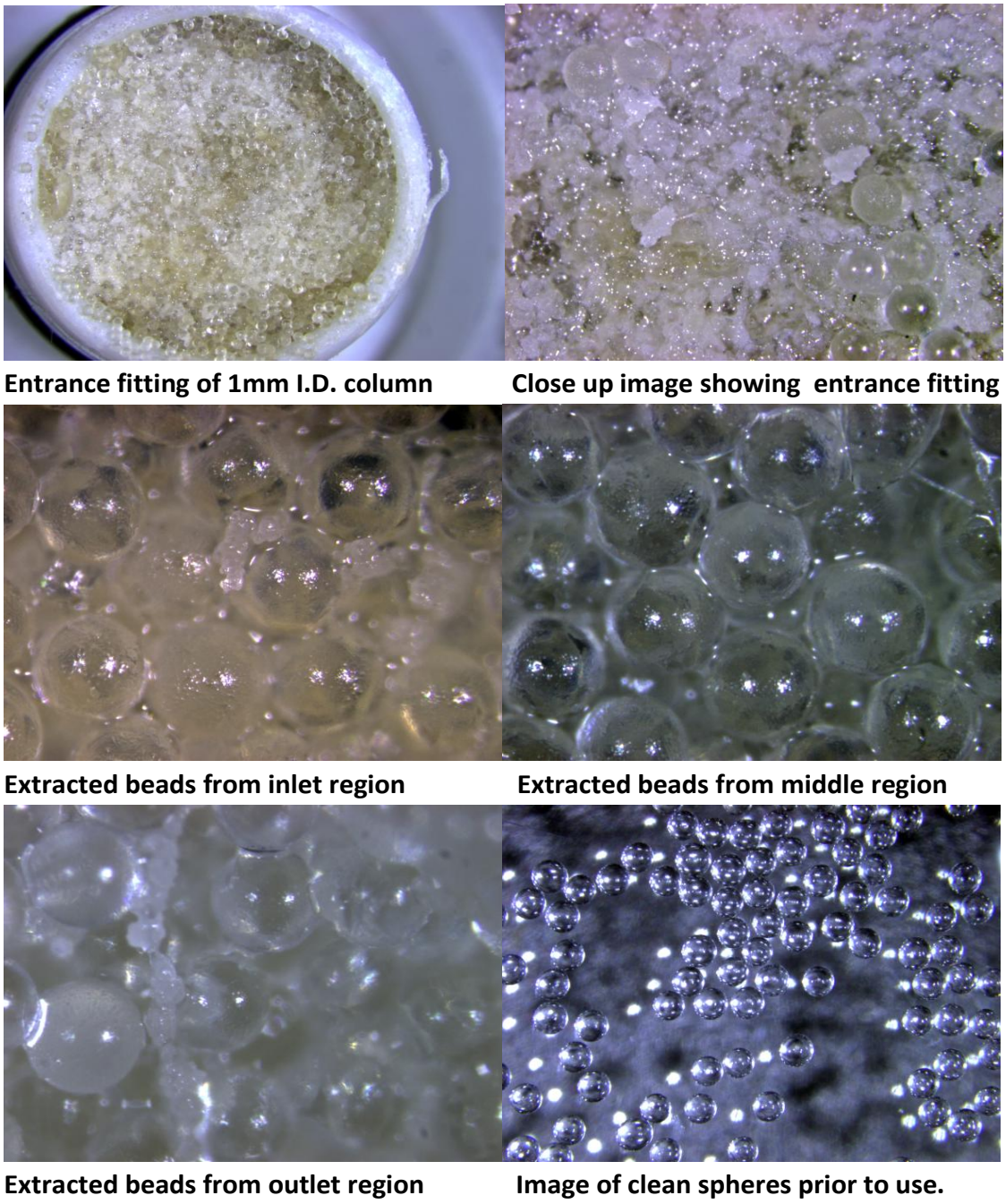

Figure D.4 Selected stereo microscope (Nikon SMZ1500) images of beads from different regions of the porous media column showing the deposition of biomass and precipitate. The diameter of each bead is 241µm, providing a scale for each image.

Stereo microscope (Nikon SMZ1500) optical images of the beads extracted from various locations in the packed column after the experimental run are shown in Figure D.4. The images indicate an axial variation in the amount of precipitate and biomass. The entrance fitting shows significant deposition. The bottom of the column, the flow inlet region, and the top flow outlet of the column appear similar while the middle region where the PGSE NMR measurements are localized has slightly less precipitate and biomass. Figure D.5 shows a stereo microscope image of a single sphere in which a deposition layer is apparent on the sphere surface.

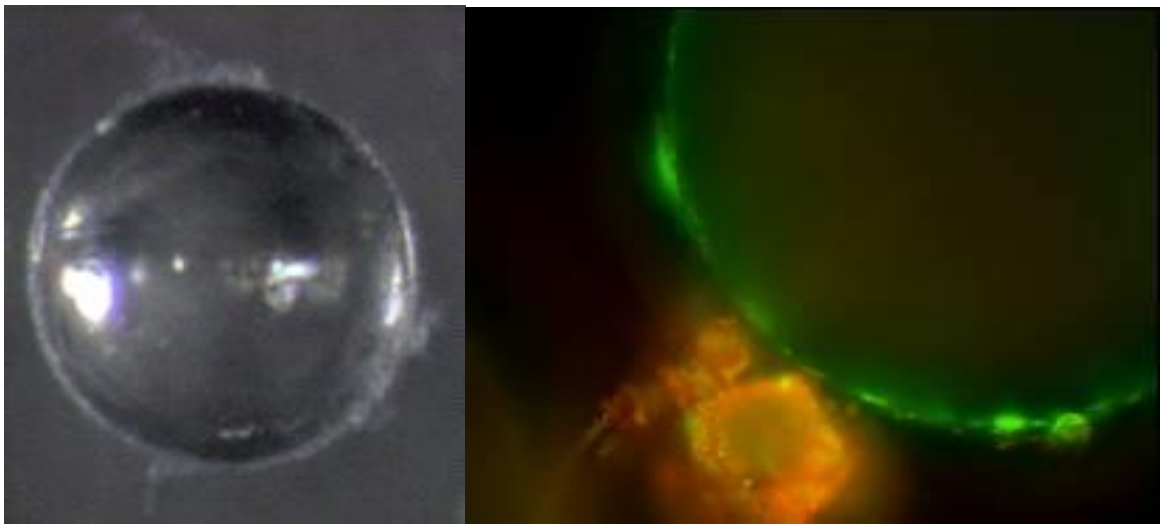

Figure D.5 A stereo microscope image (left) of biomass attached to a 241μm diameter sphere that was extracted from the column. This bead was gently treated with 10% nitric acid (HNO_3) to dissolve the precipitates and visualize only attached biomass. A fluorescent microscope image (Nikon Eclipse E800, 40x objective) (right) of an extracted sample that was stained with Syto 9 and Propidium iodide (Invitrogen LIVE/DEAD®). Syto 9 (green) highlights the bacteria with intact cellular membranes, which appear to be at a higher density surrounding the bead. Propidium iodide (red) highlights cells with compromised membranes. A precipitate crystal is highlighted by the propidium iodide. This is due to either a higher density of cells with compromised membranes surrounding the precipitate and/or staining of the organic matrix associated with the calcium carbonate by the propidium iodide.

A fluorescent microscope image indicates the deposition material in the images of Fig. D.4 is composed of attached biomass, stained green and $CaCO_3$ precipitate crystals, visible in orange/red. The microscope images in Figs. D.4 and D.5 indicate the deposition of precipitate and biomass in pores between spheres as well as fairly uniform coating around the spheres. Interestingly T_2 spin-spin magnetic relaxation maps (Blümich, 2000; Callaghan, 1991) in Fig. D.6 show little or no impact from the precipitate and biomass.

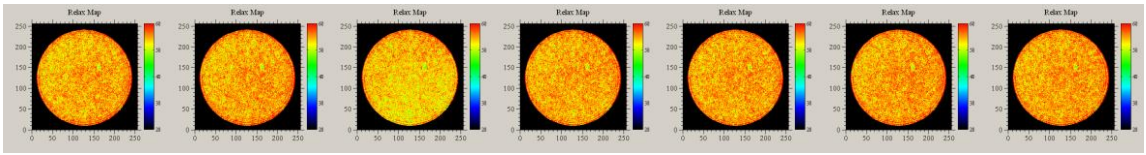

M: 54.8618	M: 55.0537	M: 53.9429	M: 55.0319	M: 55.1354	M: 55.2722	M: 55.2126
SD: 2.7770	SD: 2.7907	SD: 2.6878	SD: 2.7272	SD: 2.7467	SD: 2.7496	SD: 2.7790
T = 0min	**T = 33min**	**T = 66min**	**T = 98min**	**T = 130min**	**T = 163min**	**T = 195min**

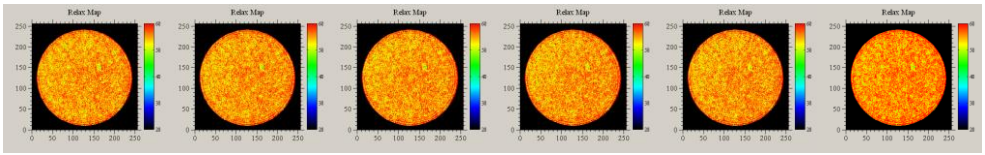

M: 55.3211	M: 55.4209	M: 55.4181	M: 55.4506	M: 55.4159	M: 55.9435
SD: 2.7807	SD: 2.7467	SD: 2.7835	SD: 2.7616	SD: 2.7604	SD: 2.7826
T = 228min	**T = 260min**	**T = 292min**	**T = 324min**	**T = 356min**	**T =1182min**

Figure D.6 T_2 magnetic relaxation maps of a slice through the column taken at varying times T in minutes, after bacterial inoculation and challenge with Ca. The mean T_2 relaxation time calculated from the image pixels in ms are given, *e.g.* M: 54.8618 ms, as are the standard deviations among pixels, *e.g.* SD: 2.7770 ms. Spatial variations occur with reaction progression but the mean values are indistinguishable.

This is in contrast to NMR studies of thick biofilm forming bacteria which give significant T_2 relaxation variations in porous media due to the impact of the extracellular polymeric substance (EPS) on the rotational mobility of water molecules constrained within the EPS hydrogel (Hoskins et al., 1999; Seymour et al., 2004). This is attributable to the fact that most of the pore blockage evident in Figure D.4 is $CaCO_3$ with thin layers of biomass as shown in Fig. D.5. The $CaCO_3$ reduces the amount of pore water but does not significantly impact the T_2 relaxation of the remaining pore water. MRI images of the signal intensity in the packed column as a function of the reaction process are shown in Figure D.7.

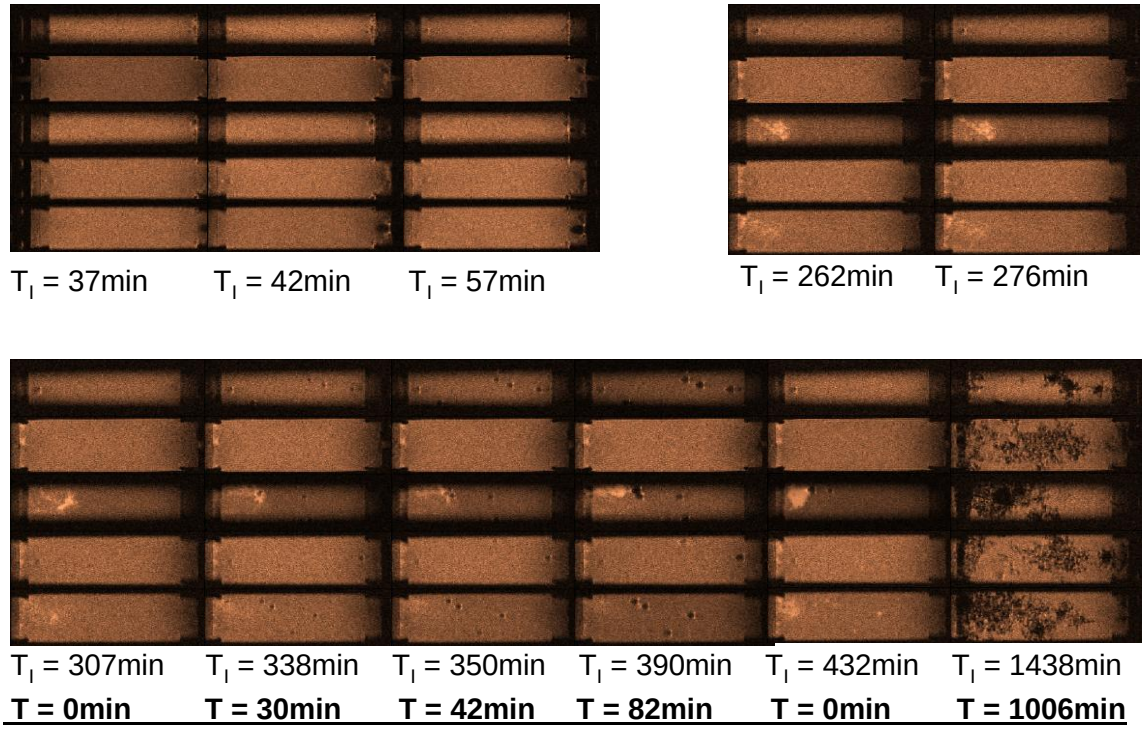

Figure D.7 A series of MR Images with 5 slices across the column obtained at various times during the reaction process. At each time the top image is one wall and the order across the column is 4th image down, 2nd image down (center region of column), 5th image down and the opposite wall 3rd image. The images are obtained of the model porous media after it has been inoculated with bacteria at $T_I = 0$, from 0min $\leq T_I <$ 77min the bacteria was allowed to attach to the bead pack (First three images are obtained during this period), for 77min $\leq T_I <$ 137 min media without calcium at 400Ml/hr was flowed (left to right) through the bead pack. At time T_I = 249 min media with calcium was flowed for 10minutes at 400Ml/hr through the bead pack and two images were obtained (Two images on the upper right). These images show the emergence of a bright region close to the wall (middle image) when compared with the initial images. After this media with calcium was flowed at 400Ml/hr for 24min and then a succession of images (note T_I) were obtained between which 10Ml/hr of media without calcium was added to the bead pack, these series show the emergence and growth of dark spots overtime. Then the bead pack was flushed with a flow of 400Ml/hr and the same process was allowed to occur for ~20hrs, it can be seen that as before the bead pack shows a growth of dark spots over time, these were then flushed out again with a flow of 400Ml/hr of media without calcium before further experiments were conducted. MRI parameters (5slices): 256x256 points, Voxel resolution: 117x43x2000μm, FOV = 30x11 mm, T_E = 14ms, T_R = 1s, SW: 50kHz.

As mentioned above the spatial resolution averages signal intensity over multiple pores. In this case 117 by 43 μm in plane over 2 mm slices. Two features are apparent. First a region of increased signal intensity near the flow entrance on one side of the column after the introduction of Ca which persists throughout the experiment. Second the appearance of low signal intensity potentially due to the generation of gas through bacterial growth. No significant details regarding the reaction process on the pore

structure is evident, again showing the limitation of NMR imaging modalities to provide significant information on pore evolution.

PGSE NMR Measurements

a)

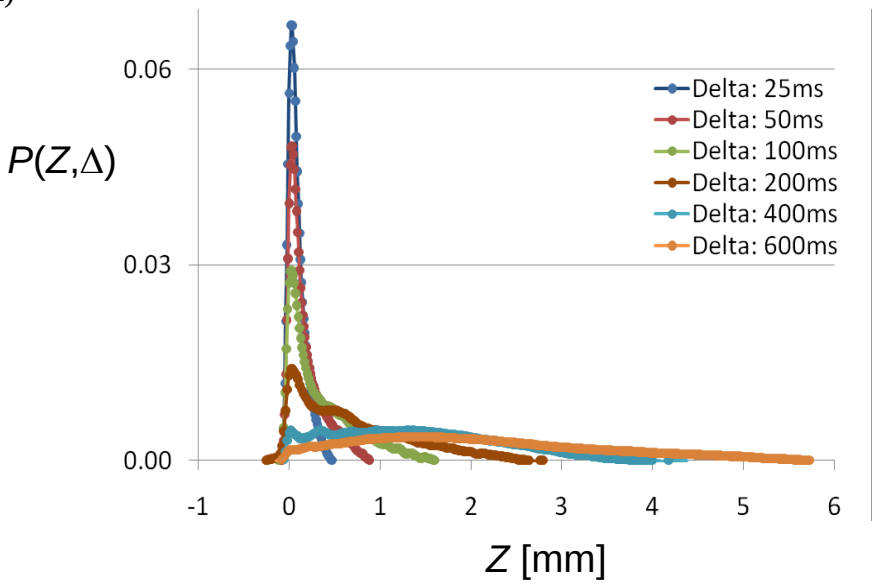

b)

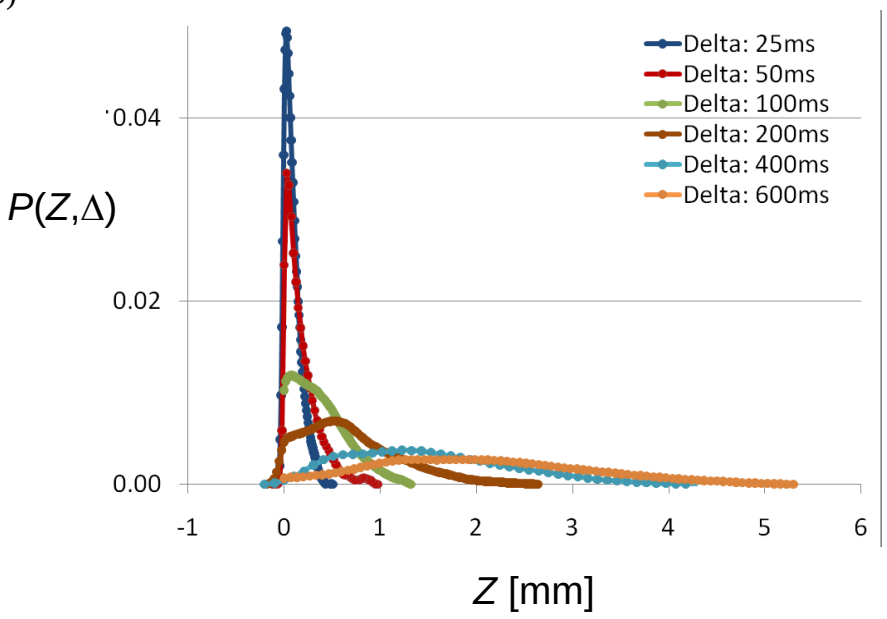

Figure D.8 Propagators as a function of displacement observation time for 400 ml/hr flow of media without calcium in a) the clean bead pack and b) the inoculated bead pack after precipitation.

In contrast to the limited information provided by spatially resolved NMR the measurement of dynamics is highly sensitive to the reaction induced pore structure change (Seymour et al., 2004; Seymour et al., 2007). Figure D.8 shows the displacement time Δ dependence of the dynamics as given by the propagator for a 400 ml/hr flow rate before (Fig. D.8a) and after (Fig. D.8b) reaction. The clean bead pack (Fig. D.8a) indicates the well known progression of the dynamics from the preasymptotic regime with a Poisson like distribution of displacements within single pores at short displacement time Δ = 25 ms to near Gaussian behavior at the longest observation time Δ = 600 ms. Interestingly the post reaction dynamics (Fig. D.8b) show a similar general progression with displacement time. However, closer inspection of the propagators at each time Δ, shown in Figure D.8, indicates significant differences in the dynamics on the pore scale.

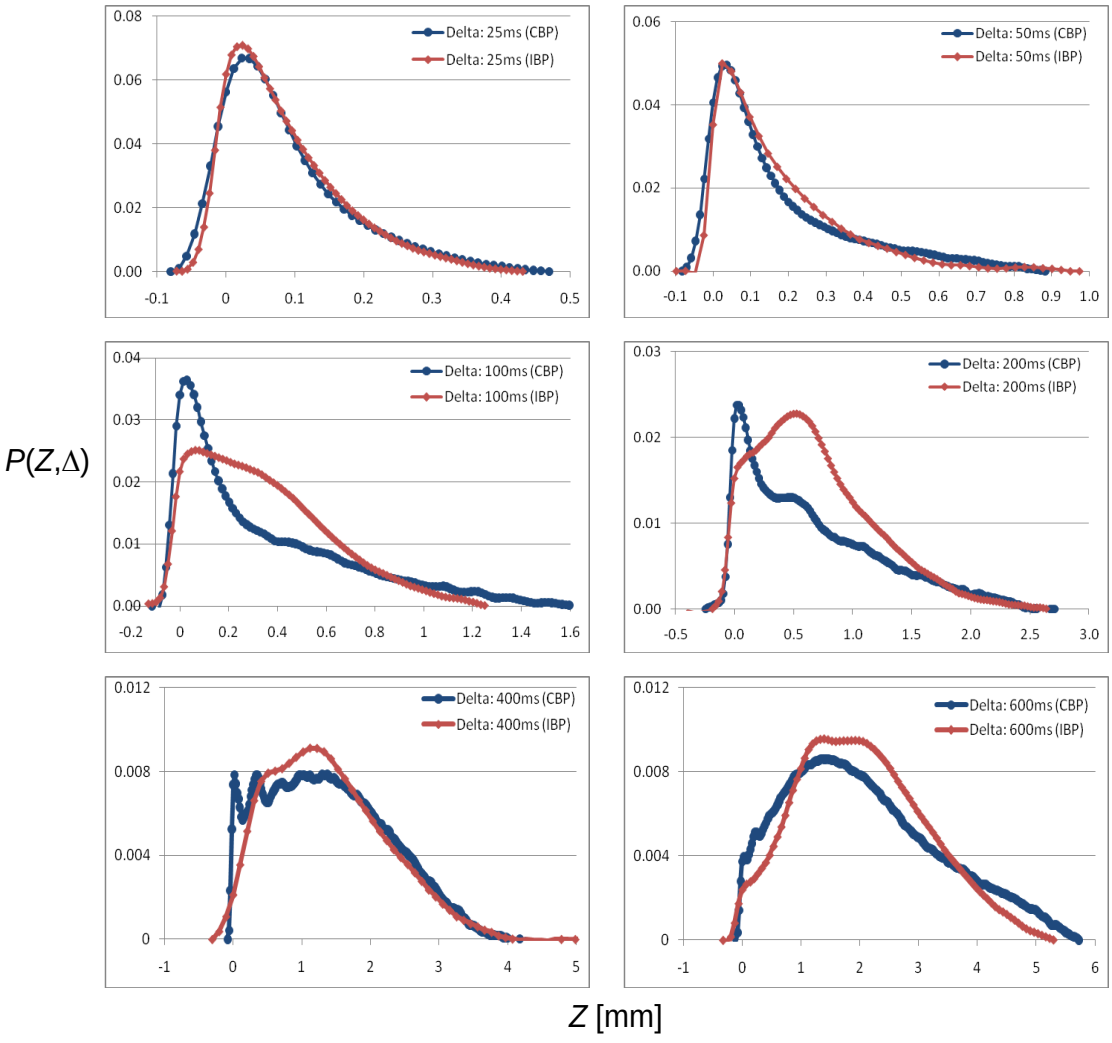

Figure D.9 Comparison of clean bead back (CBP/blue or black) and inoculated bead pack (IBP/red or grey) for displacement observations times Δ shown on each figure.

At displacement observation time Δ = 25 ms the water molecules are within a pore and the propagator reflects the distribution of velocity within the pores. Over this time little or no Taylor dispersion due to diffusion across streamlines occurs since the diffusion length $l_D = (2D_o\Delta)^{1/2} \sim 10$ μm is a small fraction of the pore size $l_p = d_p \phi/(1-\phi) \sim$ 167 μm based on the clean bead pack (CBP). Neither does mechanical mixing due to streamline crossing induced by the tortuous path the flow follows occur, since the time to transit a pore based on the superficial velocity $\langle v \rangle$ = 3.45 mm/s is $\tau_v = l_p/\langle v \rangle \sim 48$ ms. Despite the precipitate and biomass evident in Figs D.4 and D.5 the pore scale distribution of displacements due to velocity within a pore are nearly the same. At displacement time Δ = 50 ms the molecules have just transited a single pore on average and the distribution of displacements is still quite similar however some variation at displacements on the order of one or two pore lengths l_p is beginning to be evident.

Once the displacement observation time is such that significant dispersion due to sampling of multiple pores begins to occur, Δ = 100 ms a significant change in the dynamics between the CBP and the inoculated and precipitated bead pack (IBP) occur. The CBP still exhibits a strong peak at small displacements on the order of the pore length while the displacement distribution for the IBP has a sizeable number of molecules with intermediate displacements. Of interest are the absence of a large displacement tail in the IBP indicating that significant channeling is not occurring and the onset of oscillations on the CBP displacement probability due to correlations in motion from the ordering of the monodisperse packing of the CBP generating a diffraction like effect in the *q*-space data (Manz et al., 1999; Seymour and Callaghan, 1997; Seymour et al., 2004; Seymour et al., 2007). Analogous differences are present at Δ = 200 ms. By displacement time Δ = 400 ms the oscillations due to the homogeneous structure of the CBP are clearly evident and the CBP maintains a larger distribution of molecules at small displacements. The dispersion in the IBP is actually smaller than the CBP as evidenced by the narrower distribution of displacements. The distributions at displacements greater than about 1.7 mm are the same indicating a similarity in the dispersion dynamics after molecular sampling of 10 pore lengths. At the longest displacement observation time Δ = 600 ms the IBP dynamics are more narrowly distributed around the mean displacement and again more molecules have small displacements in the CBP. This persistence of a larger distribution of molecules with small displacements indicates that rather than the precipitation reaction generating significant dead end pores or greater surface area for no slip condition stagnant molecules the precipitate is decreasing the hold up of molecules. Coupled to the narrower distribution of dynamics in the IBP this indicates that the precipitate alters the pore structure such that microscale mixing is enhanced allowing the displacements to be more homogeneous. The precipitate is generating a rough and irregular surface at the micro scale smaller than a pore length, or bead diameter, which alters the dynamics at intermediate displacement scales by mechanics mixing of streamlines near pore walls in contrast to the smooth and ordered CBP. At this longest observation time the distribution of displacements for the reacted IBP is approaching a

Gaussian more rapidly than the CBP, including fewer molecules undergoing displacements greater than 4 mm.

Despite the fact that all the information on the dynamics is present in the propagator, in considering the impact of the precipitation altered pore structure on the dynamics it is useful to look at the propagator data in the reciprocal *q*-space. Figure D.10 shows data for Δ = 400 ms for the CBP with deionized (DI) water and media flowing through it, as well as data taken approximately every 5 minutes for flow of media without Ca as the reaction proceeded in the IBP after inoculation and injection of Ca enriched media.

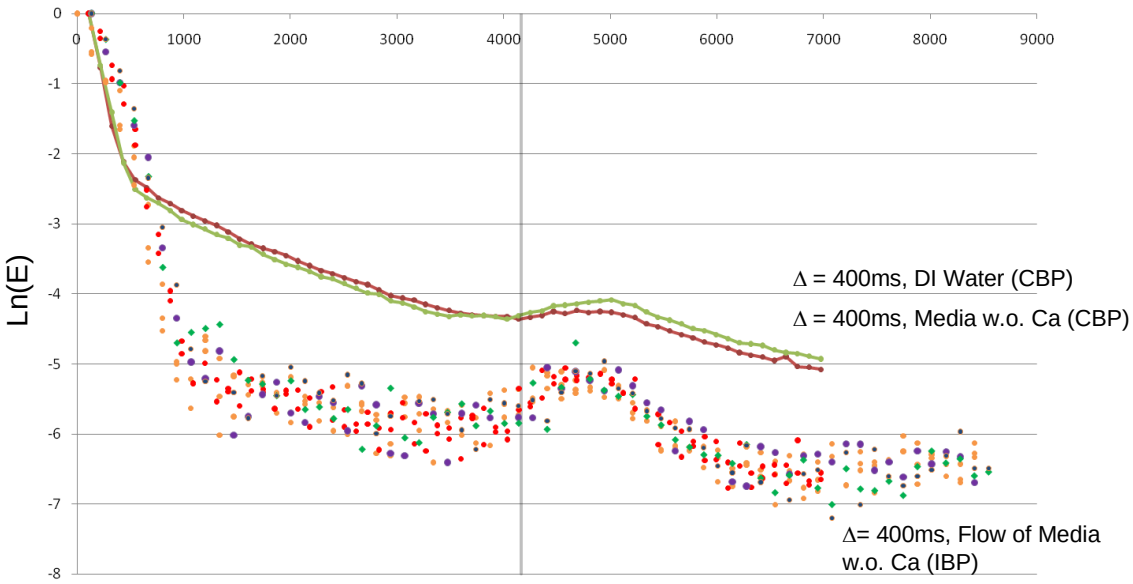

Figure D.10 PGSE data plotted in *q*-space showing the diffraction effect due to the ordered structure of the porous media for the clean bead back (CBP) and inoculated and precipitated bead pack (IBP) at displacement observation time of Δ = 400 ms. The data for the IBP taken over several hours after precipitation has occurred indicates that while there is increased noise due to the pore structure evolving the dynamics are consistent over a long time period.

Note the increase in the rate of signal decay at low *q* corresponding to large displacements. This indicates the more rapid approach to Gaussian behavior and more rapid loss of correlation in displacements. At this observation time the coherent diffraction peak at the characteristic pore structure size (Callaghan et al., 1999) is evident for both the CBP and the IBP with the maxima and minima of the diffraction peak broadened and shifted to slightly lower values of *q*. The IBP data is noisy but consistent over many hours of observation. The data clearly indicates a homogenizing effect of the precipitation reaction on the dynamics. The precipitate is not blocking the pores and increasing hold up dispersion and generating long displacements due to channeling.

Rather the precipitate alters the pore structure more subtly by coarsening the surfaces and broadening the pore size distribution so that mixing and dispersion within pores is enhanced but longer range structure is not lost as evidenced by the coherent diffraction effects in the *q*-space data.

Conclusions

NMR measurements of a model porous media were carried out before and after a biologically mediated precipitation reaction in order to explore the impact of reactive pore structure alteration on transport dynamics. MRI data is shown to be of limited use in analyzing these systems based on limitations in spatial resolution causing coarse graining across pores and a lack of significant impact on contrast mechanism like T_2 magnetic relaxation. In contrast PGSE NMR measurements of displacement scale dependent dynamics provide unique data on the impact of the precipitation on the transport dynamics. Analysis of the propagator data as a function of displacement time provides a means to determine how the pore structure has been altered in the context of the impact on the dynamics. It is shown that the precipitation reaction alters the pore structure relative to a clean bead pack such that fewer molecules undergo small displacements within individual pores over a range of displacement times and generates a narrower distribution of dynamics which approaches a Gaussian distribution more rapidly. The roughened pore surfaces serve to enhance mixing and mechanical dispersion on the pore scale resulting in the observed dynamics. Development of models based on observations such as these and the theoretical approaches discussed above has the potential to lead to quantitative prediction of the impact of reactive flows on porous media transport.

Acknowledgements

This research was supported in part by the Office of Science (BER) U.S. Department of Energy DE-FG02-07ER64416 (JDS and SLC), the US Department of Energy EPSCoR program grant number DE-FG02-08ER46527 (ABC) and the National Science Foundation DMS-0934696 (RG).

References

Berkowitz, B., Cortis, A., Dentz, M. and Scher, H., 2006. Modeling non-Fickian transport in geological formations as a continuous time random walk. Reviews of Geophysics, 44(2): RG2003.

Bird, R.B., Stewart, W.E. and Lightfoot, E.N., 1960. Transport Phenomena. Wiley & Sons, New York, 780 pp.

Blümich, B., 2000. NMR Imaging of Materials. Clarendon Press, Oxford.

Boon, J.P. and Yip, S., 1991. Molecular Hydrodynamics. Dover Publications, New York.

Brosten, T.R., Codd, S.L., Maier, R.S. and Seymour, J.D., 2009. Dynamic Length-Scale Characterization and Nonequilibrium Statistical Mechanics of Transport in Open-Cell Foams. Physical Review Letters, 103: 218001.

Callaghan, P.T., 1991. Principles of Nuclear Magnetic Resonance Microscopy. Oxford University Press, New York.

Callaghan, P.T., Codd, S.L. and Seymour, J.D., 1999. Spatial coherence phenomena arising from translational spin motion in gradient spin echo experiments. Concepts in Magnetic Resonance, 11: 181-202.

Callaghan, P.T., Coy, A., MacGowan, D., Packer, K.J. and Zelaya, F.O., 1991. Diffraction-like effects in NMR diffusion studies of fluids in porous solids. Nature, 351: 467-469.

Clement, T.P., Hooker, B.S. and Skeen, R.S., 1996. Macroscopic models for predicting changes in saturated porous media properties caused by microbial growth. Ground Water, 34(5): 934-942.

Cushman, J.H. and Ginn, T.R., 2000. Fractional advection dispersion equation: A classical mass balance with convolution-Fickian flux. Water Resources Research, 36(12): 3763-3766.

Cushman, J.H., Hu, B.X. and Ginn, T.R., 1994. Nonequilibrium statistical mechanics of preasymptotic dispersion. Journal of Statistical Physics, 75: 859-878.

Emmanuel, S. and Berkowitz, B., 2005. Mixing-induced precipitation and porosity evolution in porous media. Advances in Water Resources, 28: 337-344.

Emmanuel, S. and Berkowitz, B., 2007. Effects of pore-size controlled solubility on reactive transport in heterogeneous rock. Geophysical Research Letters, 34: L06404.

Ferris, F.G., Phoenix, V., Fujita, Y. and Smith, R.W., 2003. Kinetics of calcite precipitation induced by ureolytic bacteria at 10 to 20°C in artificial groundwater. Geochimica et Cosmochimica Acta, 67(8): 1701-1722.

Ferris, F.G. and Stehmeier, L.G., 1996. Bacteriogenic mineral plugging. Canadian Petroleum Technology, 35(8): 56-61.

Graf von der Schulenberg, D.A., Akpa, B.S., Gladden, L.F. and Johns, M.L., 2008. Non-Invasive Mass Transfer Measurements in Complex Biofilm-Coated Structures. Biotechnology and Bioengineering, 101(3): 602-608.

Hoskins, B.C., Fevang, L., Majors, P.D., Sharma, M.M. and Georgiou, G., 1999. Selective imaging of biofilms in porous media by NMR relaxation. Journal of Magnetic Resonance, 139: 67-73.

Kaszuba, J.P., Janecky, D.R. and Snow, M.G., 2005. Experimental evaluation of mixed fluid reactions between supercritical carbon dioxide and NaCl brine: Relevance to the integrity of a geologic carbon repository. Chemical Geology, 217: 277-293.

Kersting, A.B. et al., 1999. Migration of plutonium in ground water at the Nevada test site. Nature, 397: 56-59.

Koch, D.L. and Brady, J.F., 1988. Anomalous diffusion in heterogeneous porous media. Physics of Fluids, 31(5): 965-973.

Kose, K., 1994. Spatial-mapping of velocity power spectra in Taylor-Couette flow using ultrafast NMR imaging Physical Review Letters, 72(10): 1467-1470.

Lebon, L. et al., 1996. Pulsed gradient NMR measurements and numerical simulation of flow velocity distribution in sphere packings. Physics of Fluids, 8(2): 293-301.

Manz, B., Alexander, P. and Gladden, L.F., 1999. Correlations between dispersion and structure in porous media probed by nuclear magnetic resonance. Physics of Fluids, 11(2): 259-267.

Mazo, R.M., 1967. Statistical Mechanical Theories of Transport Processes. The International Encyclopedia of Physical Chemistry and Chemical Physics, Topic 9:1. Pergamon Press, Oxford, 166 pp.

Nagy, B. et al., 1991. Organic matter and containment of uranium and fissiogenic isotopes at the Oklo natural reactors. Nature, 354: 472-475.

Sahimi, M., Gavalas, G.R. and Tsotsis, T.T., 1990. Statistical and continuum models of fluid-solid reactions in porous media. Chemical Engineering Science, 45(6): 1443-1502.

Salles, J., Thovert, J.-F., Delannay, L., Auriault, J.-L. and Adler, P.M., 1993. Taylor dispersion in porous media. Physics of Fluids, 5: 2348.

Scheven, U.M., Harris, R. and Johns, M.L., 2007. Intrinsic dispersivity of randomly packed monodisperse spheres. Physical Review Letters, 99: 054502.

Sederman, A.J., Mantle, M.D., Buckley, C. and Gladden, L.F., 2004. MRI technique for measurement of velocity vectors,acceleration and autocorrelation functions in turbulent flow. Journal of Magnetic Resonance, 166: 182-189.

Seymour, J.D. and Callaghan, P.T., 1997. Generalized approach to NMR analysis of flow and dispersion in porous medium. AIChE Journal, 43: 2096-2111.

Seymour, J.D., Gage, J.P., Codd, S.L. and Gerlach, R., 2004. Anomalous fluid transport in porous media induced by biofilm growth. Physical Review Letters, 93(19): 198103.

Seymour, J.D., Gage, J.P., Codd, S.L. and Gerlach, R., 2007. Magnetic resonance microscopy of biofouling induced scale dependent transport in porous media. Advances in Water Resources, 30(6-7): 1408-1420.

Tartakovsky, A.M., Meakin, P., Scheibe, T.D. and Wood, B.D., 2007. A smoothed particle hydrodynamics model for reactive transport and mineral precipitation in porous and fractured porous media. Water Resources Research, 43: W05437.

Thullner, M. and Baveye, P., 2008. Computational pore network modeling of the influence of biofilm permeability on bioclogging in porous media. Biotechnology and Bioengineering, 99(6): 1337-1351.

APPENDIX E

NESSLER AMMONIUM ASSAY PROTOCOL

To conduct the modified Nessler Assay, the following steps were taken:

1. Make a stock solution of 1000 mg/L of NH_4^+
2. Prepare standards in 15 Ml centrifuge tubes

Table E.1. Dilutions for ammonium standards in Nessler Assay.

Standard	**Concentration (mg/L)**	**To add**	**Std. or Stock**	**DI water (Ml)**
A	1000	1.0	Stock	9.0
B	500	0.5	Stock	9.5
C	250	2.5	A	7.5
D	100	1.0	A	9.0
E	50	1.0	B	9.0
F	10	1.0	D	9.0
G (blank)	0	----	----	10.0

3. To run assay in a 96 well plate
    a. Add 0.25 ml of stocks C-G in triplicate
    b. Add 0.25 ml of 1:10, 1:100, and 1:1000 sample in triplicate
    c. To each well, add 3 µL mineral stabilizer and polyvinyl alcohol
    d. In a fume hood, add Nessler reagent to a disposable pipette basin
    e. Using a multichannel pipette, add 10 µL of Nessler Reagent to each well
    f. Incubate for 13 minutes (room T), read on spectrophotometer at 425 nm

APPENDIX F

PIERCE-COOMASSIE PROTEIN ASSAY PROTOCOL

To conduct the Pierce-Coomassie Protein Assay, the following steps were taken:

1. Make standards using pre-mixed 2 mg/mL Bovine Serum Albumin (BSA) stock from Thermo Scientific in microcentrifuge tubes (Table F.1).

Table F.1. Dilutions for protein standards in Pierce-Coomassie Protein Assay

Standard	**Concentration (mg/L)**	**To add**	**Std./Stock (µL)**	**DI water (µL)**
A	1000	500	Stock	500
B	100	100	A	900
C	75	75	A	925
D	50	50	A	950
E	25	25	A	975
F	10	100	B	900
G (blank)	0	----	----	1000

2. Base Digestion
    a. Add 200 µL sample to microcentrifuge tube
    b. Add 200 µL of 1 N NaOH
    c. Vortex and digest at 90 °C for 10 minutes
    d. Vortex and cool
    e. Add 28 µL of 6:10 (vol:vol) concentrated HCl:DI and vortex

f. Add 50 µL sample to 96 well plate in triplicate

g. Add 150 µL Pierce Coomassie Reagent

h. Incubate for 15 minutes at room temperature

i. Read on spectrophotometer at 595 nm

3. Acid Digestion

a. Instead of 200 µL of NaOH, add 28 µL of 6:10 (v/v) conc. HCl:DI

b. Instead of 6:10 (v/v) conc HCl:DI, add 200 µL of NaOH

APPENDIX G

EFFLUENT-BASED SUBSTRATE BALANCE

From the effluent samples measured with ICP-MS by Dr. Robin Gerlach, (Tables G.1 and G.2), an overall mass balance was conducted to determine the extent of precipitation. A strontium and calcium rate out was determined for each sample time, by multiplying the concentration times the flow rate (0.15 ml/min), and is illustrated in Figures G.1-G.3:

Table G.1. Effluent concentrations of calcium for each reactor at each sample time

			Calcium		
		Sr-Incl.		**Sr-Free**	
HOURS AFTER FLOW		Total (mg/L)	Dissolved	Total	Dissolved
	Abiotic batch	844			
0	**10am**	81	70	31	36
1	**11am**	22	17	17	13
6	**4pm**	17	5.6	NA	7.6
11	**9pm**	0.57	5.4	1	4.1

Table G.2. Effluent concentrations of strontium for each reactor at each sample time

			Strontium		
		Sr-Incl.		**Sr-Free**	
HOURS AFTER FLOW		Total (mg/L)	Dissolved	Total	Dissolved
	Abiotic batch	24			
0	**10am**	3.2	1.96	0.0	0.0
1	**11am**	1.9	1.79	0.0	0.0
6	**4pm**	0.83	0.70	0.0	0.0
11	**9pm**	0.54	0.57	0.0	0.0

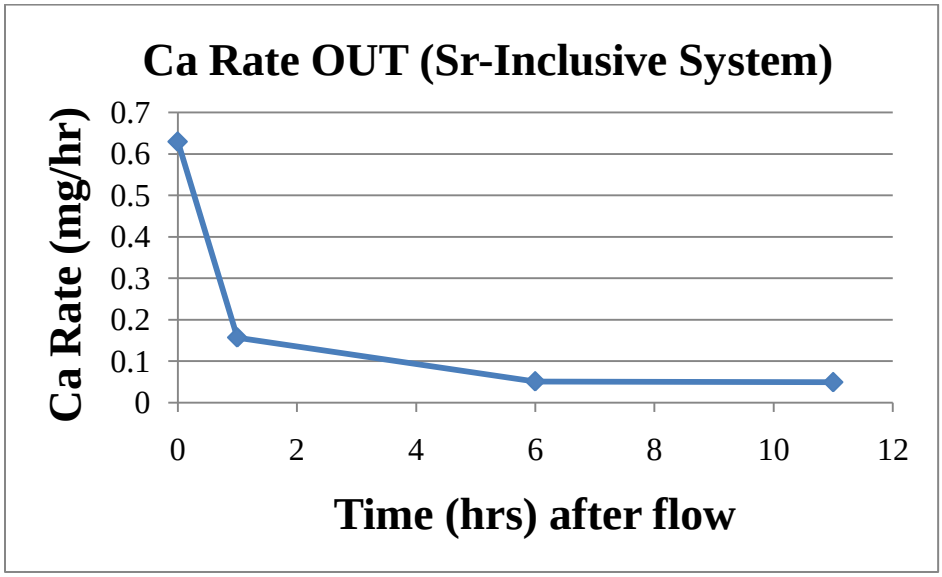

Figure G.1. Rate of calcium exiting the Sr-inclusive system at each sample time

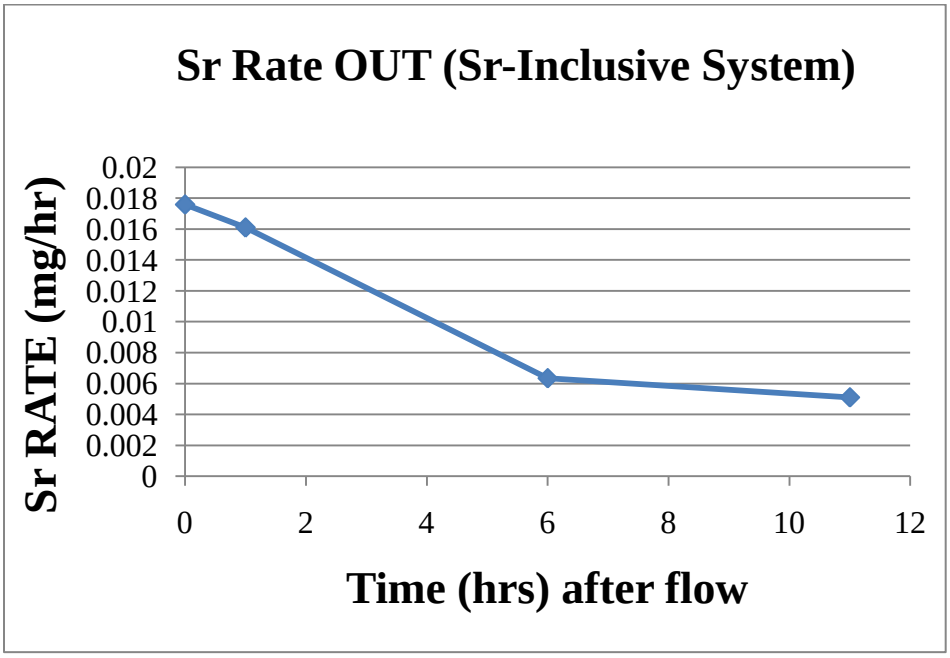

Figure G.2. Rate of strontium exiting the Sr-inclusive system at each sample time

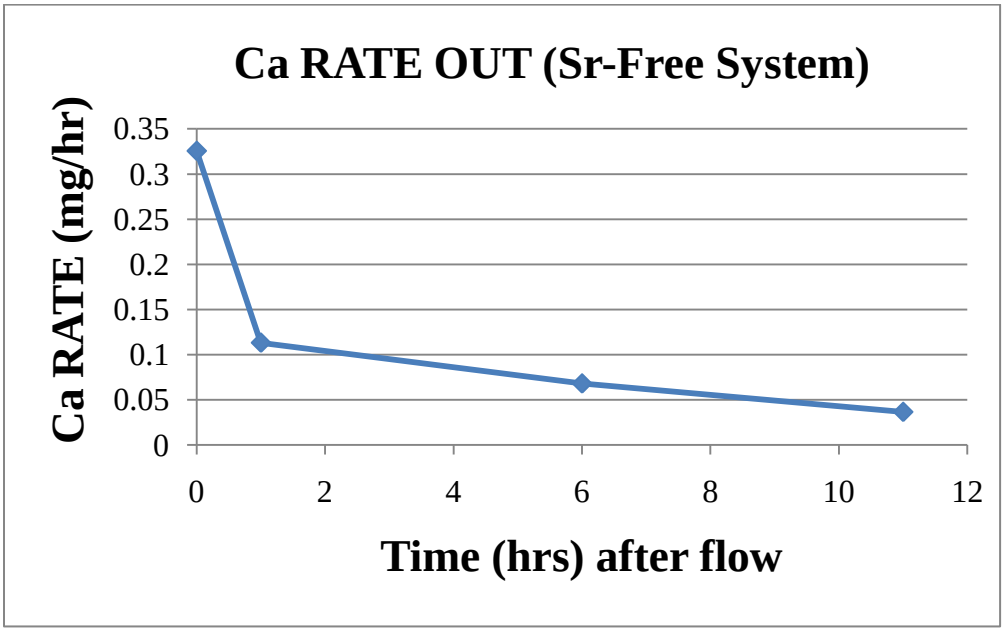

Figure G.3. Rate of calcium exiting the Sr-Free system at each sample time

The rate of calcium into the system was determined by multiplying the inlet concentration and the flow rate. From this, the overall amount of calcium and strontium into the system was calculated. The total amount of calcium and strontium that exited the systems was calculated by integrating the previous graphs of effluent samples using trapezoidal integration. From this, the amount of calcium and strontium that was accumulated (i.e., never exited) was calculated. Then, the total conversion (amount accumulated/amount in) was calculated. The data are included in Tables G.3 – G.5:

Table G.3. Calcium effluent-based mass balance data for Sr-Inclusive reactor.

Calcium Mass Balance (Sr-Inclusive System)					
Flow Rate	0.15 ml/min				
Inlet Conc.	844 mg/L				
Time	RATE IN (mg/h)	RATE OUT (mg/h)	TOTAL Ca OUT (mg)		
0	7.60	0.63			
1	7.60	0.16	0.39		
6	7.60	0.05	0.52		
11	7.60	0.05	0.25		
Total Ca IN (mg)	**83.56**	Total Ca OUT (mg)	**1.16**		
Mass Balance (ACC = IN – OUT)					
Ca Accumulated in Reactor(mg)		**82.39**			
Total Conversion of Calcium			**98.61**	**percent**	

Table G.4. Calcium effluent-based mass balance data for Sr-Free reactor.

Calcium Mass Balance (Sr-Free System)					
Flow Rate	0.15 ml/min				
Inlet Conc.	844 mg/L				
Time	RATE IN (mg/h)	RATE OUT (mg/h)	TOTAL Ca OUT (mg)		
0	7.60	0.33			
1	7.60	0.11	0.22		
6	7.60	0.07	0.45		
11	7.60	0.04	0.26		
Total Ca IN (mg)	**83.56**	Total Ca OUT (mg)	**0.93**		
Mass Balance (ACC = IN – OUT)					
Ca Accumulated in Reactor(mg)		**82.62**			
Total Conversion of Calcium			**98.88**	**percent**	

Table G.5. Strontium effluent-based mass balance data for Sr-Inclusive reactor.

Strontium Mass Balance (Sr-Inclusive System)					
Flow Rate	0.15 ml/min				
Inlet Conc.	24.216 mg/L				
Time	RATE IN (mg/h)	RATE OUT (mg/h)	TOTAL Sr OUT (mg)		
0	0.22	0.018			
1	0.22	0.016	0.017		
6	0.22	0.006	0.056		
11	0.22	0.005	0.029		
Total Sr IN (mg)	**2.40**	Total Sr OUT (mg)	**0.102**		
Mass Balance (ACC = IN – OUT)					
Sr Accumulated in Reactor(mg)		**2.296**			
Total Conversion of Strontium			**95.76**	**percent**	

APPENDIX H

X-RAY DIFFRACTION ANALYSIS OF EXTRACTED PRECIPITATES

In order to confirm that the minerals precipitated where calcite (i.e., rhombohedral), and not another form of calcium carbonate (e.g., vaterite, aragonite), XRD analysis was conducted at the Image and Chemical Analysis Laboratory at Montana State University. The obtained diffraction patterns showed a close resemblance to calcite (see Figure H.1 below):

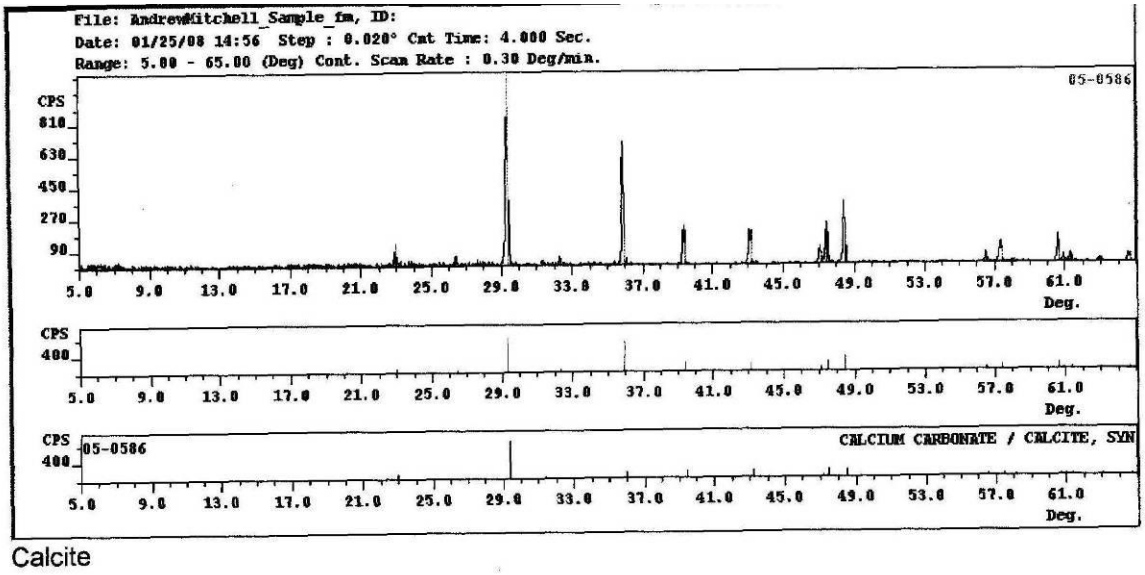

Figure H.1. XRD map showing the sample lines matching what is expected of rhombohedral calcite.

There were two other peaks that resembled halite and ammonium chloride that may have formed during the experiment. When compared to diffraction patterns of vaterite and aragonite, there was no clear resemblance (Figures H.2 and H.3).

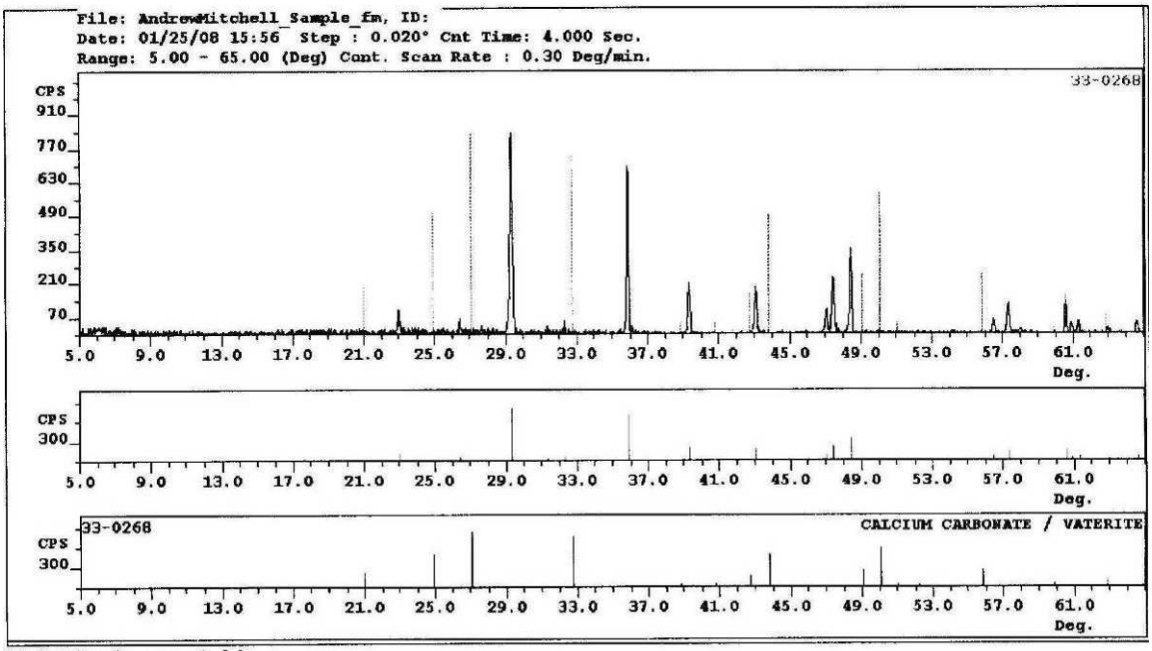

Vaterite (no match)

Figure H.2. XRD data showing sample lines that do not match up with vaterite.

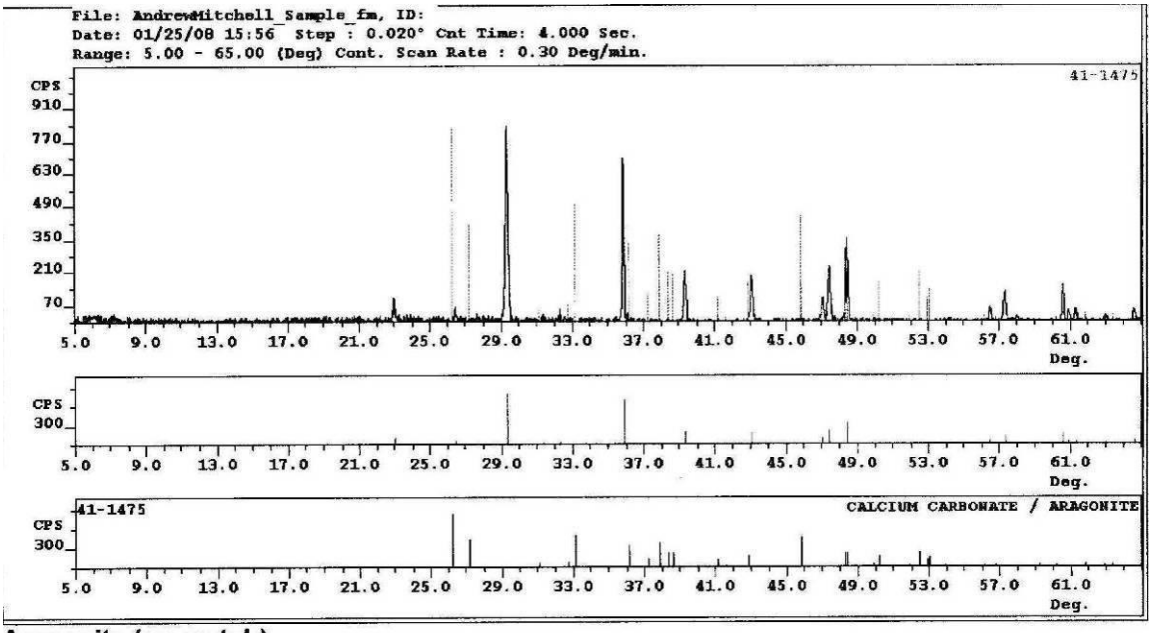

Aragonite (no match)

Figure H.3. XRD data showing sample lines that do not match up with aragonite.

APPENDIX I

VARIABILITY OF CRYSTALS ATTACHED TO GLASS AND POLYCARBONATE

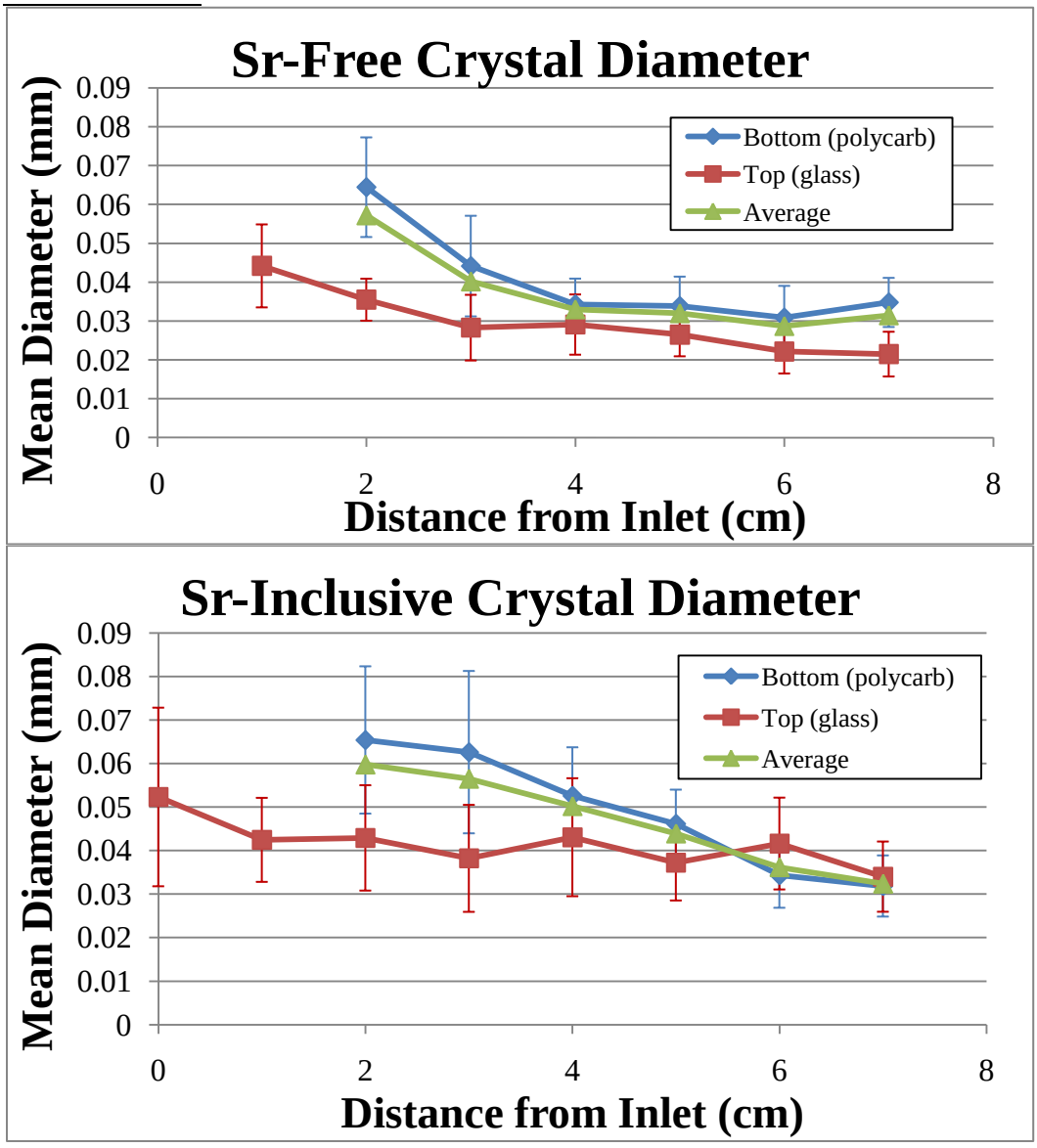

Figure I.1. Data for precipitate diameters as measured with ImageJ. All data shows decreasing diameters from inlet to outlet, with the crystals measured on the polycarbonate surface being larger.

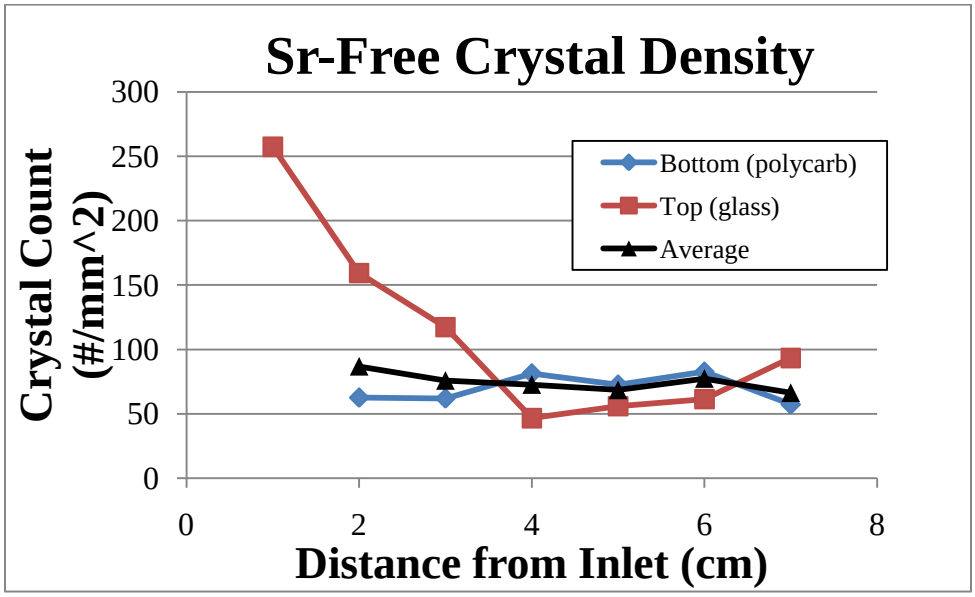

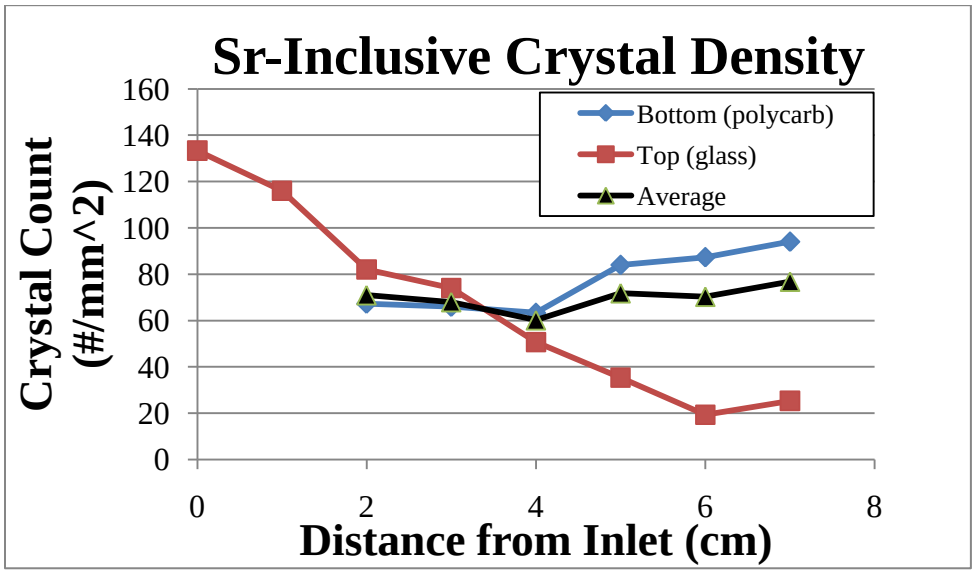

Figure I.2. Data for crystal density for each reactor and surface. Data from the bottom (polycarbonate) surface is omitted at 0 and 1 cm into the reactor because the crystal accumulation on the glass surface was too prolific to image through.

APPENDIX J

CRYSTAL SIZE AND DENSITY IMAGES AND DATA

As mentioned in the manuscript titled ‘Bacterially Induced Calcite Precipitation and Strontium Co-Precipitation’, images were taken at each location in the reactor and the average size and density were analyzed with ImageJ software. The Sr-free reactor images are shown in Figures J.1 – J.14:

Figure J.1. Sr- Inlet (glass)

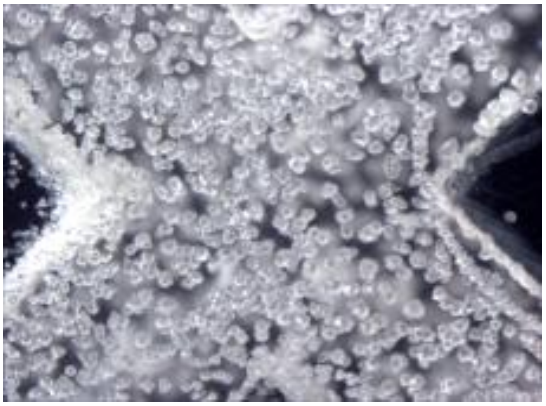

Figure J.2. Sr- 1cm from Inlet (glass)

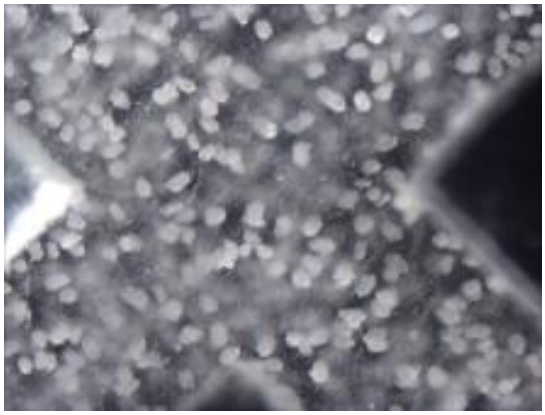

Figure J.3. Sr- 2cm from Inlet (polycarb)

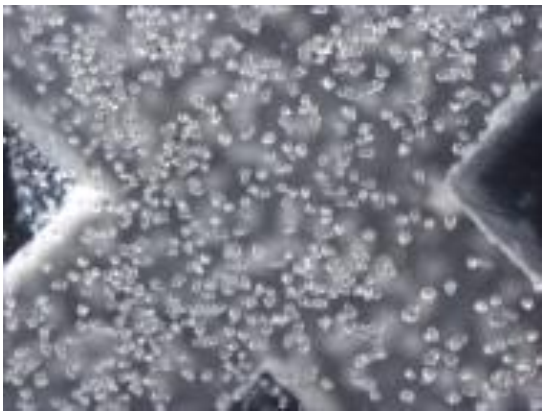

Figure J.4. Sr- 2cm from Inlet (glass)

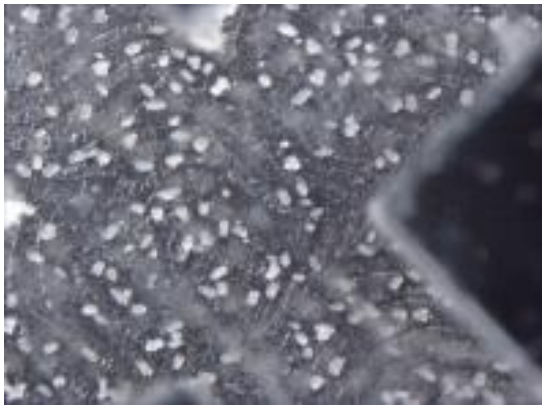

Figure J.5. Sr- 3cm from Inlet (polycarb)

Figure J.6. Sr- 3cm from Inlet (glass)

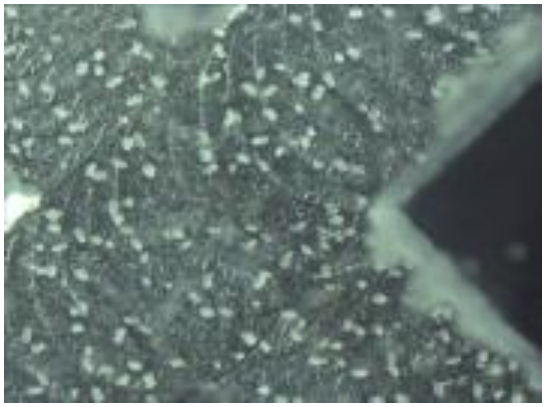

Figure J.7. Sr- 4cm from Inlet (polycarb)

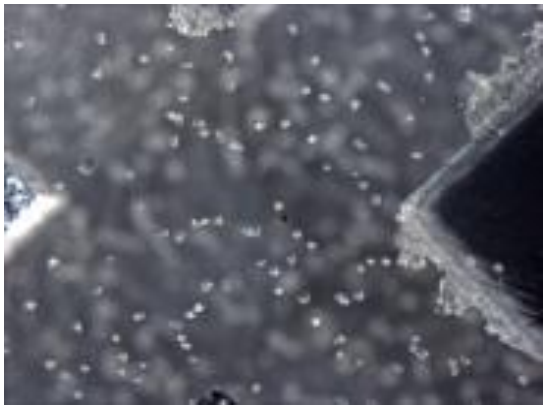

Figure J.8. Sr- 4cm from Inlet (glass)

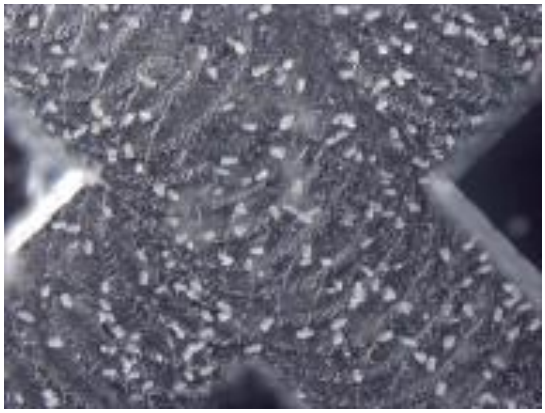

Figure J.9. Sr- 5cm from Inlet (polycarb)

Figure J.10. Sr- 5cm from Inlet (glass)

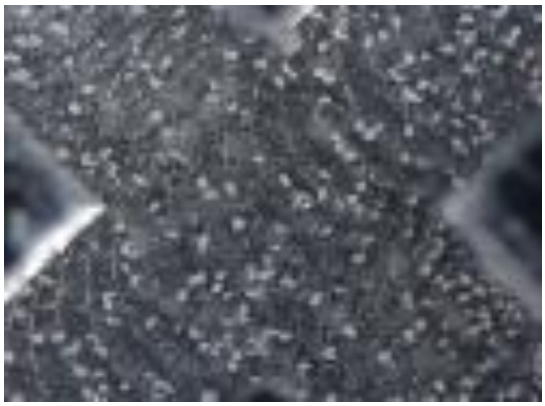

Figure J.11. Sr- 6cm from Inlet (polycarb)

Figure J.12. Sr- 6cm from Inlet (glass)

Figure J.13. Sr- Outlet (polycarb)

Figure J.14. Sr- Outlet (glass)

Twenty (20) precipitates from each image were randomly selected and the diameters were measured. The data is included below in Table J.1.

Table J.1. Data for the diameter of precipitates measured in the Sr-Free reactor at various locations. 'GL' indicates a measurement taken from the glass surface, and 'PC' indicates a measurement taken from the polycarbonate surface. All values given are in (mm).

Sr-Free														
	inlet	1cmGL	2cmPC	2cmGL	3cmPC	3cmGL	4cmPC	4cmGL	5cmPC	5cmGL	6cmPC	6cmGL	Outlet PC	Outlet GL
Position	**0**	**1**	**2**	**2**	**3**	**3**	**4**	**4**	**5**	**5**	**6**	**6**	**7**	**7**
		0.053	0.07	0.039	0.045	0.05	0.04	0.029	0.03	0.034	0.039	0.017	0.043	0.023
		0.055	0.068	0.033	0.024	0.037	0.039	0.036	0.04	0.028	0.024	0.02	0.038	0.022
		0.042	0.053	0.037	0.048	0.028	0.042	0.029	0.027	0.031	0.031	0.028	0.034	0.014
		0.047	0.06	0.043	0.066	0.028	0.03	0.014	0.023	0.032	0.036	0.025	0.032	0.022
		0.057	0.052	0.037	0.053	0.016	0.049	0.017	0.02	0.034	0.03	0.026	0.035	0.011
		0.048	0.062	0.035	0.028	0.032	0.028	0.03	0.028	0.021	0.034	0.014	0.039	0.022
		0.032	0.047	0.038	0.05	0.028	0.028	0.022	0.043	0.023	0.032	0.017	0.043	0.025
		0.049	0.077	0.035	0.051	0.028	0.026	0.027	0.038	0.019	0.033	0.019	0.034	0.027
		0.04	0.053	0.032	0.064	0.018	0.034	0.025	0.033	0.025	0.031	0.03	0.033	0.024
		0.067	0.083	0.027	0.03	0.035	0.025	0.036	0.041	0.021	0.025	0.02	0.044	0.015
		0.026	0.069	0.025	0.026	0.03	0.03	0.023	0.032	0.018	0.026	0.012	0.025	0.011
		0.032	0.08	0.031	0.056	0.041	0.037	0.021	0.031	0.021	0.029	0.02	0.032	0.016
		0.043	0.053	0.041	0.056	0.028	0.034	0.036	0.047	0.03	0.02	0.015	0.021	0.028
		0.034	0.076	0.043	0.044	0.027	0.042	0.04	0.03	0.032	0.02	0.023	0.032	0.023
		0.053	0.045	0.035	0.044	0.027	0.023	0.029	0.028	0.035	0.033	0.029	0.039	0.026
		0.03	0.05	0.033	0.035	0.019	0.033	0.03	0.03	0.027	0.033	0.025	0.041	0.018
		0.032	0.089	0.028	0.045	0.026	0.038	0.047	0.035	0.027	0.058	0.031	0.025	0.025
		0.046	0.069	0.042	0.047	0.032	0.034	0.032	0.038	0.028	0.029	0.019	0.039	0.031
		0.051	0.073	0.033	0.021	0.016	0.039	0.029	0.034	0.026	0.032	0.025	0.03	0.019
		0.047	0.06	0.043	0.05	0.02	0.035	0.03	0.049	0.018	0.023	0.028	0.037	0.028
weighted MEAN		0.0442	0.0644	0.0355	0.0441	0.0283	0.0343	0.0291	0.0338	0.0265	0.0309	0.02215	0.034	0.0215
STD DEV		0.0107	0.0129	0.0054	0.0130	0.0084	0.0066	0.0077	0.0076	0.0056	0.0082	0.0056	0.006	0.0058
POSITION				2	3	4	5	6	7					
AVERAGE				0.0500	0.0362	0.0317	0.0302	0.0265	0.0281					
AVERAGE(weighted)				0.0572	0.0402	0.0330	0.0320	0.0287	0.0315					

A graphical display of these diameters is shown in Figure J.15:

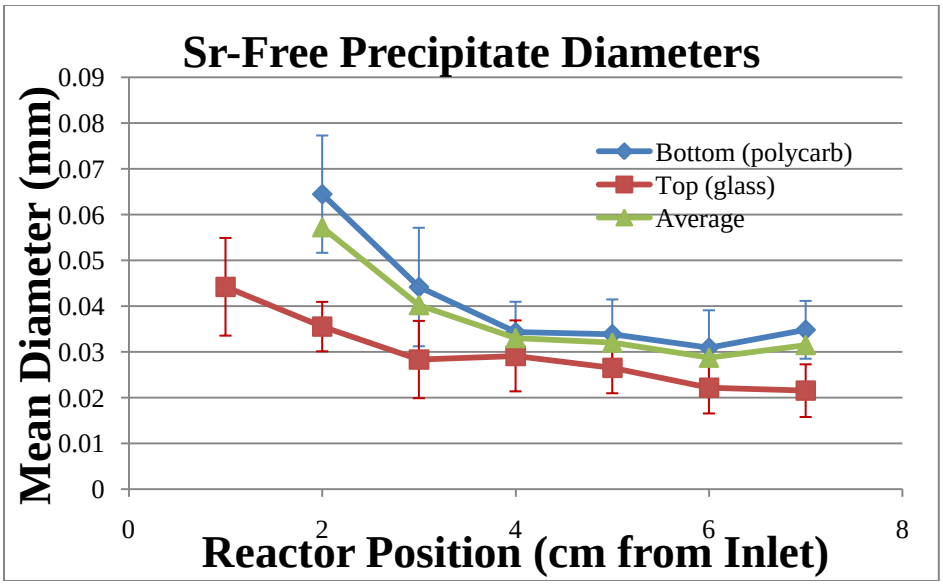

Figure J.15. Graphical interpretation of the precipitate diameters in the Sr-free reactor. The average value is weighted according to the fact that 75% of the reactor surface is polycarbonate (bottom and side walls of pores) and 25% of the reactor surface is glass (top cover).

The images taken of the Sr-inclusive reactor that were used from precipitate size and density analysis are shown in Figure J.16 – J.29:

Figure J.16. Sr+ Inlet (glass)

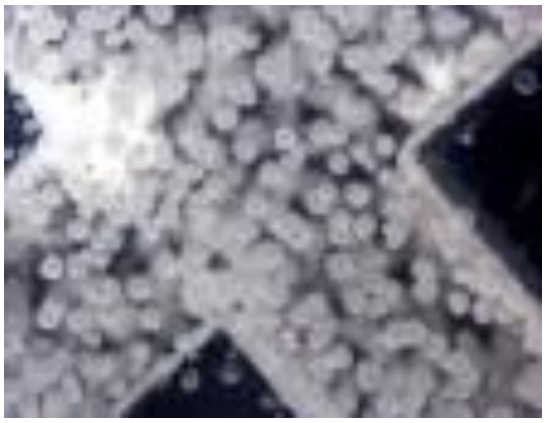

Figure J.17. Sr+ 1cm from Inlet (glass)

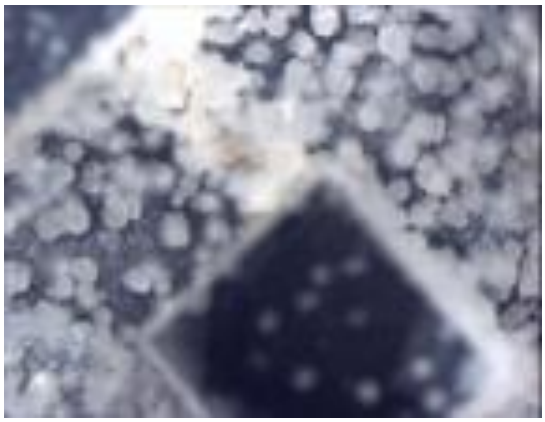

Figure J.18. Sr+ 2cm from Inlet (polycarb)

Figure J.19. Sr+ 2cm from Inlet (glass)

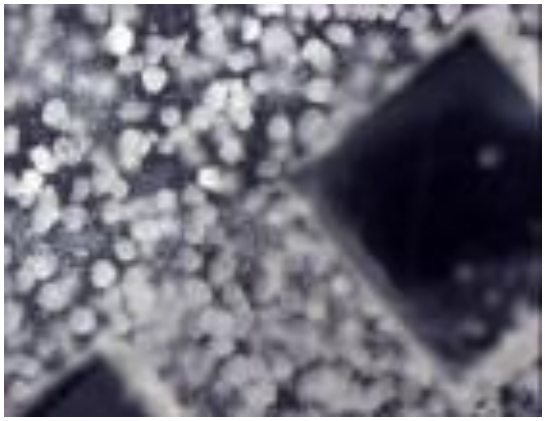

Figure J.20. Sr+ 3cm from Inlet (polycarb)

Figure J.21. Sr+ 3cm from Inlet (glass)

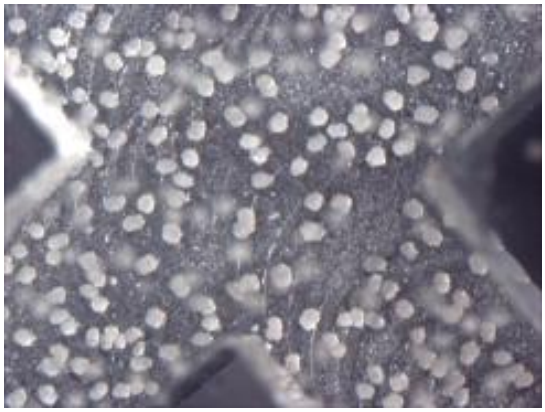

Figure J.22. Sr+ 4cm from Inlet (polycarb)

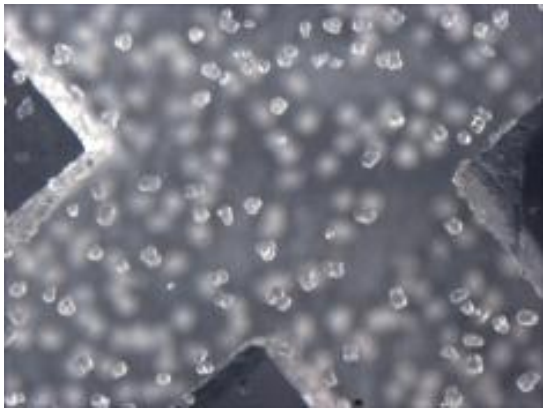

Figure J.23. Sr+ 4cm from Inlet (glass)

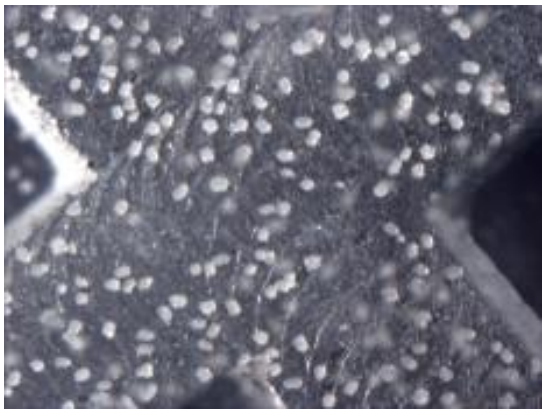

Figure J.24. Sr+ 5cm from Inlet (polycarb)

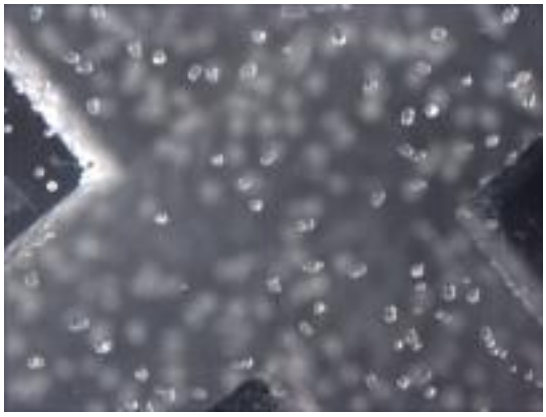

Figure J.25. Sr+ 5cm from Inlet (glass)

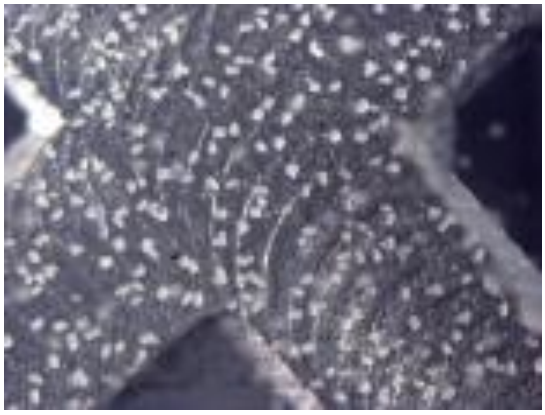

Figure J.26. Sr+ 6cm from Inlet (polycarb)

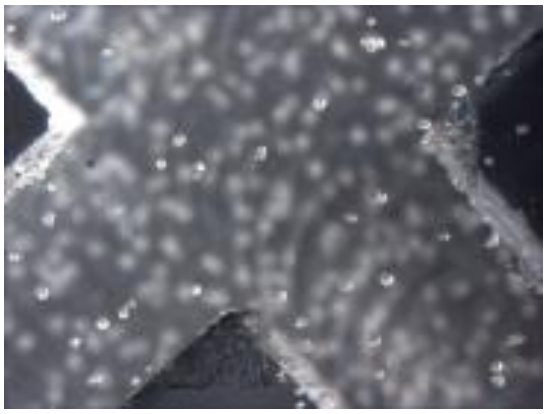

Figure J.27. Sr+ 6cm from Inlet (glass)

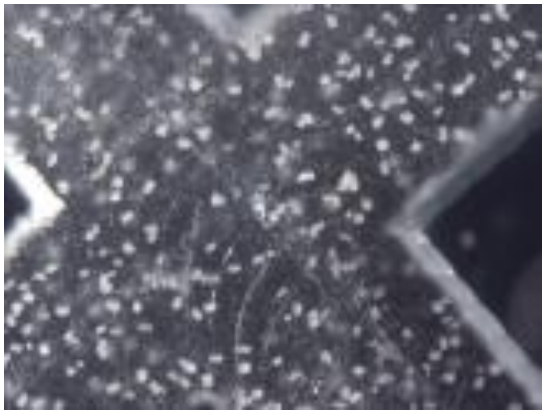

Figure J.28. Sr+ Outlet (polycarb)

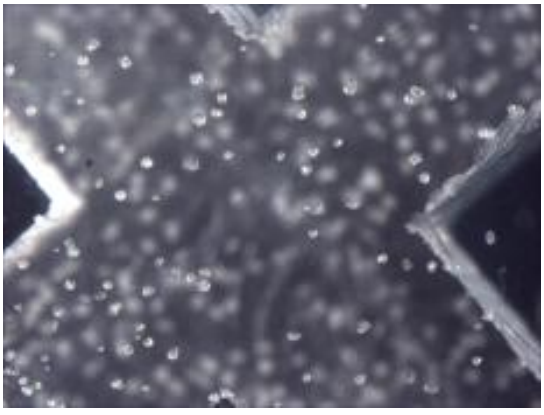

Figure J.29. Sr+ Outlet (glass)

Twenty precipitates from each image were randomly selected and the diameters were measured. The data are included below in Table J.2,

Table J.2. Data for the diameter of precipitates measured in the Sr-Inclusive reactor at various locations. 'GL' indicates a measurement taken from the glass surface, and 'PC' indicates a measurement taken from the polycarbonate surface. All values given are in (mm).

Sr-Incl.														
	Inlet	1cmGL	2cmPC	2cmGL	3cmPC	3cmGL	4cmPC	4cmGL	5cmPC	5cmGL	6cmPC	6cmGL	Outlet PC	Outlet GL
Position	**0**	**1**	**2**	**2**	**3**	**3**	**4**	**4**	**5**	**5**	**6**	**6**	**7**	**7**
	0.095	0.032	0.092	0.036	0.113	0.058	0.061	0.061	0.044	0.052	0.047	0.045	0.029	0.028
	0.042	0.055	0.082	0.058	0.075	0.044	0.065	0.042	0.061	0.034	0.036	0.053	0.024	0.032
	0.033	0.045	0.059	0.061	0.07	0.032	0.04	0.052	0.051	0.047	0.028	0.039	0.028	0.024
	0.035	0.043	0.053	0.053	0.06	0.058	0.043	0.022	0.046	0.039	0.042	0.031	0.043	0.028
	0.073	0.057	0.092	0.037	0.041	0.044	0.049	0.071	0.059	0.043	0.033	0.036	0.031	0.033
	0.048	0.046	0.074	0.02	0.037	0.024	0.069	0.059	0.055	0.046	0.035	0.05	0.019	0.04
	0.045	0.037	0.059	0.029	0.037	0.033	0.063	0.048	0.031	0.046	0.028	0.048	0.024	0.056
	0.042	0.047	0.067	0.056	0.081	0.034	0.046	0.051	0.052	0.044	0.034	0.051	0.037	0.031
	0.068	0.035	0.048	0.045	0.065	0.022	0.061	0.054	0.048	0.037	0.035	0.057	0.041	0.027
	0.038	0.049	0.049	0.038	0.078	0.023	0.048	0.048	0.042	0.02	0.04	0.015	0.036	0.045
	0.077	0.025	0.051	0.033	0.078	0.042	0.057	0.043	0.053	0.035	0.034	0.038	0.034	0.029
	0.04	0.045	0.099	0.03	0.038	0.035	0.038	0.038	0.032	0.03	0.021	0.057	0.029	0.035
	0.038	0.044	0.054	0.055	0.046	0.046	0.04	0.045	0.04	0.031	0.039	0.043	0.025	0.026
	0.031	0.037	0.074	0.052	0.07	0.03	0.045	0.046	0.051	0.028	0.034	0.029	0.035	0.047
	0.083	0.062	0.049	0.057	0.062	0.025	0.035	0.019	0.04	0.032	0.037	0.051	0.027	0.03
	0.059	0.036	0.068	0.052	0.065	0.03	0.054	0.025	0.043	0.047	0.044	0.038	0.035	0.03
	0.087	0.049	0.063	0.041	0.064	0.056	0.07	0.029	0.045	0.034	0.043	0.033	0.037	0.036
	0.033	0.036	0.035	0.032	0.055	0.052	0.054	0.042	0.044	0.031	0.017	0.034	0.036	0.028
	0.043	0.043	0.076	0.028	0.069	0.051	0.068	0.029	0.045	0.024	0.027	0.038	0.044	0.036
	0.036	0.026	0.064	0.045	0.048	0.025	0.046	0.037	0.041	0.044	0.033	0.046	0.023	0.039
MEAN	0.052	0.042	0.065	0.043	0.063	0.038	0.053	0.043	0.046	0.037	0.034	0.042	0.032	0.034
STD DEV	0.021	0.010	0.017	0.012	0.019	0.012	0.011	0.013	0.008	0.009	0.007	0.011	0.007	0.008
POSITION				2	3	4	5	6	7					
AVERAGE (nonweighted)				0.054	0.050	0.048	0.0417	0.038	0.033					
AVERAGE (weighted)				0.060	0.057	0.050	0.044	0.036	0.032					

A graphical display of these diameters is shown in Figure J.30:

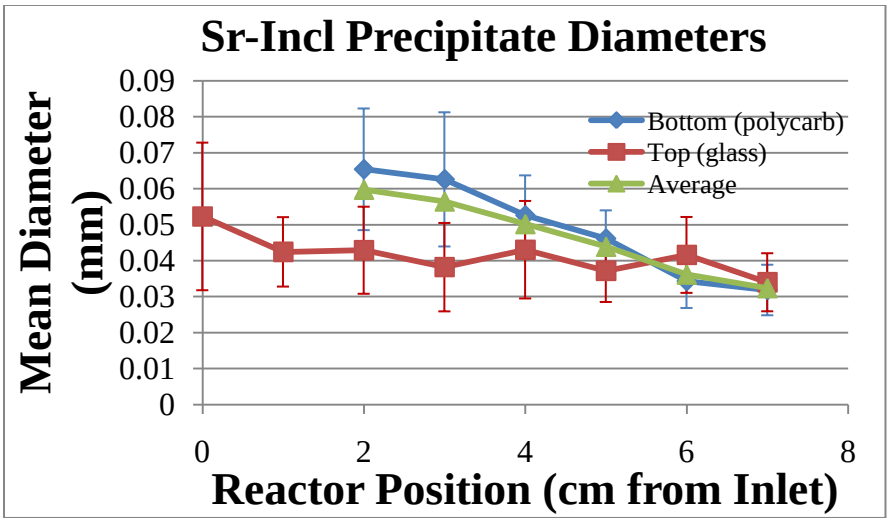

Figure J.30. Graphical summary of the precipitate diameters in the Sr-inclusive reactor. The average value is weighted according to the fact that 75% of the reactor surface is polycarbonate (bottom and side walls of pores) and 25% of the reactor surface is glass (top cover).

Table J.3. Data for the number of precipitates counted from each image containing 1.5 mm^2 of surface area at a specified reactor location.

Crystal Density Counts (crystals/1.5mm^2 area)														
	Raw	per mm^2												
	Sr-Free								**Sr-Incl.**					
				Position	Avg.	Weighted average						Position	average	Weighted average
Inlet GL	Too Dense					3xBot1xtop		Inlet GL	200	133.33				3xBot1xtop
1cm GL	386	257.33						1cm GL	174	116.00				
2cm PC	94	62.67						2cm PC	101	67.33				
2cm GL	239	159.33		2	111	86.83		2cm GL	123	82.00		2	74.67	71.00
3cm PC	93	62.00		3	89.67	75.83		3cm PC	99	66.00		3	70.00	68.00
3cm GL	176	117.33		4	64.00	72.67		3cm GL	111	74.00		4	57.00	60.17
4cm PC	122	81.33		5	64.33	68.50		4cm PC	95	63.33		5	59.67	71.83
4cm GL	70	46.67		6	72.00	77.33		4cm GL	76	50.67		6	53.33	70.33
5cm PC	109	72.67		7	75.33	66.33		5cm PC	126	84.00		7	59.67	76.833
5cm GL	84	56.00						5cm GL	53	35.33				
6cm PC	124	82.67						6cm PC	131	87.33				
6cm GL	92	61.33						6cm PC	29	19.33				
Outlet PC	86	57.33						Outlet PC	141	94.00				
Outlet GL	140	93.33						Outlet GL	38	25.33				

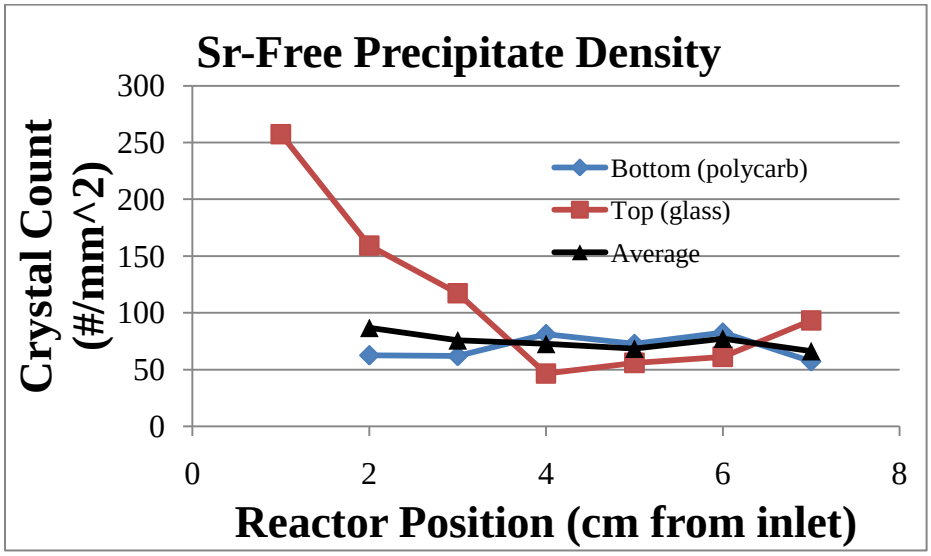

Figure J.31. Graphical summary of the density of precipitates in each field of view in the Sr-free reactor. At position 1, there is no data from the polycarbonate surface, because the viewing was optically-limited by the dense precipitation on the glass surface. The weighted average is based on the assumption that 75% of the reactor surface area is polycarbonate, and 25% is glass

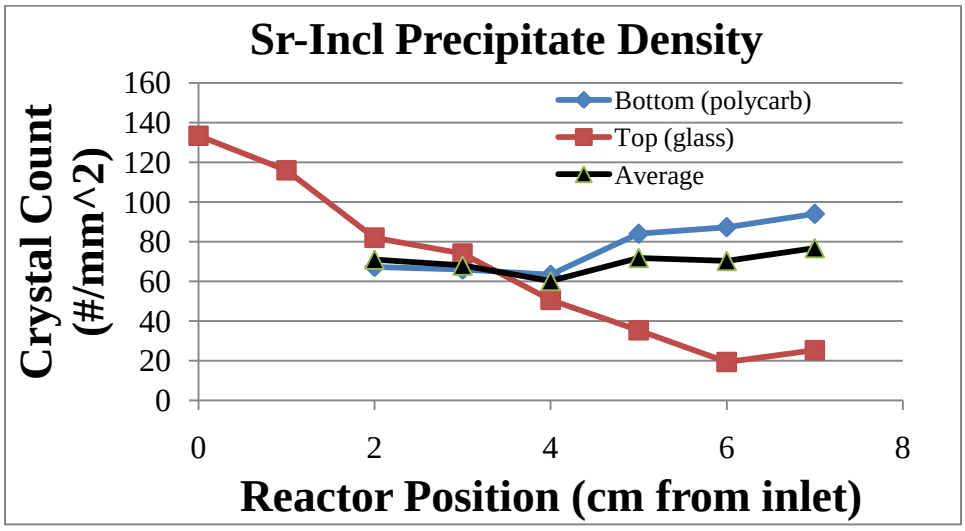

Figure J.32. Graphical summary of the density of precipitates in each field of view in the Sr-inclusive reactor. At position 1, there is no data from the polycarbonate surface, because the viewing was optically-limited by the dense precipitation on the glass surface. The weighted average is based on the assumption that 75% of the reactor surface area is polycarbonate, and 25% is glass

APPENDIX K

IMAGE-BASED SUBSTRATE BALANCE

Based on the image data that was collected in the experiment that was formulated into the manuscript titled “Bacterially Induced Calcite Precipitation and Strontium Co-Precipitation” that will be submitted to Environmental Science and Technology, an overall conversion of calcium to calcite was calculated. First, the overall volume of crystals in the reactor was estimated based on the assumption of spherical crystals with the average diameter determined by ImageJ analysis. An overall mass of crystal was then calculated, assuming the density of calcite (2.71 g/cm^3). Finally, an overall mass of calcium was calculated, assuming calcite to be 40% (by weight) calcium. The values for these calculations are included in Table K.1.

Overall results indicated that the amounts of calcium immobilized in the Sr-Free and Sr-Inclusive systems were 30.84 mg (36.9% conversion) and 49.13 mg (58.7% conversion) respectively. These values are lower than those calculated by the effluent-based analysis (98.88% and 98.61% respectively). This might be due to the fact that the region with the densest precipitation (inlet) was not accounted for in the image based analysis, since the precipitate size and density could not be measured accurately. Also, the image based analysis did not account for precipitates that were smaller than the detection limit of the stereo microscope.

Table K.1. Calculations for image-based balance of calcium**.**

Overall Reactor Surface Area:			9194	mm2							
Overall Volume of Crystal in Reactor											
	=density(crystals/mm2)*SA(mm2)*volume(mm3/crystal)										
Density of Calcite = 2.71 g/cm3			0.00271	g/mm3							
Mass percentage Ca = 0.4											
Mass of Ca in Reactor											
	Sr-Free										
		POSITION			1	2	3	4	5	6	7
		AVERAGE Diameter (weighted) (mm)			0.075	0.057	0.040	0.033	0.032	0.029	0.031
		AVERAGE Density (weighted) (crystals/mm2)			91.8	86.8	75.8	72.7	68.5	77.3	66.3
		Overall avg. diameter		0.042	mm						
		Overall Average Volume		4.01E-05	mm3						
		Overall avg. density		77.0	crystals/mm2						
	Overall Crystal Vol. in Reactor		28.4	mm3							
	Mass of Ca in Reactor		0.0318	g Ca							
			30.8	mg Ca							
			36.91	% conversion							
	Recall: Effluent-based mass balance indicated an accumulation of						83	mg			
	Sr-Incl										
		POSITION			1	2	3	4	5	6	7
		AVERAGE Diameter (weighted)			0.077	0.060	0.057	0.050	0.044	0.036	0.032
		AVERAGE Density (weighted)			80.7	71.0	68.0	60.2	71.8	70.3	76.8
		Overall avg. diameter		0.051							
		Overall Average Volume		6.9E-05							
		Overall avg. density		71.3							
	Overall Crystal Vol. in Reactor		45.3	mm3							
	Mass of Ca in Reactor		0.049	g Ca							
			49.10	mg Ca							
			58.79	% conversion							
	Recall: Effluent-based mass balance indicated an accumulation of						82	mg Ca			

APPENDIX L

REACTOR DISASSEMBLY DATA

As mentioned in the ES&T manuscript, after flow ceased, the glass cover slide was removed, and the interior was destructively sampled by Dr. Andrew Mitchell. He swabbed the glass cover slip at locations throughout the reactors, dissolved the swabs in dilute nitric acid, and measured the dissolved metal concentrations with ICP-MS. The purpose of this was to analyze the immobilized ratio of Sr to Ca throughout the reactor, and include the ions that may be in the hydrated biofilm. The raw data and graphs of this are shown in Table L.1 and Figures L.1 and L.2:

Table L.1. ICP-MS concentration data measured from swabbed samples in the reactors. Sr+ indicates the Sr-inclusive system, and Sr- indicates the Sr-free system.

Calcium concentration in ICP-MS sample	**mg/L**	**cm**	**Strontium concentration in ICP-MS sample**	**mg/L**	**Ratio (Sr/Ca)**
Sr + Glass swab blk	1.5		Sr + Glass swab blk	0.02	0.0110
Sr + Glass swab inlet digest 1	21.1		Sr + Glass swab inlet digest 1	0.41	0.0192
Sr + Glass swab inlet digest 2	32.2	1	Sr + Glass swab inlet digest 2	0.61	0.0191
Sr + Glass swab 2-3cm in digest	12.4	3	Sr + Glass swab 2-3cm in digest	0.24	0.0197
Sr + Glass swab 4-5cm in digest	4.6	5	Sr + Glass swab 4-5cm in digest	0.08	0.0176
Sr + Glass swab 6-7cm in digest	3.3	7	Sr + Glass swab 6-7cm in digest	0.05	0.0163
Sr + Glass swab 8-9cm in digest	2.0	9	Sr + Glass swab 8-9cm in digest	0.03	0.0135
Sr – Glass swab blk	1.1		Sr – Glass swab blk	0.02	0.0154
Sr – Glass swab inlet digest 1	43.7		Sr – Glass swab inlet digest 1	0.02	0.0005
Sr – Glass swab inlet digest 2	53.3	1	Sr – Glass swab inlet digest 2	0.02	0.0004
Sr – Glass swab 2-3cm in digest	14.5	3	Sr – Glass swab 2-3cm in digest	0.03	0.0019
Sr – Glass swab 4-5cm in digest	6.8	5	Sr – Glass swab 4-5cm in digest	0.02	0.0029
Sr – Glass swab 6-7cm in digest	2.9	7	Sr – Glass swab 6-7cm in digest	0.02	0.0058
Sr – Glass swab 8-9cm in digest	3.1	9	Sr – Glass swab 8-9cm in digest	0.02	0.0056

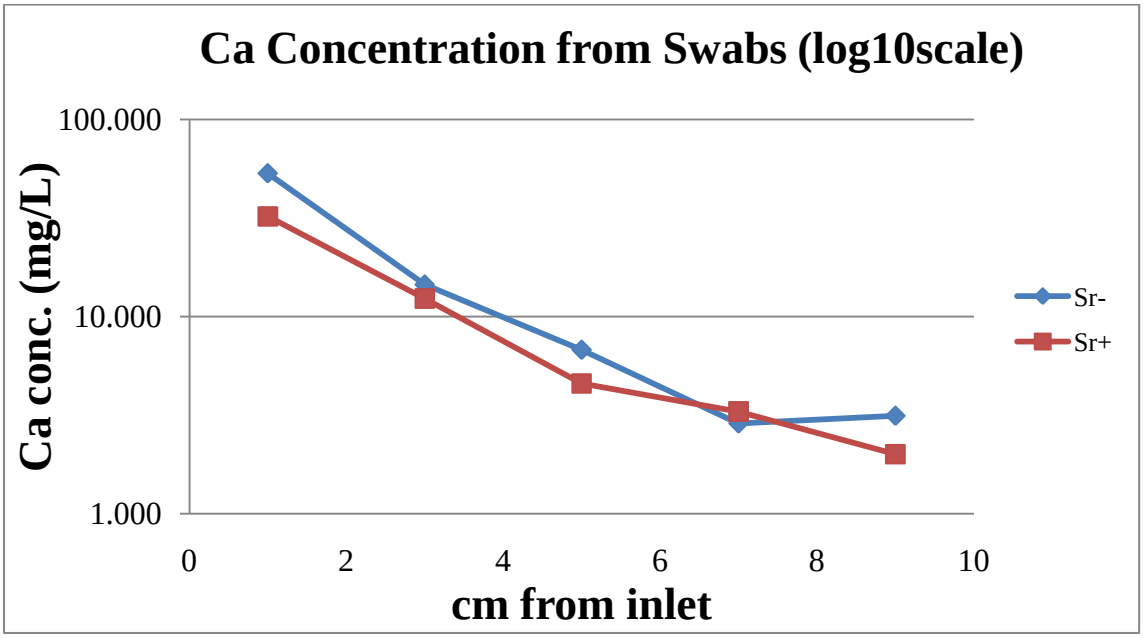

Figure L.1. Raw data of calcium concentration in swabbed samples at various reactor locations. This data was used to calculate relative concentrations of calcium and strontium

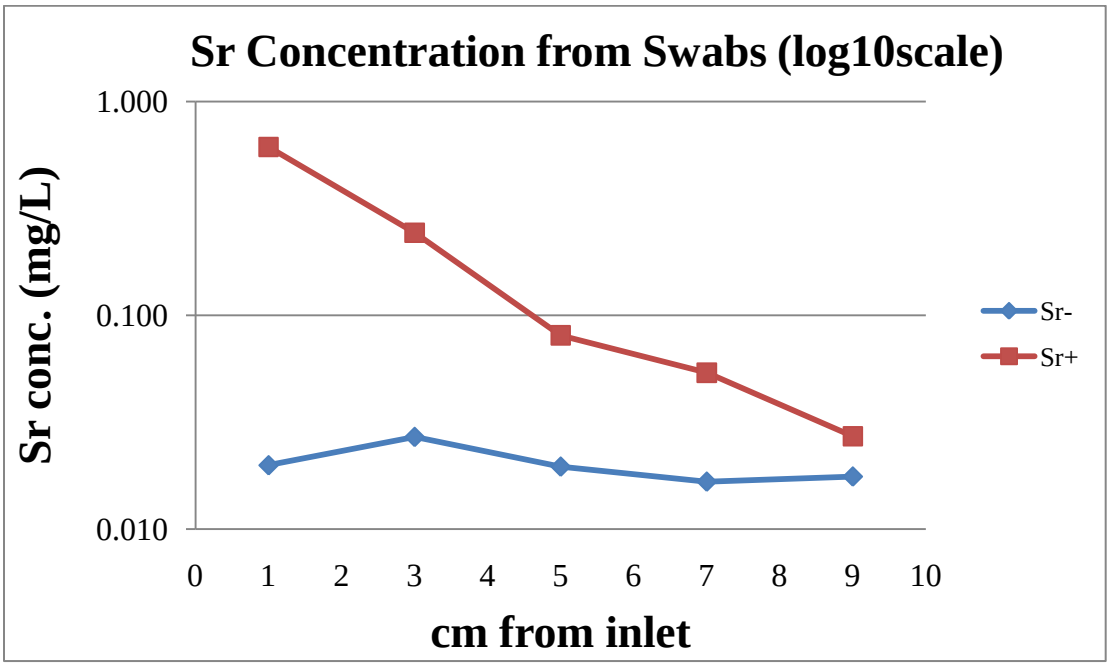

Figure L.2. Raw data of strontium concentration in swabbed samples at various reactor locations. This data was used to calculate relative concentrations of calcium and strontium

After the swabbed samples were collected, Dr. Mitchell extracted precipitated crystals. The precipitates were dried in an oven, weighed, and then dissolved in dilute nitric acid. The purpose was to analyze the total amount of Sr and Ca as a function of the total precipitate mass. The data and image interpretation are in Table L.2 and Figure L.3:

Table L.2. Data from precipitates that were extracted from the Sr-inclusive reactor.

		Ca(mg/L) in 1:2)	mg in 1000ul sample	Wt. % Ca in cystal	Sr (mg/L in 1:2)	mg in 1000ul sample	Wt. % Sr in crystal	Empty tube wt.	Tube + Sample	Dry Crystal (mg)
Inlet port	Sr + tube 1 digest	13.92	0.0278	1.638	0.185	0.0004	0.0217	1.3024	1.3041	1.7
beginning of pores	Sr + tube 2 digest	24.26	0.0485	3.234	0.361	0.0007	0.0481	1.3050	1.3065	1.5
1 cm in	Sr + tube 3 digest	5.97	0.0119	2.987	0.108	0.0002	0.0542	1.3135	1.3139	0.4
2 cm in	Sr + tube 4 digest	2.06	0.0041	0.825	0.042	8.43E-05	0.0169	1.3033	1.3038	0.5
middle	Sr + tube 5 digest	0.40	0.0008	0.403	0.009	1.79E-05	0.0089	1.3040	1.3042	0.2
end	Sr + tube 6 digest	0.35	0.0007	0.010	0.009	1.89E-05	0.0027	1.3035	1.3042	0.7
beginning far Left	Sr + tube 7 digest	7.36	0.0147	2.944	0.137	27.38E-05	0.0548	1.2761	1.2766	0.5
beginning far Right	Sr + tube 8 digest	5.44	0.0109	1.360	0.107	21.35E-05	0.0267	1.3139	1.3147	0.8
end far left	Sr + tube 9 digest	0.47	0.0010	0.237	0.011	2.10E-05	0.0052	1.2929	1.2933	0.4
end far right	Sr + tube 10 digest	0.38	0.0008	0.094	0.008	1.59E-05	0.0020	1.2929	1.2937	0.8
Inlet port	Sr – tube 1 digest	22.98	0.0460	2.554	0.002	4.82E-06	0.0003	1.2923	1.2941	1.8
beginning of pores	Sr – tube 2 digest	21.72	0.0434	2.715	0.002	4.94E-06	0.0003	1.3138	1.3154	1.6
1 cm in	Sr – tube 3 digest	2.00	0.0040	0.401	0.000	9.42E-07	9.41E-05	1.3041	1.3051	1
2 cm in	Sr – tube 4 digest	0.68	0.0014	0.151	0.000	6.63E-07	7.36E-05	1.3026	1.3035	0.9
middle	Sr – tube 5 digest	0.19	0.0004	0.032	0.000	4.70E-07	3.95E-05	1.3033	1.3045	1.2
end	Sr – tube 6 digest	0.16	0.0003	0.027	0.000	3.79E-07	3.15E-05	1.2930	1.2942	1.2
beginning far Left	Sr – tube 7 digest	10.39	0.0208	1.485	0.001	2.74E-06	0.0002	1.3132	1.3146	1.4
beginning far Right	Sr – tube 8 digest	4.22	0.0084	0.603	0.001	1.36E-06	9.71E-05	1.3136	1.315	1.4
end far left	Sr – tube 9 digest	0.48	0.0010	0.963	0.000	4.75E-07	0.0005	1.3132	1.3133	0.1
end far right	Sr – tube 10 digest	0.31	0.0006	0.056	0.000	3.56E-07	3.23E-05	1.3028	1.3039	1.1

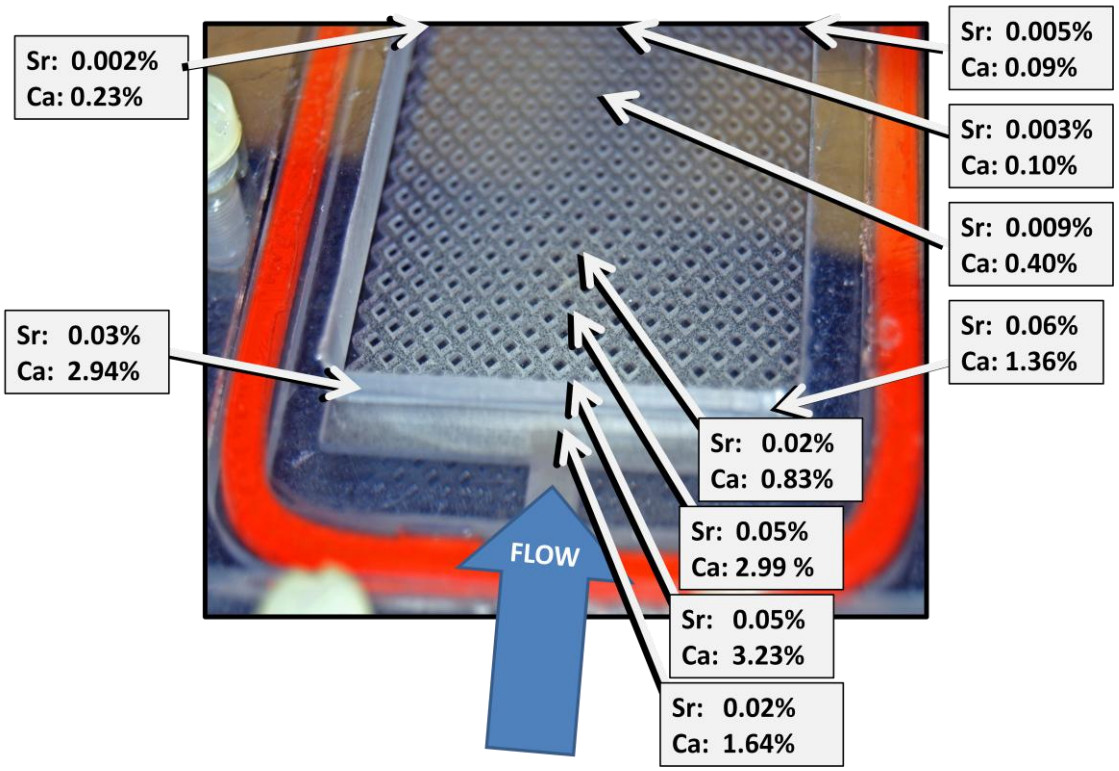

Figure L.3. Precipitates were taken from various locations, dried, weighed, dissolved in acid, and the ionic metal concentrations were measured by ICP-MS. The percentages displayed are the mass percentages of each ion calculated for each extracted precipitate, assuming the precipitates to be calcite. These data were not used to calculate Sr-partitioning due to uncertainty associated with instrumental quantification limits.

APPENDIX M

DETERMINATION OF PARTITION COEFFICIENT

As mentioned in the manuscript titled 'Bacterially Induced Calcite Precipitation and Strontium Co-Precipitation', a strontium partition coefficient was calculated for each reactor in the flat plate strontium co-precipitation study. The equation for the homogeneous partition coefficient is as follows:

$$D_{Sr} = \frac{X_{Sr}}{X_{Ca}} * \frac{[Ca]}{[Sr]} \qquad \text{(Eqn. M.1)} \qquad \text{(Curti et al., 1997)}$$

In this equation, X_i is the mass fraction of component I in the precipitate, and [i] is the concentration of component I in the fluid. For the calculations in Table M.1, the relative fluid concentrations were predicted based on a linearly decreasing spatial concentration gradient between the inlet (media) concentration and the effluent concentration at each time point. In Table M.2, the relative fluid concentrations were predicted based on an exponentially decreasing spatial concentration gradient between the inlet and effluent concentration. An exponential gradient was generated assuming the following exponential equation.

$$y = ae^{-bx} \qquad \text{(Eqn. M.2)}$$

In this equation, x is the location, y is the concentration, and *a* and *b* are fitting parameters. The value for *a* was assumed to be the inlet concentration (y at x = 0), and the value of *b* was determined to fit the value of y (concentration) at location x = 8cm that was measured in the effluent sample.

The mass fraction data was obtained from the swab analyses described above. From this, a D_{sr} was calculated for each time and location, and an average D_{sr} was determined at each reactor location (right column).

Table M.1. Data for prediction of the partition coefficient, based on a linearly decreasing fluid concentration gradient in the reactor

Method 1: Prediction of partition coefficient based on linear gradient of [Ca]/[Sr]												
	[Ca]/[Sr]					**Xsr/Xca**		**Dsr**				
	hr0	hr1	hr6	hr11				hr0	hr1	hr6	hr11	**Avg. Dsr**
inlet	15.95	15.95	15.95	15.95	**inlet**		**inlet**					
1	16.00	14.51	14.41	14.50	**1**	0.0087	**1**	0.139	0.126	0.125	0.126	**0.129**
2	16.05	13.07	12.88	13.06	**2**	0.0090	**2**	0.144	0.117	0.116	0.117	**0.124**
3	16.10	11.64	11.34	11.61	**3**		**3**					
4	16.16	10.20	9.81	10.16	**4**	0.0080	**4**	0.130	0.082	0.078	0.081	**0.093**
5	16.21	8.76	8.27	8.72	**5**		**5**					
6	16.26	7.32	6.74	7.27	**6**	0.0074	**6**	0.121	0.054	0.050	0.054	**0.070**
7	16.31	5.88	5.20	5.82	**7**		**7**					
outlet	16.37	4.45	3.67	4.38	**outlet**	0.0061	**outlet**	0.101	0.027	0.022	0.027	**0.045**

Table M.2. Data for prediction of the partition coefficient, based on an exponentially decreasing fluid concentration gradient in the reactor

Method 2: Prediction of partition coefficient based on exponential gradient of [Ca]/[Sr]												
	[Ca]/[Sr]					**Xsr/Xca**		**Dsr**				
	hr0	hr1	hr6	hr11				hr0	hr1	hr6	hr11	**Avg. Dsr**
inlet	15.95	15.95	15.95	15.95	**inlet**		inlet					
1	16.00	13.60	13.27	13.57	**1**	0.0087	1	0.139	0.118	0.115	0.118	**0.123**
2	16.05	11.59	11.04	11.54	**2**	0.0090	2	0.144	0.104	0.099	0.104	**0.113**
3	16.10	9.88	9.19	9.82	**3**		3					
4	16.16	8.42	7.65	8.36	**4**	0.0080	4	0.130	0.067	0.061	0.067	**0.082**
5	16.21	7.18	6.36	7.11	**5**		5					
6	16.26	6.13	5.29	6.05	**6**	0.0074	6	0.121	0.045	0.039	0.045	**0.063**
7	16.31	5.22	4.41	5.15	**7**		7					
outlet	16.37	4.45	3.67	4.38	**outlet**	0.0061	outlet	0.101	0.027	0.022	0.027	**0.045**
Exp. Equation Values												
a	15.95	15.95	15.95	15.95								
b (goal seek)	0.0032	0.1595	0.1836	0.1615								
value at x=8	16.370	4.452	3.670	4.382								

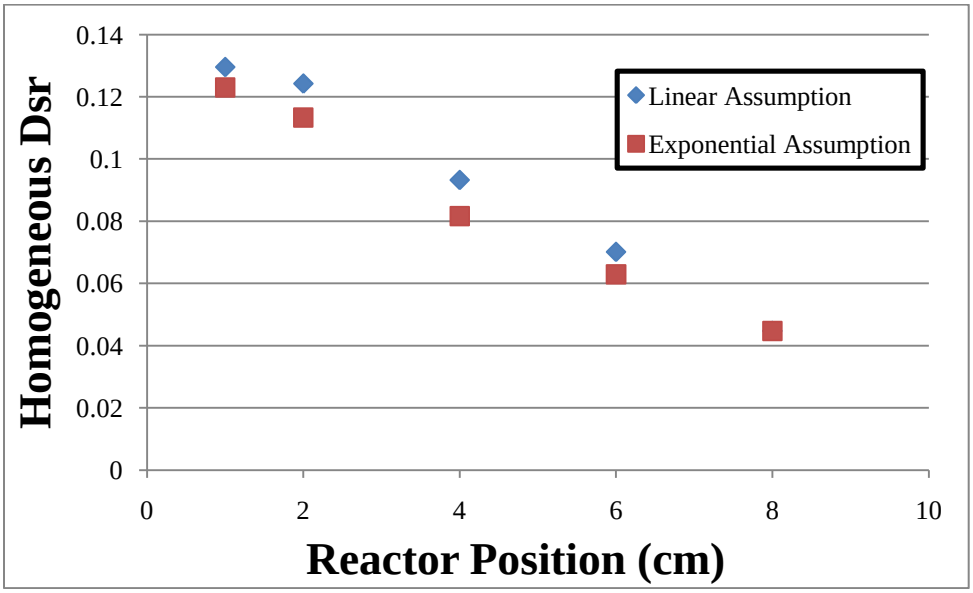

Figure M.1. Graphical representation of the average homogeneous partition coefficient at each location in the reactor based on the linear and exponential assumptions.

An alternative approach was taken to measure the overall average partition coefficient in the reactor. In this method, the overall amount of Ca and Sr that was precipitated throughout the course of the experiment was determined, based on effluent analysis, and a precipitate ratio was calculated. Based on an average between the influent and effluent fluid concentration at each sample time point, an average Ca and Sr fluid concentration in the reactor was calculated, and this ratio was used to determine the fluid concentration ratio. These values are illustrated in Table M.3.

Table M.3. Values for the determination of the overall average partition coefficient in the reactor.

Overall average partition coefficient			
Sr precipitated	2.2958	mg	
	0.0262	mMoles	
Ca precipitated	82.62	mg	
	2.0614	mMoles	
Precipitate Molar Ratio Sr/Ca	**0.0127**		
Sr average concentration (mg/L)	12.92	mg/L	
	0.1475	mMol/L	
Ca average concentration (mg/L)	437.4	mg/L	
	10.91	mMol/L	
Average Fluid Molar ratio [ca]/[sr]	**73.99**		
Overall Average Homogeneous Partition Coefficient			**0.940**

In comparing the two approaches to determine a partition coefficient, it becomes immediately clear that the ‘overall average’ method predicts a much larger partition coefficient (i.e., 0.940 compared to less than 0.123). This is mainly a result of a much higher average fluid ratio, [Ca]/[Sr], in the ‘overall average’ method.

APPENDIX N

MICROSCOPY AND MICROANALYSIS CONFERENCE ABSTRACT

The imaging techniques used to assess biomineralization in capillary flow cells were presented at the 2009 Microscopy and Microanalysis Conference (Microscopy Society of America) in Richmond, VA on July 27, 2009. The abstract for the presentation is as follows:

Imaging Biomineralization in Flow Systems

Logan Schultz, Betsey Pitts,* Robin Gerlach**
**Center for Biofilm Engineering, Montana State University, 366 EPS, Bozeman, MT, 59717*

The precipitation and stability of minerals is strongly correlated with the local chemical environment. The significant influence of bacteria and other micro-organisms on local chemistry in flow scenarios can lead to biologically-induced mineral precipitation. Microscopy can be utilized to characterize the spatial and temporal development of microbes, minerals, and extracellular polymeric substances (EPS) in a fully hydrated and non-invasive manner. Due to a lack of dehydration artifacts, this imaging situation is tremendously useful for elucidating spatial relationships of these components.

In this study, the soil bacterium *Sporosarcina pasteurii* was introduced in flow cells with 1mm pore spaces and grown in the presence of a medium containing dissolved calcium and urea. *S. pasteurii* effectively hydrolyzes urea, which increases the pH and induces calcite precipitation. Stereo microscopy conducted in real-time demonstrated temporal and spatial differences in precipitation. Analysis of these images quantified precipitate size and density, providing a basis for calculations in pore-space reduction and substrate conversion.

Confocal scanning laser microscopy after staining with Syto11 and C_2-dichlorotriazine was used to image the spatial relationships of the cells, EPS, and minerals. It was expected that the Syto11 would bind to nucleic acids associated with cells and the C_2-dichlorotriazine would bind to alcohols and polysaccharides associated with EPS. While maintaining a fully hydrated state in the reactors, two-dimensional images were taken at 0.5μm depth increments through the samples and compiled in z-stacks to reproduce three-dimensional topographical images. It was evident from the images that the bacteria adhered preferentially to the calcite surfaces. Ongoing investigations are seeking to gain a better understanding of the association of bacteria throughout the developmental stages of the precipitates and better understand the biological environment at the interior of the precipitates.

In designing methods to control biomineralization in fouling scenarios or to manipulate hydraulic transport properties of porous media, novel methods in microscopy prove to be an invaluable tool. This presentation will highlight some techniques, capabilities, and difficulties associated with imaging biomineralization in flow systems.

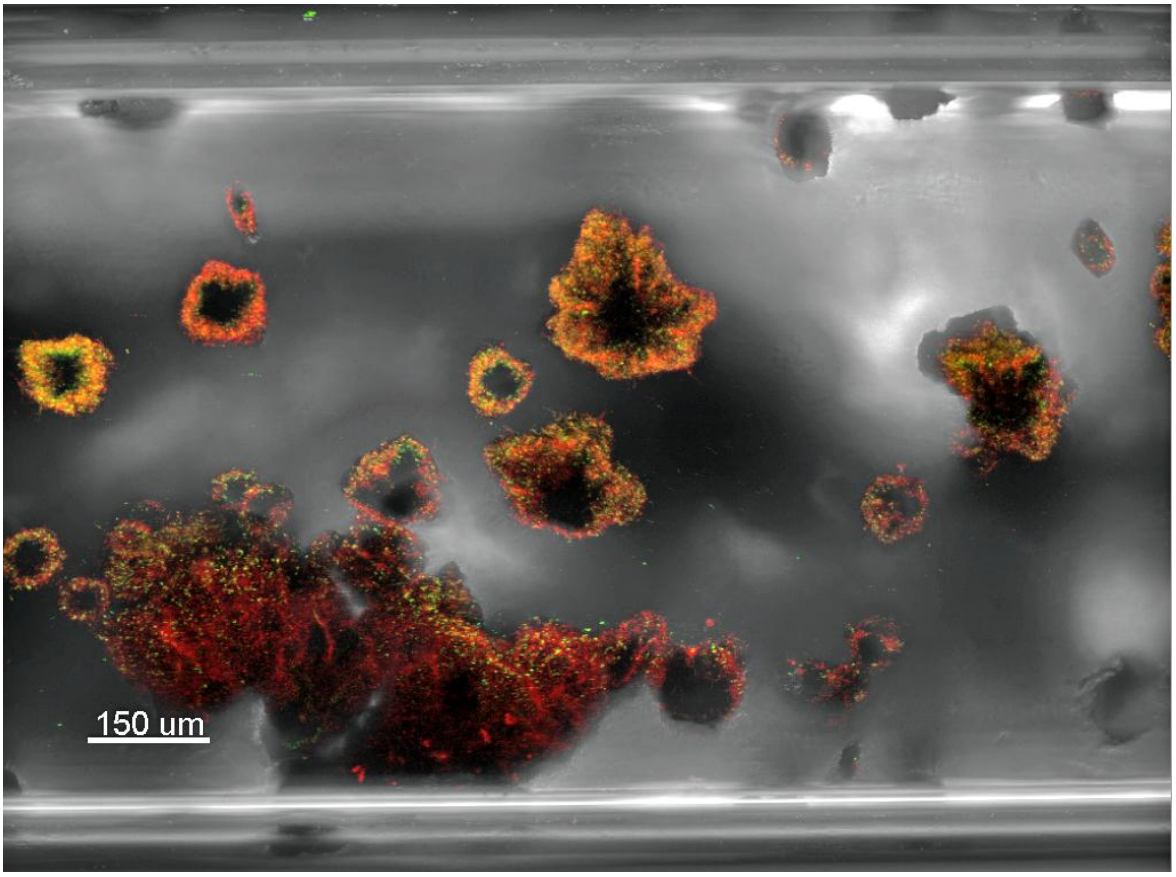

Figure N.1. Confocal scanning microscope image of a capillary flow cell with biomineralized $CaCO_3$ surrounded by fluorescence stained microbial communities.

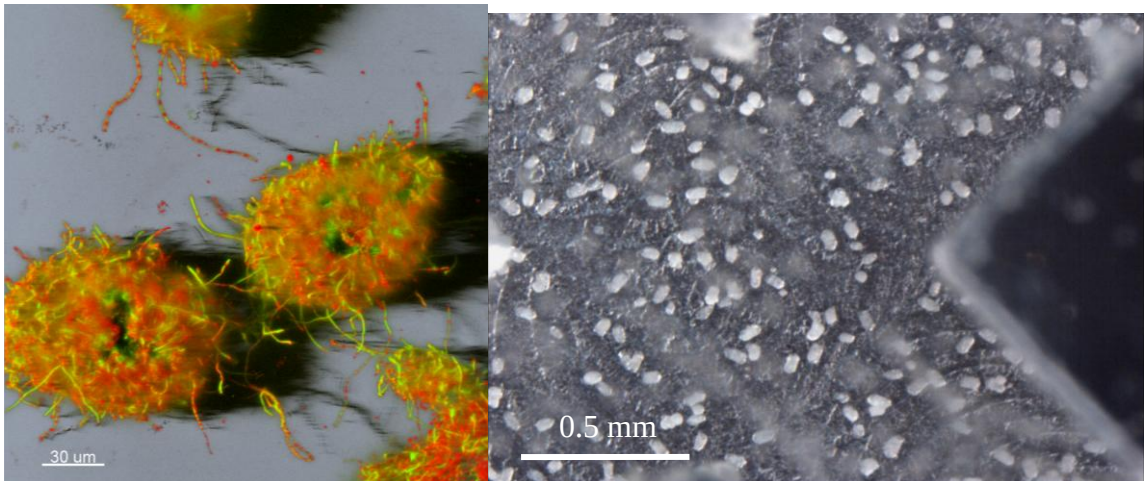

Figure N.2. (left) Three-dimensional reconstruction of surface-attached $CaCO_3$, elucidating the prolific attachment of microbes to the calcite exterior. (right) Stereo microscope image of $CaCO_3$ attached to the bottom of a flow cell, providing the means to characterize size and distribution of precipitates.

APPENDIX O

TIME LAPSE IMAGES

Figure O.1. System being viewed under stereo microscope

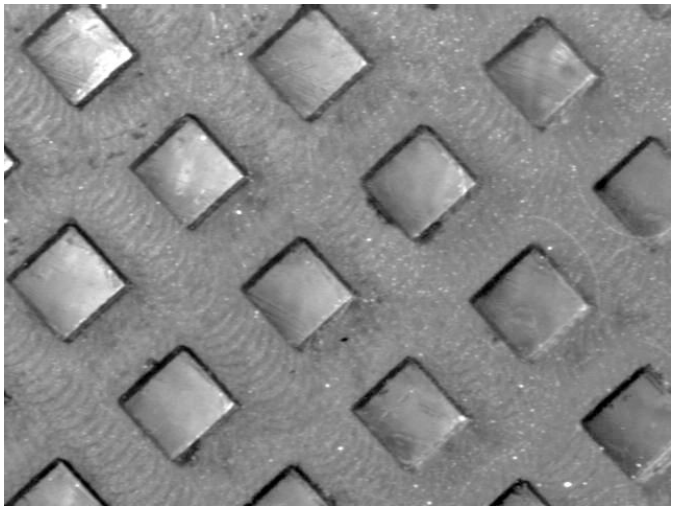

Figure O.2. Mineral deposition after 40 minutes

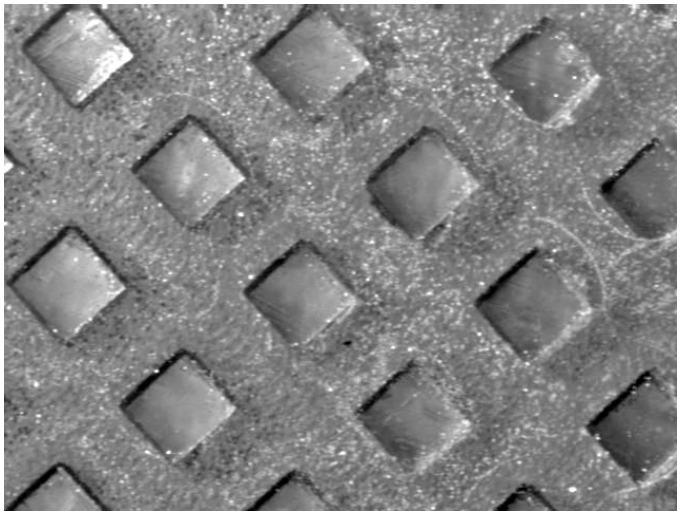

Figure O.3. Mineral deposition after 100 minutes

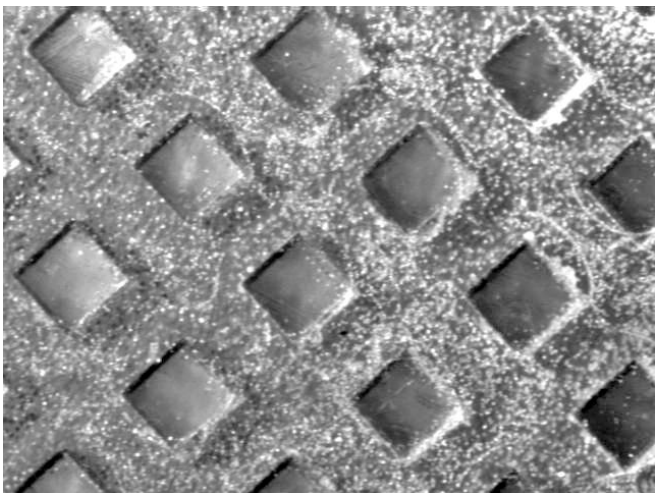

Figure O.4. Mineral deposition after 200 minutes

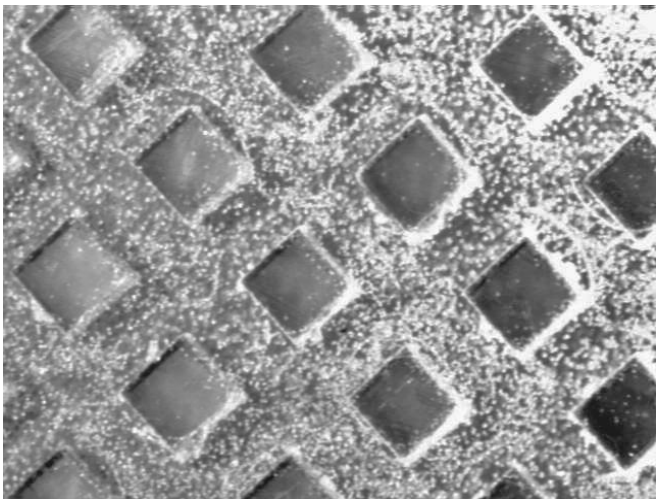

Figure O.5. Mineral deposition after 340 minutes

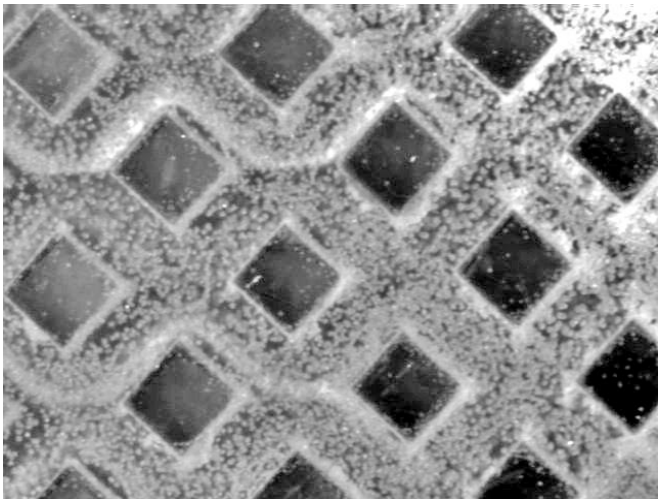

Figure O.6. Mineral deposition after 620 minutes

APPENDIX P

ADDITIONAL CONFOCAL IMAGES

The following images, taken on the confocal microscope, were not included in the manuscript submitted to Microscopy Today.

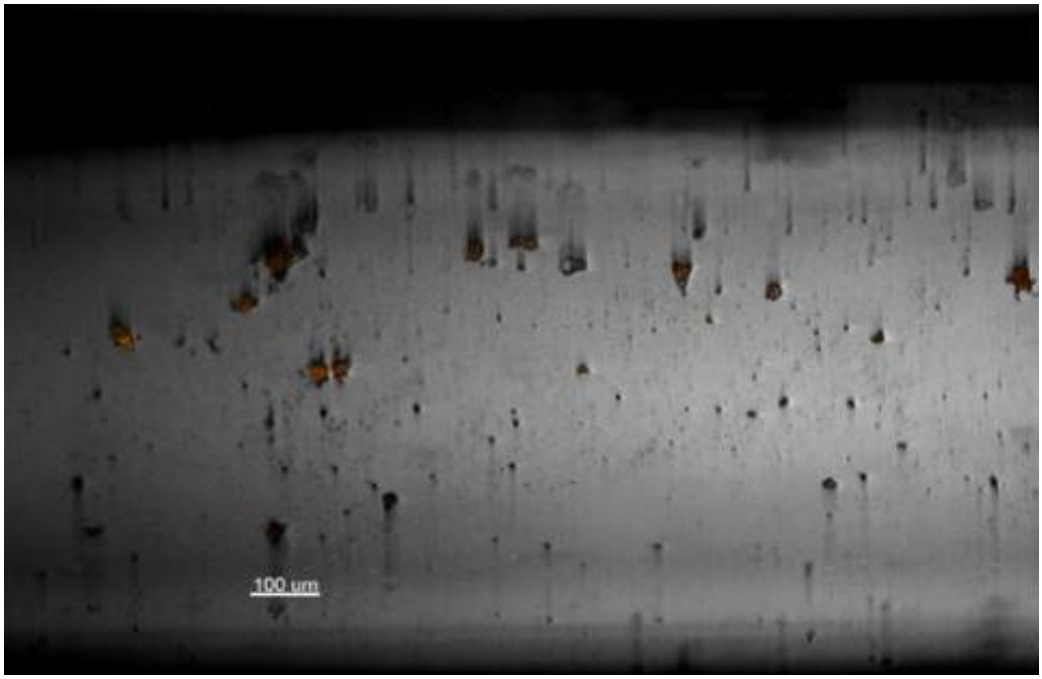

Figure P.1. Confocal image of capillary reactor one hour after inoculation

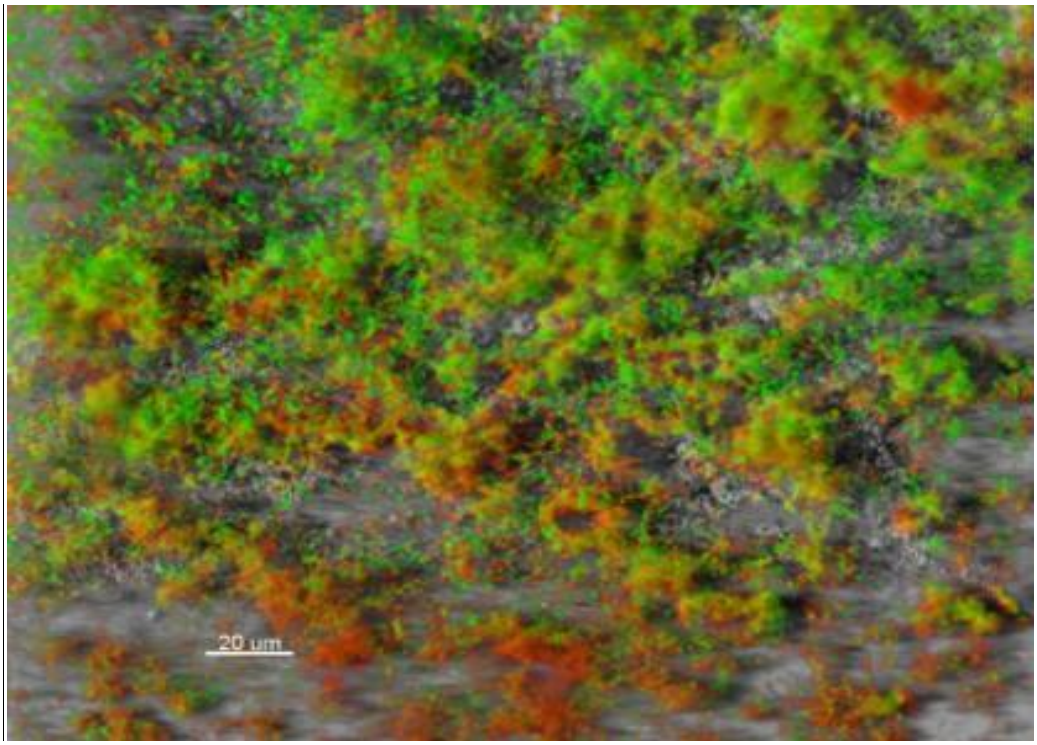

Figure P.2. Confocal image of capillary reactor one day after inoculation

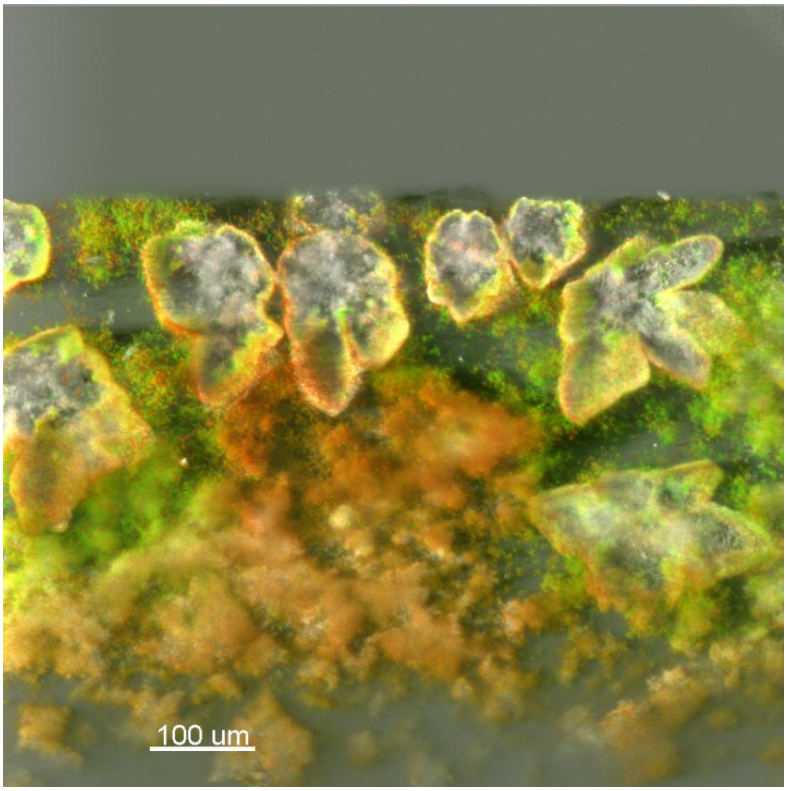

Figure P.3. Confocal image showing large precipitates surrounded by biomatter

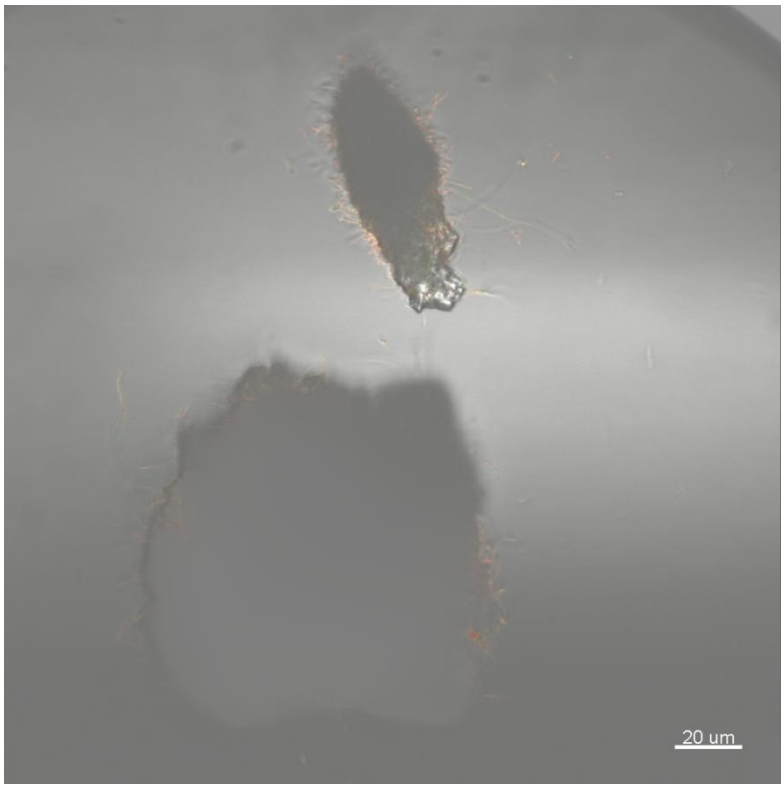

Figure P.4. Confocal image showing individual rod-shaped bacteria attached to precipitates

APPENDIX Q

COLUMN REACTOR STUDY

A constant flow reactor system (Figure Q.1) was designed to conduct RTD analysis through packed bed columns of 1cm inner diameter and 2.5cm length. *Cellulomonas* sp. ES6 was the inoculum, and 1:10 dilution TSB was the flow medium.

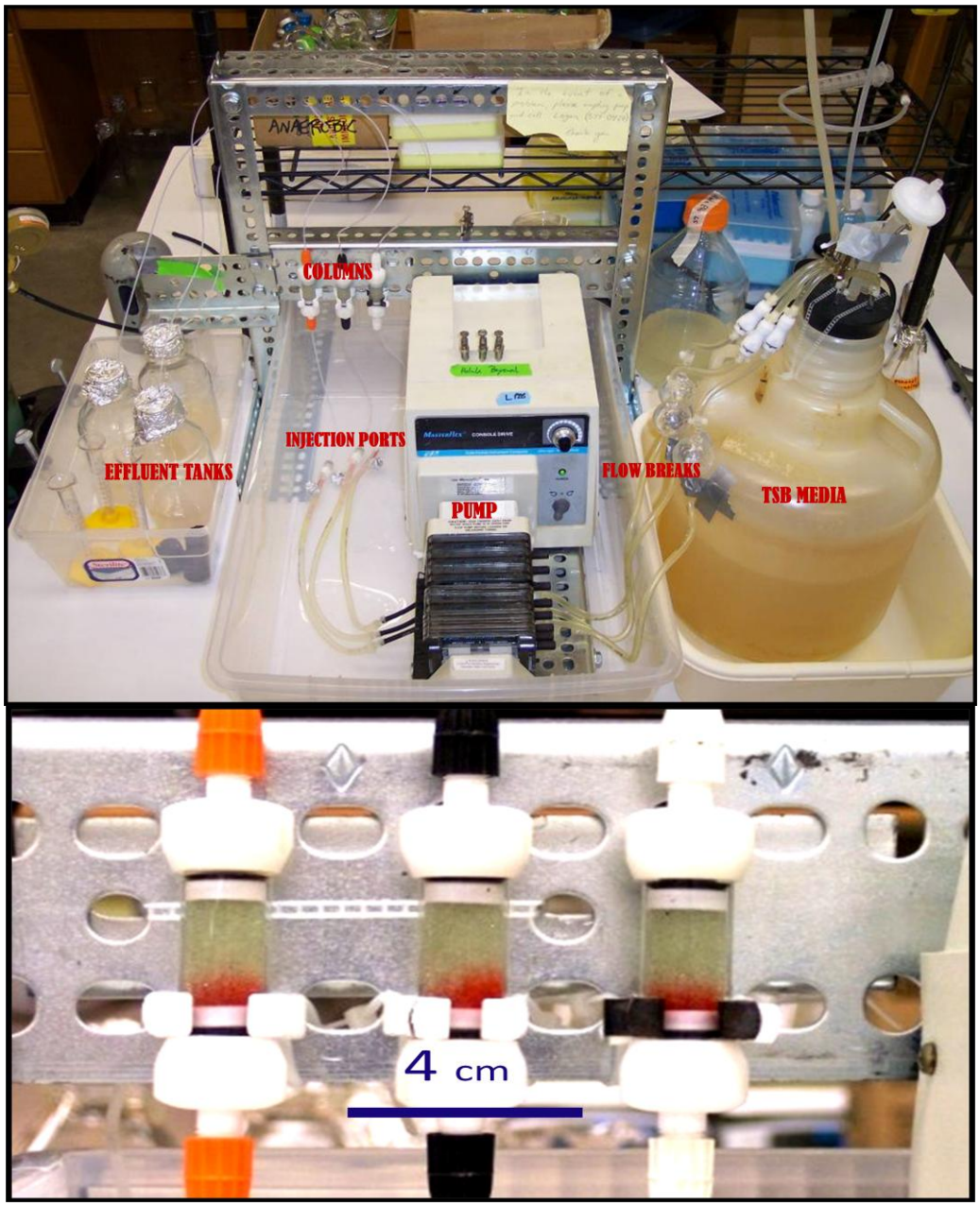

Figure Q.1. (above) Constant flow reactor system with packed bead columns. Flow proceeds from right to left across the system and upward through the columns. (below) Image of dye flowing through packed bead columns.

RTDs were taken over several days through four unique columns (Figure Q.2). One column contained 0.5mm (diameter) glass beads, one column contained 1mm beads, one column contained 2mm beads, and one column contained a gradient mixture of the three sizes. For the gradient mixture, 2mm beads were first placed in the column until it was one third full, then followed by 1mm beads and finally 0.5 mm beads on the top one third.

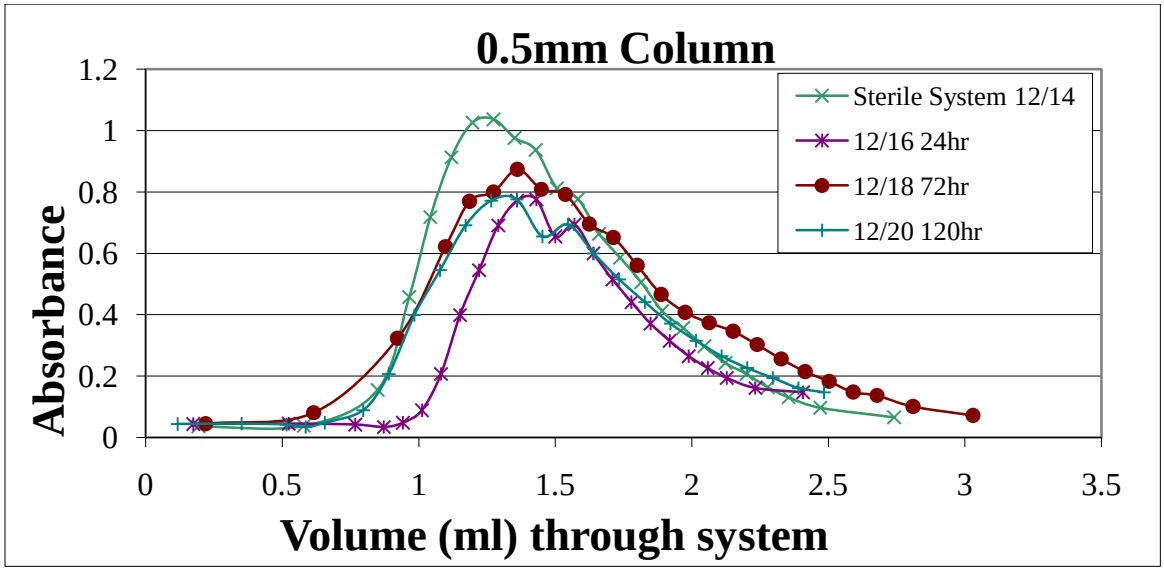

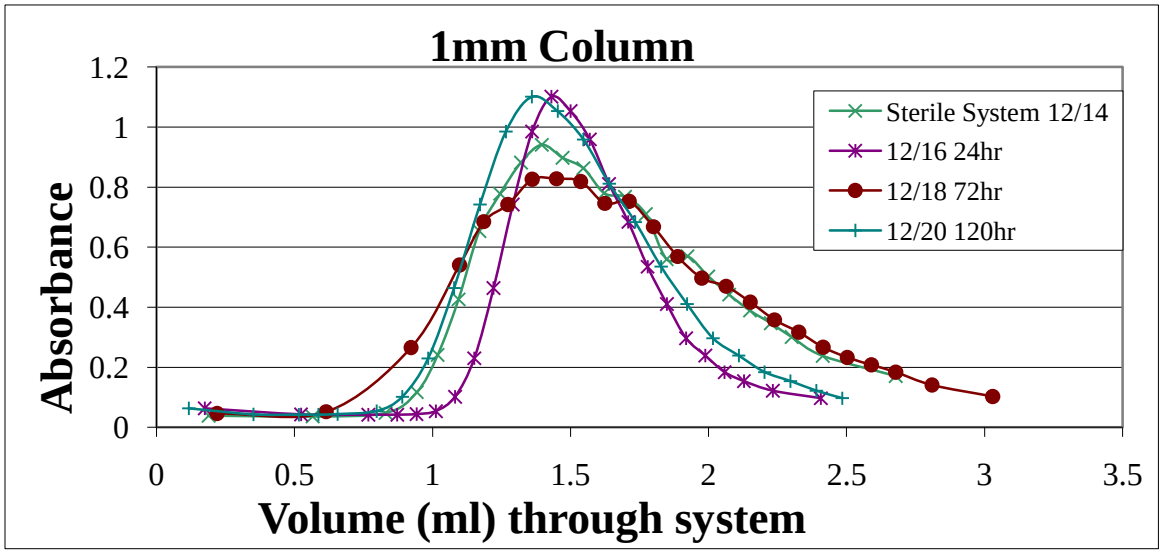

Figure Q.2. Residence time distributions for columns with 0.5 and 1mm glass beads

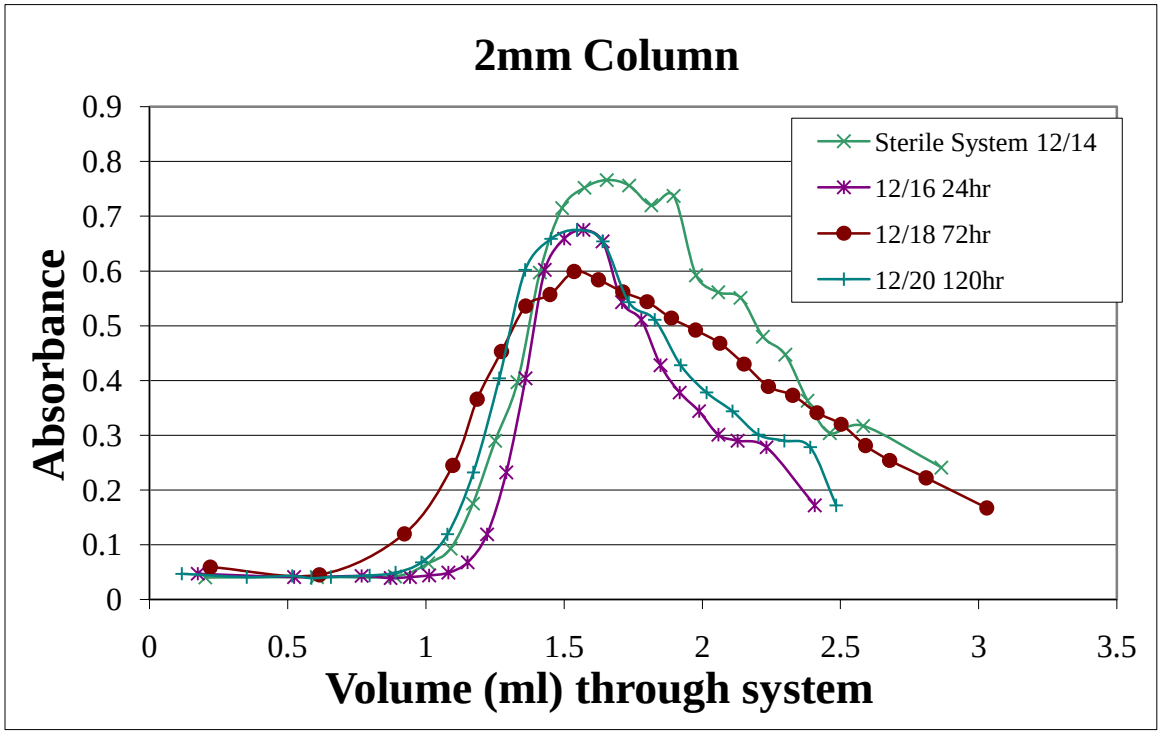

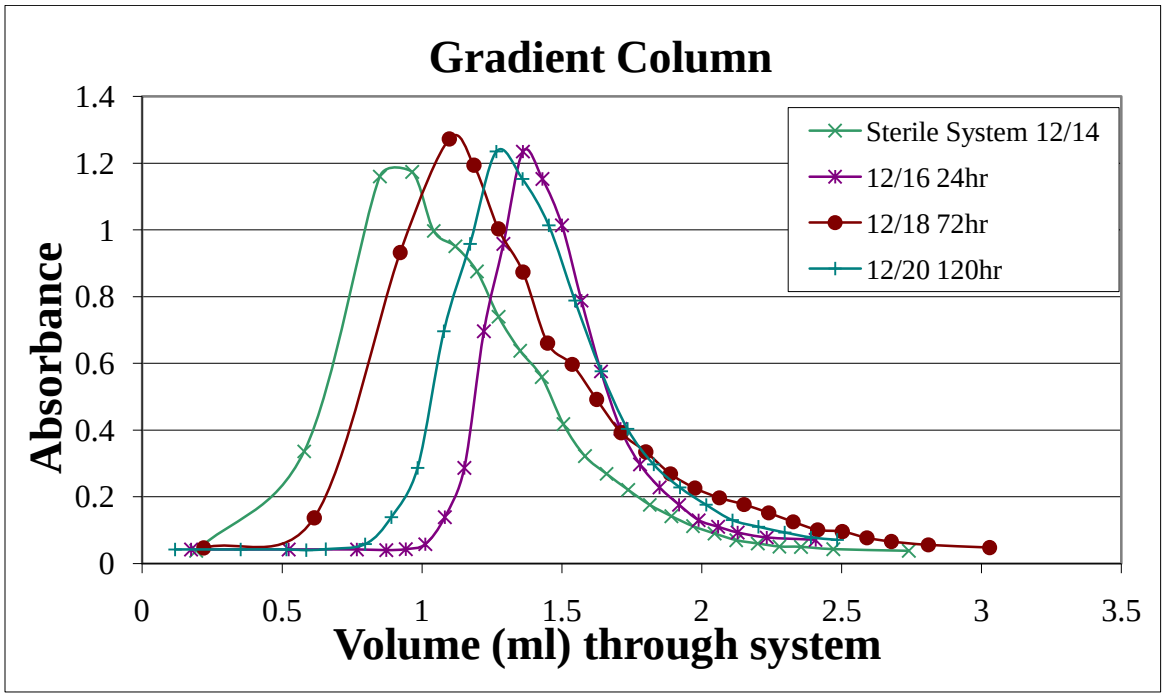

Figure Q.3. Residence time distributions for columns with 2mm and gradient glass beads

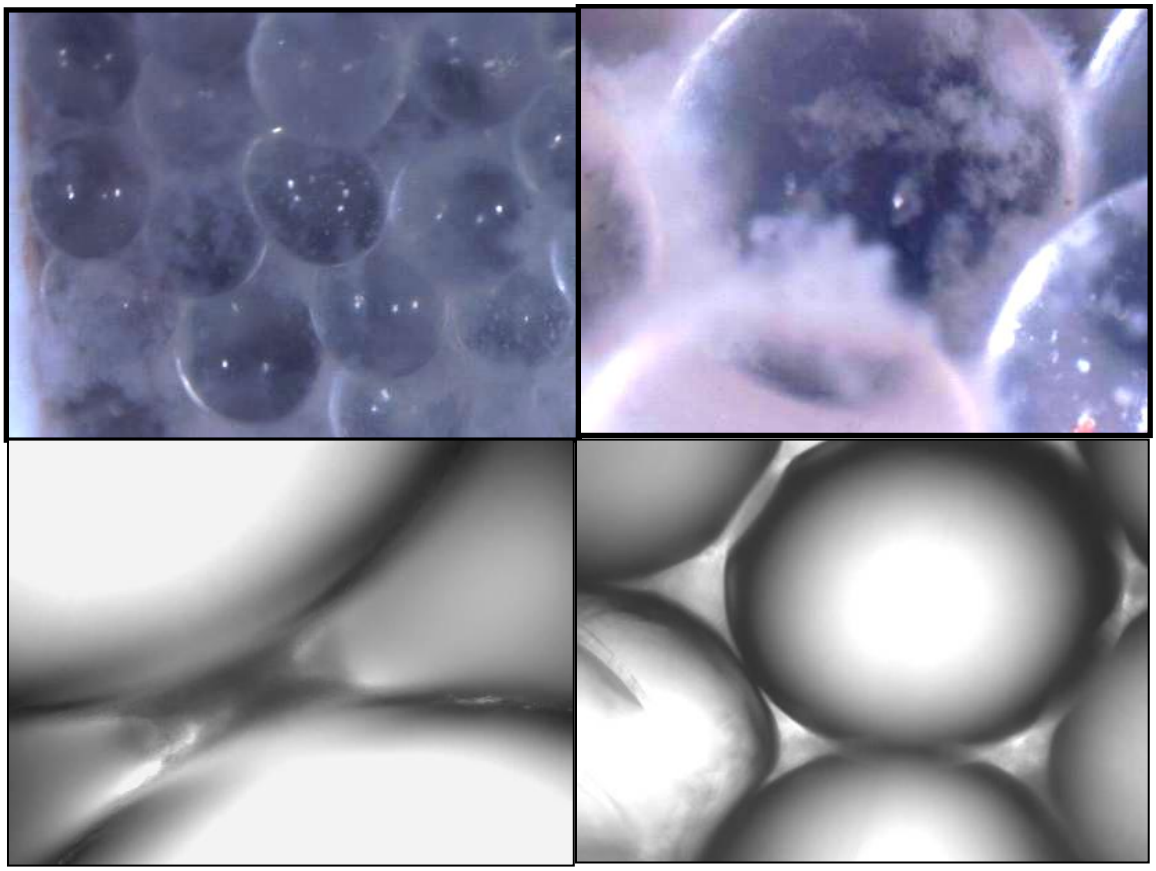

Figure Q.4. Selected stereo microscope images taken of the beads. The images on the top were taken through the wall of the column (i.e., *in situ*). The images on the bottom were taken of beads that were extracted from the columns. The cloudy substance that appears to surround the beads is believed to be biofilm.

In all columns, the effective porosity did not appear to decrease significantly in spite of visible biofilm accumulation. This is believed to be caused by the observation of distinct, preferential flow paths in the clean reactors (i.e., heterogeneous flow). Since the column diameters were small relative to the bead sizes, the wall effects were evident as well as visual air pockets within the bead packs that led to heterogeneous flow. The gradient column in particular had an apparent increase in porosity. This may have been due to the ability of attached microbes to effectively homogenize the flow path.

APPENDIX R

POROSITY AND PRESSURE DROP MODEL SPREADSHEET

Table R.1. Porosity and Pressure Drop Model Spreadsheet

A1	B	C	B	C	B	C	B	C	
2									
3		DATA							
4	Day	K/Ko (ΔP0/ΔP)	β (V/Vo)						
5	0	1	1.00						
6	1	1	1.00		g	981	cm/s^2		
7	5	0.006666667	0.62		L	10.66	cm		
8	7	0.001818182	0.33		λ	0.1			
9	9	0.002857143	0.40		Δho	1.80679E-05	cm		
10	12	0.005128205	0.38		Surface Area	67.94968	cm^2		
11	24	0.005882353	0.38		Vo	3.98	cm^3		
12	34	0.005263158	0.48		initial velocity	0.057666667	cm/s		
13	35	0.006666667	0.53						
14	37	0.01	0.63					βmin	
15	42	0.04	0.53					0.20	
16	49	0.003508772	0.30				c	a	
17							3	-0.75	
18									
19	β (V/Vo)	bf thickness	pore diam.	Velocity	bf predicted Δh	bf predicted Δho/Δh	par. Model	pore net. Model	
20	0.20	4.69E-02	6.28E-03	2.88E-01	7.19E-03	2.51E-03	3.20E-04	0.00E+00	
21	0.25	4.39E-02	1.21E-02	2.31E-01	2.38E-03	7.59E-03	9.77E-04	6.65E-03	=$H$17*(((A21-$H$15)/(1-$H$15))^3)+(1-$H$17)*(((A21-$H$15)/(1-$H$15))^2)
22	0.30	4.10E-02	1.80E-02	1.92E-01	1.12E-03	1.62E-02	2.43E-03	2.59E-02	
23	0.35	3.81E-02	2.39E-02	1.65E-01	6.18E-04	2.92E-02	5.25E-03	5.66E-02	=A23^$G$17
24	0.40	3.51E-02	2.97E-02	1.44E-01	3.80E-04	4.75E-02	1.02E-02	9.77E-02	
25	0.45	3.22E-02	3.56E-02	1.28E-01	2.51E-04	7.20E-02	1.85E-02	1.48E-01	=$F$9/E25
26	0.50	2.93E-02	4.14E-02	1.15E-01	1.74E-04	1.04E-01	3.13E-02	2.07E-01	
27	0.55	2.64E-02	4.73E-02	1.05E-01	1.26E-04	1.43E-01	5.03E-02	2.72E-01	=$F$8*($F$7/C27)*((D27^2)/(2*$F$6))
28	0.60	2.34E-02	5.31E-02	9.61E-02	9.44E-05	1.91E-01	7.78E-02	3.44E-01	
29	0.65	2.05E-02	5.90E-02	8.87E-02	7.25E-05	2.49E-01	1.16E-01	4.20E-01	=3.46/(A29*60)
30	0.70	1.76E-02	6.49E-02	8.24E-02	5.69E-05	3.18E-01	1.68E-01	5.00E-01	
31	0.75	1.46E-02	7.07E-02	7.69E-02	4.54E-05	3.98E-01	2.37E-01	5.83E-01	=0.1-(2*B31)
32	0.80	1.17E-02	7.66E-02	7.21E-02	3.69E-05	4.90E-01	3.28E-01	6.68E-01	
33	0.85	8.79E-03	8.24E-02	6.78E-02	3.03E-05	5.96E-01	4.44E-01	7.53E-01	=($F$11-(A33*$F$11))/$F$10
34	0.90	5.86E-03	8.83E-02	6.41E-02	2.53E-05	7.15E-01	5.90E-01	8.37E-01	
35	0.95	2.93E-03	9.41E-02	6.07E-02	2.13E-05	8.50E-01	7.74E-01	9.20E-01	
36	1.00	0.00E+00	1.00E-01	5.77E-02	1.81E-05	1.00E+00	1.00E+00	1.00E+00	

APPENDIX S

EMBEDDED CAPILLARY EXPERIMENTAL PROTOCOL

This experiment has been designed to supplement previous confocal studies. This experiment embeds the interior of the capillaries in LR White epoxy resin, and allows for the potential of cross-sectional slicing and TEM tomography. This will hopefully address the biological environment at the interior of the precipitates which has been optically-limited in confocal imaging.

Protocol for Capillary Experiment (March 2009)

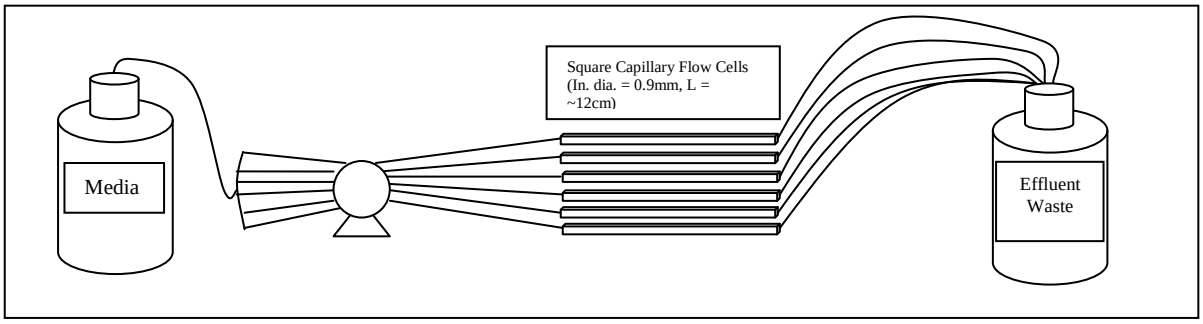

Figure S.1. Capillary flow cell system schematic

Purpose:

- *Supplement and build upon previous capillary studies*

Specific Goals:

1. Embed 2 flow cells in LR White to be sent to Alice Dohnalkova (Pacific Northwest National Laboratory)
2. Obtain a time series of 4 reactors to more accurately assess nucleation and growth stage
3. Add a stack of reflection images to visualize calcite and overlay with fluorescent stacks

Necessary Equipment:

- 6 capillary flow cells connected to peristaltic pump
- BHI and Urea (20 g/L) for culturing
- Calcium-containing F&S media
- LR white resin
- PBS
- Ethanol series for dehydration (30, 50, 75, 90, 100) made in appropriate buffer (match salt content of F&S media)
- *Sporosarcina pasteurii* frozen culture
- 2.5% gluteraldehyde for fixation

Timeline:

Day 1:

- Start culture (frozen stock in 50ml BHI/Urea) on shaker at 30C

Day 2:

- Autoclave capillary systems, connect to CMM+ media source
- Begin flowing at 0.02 ml/min (velocity: ~2 cm/min)
    - Note: This FR was previously attained at a pump setting of 0:80 with size 13 tubing
- Transfer culture at 24 hours

Day 3:

Hour 0: (with 18 hr culture) inoculate each clamped-off system with 1ml
Hour 3: Start flow

Day 4: Confocal Day 1

- With one capillary, take a few stereoscope images, then go through staining procedure (see below) and image on confocal with Betsey

Days 5 and 6:

- *Same procedure as Confocal day 1*

Day 7: Confocal Day 4 and Embedding Day

- *Same procedure for confocal imaging of one capillary*
- Embedding Procedure (See Below) if precipitates are visible… otherwise, wait longer

Embedding procedure

For two identical reactors

1. Fixation
    a. Attach system to 2.5% gluteraldehyde source
    b. Pump at same flow rate (0.02 ml/min) for 2 hours
2. Wash in PBS
    a. Attach to PBS and flow for 20 minutes (over three pore volumes)
3. Dehydrate in Ethanol series
    a. Attach to 30% ethanol and flow for 20 minutes
    b. Repeat (a) for 50% EtOH
    c. Repeat (a) for 75% EtOH
    d. Repeat (a) for 90% EtOH
    e. Repeat (a) for 100% EtOH
4. Resin infiltration
    a. Attach to 50:50 Resin/EtOH mix and flow for 20 minutes
    b. Attach 100 percent Resin and flow for 40 minutes
    c. Stop flow, clamp system and let sit overnight (Thermal Cure) at 60°C
5. Store cured capillaries in refrigerator (4°C) until sending off for imaging
6. Prior to sending, remove glass from hardened resin
    a. Remove tubing from each end of capillary
    b. With gloves, gently rub capillaries lengthwise along coarse stained-glass etching stone
        i. In the event that a capillary breaks, mark with the following system:

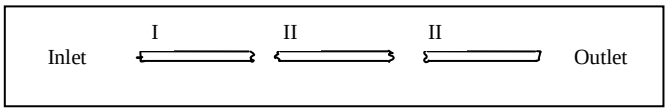

APPENDIX T

RADIAL FLOW REACTOR

The images below show a tracer dye flowing through a radial flow reactor with etched 1mm pore spaces. This reactor is similar in construction to the flat plate reactors used in this thesis, but provides a unique flow environment with an average pore velocity that decreases with distance from the inlet port. Biofouling and biomineralization investigations in these reactors will provide valuable information to future researchers.

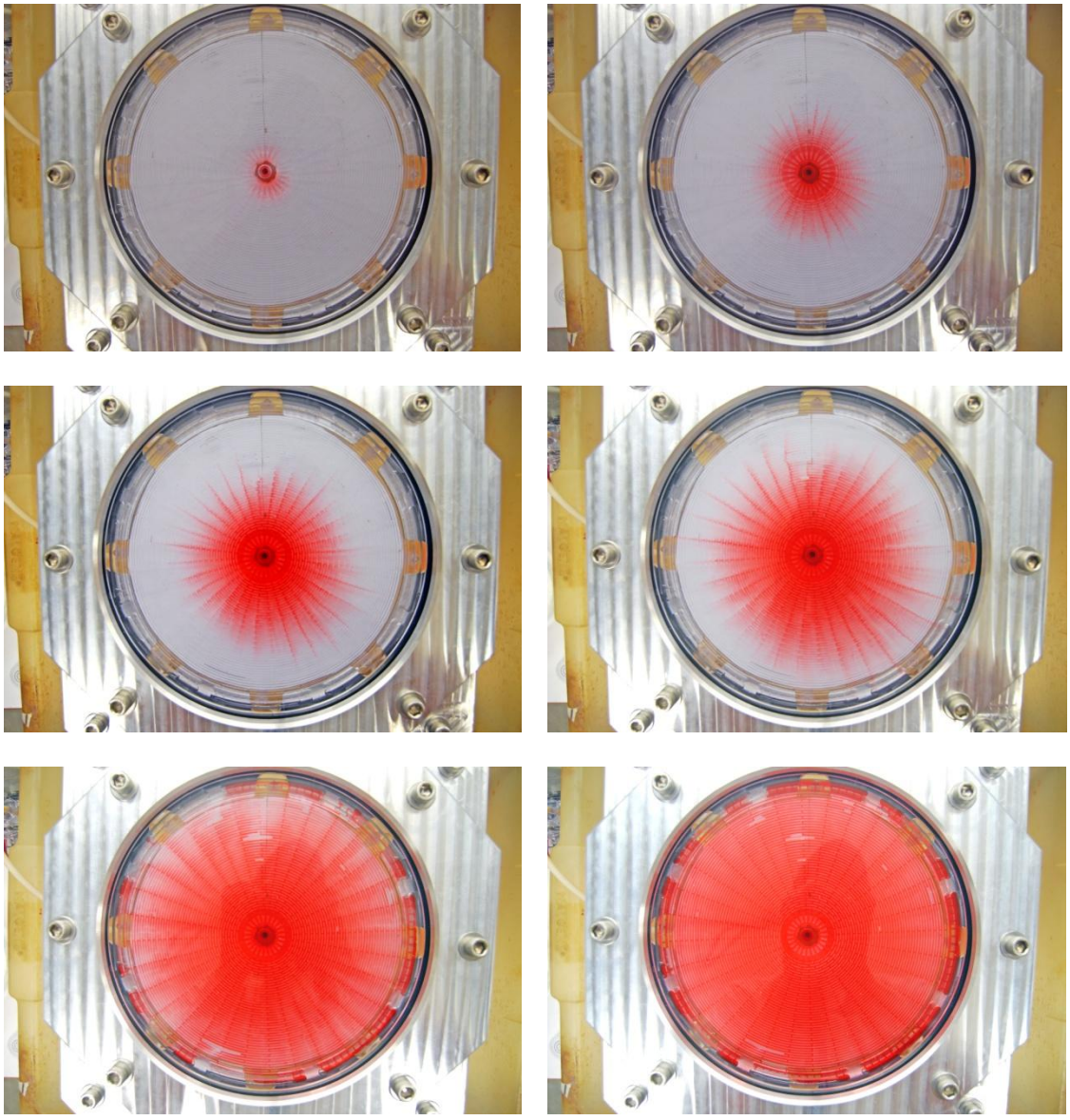

Figure T.1. The top left image shows a tracer dye entering the radial reactor. The time series proceeds from left to right and top to bottom, showing dye flowing outward towards 8 effluent ports.